Mathematical modeling of cancer cell migration
-
from *in vitro* to *in vivo*

by

Jahn Otto Waldeland

Thesis submitted in fulfillment of
the requirements for degree of
PHILOSOPHIAE DOCTOR
(PhD)

University
of Stavanger

Faculty of Science and Technology
Department of Energy and Petroleum Engineering
2020

Acknowledgements

First and foremost, I am very grateful to have had Steinar Evje as my supervisor. After every encounter with Dr. Evje I have become highly motivated to continue my research and to generate results. He has been a wonderful mentor providing valuable feedback and thoughts on future developments with regard to the mathematical model, while also encouraging me to pursue my own ideas.

I also want to thank Professor William Polacheck, and members of his team, for allowing me to visit their laboratory at The Universtiy of North Carolina in Chapel Hill. Through the visit I gained more on-hands experience as to what I am actually modeling, and made me respect the field of bioengineering even more. Dr. Geir Nævdal also deserves a thank for taking the time to introduce me to the exciting field of parameter optimization.

Furthermore, I would also like to thank members of the department of Energy and Petroleum Engineering for helping me whenever I had practical questions related to my PhD. In addition, I want to thank my colleagues, and a special thank to Yangyang Qiao, for creating a happy work environment.

I want to thank my parents for showing interest in what I am researching and making sure I stay motivated throughout my research. Finally I want to thank my supportive spouse for encouraging me from the moment I started my PhD study.

Abstract

T UMORS has been the object of computational model studies for nearly five decades. The early models considered simple tumor growth based on nutrients, whereas models now can simulate from microscale gene expressions in cells to the larger scale tissue, and even a combination of micro and macroscale models in hybrid models. In this thesis we apply a continuum model to capture different mechanisms that cause tumor cells to move. More precisely, the interaction between different cells and the flowing fluid in tissue through forces are investigated upon. The first versions of the model attempt to capture behavior found in experimental work performed in controlled environments, and evolves to better align with how a realistic tumor may act.

The first paper (Paper I) in this thesis formulates a two-phase model consisting of a tumor cell and interstitial fluid phase. It relies upon the experience gained from creeping flow in petroleum reservoirs with regards to the interaction forces and how fluid flow is described. The model in Paper 1 is motivated by the experimental work by Shields et al. 2007 that identifies a tumor cell migration mechanism called autologous chemotaxis. This means that due to interstitial fluid flow, tumor cells creates a chemical gradient in the flow direction of its own fruition, letting cancer cells migrate downstream.

The second part of this thesis (Paper II & III) extends the two-phase model in Paper I to include a new mechanism. Paper II maintains autologous chemotaxis as a migration mechanism and introduces a new one, rheotaxis. Rheotaxis is considered a competing mechanism to chemotaxis in the study by Polacheck et al. 2011, where fluid flow imposes a stress on the cancer cells and causes them to migrate in the upstream direction. These two competing mechanisms are explored in a computational context in Paper II. After in-depth investigation into the different parameters in the model in Paper II, the model is extended to a two-dimensional domain. This allows for better visualization, while at the same time illustrating the potential of the model as a tool to explore how tumor cells may escape from the primary tumor to metastasize.

In the next part (Paper IV & V) a new phase in introduced, resulting in a three-phase model. The new phase is a common component of both normal and cancerous tissue, namely fibroblast cells. In our model we look at tumor-associated fibroblasts (TAFs) which behave differently from their normal counterpart. Motivated by the experimental work by Gaggioli et al. 2007; Labernadie et al. 2017; Shieh et al. 2011, we investigate two different methods TAFs use to enhance tumor cell migration, in the presence of interstitial fluid flow (Paper IV). In Paper V the model is used in a 2D setting, showing that fibroblasts may lead

cancer cells in a collective manner towards draining lymphatics as a means for metastasis. It is also suggested targeting fibroblast-cancer cell interaction as a method to decrease metastasis.

In the last part (Paper VI) the three-phase model is used to elucidate that ECM structures within the tumor can cause heterogeneous interstitial fluid pressure based on preclinical data from xenograft models in Hansem et al. 2019. One important aspect of the computational model is to achieve a realistic interstitial fluid pressure and fluid velocity, which is measured in the experimental data. We achieve similar results with regards to the pressure under the various circumstances explored in Hansem et al. 2019, and give rise to heterogeneous migration pattern with possibility for formation of isolated islands of tumor cells.

List of Papers

Paper I

Waldeland, Jahn Otto, Evje, Steinar. 'A multiphase model for exploring tumor cell migration driven by autologous chemotaxis' In: *Chemical Engineering Science,* **191** pp. 268-287 (2018)

Paper II

Waldeland, Jahn Otto, Evje, Steinar. 'Competing tumor cell migration mechanisms caused by interstitial fluid flow' In: *Journal of Biomechanics,* **81** pp. 22-35 (2018)

Paper III

Evje, Steinar, Waldeland, Jahn Otto. 'How tumor cells can make use of interstitial fluid flow in a strategy for metastasis' In: *Cellular and Molecular Bioengineering,* **12** pp. 227-254 (2019)

Paper IV

Urdal, Jone, Waldeland, Jahn Otto, Evje, Steinar. 'Enhanced cancer cell invasion caused by fibroblasts when fluid flow is present' In: *Biomechanics and Modeling in Mechanobiology,* **18** pp. 1047-1078 (2019)

Paper V

Waldeland, Jahn Otto, Polacheck, William, Evje, Steinar. 'Collective tumor cell migration in the presence of fibroblasts' In: *Journal of Biomechanics,* **100** (2020)

Paper VI

Waldeland, Jahn Otto, Gaustad, Jon-Vidar, Rofstad, Einar K., Evje, Steinar. 'In silico investigations of intratumoral heterogeneous interstitial fluid pressure' Submitted

Contents

Contents

Chapter 1

Introduction

Cancer has for a long time been considered to originate through a series of mutations, consequently leading to the acquisition of typical hallmarks such as uncontrolled tumor growth, evasion of apoptosis and may also induce angiogenesis, formation of new blood vessels (Hanahan et al. 2011). However, the main majority of cancer-related death are not caused by the primary tumor, but by metastasis in other parts of the body (close to 90%). Therefore, the activation of cancer cells to start invading and metastasize is the most important hallmark of cancer.

1.1 The tumor and its environment
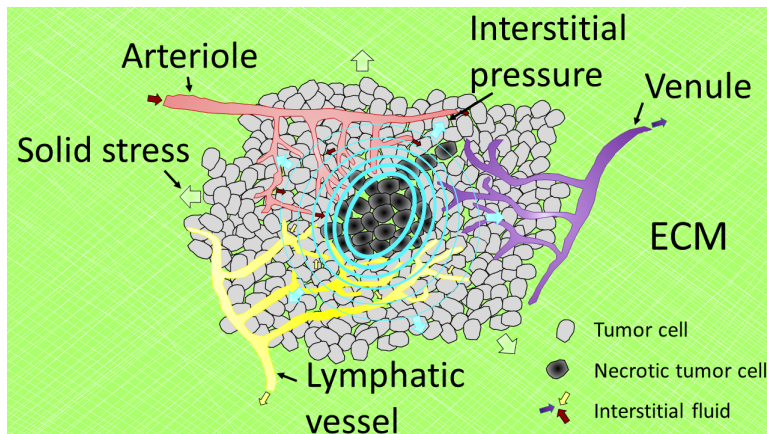
Figure 1.1: **Tumor Microenvironment (TME):** a simplified schematic to illustrate some of the components of the tumor microenvironment. In addition, some of the mechanical properties are illustrated: solid stress exerted by the growing tumor (gray arrows), extracellular matrix (green), elevated levels of interstitial pressure (blue arrows) and also increased interstitial flow (red, purple and yellow arrows).

The tumor microenvironment which surrounds and encapsulates the tumor consists of extracellular matrix (ECM), stromal cells (such as fibroblasts) and immune cells (T cells) (Chen et al. 2015). The ECM is made out of a non-cellular meshwork of a wide variety of proteins. One can consider the ECM a physical scaffold for its surrounding cells when structured in an orderly fashion. The majority of the ECM consists of collagens, which accumulates to about 30% of the total protein mass in the human body (Frantz et al. 2010).

In healthy human tissue the ECM is being remodeled to maintain its tissue integrity and function, meaning that new collagens are being synthesized to replace older proteins that are degraded. The process of production and assembly of collagen is highly regulated in healthy tissue by a perfect interplay between metalloproteinases (MMPs) and the inhibitors of MMPs (Bonnans et al. 2014).

In the event of cancer, the dynamics pertained to the ECM is altered. The amount of MMP secreted by cancer cells is increased, which in turn will remodel and degrade more of the collagen tissue. The degradation of the ECM liberates an abundance of pro- and antitumor signals that is chemically bound to the ECM, leading to a complex chaos (Nissen et al. 2019).

1.2 Interstitial fluid flow

Aside from the structural molecules of the ECM and cells in the interstitium, there is interstitial fluid (IF). The IF is filtrated through the blood vessels and consequently drained by the lymphatics. The fluid transport nutrients and waste products between the cells in addition to signaling molecules. As IF is produced from transcapillary filtration and cleared by lymphatic vessels at a different location in the tissue, a fluid flow field is established.

The blood vessels within a tumor are considered more permeable and leaks IF into the tumor interstitial space. At the same time, the lymphatics that resides within the tumor are dysfunctional and has trouble absorbing the excess fluid. This increases the interstitial fluid pressure (IFP) within the tumor (Jain 1987). Having an elevated IFP is one of the hallmarks of the TME, and causes a major physiological barrier to the transport of drugs through the vasculature. As the vessels are inside the tumor and causes a pressure buildup, the IFP drops steeply close to the surface which creates a steep pressure gradient and fast IF flow from the tumor, see Figure 1.2 (Boucher et al. 1990).

The ECM, with all its components, contributes to the hydraulic conductivity of the tissue. This conductivity is a mechanical property of the interstitium that decides how fast the fluid will flow through the tissue under a specific IFP.

1.3 Tumor cell migration

In order for tumors cells to metastasize the cells may use functioning lymphatics to escape from their current location. These lymphatics are often found outside of the primary tumor. Tumor cells reach the vessels through directional migration, meaning there are mechanisms which tumor cells uses to invade into the surrounding tissue. Although tumor cells can migrate randomly, directional migration is the most efficient way to establish a metastasis at a distant site.

There are many migration mechanisms suggested as to how tumor cells may progress into the tissue (galvanotaxis, haptotaxis, durotaxis etc.), yet in this particular work we have focused on only a few main mechanisms. These are chemotaxis, rheotaxis and fibroblast-enhanced migration.
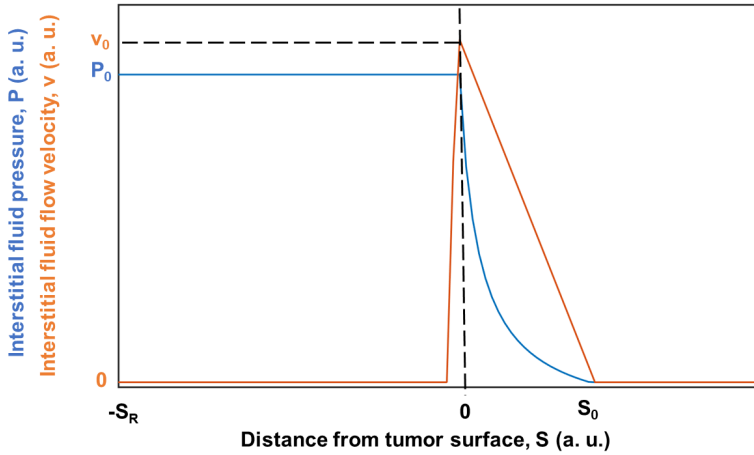
Figure 1.2: **Interstitial fluid pressure gradient:** a simplified illustration of the IFP inside a tumor and the resulting fluid velocity inspired by Hompland et al. 2012. The blue curve represents IFP while the red curve is the fluid velocity, the dashed line shows where the periphery of the tumor starts and where the fluid starts to flow.. In this particular tumor there is a uniform IFP within the tumor and at the periphery (S=0) it starts to rapidly decrease until it reaches the normal tissue pressure at $S = S_0$. There is no convection within the tumor from the tumor center $(S = -S_R)$ to the periphery, where it has a high velocity $(v = v_0)$, and reaches zero again in the normal tissue. (a. u. - arbitrary unit)

Chemotaxis are one of the key drivers of tumor cell invasion and contributes to tumor cell extravasation and intravasation to promote metastasis. Chemotaxis is the mechanisms by which the migration of cells is directed in response to an extracellular chemical gradient (Roussos et al. 2011). These chemicals are often secreted by the tumor cells themselves, or released by proteolytically degrading the ECM. In a static tissue with no fluid flow, the chemicals will only transport through diffusion. Yet, in a tumor environment, there is elevated pressure within the tumor and is decreasing towards the lymphatics, resulting in a pressure gradient (Jain 1987) and a fluid flow field. The chemical components are no longer only transported by diffusion but now also through advection. Consequently, the chemical gradient takes a new form and is skewed towards the draining lymphatics, creating a positive chemical gradient in the direction of lymphatics. Now, the tumor cells are able to migrate in the direction of the lymphatics as well. This type of migration has its own term: autologous chemotaxis (Fleury et al. 2006; Shields et al. 2007) In particular, if the chemical component is ECM-bound and is liberated proteolytically, the protease is also skewed in the direction of flow causing even more defined chemical gradient in the flow direction.
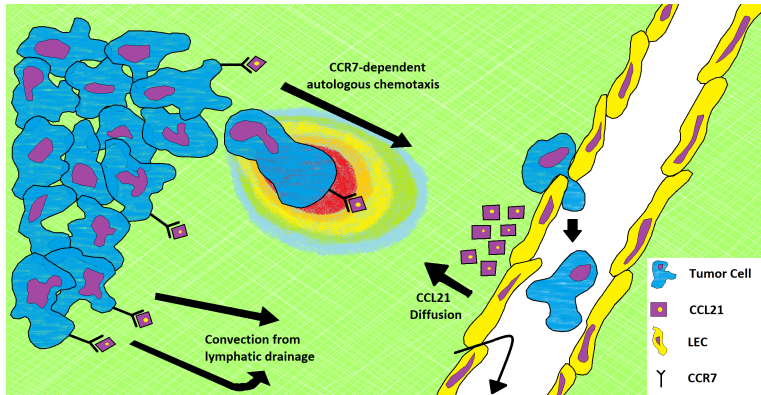
Figure 1.3: **Autologous chemotaxis:** a simplified illustration of autologous chemotaxis. This particular schematic is inspired by Shields et al. 2007. There is fluid flow from upper left to the lymphatic vessel. Tumor cells secrete protease which in turn liberates ECM-bound chemoattractant chemokine CCL21. The chemical gradient is illustrated by the different colors surrounding one of the tumor cells, where the color red shows the largest concentration. The gradient is skewed in the direction of flow, and causes the tumor cell to migrate towards the lymphatics.

While chemotaxis causes tumor cells to migrate in the flow direction, there is a mechanism that causes cells to migrate opposite of flow, or in the upstream direction. In the seminal work of Polacheck et al. 2011, they showed that fluid flow imposes a strain on the cancer cells which they can sense, and consequently migrate against the flow. Chemotaxis is also present in the experiments, yet it turns out that the cell seeding density, the number of cells, had an impact as to how effective chemotaxis is. In addition, the magnitude of the interstitial velocity imposed on the cancer cells plays a role whether the upstream migration is effective.

With regards to a real life tumor, this upstream mechanism in combination with chemotaxis downstream migration, is capable of explaining how tumor cells may escape from the primary tumor to invade the tissue in groups or single cells. Considering that fluid flow originates from the primary tumor and moves outwards, the upstream mechanism will keep the cancer cells in check near the tumor. The fluid flow also skews the chemical gradient toward the lymphatics, yielding chemotaxis downstream as a competing mechanism to the upstream strain-induced mechanism. Consequently, at some point tumor cells will be able to escape from the primary tumor and invade into the tissue, as the fluid velocity is strongest near the tumor periphery (Boucher et al. 1990) which 'arrest' some cells through upstream migration.

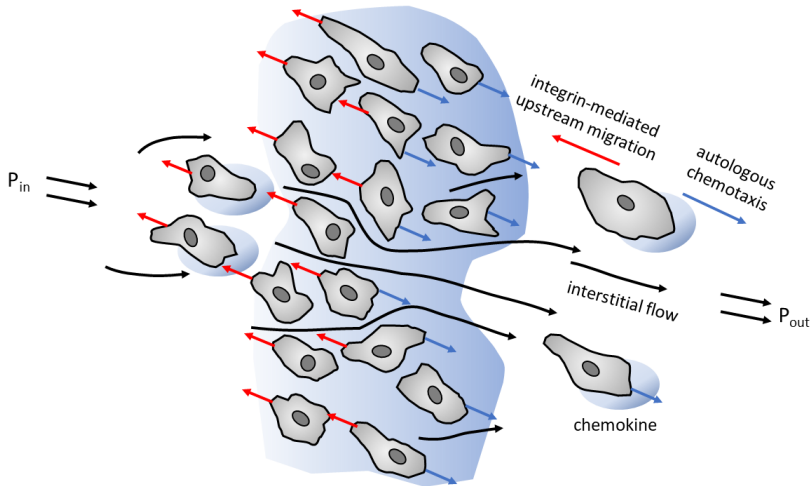In 1.1 it was mentioned that there are stromal cells residing in the tumor

Figure 1.4: **Rheotaxis:** a schematic of the experimental setup in Polacheck et al. 2011. The black lines illustrate fluid flow from left to right. Each cell contributes to the chemokine production and there is a chemical gradient seen in light blue/blue. The cells experience both chemotaxis and rheotaxis.

microenvironment, one of which are the fibroblast cells. Normal, healthy fibroblasts are found within the fibrillar matrix of the connective tissue and are largely responsible for its synthesis. The fibroblasts produce many of the ECM components such as type I, III and type V collagen and fibronectin (Tomasek et al. 2002). They are also an important source to MMPs to regulate the ECM through degradation and remodeling, and are thus an important player to tissue homeostasis.

While the above is also true for fibroblasts in the tumor microenvironment, there is another subpopulation of fibroblasts called cancer-associated fibroblasts (CAFs) or tumor-associated fibroblasts (TAFs) and are considered 'activated' fibroblasts (Mueller et al. 2004). TAFs secrete growth factors that directly affect the mobility of cancer cells, and the upregulation of MMP production degrades the ECM in such a way it is beneficial for tumor cell invasion.

As TAFs remodel the ECM, they can create paths within the tissue for tumors cells to migrate (Conklin et al. 2012; Gaggioli et al. 2007).However, it is not clear as to how tumor cells enter these paths. One simple explanation is that cancer cells migrate in the path of least resistance, seeing as the ECM is more or less remodeled or degraded in certain areas. There is also the possibility that cancer cells and TAFs may communicate to invade cooperatively. The fibroblasts and tumor cells can communicate through secretion of growth factors and chemokines in order to direct cell migration towards a chemical gradient. In the work by Labernadie et al. 2017, it was discovered that tumor cells and TAFS interact
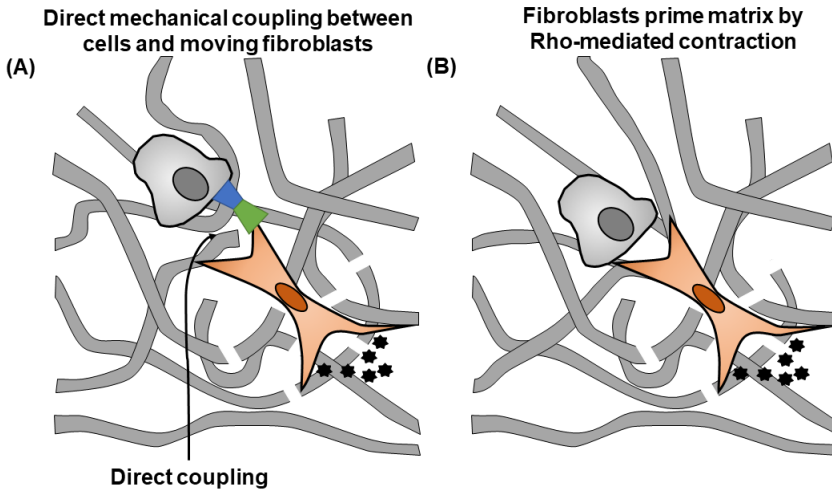
Figure 1.5: **Fibroblast enhanced migration:** two methods on how fibroblast may enhance tumor cell migration. **(A)** Here, the fibroblasts and tumor cells are directly coupled amd the fibroblats guide the tumor cells by migrating towards their chemoattractant. **(B)** Fibroblasts degrade and remodel the local ECM to making it easier for the tumor cells to migrate. At the same time, the fibroblasts migrate toward the chemical gradient, making a path for the tumor cells in the same direction as the fibroblasts are migrating.

with each other directly through mechanical coupling, causing fibroblasts to lead tumor cells away from the primary tumor. As fibroblasts also use chemotaxis to migrate (Shieh et al. 2011), they can guide the cancer cells to the lymphatics more effectively. These two methods may not be mutually exclusive, and having both these functions yields a highly aggressive tumor invasion as will be seen in our model.

1.4 Scope of this work

The background of the computational model used in this thesis is in multiphase flow in porous medium, often associated with reservoir modelling in petroleum engineering. However, while the models considering reservoirs try to explain how oil may flow towards a draining borehole, the focus in this thesis has shifted towards the different mechanisms tumor cells use to detach from the primary tumor and migrate towards draining lymphatics.

The long term goal of this model is to capture tumor cell behavior from experimental work in controlled environments in mathematical equations. This can in turn bridge the gap between *in vitro* cell behavior and *in vivo* tumor behavior. In essence, using a computational model armed with a good description

of how tumor cells react to many environments and circumstances will potentially help determining patient specific drug strategy selection. It can also be used, based on lab experiments, to specify which component in the tumor development that needs to be targeted.

We gain information of tumor cell migration mechanisms through experimental *in vitro* work, which allows us to formulate mathematical equations/terms that correspond to these mechanisms through a continuum based approach. In this study it has, from experience performing simulations, been essential to first achieve realistic fluid flow velocity in order to have realistic tumor cell behavior.

Next we upscale the model to two-dimensions when the model is able to capture the tumor cell behavior. This upscaling is beneficial when illustrating the model, but it may also reveal hidden functionalities within the model which can help identify how the model relates to biological characteristics of a tumor. If the model is fed with preclinical or clinical data, it can show how the tumor cells spread from the primary site, which there is little information about.

Chapter 2

Mathematical model

In this chapter, we summarize a multiphase model that has been developed which attempts to capture the complex tumor microenvironment and cell migration described in Chapter 1. We begin with the early version of the model and will show the extensions made to the model.

2.1 Two-phase model

A multiphase approach is a general approach where more details pertained to the physical forces and interactions between the different phases can be taken into consideration. In this two-phase model the tumor environment is a mixture of two interacting continua: the cellular phase of tumor cells represented by a volume fraction α_c moving with a velocity $\mathbf{u}_c$ and the IF phase represented by the volume fraction α_w moving with a velocity $\mathbf{u}_w$. While the ECM is also part of the total volume, the volume of ECM is considered as a constant, meaning there are no dynamic change in the volume of ECM by degradation/deposition. We therefore can write that

$$\alpha_c + \alpha_w = 1 \tag{2.1}$$

to account for the volume where cells and fluid can move. As a natural continuation of Evje 2017, where a model is used to investigate the role of cell-cell and cell-substrate adhesion among other things, the focus is now moved to research the interplay between cancer cells and interstitial fluid flow. This model has used the experimental results from Shields et al. 2007 to incorporate the migration mechanism termed autologous chemotaxis[1], explained in Section 1.3.

---

[1]The equation $(2.2)_7$ (C) contains a term which is not included in the early papers, but is implemented in later works to account for the chemokine absorption by the lymphatics.

Variable	Description
$\alpha_c, \alpha_f, \alpha_w$	volume fraction of cell, fibroblast and fluid
S_c, S_f	cell growth/death
$\mathbf{u}_c, \mathbf{u}_f, \mathbf{u}_w$	interstitial cell, fibroblast and fluid velocity
ρ, G, C, H	ECM component, protease, chemokine and TGF
P_w	IF pressure
$\Delta P_{fw}, \Delta P_{cw}, \Lambda_C, \Lambda_H$	caf-caf, cell-cell, chemokine, and TGF chemotaxis stress
$\hat{\zeta}_c, \hat{\zeta}_f, \hat{\zeta}_w, \hat{\zeta}_{cw}, \hat{\zeta}_{cf}$	cell-ECM, fibroblast-ECM, fluid-ECM, cell-fluid and cell-fibroblast interaction coefficients
λ_{ij}	production/decay rates
D_G, D_C, D_H	diffusion coefficients associated with G, C, H
ν_G, ν_C, ν_H	exponents in logistic function associated with chemical component G, C, H
M_C, M_H	absorption percentage of chemical component C, H into lymphatics
T_v, T_l	conductivity of vascular vessel wall, lymphatic vessel wall
$\widetilde{P}_v^*, \widetilde{P}_l^*$	effective vascular pressure, lymphatic pressure
$\Omega, \Omega_v, \Omega_l$	tumor region, region of intratumoral vascular, peritumoral lymphatic network

$$
(\alpha_c)_t + \nabla \cdot (\alpha_c \mathbf{u}_c) = S_c, \qquad S_c = \alpha_c \Big(\lambda_{11} - \lambda_{12} \alpha_c - \lambda_{13} \frac{\rho}{\rho_M} \Big)
$$

$$
(\alpha_w)_t + \nabla \cdot (\alpha_w \mathbf{u}_w) = -S_c + Q, \quad Q = Q_v - Q_l
$$

$$
\alpha_c \nabla P_c = -\hat{\zeta}_c \mathbf{u}_c
$$

$$
\alpha_w \nabla P_w = -\hat{\zeta}_w \mathbf{u}_w
$$

$$
\rho_t = -\lambda_{21} G \rho + \rho \Big(\lambda_{22} - \lambda_{23} \alpha_c - \lambda_{24} \frac{\rho}{\rho_M} \Big) \tag{2.2}
$$

$$
G_t = \nabla \cdot (D_G \nabla G) - \nabla \cdot (\mathbf{u}_w G) - \lambda_{31} G
$$

$$
\qquad + \alpha_c \Big(\lambda_{32} - \lambda_{33} \big(\frac{G}{G_M} \big)^{\nu_G} \Big)
$$

$$
C_t = \nabla \cdot (D_C \nabla C) - \nabla \cdot (\mathbf{u}_w C) - C M_C Q_l
$$

$$
\qquad + G \rho \Big(\lambda_{41} - \lambda_{42} \big(\frac{C}{C_M} \big)^2 - \lambda_{43} \big(\frac{C}{C_M} \big)^{\nu_C} \Big) - \lambda_{44} \alpha_c.
$$

Here the two phases, cancer cells and interstitial fluid, are represented by α_c

and α_w, respectively. Each individual phase has a mass balance and momentum balance equation, $(2.2)_{1,3}$ for the cancer cells and $(2.2)_{2,4}$ for the IF. $\mathbf{u}_i = (u_i^x, u_i^y, u_i^z)$ is the phase velocity for $i = c, w$. S_c is a source term to account for the growth and death of cells where also the presence of ECM which competes for space, is accounted for (Chaplain et al. 2006).

P_c is the cellular pressure and is expressed as

$$P_c = P_w + \Delta P(\alpha_w) + \Lambda(C). \tag{2.3}$$

P_c differs from the interstitial fluid pressure (IFP) P_w due to the cell-cell stress term ΔP and a chemotaxis term $\Lambda(C)$.

The cell-cell stress term is defined as

$$\Delta P = \gamma J(\alpha_w \rho_w), \tag{2.4}$$

where $\gamma > 0$ is a coefficient that depends linearly on the surface tension, whereas $J(\alpha_w \rho_w)$ is a monotonic decreasing dimensionless function with respect to the fluid mass $\alpha_w \rho_w$.

The stress term of chemotaxis, Λ, has the functional form

$$\Lambda(C) = \Lambda_0 - \frac{\Lambda_1}{1 + \exp(-\xi(C - C_M))} \tag{2.5}$$

Here $\Lambda_{0,1}$ and ξ are constant parameters, while C is the chemoattractant chemokine CCL19/21 where tumor cells migrate towards a positive chemical gradient. If we take a closer look at the chemokine equation in (2.2)

2.1.1 Chemical components

The main component of tumor cell chemotaxis in the model is chemokine and is described as

$$\begin{aligned} C_t = \nabla \cdot (D_C \nabla C) - \nabla \cdot (\mathbf{u}_w C) - CM_C Q_l \\ + G\rho\Big(\lambda_{41} - \lambda_{42}\big(\frac{C}{C_M}\big)^2 - \lambda_{43}\big(\frac{C}{C_M}\big)^{\nu_C}\Big) - \lambda_{44}\alpha_c. \end{aligned} \tag{2.6}$$

Chemokine is transported by diffusion and advection and produced by protease G. The protease liberates ECM-bound chemokine, which require the production term to be in product with ρ, the ECM density. It is possible for chemokine to be absorbed by the lymphatics through the term $CM_C Q_l$. The terms inside the parenthesis in product with $\lambda_{41,42,43}$ are a part of logistic growth function. It regulates the production of chemokine in a controlled manner. The final term with constant λ_{44} represents consumption. The idea that protease liberates the chemokine, instead of chemokine being only secreted by tumor cells, is based on the work by Fleury et al. 2006. In essence, when chemokine is liberated from the ECM it increases the effect IF flow has on the advection of the chemical. The chemical gradient is skewed even further from the tumor cells and causes invasive

behavior from the tumor cells. This becomes clear when we look at the chemical component that liberates chemokine, protease:

$$
\begin{aligned}
G_t = \nabla \cdot (D_G \nabla G) - \nabla \cdot (\mathbf{u}_w G) - \lambda_{31} G \\
+ \alpha_c \Big(\lambda_{32} - \lambda_{33} \big(\frac{G}{G_M} \big)^{\nu_G} \Big)
\end{aligned}
\tag{2.7}
$$

In a similar manner as (2.6), protease is transported through the tissue by diffusion and advection in the first two terms, followed by natural decay and the last terms are production through a logistic function, secreted by tumor cells. Since protease is also transported by IF flow, the resulting chemokine (C) distribution incite tumor cell migration in the flow direction.

2.1.2 Interaction coefficients

In the momentum balance equation for cells $(2.2)_3$ we find a drag force between the cells and the ECM fibers that acts in the opposite direction of the movement of cells (represented by $\mathbf{u}_c$). We use the following expression for this force, which is motivated by general multiphase modeling

$$
\hat{\zeta}_c = I_c \hat{k}_c \alpha_c^{r_c}, \qquad I_c, \hat{k}_c > 0, \quad r_c < 2,
\tag{2.8}
$$

where I_c, $\hat{k}_c$ and r_c must be specified. Similarly there is a drag force between the IF represented by the fluid velocity $\mathbf{u}_w$ and the ECM structure.

$$
\hat{\zeta}_w = I_w \hat{k}_w \alpha_w^{r_w}, \qquad \hat{k}_w > 0, \quad r_w < 2,
\tag{2.9}
$$

The parameters I_w and I_c can be considered static properties of the ECM, while $\hat{k}_w$ and $\hat{k}_c$ can account for dynamic properties related to ECM fiber alignment or other changes in the microenvironment.

2.1.3 Phase velocities

After algebraic manipulation of the mass balance and momentum equations, the resulting cell velocity consists of three different terms and also three different cell migration mechanisms

$$
\mathbf{u}_c = \mathbf{u}_{c,\text{fluid stress}} + \mathbf{u}_{c,\text{cell-cell}} + \mathbf{u}_{c,\text{chemotaxis/haptotaxis}}
$$

with

$$
\mathbf{u}_{c,\text{fluid stress}} = \mathbf{U}_T \Big[\frac{\alpha_c \hat{\zeta}_w}{\alpha_c^2 \hat{\zeta}_w + \alpha_w^2 \hat{\zeta}_c} \Big]
$$

$$
\mathbf{u}_{c,\text{cell-cell}} = - \Big[\frac{\alpha_c \alpha_w^2}{\alpha_c^2 \hat{\zeta}_w + \alpha_w^2 \hat{\zeta}_c} \Big] \nabla(\Delta P)
\tag{2.10}
$$

$$
\mathbf{u}_{c,\text{chemotaxis/haptotaxis}} = - \Big[\frac{\alpha_c \alpha_w^2}{\alpha_c^2 \hat{\zeta}_w + \alpha_w^2 \hat{\zeta}_c} \Big] \nabla \Lambda(C)
$$

The first term $\mathbf{u}_{c,fluidstress}$ is stress caused by the IF flow on the cancer cells. The second term $\mathbf{u}_{c,cell-cell}$ represents the diffusive cell-cell repelling force that leads to more or less a non-directional migration. The last term, $\mathbf{u}_{chemotaxis}$ is the directional migration towards a positive gradient in chemokine C. $\mathbf{U}_T$ is the total velocity of the two phases, and is mainly governed by the interstitial fluid velocity as this is much larger than cell migration speed.

There is also a similar expression for the interstitial fluid velocity

$$\mathbf{u}_w = \mathbf{U}_T \Big[\frac{\alpha_w \hat{\zeta}_c}{\alpha_c^2 \hat{\zeta}_w + \alpha_w^2 \hat{\zeta}_c}\Big] + \Big[\frac{\alpha_c^2 \alpha_w}{\alpha_c^2 \hat{\zeta}_w + \alpha_w^2 \hat{\zeta}_c}\Big]\nabla(\Delta P)$$
$$+ \Big[\frac{\alpha_c^2 \alpha_w}{\alpha_c^2 \hat{\zeta}_w + \alpha_w^2 \hat{\zeta}_c}\Big]\nabla(\Lambda(C)) \tag{2.11}$$

While the equation is very similar to 2.10, one of the key differences is that the second and third term now has a $(+)$ sign in front of it. This is used to signify that if cells are moving in one direction, it will push the fluid in the other direction in a counter-current fashion.

In order to compute the total velocity of the two phases, U_T, which is needed in the calculation of phase velocities (2.10)-2.11, we first have to solve the interstitial fluid pressure equation

$$\nabla \cdot (\hat{\lambda}_T \nabla P) = -(Q_v - Q_l) - \nabla \cdot (\hat{\lambda}_c \nabla(\Delta P + \Lambda(C))), \tag{2.12}$$

Where $\hat{\lambda}_c$ and $\hat{\lambda}_T$ are mobility functions which are based on cell and fluid volume fractions and interaction forces. The total velocity is given by

$$\mathbf{U}_T = -\hat{\lambda}_T \nabla P_w - \hat{\lambda}_c \nabla(\Delta P + \Lambda(C)) \tag{2.13}$$

the total velocity is dominated by the first term on the RHS of 2.13 which contains the IFP.

2.1.4 Starling Law

The fluid flow originates from the vascular system within the tumor and is drained by the lymphatics, see Section 1.2. In our model, this system is expressed in the fluid mass balance equation through the variable Q $(2.2)_2$. The main contributors to interstitial flow Q_v are hydrostatic and osmotic pressure gradients between the vascular and interstitial space. Starling Law is used for the flow of fluid into the interstitium given by

$$Q_v = T_v\big(P_v^* - P_w - \sigma_T(\pi_v^* - \pi_w)\big) = T_v\big(\widetilde{P}_v^* - P_w\big) \qquad T_v = L_v \frac{S_v}{V} \tag{2.14}$$

Here $\tilde{P}_v^* = P_v - \sigma_T(\pi_v^* - \pi_w)$. L_v is the hydraulic conductivity $(\mathrm{m^2 s/kg = m/Pa\ s})$ of the vessel wall, S_v/V $(\mathrm{m^{-1}})$ the exchange area of blood vessel per unit volume of tissues V. P_v^* and P_w are the vascular and interstitial pressure, respectively,

while π_v^* and π_w are the osmotic pressure in the vascular and interstitial space. Finally, σ_T is the osmotic reflection coefficient for plasma proteins.

The lymphatic system drains the excessive fluid from the interstitial space and returns it back to the blood circulation and is expressed by Q_l. In the intratumoral region, the lymphatics are often not functional (Jain et al. 2014). This is caused the high compressive solid stress that is developed in tumors. The expression for lymphatic draining is similar to (2.14)

$$Q_l = T_l(P_w - \widetilde{P}_l^*), \qquad T_l = L_l \frac{S_l}{V}. \tag{2.15}$$

Here L_l is the hydraulic conductivity of the lymphatic vessel walls. S_l/V is the surface area of the lymphatic vessel per volume unit of tissues V and $\tilde{P}_l^*$ is the effective lymphatic pressure.

2.1.5 Numerical computations

If we regard the full model (2.2), we use an approximate solution procedure based on operator splitting (Holden et al. 2010; LeVeque et al. 2002): let L_t denote the solution operator of (2.2). This means that, if we have the initial state $S_0 = (\alpha_{c0}, \alpha_{w0}, u_{c0}, u_{w0}, \rho_0, G_0, C_0)$, $L_t S_0$ denotes the solution of (2.2) after a time t. The next step we use is to split the solution operator L_t into two operators R_t and T_t, where R_t accounts for source term effects whereas T_t solves for the transport effects. The R_t operator is defined as

$$\begin{aligned} R_t : \alpha_{ct} &= S_c, \\ \alpha_{wt} &= -S_c, \\ \rho_t &= -\lambda_{21}G\rho + \rho\big(\lambda_{21} - \lambda_{23}\alpha_c - \lambda_{24}\frac{\rho}{\rho_M}\big) \end{aligned} \tag{2.16}$$

and T_t to be the solution operator associated with the subsystem

$$\begin{aligned} T_t : \alpha_{ct} &+ \nabla \cdot (\alpha_c \mathbf{u}_c) = 0, \\ \alpha_{wt} &\ \nabla \cdot (\alpha_w \mathbf{u}_w) = 0, \\ G_t &= \nabla \cdot (D_G \nabla G) - \nabla \cdot (\mathbf{u}_w G) - \lambda_{31}G \\ &+ \alpha_c\big(\lambda_{32} - \lambda_{33}\big(\frac{G}{G_M}\big)^{\nu_G}\big), \\ C_t &= \nabla \cdot (D_C \nabla C) - \nabla \cdot (\mathbf{u}_w C) - CM_C Q_l \\ &+ G\rho\big(\lambda_{41} - \lambda_{42}\big(\frac{C}{C_M}\big)^2 - \lambda_{43}\big(\frac{C}{C_M}\big)^{\nu_C}\big) - \lambda_{44}\alpha_c. \end{aligned} \tag{2.17}$$

We assume that we have a discretization of the time interval $[0, T]$ into N timesteps of length Δt, such that $N\Delta t = T$. Given an approximate solution S^n at time t^n, we find a new approximation at time t^{n+1} using a three-step sequential procedure

$$S^{n+1} = (R_{\Delta t/2} \circ T_{\Delta t} \circ R_{\Delta t/2})S^n. \tag{2.18}$$

To solve the ODE source solution operator R_t we apply a standard numerical method. The transport operator T_t need some elaboration. If we consider a spatial two dimensional domain $[0, L_x] \times [0, L_y]$ and assume a cartesian grid of space step in x direction is Δx and Δy in y direction. The center of a cell is designated $N_{i,j}$, with points $i = 1, ..., I$ and $j = 1, ..., J$, such that $I\Delta x = L_x$ and $J\Delta y = L_y$. The interfaces of cell i, j are located, respectively, at $N_{(i-1/2,j)} = N_{i,j} - \Delta x/2$, $N_{(i+1/2,j)} = N_{i,j} + \Delta x/2$, $N_{(i,j-1/2)} = N_{i,j} - \Delta y$ and $N_{(i,j+1/2)} = N_{i,j} + \Delta y$. We assume that we have given the solution operator $S_{i,j}^n$ at time t^n for $i = 1, ..., I$, $j = 1, ..., J$. The steps taken to solve for T_t are as follows

1. First we calculate the interstitial pressure within the domain, P_w, using (2.12)

2. Then we can compute the total velocity $\mathbf{U}_T$ from (2.13), which in turn can be used to calculate cell and IF velocities $\mathbf{u}_c$ and $\mathbf{u}_w$ using (2.10) and (2.11), respectively.

3. Armed wth the interstitial velocities $\mathbf{u}_c^n$ and $\mathbf{u}_w^n$ at time level t^n, we can compute updated cancer cell volume fraction α_c^{n+1} and concentrations ρ^{n+1}, G^{n+1} and C^{n+1} where we employ a standard upwind in space discretization (explicit in time) of convective terms whereas diffusion terms are treated implicitly in time.

In papers where we perform simulations on two-dimensional domains, we make use of a alternating direction implicit method (ADI), more specifically the Douglas-Gunn method (Douglas et al. 1964) in order to have a stable and efficient scheme.

2.2   Upstream migration

In the two-phase model 2.2, which is based on the experimental work by Shieh et al. 2011, cancer cells only migrate through chemotaxis in the fluid flow direction as the chemical gradient becomes positive downstream. However, Polacheck et al. 2011 found that there is a competing mechanisms that causes cells to migrate upstream.

The momentum equations of cell and IF include cell-ECM and fluid-ECM resistance forces as before, $\hat{\zeta}_c$ and $\hat{\zeta}_f$ in 2.2$_{3,4}$. The upstream migration is introduced through an interaction term between the cell and IF phase to account for a indirect effect that fluid-generated stress can have on cancer cells.

The model now takes the following form

$$(\alpha_c)_t + \nabla \cdot (\alpha_c \mathbf{u}_c) = S_c, \qquad S_c = \alpha_c \Big(\lambda_{11} - \lambda_{12}\alpha_c - \lambda_{13}\frac{\rho}{\rho_M} \Big)$$

$$(\alpha_w)_t + \nabla \cdot (\alpha_w \mathbf{u}_w) = -S_c + Q, \quad Q = Q_v - Q_l$$

$$\alpha_c \nabla (P_w + \Delta P(\alpha_w) + \Lambda(C)) = -\hat{\zeta}_c \mathbf{u}_c + \hat{\zeta}_{cw}(\mathbf{u}_w - \mathbf{u}_c)$$

$$\alpha_w \nabla P_w = -\hat{\zeta}_w \mathbf{u}_w - \hat{\zeta}_{cw}(\mathbf{u}_w - \mathbf{u}_c)$$

$$\rho_t = -\lambda_{21}G\rho + \rho\Big(\lambda_{22} - \lambda_{23}\alpha_c - \lambda_{24}\frac{\rho}{\rho_M} \Big) \qquad (2.19)$$

$$G_t = \nabla \cdot (D_G \nabla G) - \nabla \cdot (\mathbf{u}_w G) - \lambda_{31}G$$

$$\quad + \alpha_c \Big(\lambda_{32} - \lambda_{33}\Big(\frac{G}{G_M}\Big)^{\nu_G} \Big)$$

$$C_t = \nabla \cdot (D_C \nabla C) - \nabla \cdot (\mathbf{u}_w C) - C M_C Q_l$$

$$\quad + G\rho\Big(\lambda_{41} - \lambda_{42}\Big(\frac{C}{C_M}\Big)^2 - \lambda_{43}\Big(\frac{C}{C_M}\Big)^{\nu_C} \Big) - \lambda_{44}\alpha_c.$$

where the last term of $(2.19)_{3,4}$ is the interaction term between the cell and fluid phase. The functional form of the interaction coefficient becomes

$$\hat{\zeta}_{cw} = I_{cw}\hat{k}_{cw}\alpha_w\alpha_c^{1+r_{cw}}, \qquad \hat{k}_{cw} > 0, \quad r_{cw} > 0. \qquad (2.20)$$

$\hat{\zeta}_{cw}$ needs to become negative in order to generate a momentum translation opposite of fluid flow direction. That can be achieved by setting $I_{cw} < 0$. This can be made clearer by taking a closer look on the rewritten momentum equation for cells

$$\alpha_c \nabla P_c = -(\hat{\zeta}_c + \hat{\zeta}_{cw})\mathbf{u}_c + \hat{\zeta}_{cw}\mathbf{u}_w. \qquad (2.21)$$

Cell pressure P_c is to a large extent dictated by IFP, P_w. Thus, if we consider a fluid flow from left to right in one dimension, the LHS of (2.21) gives a negative value. This needs to be balanced by the terms on the RHS. The term $\hat{\zeta}_{cw}\mathbf{u}_w$ shows that the tumor cells can generate a force that has opposite direction of $\mathbf{u}_w$ (i.e., $\hat{\zeta}_{cw}$ should have a negative sign), which can completely balance the pressure gradient $\alpha_c \nabla P_c$. If we assume that $\hat{\zeta}_{cw} \sim I$ is the same order as I_w, it will force the first term RHS of (2.21) to generate a negative cell velocity $\mathbf{u}_c$ to balance the LHS since the coefficient $(\hat{\zeta}_c + \hat{\zeta}_{cw})$ is positive $(\hat{\zeta}_c \gg |I_{cw}| \sim I_w)$. Meaning, if the negative drag $\hat{\zeta}_{cw}$ is sufficiently large, the first term on the RHS of (2.21) will yield a change in cell migration direction.

2.3 Three-phase model

It is natural to assume that only the malignant tumor cells are causing tumor growth and metastasis. However, studies show that also the tumor microenvironment contribute to cancer progression (Kalluri 2003). As described in the last

part of (1.3), activated fibroblasts, or CAFs, plays a major role to the survival, growth and migration of cancer cells.

In order to incorporate fibroblasts into the two-phase model (2.2), we need to extend it to a three-phase model. Fibroblasts are a type of cell and therefore takes up some of the tissue volume. The constraint on the volume becomes

$$\alpha_c + \alpha_w + \alpha_f = 1, \qquad (2.22)$$

where the volume fraction of fibroblasts is represented by α_f.

The three phase model has a similar form as the two phase model (2.2), but more interaction coefficients and a new chemical component is added. The most recently published version of the cell-fibroblast-fluid model takes the following form

$$
\begin{aligned}
&(\alpha_c)_t + \nabla \cdot (\alpha_c \mathbf{u}_c) = S_c \\
&(\alpha_f)_t + \nabla \cdot (\alpha_f \mathbf{u}_f) = S_f, \qquad \alpha_c + \alpha_f + \alpha_w = 1 \\
&(\alpha_w)_t + \nabla \cdot (\alpha_w \mathbf{u}_w) = -S_c - S_f + Q, \quad Q = Q_v - Q_l \\
&\alpha_c \nabla(P_w + \Delta P_{cw} + \Lambda_C) = -\hat{\zeta}_c \mathbf{u}_c + \hat{\zeta}_{cf}(\mathbf{u}_f - \mathbf{u}_c) \\
&\alpha_f \nabla(P_w + \Delta P_{fw} + \Lambda_H) = -\hat{\zeta}_f \mathbf{u}_f - \hat{\zeta}_{cf}(\mathbf{u}_f - \mathbf{u}_c) \\
&\alpha_w \nabla P_w = -\hat{\zeta}_w \mathbf{u}_w \\
&\rho_t = -\lambda_{21} G\rho + \rho\Big(\lambda_{22} - \lambda_{23}\alpha_c - \lambda_{24}\big(\frac{\rho}{\rho_M}\big)\Big) \\
&G_t = \nabla \cdot (D_G \nabla G) - \nabla \cdot (\mathbf{u}_w G) - \lambda_{31} G \\
&\quad + (\alpha_c + \alpha_f)\Big(\lambda_{32} - \lambda_{33}\big(\frac{G}{G_M}\big)^{\nu_G}\Big) \\
&C_t = \nabla \cdot (D_C \nabla C) - \nabla \cdot (\mathbf{u}_w C) - CM_C Q_l \\
&\quad + G\rho\Big(\lambda_{41} - \lambda_{42}\big(\frac{C}{C_M}\big)^2 - \lambda_{43}\big(\frac{C}{C_M}\big)^{\nu_C}\Big) - \lambda_{44}\alpha_c C, \\
&H_t = \nabla \cdot (D_H \nabla H) - \nabla \cdot (\mathbf{u}_w H) - HM_H Q_l - \lambda_{51} H \\
&\quad + \alpha_f\Big(\lambda_{52} - \lambda_{53}\big(\frac{H}{H_M}\big)^2 - \lambda_{54}\big(\frac{H}{H_M}\big)^{\nu_H}\Big) - \lambda_{55}\alpha_f H
\end{aligned}
\qquad (2.23)
$$

A mass and momentum balance equation for the fibroblast phase is seen in $(2.23)_{2,5}$. In addition, the momentum balance equations for tumor cells and fibroblasts have an interaction term, $\hat{\zeta}_{cf}$, which accounts for the direct mechanical coupling described in Section 1.3. Similar to cancer cells, fibroblasts also chemotact towards a chemical component through its potential function Λ_H which has the same form as (2.5).

The direct mechanical coupling between cancer cells and fibroblasts are reflected in the interaction coefficient $\hat{\zeta}_{cf}$. It has the following form

$$\hat{\zeta}_{cf} = I_{cf}\alpha_c^{r_{cf}}\alpha_f^{r_{fc}} \qquad (2.24)$$

17

when both cell types are present, they will interact with eachother. The magnitude of I_{cf} plays an important role on whether this interaction will make fibroblasts able to pull on cancer cells.

While direct interaction is one of the abilities TAFs have, another mechanism has to be accounted for. Fibroblasts may degrade or remodel the ECM in order to make paths for cancer cells to move in. This is implemented in the cell-ECM interaction coefficient 2.8 through the paramter $\hat{k}_c$.

$$\hat{k}_c = 1 - A(1 - \exp(-B\alpha_f)) \tag{2.25}$$

where A and B are dimensionless constants.

Fibroblasts chemotact towards a different chemical species than cancer cells, transforming growth factor-$\beta 1$ (TGF-$\beta 1$, or just TGF) Shieh et al. 2011.

$$\begin{aligned} H_t = \nabla \cdot (D_H \nabla H) - \nabla \cdot (\mathbf{u}_w H) - H M_H Q_l - \lambda_{51} H \\ + \alpha_f \Big(\lambda_{52} - \lambda_{53} \big(\frac{H}{H_M} \big)^2 - \lambda_{54} \big(\frac{H}{H_M} \big)^{\nu_H} \Big) - \lambda_{55} \alpha_f H \end{aligned} \tag{2.26}$$

TGF has a similar form as chemokine $(2.23)_9$. The first and second term are diffusion and advection, respectively. The third term represents absorption through the lymphatics, where M_H is a percentage of how much is absorbed. The following terms are a decay term, a logistic function for production and finally a consumption term.

While we through the development of the model only considers a few migration mechanisms, there are many others that can be implemented in the momentum balance equations as stress contributions. Some of the other migration mechanisms are haptotaxis and durotaxis, among others.

Chapter 3

Paper contributions

This work consists of five articles published in peer-reviewed journals and one article under review. In this chapter a brief summary of each of the six articles is presented.

Paper I - A multiphase model for exploring tumor cell migration driven by autologous chemotaxis

This paper presents the first version of the cell-fluid model on a one-dimensional domain. The model attempts to shed some light on how tumor cells can use a chemical gradient which is the result of proteolytically released chemokine to migrate in the direction of fluid flow. The work in this paper is heavily inspired by the experimental work in Fleury et al. 2006 and Shields et al. 2007.

Interaction between the fluid-ECM and cell-ECM is implemented as drag forces, which affects the velocity of these phases. This in turn affects the distribution of the chemical components. The cell-produced protease diffuses and advects with fluid flow, which consequently releases ECM-bound chemokine that also diffuses and advects in flow direction. The tumor cells then sense this chemical gradient which is skewed in the flow direction and starts migrating towards it.

We identify parameters within the model which can be translated into biological characteristics of different tumor types with regards to their invasiveness. Figure 3.1 is a simulation of the model showing the downstream migration of a cell aggregate.

Paper II - Competing tumor cell migration mechanisms caused by interstitial fluid flow

In this work, the extension to the model is inspired by the seminal work by Polacheck et al. 2011. While maintaining chemotaxis as a means of cell migration, a new mechanism is applied to the cancer cells where the stress imposed by the interstitial fluid flow on cancer cells is transformed to cell migration. When considering the flow direction, the chemotaxis makes cells migrate with the flow in the downstream direction, whereas the flow-dependent migration mechanism causes cells to migrate against the flow in the upstream direction. These two mechanisms compete to determine which direction tumor cells are migrating, or they can even balance each other out leading to no migration.

Through the mathematical model, the non-chemical migration mechanism can be explained by a proper balance between cell-ECM, fluid ECM, and cell-fluid interaction forces. The correlations used for these interactions are largely borrowed from experience with multiphase water-oil-gas flow in porous media.
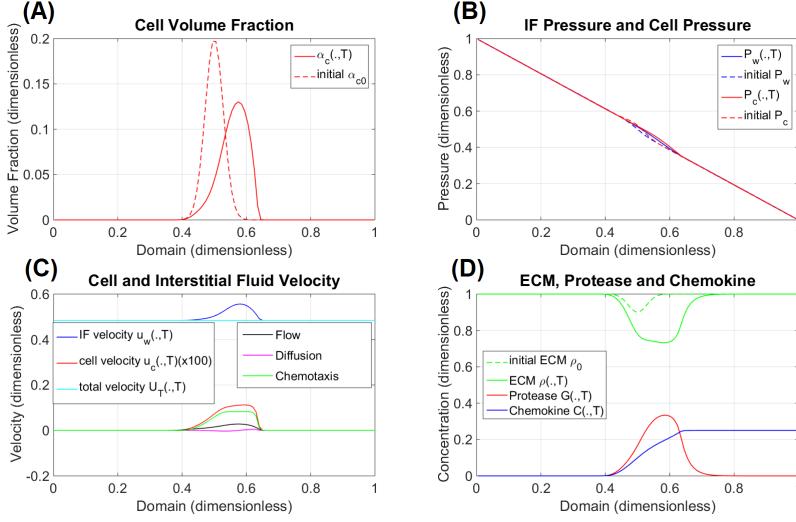
Figure 3.1: **Downstream cell migration**. **(A)** Tumor cell migration in the downstream direction. The solid line shows the cell volume fraction after 5.8 days, whereas the dotted line is the initial distribution. **(B)** The IF pressure is higher on the left side of the domain ($P_L = P_{atm} + 10$kPa, $P_R = P_{atm}$) in order to create a pressure gradient similar to lab experiments. **(C)** The blue solid line is the IF velocity and is a result of the IFP gradient. The cell velocity and its components are also shown, where chemotaxis is the dominating migration mechanism. **(D)** The distribution of chemokine (blue line) is positive in the direction of flow, leading to the strong chemotaxis effect. This distribution is the result of protease (red line) releasing the chemokine.

Yet, a novel use of the interaction coefficients was required in order to generate upstream migration.

The competing mechanisms are shown in Figure 3.2, where on the upstream side there is upstream migration, whereas at the downstream side chemotaxis is the dominant mechanism.

Paper III - How tumor cells possibly can make use of interstitial fluid flow in a strategy for metastasis

The model with chemotaxis and upstream stress-mediated cell migration caused by IF flow is used on a idealized two-dimensional tumor setting. In order to achieve realistic flow, a vascular system is placed within the tumor and the lymphatic system is placed in the normal tissue outside of the tumor. A fluid flow field is generated which originates from the primary tumor and ends near
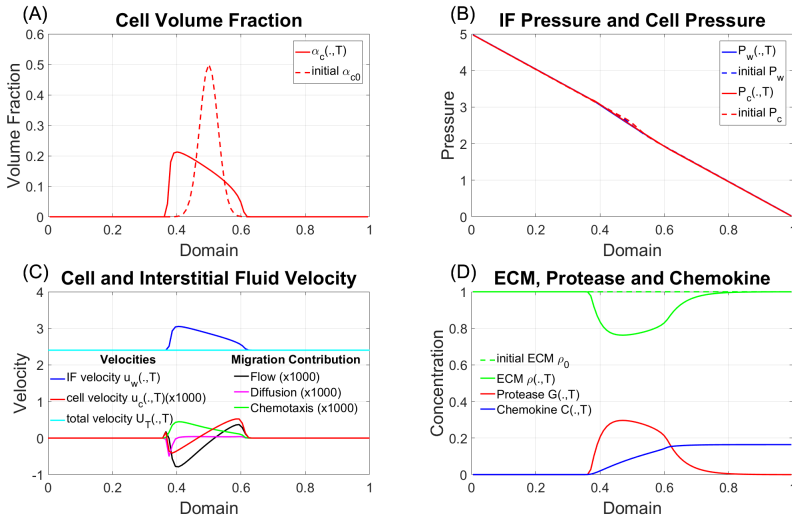
Figure 3.2: **Two competing migration mechanisms**. **(A)** The upstream cell migration is dominant on the upstream side of the cell aggregate. Whereas on the downstream side there is still migration dominated by chemotaxis. **(B)** This IFP profile is the result of the boundary conditions set, yielding flow from left to right. **(C)** This case has a high IF velocity which causes upstream migration to be very dominant on the upstream side. **(D)** The high IF velocity results in a mild chemokine gradient.

the lymphatics.

This work attempts to illustrate what happens when two competing migration mechanisms explored in a experimental setting plays out in a tumor setting. More specifically, the paper investigates whether these two mechanisms may be a means for tumor cells to detach themselves from the primary tumor and subsequently migrate to the draining lymphatics which can cause metastasis.

One of the advantages of using a model when investigating migration mechanisms is that we can easily change the tumor microenvironment. In this work we vary the conductivity of the tissue, i.e. we change how easily the fluid may flow through the tissue. While this heavily affects the fluid-ECM interaction, it also plays a role in how the cell-fluid interaction behaves and causes some interesting results as seen in Figure 3.3.

Paper IV - Enhanced cancer cell invasion caused by fibroblasts when fluid flow is present

In this work the proposed cell-fluid mathematical model for autologous chemotaxis is extended to also include fibroblasts, which becomes a cell-fibroblast-fluid model. The model is motivated by the experimental findings by Shieh et al. 2011 and includes a new set of mass and momentum balance equations for fibroblasts. The addition of fibroblasts to the model is due to the reported findings that fibroblasts are a part of a synergetic enhancement of tumor cell invasion caused by interaction between tumor cells and fibroblasts in the presence of fluid flow.

Two different methods on how fibroblasts enhances tumor cell migration is explored. The first one is through fibroblast mediated ECM reorganiation. Here fibroblasts primes the ECM, making it easier for tumor cells to migrate through the tissue. The second is a more direct method through a mechanical coupling between the two cell types, letting fibroblasts pull on the cancer cells.

The model demonstrates that both of the methods induces fibroblast-enhanced tumor cell invasion, but in a different way. The ECM remodeling causes large cell volume fractions to migrate, whereas the direct coupling has a stronger ability to mobilize the smaller cell volume fractions. Overall it seems that the direct coupling method capture several aspects of the observed experimental results which is not well enough accounted for in the remodeling of ECM method. In Figure 3.4 we see the effect of fibroblast-enhanced tumor cell migration through direct coupling.

Paper V - Collective cell migration in the presence of fibroblasts

The three-phase computational model is used to investigate fibroblast-enhanced tumor cell migration in an idealized tumor setting. The three phases are tumor cells, fibroblasts and interstitial fluid. We explore how tumor cells will migrate in a heterogeneous tumor environment compared to controlled *in vitro* microfluidic based experiments, which this model is inspired by (Shieh et al. 2011; Shields et al. 2007)

Now, the two methods of fibroblast-enhanced tumor cell migration are active, allowing the model to elucidate how fibroblasts can guide tumor cells towards draining lymphatics and consequently lead to metastasis. Fibroblasts can act as leader cells, where they create paths within the ECM by matrix remodeling and contraction. In combination with a direct mehcanical adhesion between the two cell types, fibroblasts can pull the tumor cells in their wake.

Effectively, in a tumor setting, tumor cell chemotaxis and fibroblast-enhanced tumor cell migration yields collective migration. Meaning that tumor cells migrates as a collective to invade the adjacent tissue. In addition, in order to initiate tumor cell migration, fibroblasts are required to be present. The model clearly illustrates that fibroblasts are guiding the tumor cells towards the lymphatics, as seen in Figure 3.5

Paper VI - In silico investigations of intratumoral heterogeneous interstitial fluid pressure (working title)

Hansem et al. 2019 shows through preclinical studies that IFP within tumors can be heterogeneous. Two different types of tumors are investigated in that study as to what is causing the heterogeneous IFP, and whether there are any correlations between IFP measurements and metastasis. The characteristics of the first tumor, HL-16 cervical carcinoma, are thick connective tissue bands within the tumor when the IFP was heterogeneous. For the second tumor, Panc-1 pancreatic carcinoma, a homogeneous and dense tissue is observed for tumors with heterogeneous IFP. In essence, the tissue within the tumor affects the intratumor IFP profile.

We use a three-phase computational model to first achieve heterogeneous IFP due to the respective tissue characteristic of each tumor type, then we simulate the cancer cell migration to investigate whether the model can predict the outcome of these tumor types when the IFP is heterogeneous or not.

The *in silico* model is able to capture heterogeneous IFP in cases which are expected to be heterogeneous, in accordance with the preclinical study (Hansem et al. 2019). The model shows that cells can form an invasive front consisting of groups of cells that detach themselves from the primary tumor and form isolated islands, a behavior which is natural to associate with metastatic propensity (Figure 3.6).
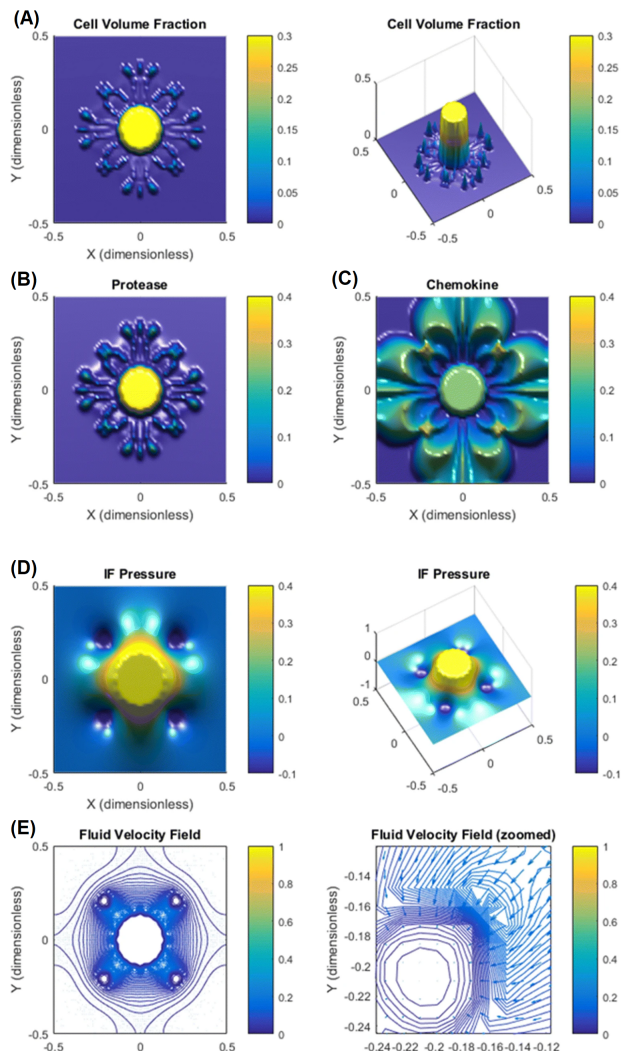
Figure 3.3: **Deep invasion into the tissue is caused by competing migration mechanisms**. **(A)** Clusters of cells are able to detach themselves from the tumor and invade the surrounding tissue. This is the result of upstream migration that arrests tumor cells to stay at the primary tumor, while chemotaxis lets the cells near the periphery to migrate downstream towards the lymphatcs. **(B)** Protease distribution is a direct result of cell secretion. **(C)** Chemokine is proteolytically released from the ECM by protease and has positive gradients in the downstream direction. **(D)** There is a high IFP inside the primary tumor, which is a characteristic common in tumors. **(E)** In this particular case the IF flow is fairly low due to a low tissue conductivity, or a high resistance to flow.
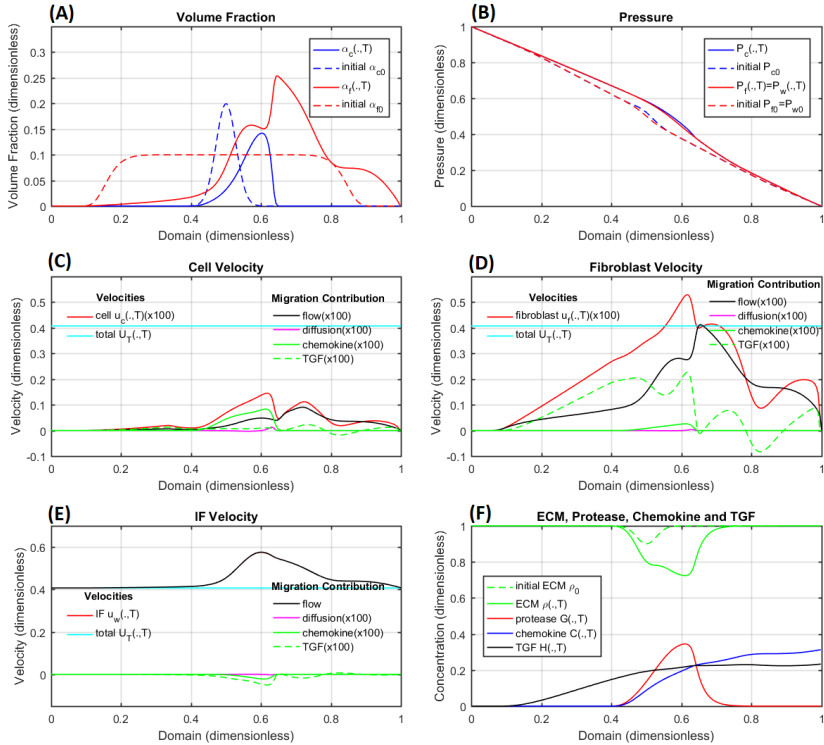
Figure 3.4: **Fibroblast enhances tumor cell migration** In this particular case there are no tumor cell chemotaxis migration mechanism. Cancer cells may only migrate through direct coupling with fibroblasts. **(A)** Tumor and fibroblast cell volume fractions. The fibroblasts are migrating in the downstream direction and causes tumor cells to migrate in the same direction. **(B)** The IFP is higher on the left boundary than the right boundary, leading to a pressure gradient and flow from left to right. **(C)** Tumor cell velocity is comprised of four different components: flow-stress imposed on cells, diffusion-like migration, chemotaxis towards chemokine and migration due to fibroblast chemotaxis. **(D)** Fibroblast migration velocity has similar components as the tumor cell velocity **(E)** IF velocity is heavily governed by the IFP pressure. **(F)** The chemical components are advected by the fluid flow, creating positive gradients in the downstream direction.
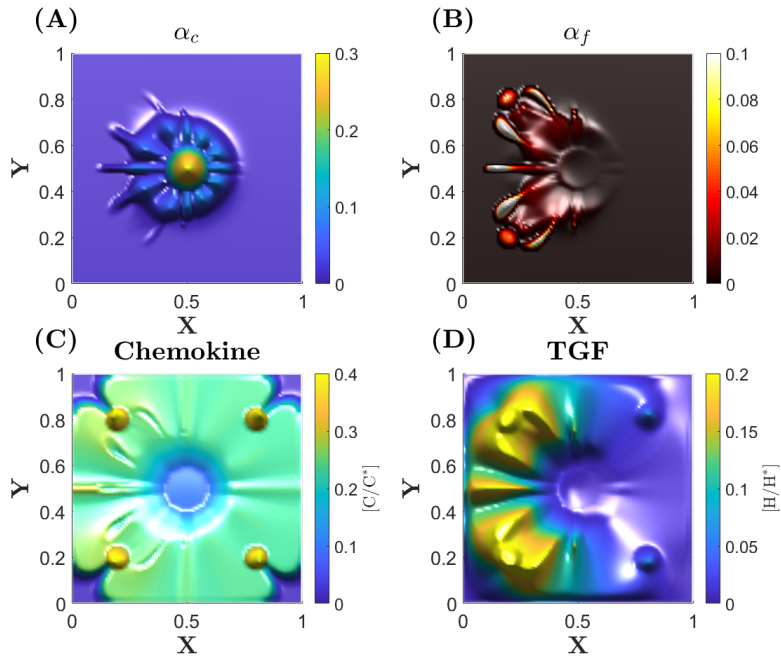
Figure 3.5: **Collective tumor cell migration**. Fibroblasts lead tumor cells towards the lymphatics. The initial conditions put fibroblasts in a "half-moon" on the left side of the primary tumor. **(A)** Tumor cells follow the tracks made by fibroblasts which determines their direction while also increasing their migration velocity. **(B)** The draining lymphatics are placed in the corners of the domain, where the fibroblasts are migrating towards. **(C)** Chemokine is transported by the flowing fluid and is drained by the lymphatics. There is however accumulation of chemokine at the lymphatics. **(D)** TGF has a similar distribution as chemokine, but only on the left side of the domain.
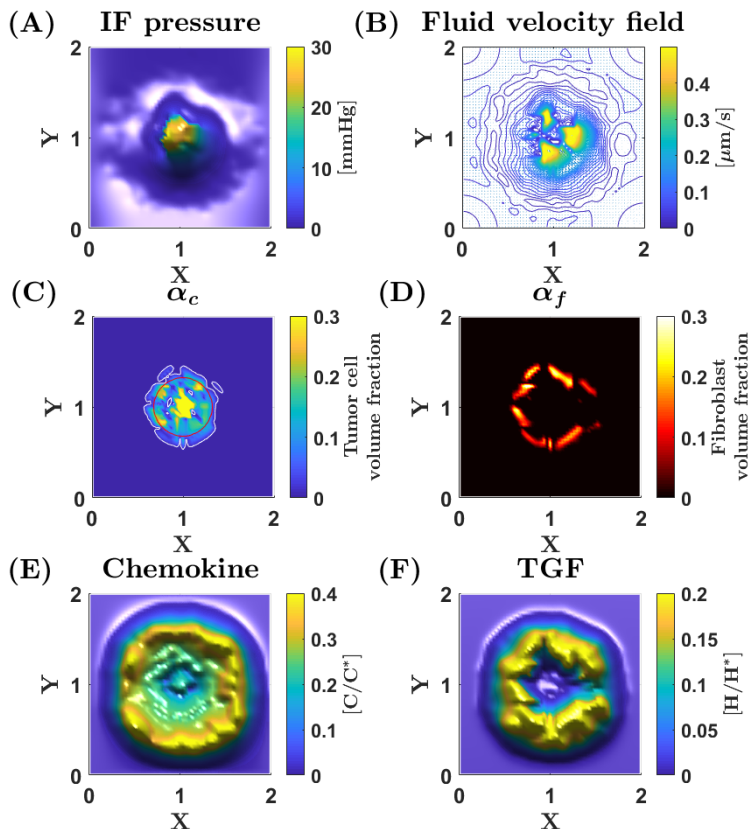
Figure 3.6: **Simulation results of cervical carcinoma**. There are thick ECM bands within the tumor that causes high heterogeneity in intratumoral IFP. **(A)** Interstitial fluid pressure in mmHg. **(B)** The resulting interstitial fluid velocity. It is highly heterogeneous due to the ECM bands that do not allow fluid to flow through them. **(C)** Tumor cell volume fraction at the end of simulation. At the northeast part of the tumor, a group of cells have detached themselves from the primary tumor. **(D)** Fibroblast volume fraction is invading the tissue fairly heterogeneously. **(E)** Chemokine is increasing in concentration towards the lymphatics, where it is drained. **(F)** TGF is produced by the fibroblasts and transported towards the lymphatics, leading the fibroblasts to migrate in the same direction.

Chapter 4

Conclusions and further work

This work started out with a fairly simple two-phase model, inspired by oil-water multiphase flow modeling (Standnes et al. 2017), to investigate the interaction between cancer cells/fluid and the solid matrix in simulations of tumor cell migration. It consists of two continua, the tumor cells and interstitial fluid, and consider both the direct and indirect interaction between these two phases. Motivated by the *in silico* and experimental work by Fleury et al. 2006 and Shields et al. 2007 we capture the cell migration mechanism described in these work in our model (Paper I), autologous chemotaxis. The cancer cells now has the ability to both randomly migrate with no directionality through cell-cell interaction, but also directed migration towards a chemical gradient. We also identify parameters within the model that can pertain biological characteristics with regards to cell aggressiveness.

However, if we consider a tumor, our model suggests that only having chemotaxis as the migration mechanism is not sufficient to cause tumor cells to detach themselves from the primary tumor. This is due to chemotaxis often only causes cancer cells to migrate in the downstream direction and nothing in the opposite direction to arrest the cells in the primary tumor. There has been reports on many different migration mechanisms (see Section 1.3), yet the mechanism we investigate next in our model relies on interstitial fluid flow velocity. The computational model uses well established methods from water-oil modeling to create realistic interstitial flow fields, making it natural to pursue a cell migration mechanism related to flow velocity. The extension to the two-phase model is motivated by the experimental work by Polacheck et al. 2011, where it was discovered that tumor cells may, in competition to downstream chemotaxis, migrate in the upstream direction due to fluid stress imposed on the cancer cells. The mathematical model is able to demonstrate the relative strength of these opposing mechanisms, and elucidate how one of the mechanisms can be dominant under certain circumstances. In addition, the balance between all the different interaction forces are investigated in depth (Paper II).

We expand the one-dimensional model in Paper II to a two-dimensional idealized tumor. In the experimental one-dimensional setting, we achieve fluid flow by applying boundary pressure. To imitate a tumor, a vascular and lymphatic system is introduced, which will produce and drain the fluid. This in turn yields a pressure buildup within the tumor, through a sophisticated production and drainage term, which causes the fluid to flow. This allows us to use the experimentally observable behavior of cancer cells in our model to envision how it will all play out in a tumor setting. In particular, how the interplay is between the competitive upstream and downstream migration. The simulations show that

these opposing mechanisms can cause invasion into the tissue by cancer cells, which consequently may lead to metastasis. While chemotaxis is leading cancer cells to migrate in the direction of flow, the upstream migration is arresting cancer cells to stay put. Groups of cancer cells can detach from the primary tumor and migrate towards the lymphatics (Paper III).

Another direction is taken from the two-phase model in I to include another phase, making it a three-phase model consisting of tumor cells, interstitial fluid and fibroblasts. The new addition of fibroblasts is proposed to enhance the tumor cell migration, making it more robustly invade the adjacent tissue. A study performed by Shieh et al. 2011 suggests that fibroblasts also migrate due to autologous chemotaxis, and leads cancer cells through primed ECM, making it easier for cancer cells to migrate through the tissue.

A different study suggests that there is a direct mechanical interaction between cancer cells and fibroblasts, allowing cancer cells to be pulled by fibroblasts in the direction they are going Labernadie et al. 2017.

In Paper IV these two fibroblast-enhanced migration mechanisms are investigated further in a computational setting. The computational model also confirms that these two effects, or a combination of the two, can explain the fibroblast-enhanced tumor cell invasion. Furthermore, the direct coupling has a stronger ability to mobilize small cancer cell densities, as opposed to the ECM remodeling which increases the larger cell densities.

We extend the three-phase model to a two-dimensional perspective to look at the outcomes of fibroblast-enhanced cancer cell migration when we consider an idealized tumor. Cancer cells *in vivo* often tend to migrate as a collective of cells, in forms of for example sheets or strands Friedl et al. 2012. In combination with what is reported in Gaggioli et al. 2007, that fibroblasts are able to act as leader cells, we study how fibroblasts may lead cancer cells that maintain their cell-cell contacts while invading the tissue (Paper V). The two methods of fibroblast-enhaned tumor cell migration described in Paper IV are activated simultaneously. It is evident that due to the presence of fibroblasts, tumor cells are able to invade the adjacent tissue. The model suggests that tumor cells are able to reach functioning lymphatic vessels through solely using fibroblasts as their leader cells. These results support the strategy of targeting fibroblast-cancer cell interactions as a method to decrease metastasis in patients.

In the preclinical study by Hansem et al. 2019, two xenograft models, HL-16 cervical carcinoma and Panc-1 pancreatic carcinoma, were investigated. It was reported significant heterogeneity in IFP and it was proposed that this was associated with division of tissue into compartments separated by thick connective tissue bands for the HL-16 tumors and with dense collagen rich ECM for the Panc-1 tumors. The computational model has been trained to comply with the experimental *in vitro* results by Shieh et al. 2011, which has identified autologous chemotaxis, ECM remodeling and cancer cell-fibroblast interaction as

drivers for invasive tumor cell behavior. Parameters that characterize the leaky intratumoral vascular network, the peritumoral lymphatics tat drain the fluid, and the density of ECM as represented through the hydraulic conductivity of the interstitial space is fed into the model. The *in silico* HL-16 model illustrates that sparse ECM, low ECM density, was associated with uniform intratumoral IFP in spite of a heterogeneous microvascular network, whereas compartment structures resulted in more heterogeneous IFP. In addition, the Panc-1 model shows that the heterogeneity in the microvascular network in combination with dense ECM structure prevents IFP to even out and gives rise to heterogeneous IFP. These two models are aligned with the preclinical observations in Hansem et al. 2019. Furthermore, the computer model illustrates how tumor cell may detach from the primary tumor to create isolated islands within the adjacent tissue. However, unlike the experimental study, the current version of the *in silico* model does not show an association between the elevated IFP and the aggressiveness of the tumor.

While the model thus far has been effective at recreating the experimental results, there are many aspects of the model that can either be improved upon or extended in some way.

- The model is in a unique position to model the effect of therapeutic agents, as the model is able to simulate the interstitial fluid flow field effectively and fast. With the inclusion of a sophisticated way of calculating the production and drainage of fluid, from the vascular and lymphatic system, the model can be used to assess the drug distribution. This in turn could be very helpful with regards to patient specific treatment, where several of the parameters in the model can be specified for a certain type of tumor and tissue.

- The first two-phase computational model in Paper I has been split into two different directions, one model investigating upstream migration and one model is extended to three phases. However, it may be viable to explore the possibility of those two model in combination. How will the model respond to so many mechanisms? Will it be possible to achieve both collective tumor cell migration and more distinct detachment from the primary tumor?

- Similar to the work by Weis et al. 2013 and their subsequent research, where parameter optimization methods are used to improve the accuracy of a mathematical model describing tumor development, a parameter optimization technique could be applied to our model. This would further improve the ability of the model to forecast how tumor cell will migrate, and in combination with treatment strategies, the therapy efficiency Paper VI. A parameter estimation study is currently being worked upon using the mathematical model described in this thesis.

- Currently we assume that the vascular system is constant both in density, permeability and its location. However, angiogenesis, i.e. formation of

blood vessels, would play a major role in how our mathematical model behaves. This is due to how the vascular system indirectly affects the chemical distribution through the interstitial flow field. In order to make the model more realistic, inclusion of angiogenesis should be explored.

- The computer model can be extended to also involve a multi-scale approach where one can explore tumor growth by considering major biological events at both tissue, cellular and subcellular scale, similar to Rahman et al. 2017.

Bibliography

Bonnans, C., Chou, J., and Werb, Z. (2014). "Remodelling the extracellular matrix in development and disease". In: *Nature reviews Molecular cell biology* 15.12, pp. 786–801.

Boucher, Y., Baxter, L. T., and Jain, R. K. (1990). "Interstitial pressure gradients in tissue-isolated and subcutaneous tumors: implications for therapy". In: *Cancer research* 50.15, pp. 4478–4484.

Chaplain, M. A. and Lolas, G. (2006). "Mathematical modelling of cancer invasion of tissue: dynamic heterogeneity". In: *Networks & Heterogeneous Media* 1.3, p. 399.

Chen, F., Zhuang, X., Lin, L., Yu, P., Wang, Y., Shi, Y., Hu, G., and Sun, Y. (2015). "New horizons in tumor microenvironment biology: challenges and opportunities". In: *BMC medicine* 13.1, p. 45.

Conklin, M. W. and Keely, P. J. (2012). "Why the stroma matters in breast cancer: insights into breast cancer patient outcomes through the examination of stromal biomarkers". In: *Cell adhesion & migration* 6.3, pp. 249–260.

Douglas, J. and Gunn, J. E. (1964). "A general formulation of alternating direction methods". In: *Numerische Mathematik* 6.1, pp. 428–453.

Evje, S. (2017). "An integrative multiphase model for cancer cell migration under influence of physical cues from the microenvironment". In: *Chemical Engineering Science* 165, pp. 240–259.

Fleury, M. E., Boardman, K. C., and Swartz, M. A. (2006). "Autologous morphogen gradients by subtle interstitial flow and matrix interactions". In: *Biophysical journal* 91.1, pp. 113–121.

Frantz, C., Stewart, K. M., and Weaver, V. M. (2010). "The extracellular matrix at a glance". In: *Journal of cell science* 123.24, pp. 4195–4200.

Friedl, P., Locker, J., Sahai, E., and Segall, J. E. (2012). "Classifying collective cancer cell invasion". In: *Nature cell biology* 14.8, pp. 777–783.

Gaggioli, C., Hooper, S., Hidalgo-Carcedo, C., Grosse, R., Marshall, J. F., Harrington, K., and Sahai, E. (2007). "Fibroblast-led collective invasion of carcinoma cells with differing roles for RhoGTPases in leading and following cells". In: *Nature cell biology* 9.12, pp. 1392–1400.

Hanahan, D. and Weinberg, R. A. (2011). "Hallmarks of cancer: the next generation". In: *cell* 144.5, pp. 646–674.

Hansem, L. M. K., Huang, R., Wegner, C. S., Simonsen, T. G., Gaustad, J.-V., Hauge, A., and Rofstad, E. K. (2019). "Intratumor Heterogeneity in Interstitial Fluid Pressure in Cervical and Pancreatic Carcinoma Xenografts". In: *Translational oncology* 12.8, pp. 1079–1085.

Holden, H., Karlsen, K. H., and Lie, K.-A. (2010). *Splitting methods for partial differential equations with rough solutions: Analysis and MATLAB programs*. Vol. 11. European Mathematical Society.

Hompland, T., Ellingsen, C., Øvrebø, K. M., and Rofstad, E. K. (2012). "Interstitial fluid pressure and associated lymph node metastasis revealed in tumors by dynamic contrast-enhanced MRI". In: *Cancer research* 72.19, pp. 4899–4908.

Jain, R. K. (1987). "Transport of molecules across tumor vasculature". In: *Cancer and Metastasis Reviews* 6.4, pp. 559–593.

Jain, R. K., Martin, J. D., and Stylianopoulos, T. (2014). "The role of mechanical forces in tumor growth and therapy". In: *Annual review of biomedical engineering* 16, pp. 321–346.

Kalluri, R. (2003). "Basement membranes: structure, assembly and role in tumour angiogenesis". In: *Nature Reviews Cancer* 3.6, pp. 422–433.

Labernadie, A., Kato, T., Brugués, A., Serra-Picamal, X., Derzsi, S., Arwert, E., Weston, A., González-Tarragó, V., Elosegui-Artola, A., Albertazzi, L., et al. (2017). "A mechanically active heterotypic E-cadherin/N-cadherin adhesion enables fibroblasts to drive cancer cell invasion". In: *Nature cell biology* 19.3, pp. 224–237.

LeVeque, R. J. et al. (2002). *Finite volume methods for hyperbolic problems.* Vol. 31. Cambridge university press.

Mueller, M. M. and Fusenig, N. E. (2004). "Friends or foes—bipolar effects of the tumour stroma in cancer". In: *Nature Reviews Cancer* 4.11, pp. 839–849.

Nissen, N. I., Karsdal, M., and Willumsen, N. (2019). "Collagens and Cancer associated fibroblasts in the reactive stroma and its relation to Cancer biology". In: *Journal of Experimental & Clinical Cancer Research* 38.1, p. 115.

Polacheck, W. J., Charest, J. L., and Kamm, R. D. (2011). "Interstitial flow influences direction of tumor cell migration through competing mechanisms". In: *Proceedings of the National Academy of Sciences* 108.27, pp. 11115–11120.

Rahman, M. M., Feng, Y., Yankeelov, T. E., and Oden, J. T. (2017). "A fully coupled space–time multiscale modeling framework for predicting tumor growth". In: *Computer methods in applied mechanics and engineering* 320, pp. 261–286.

Roussos, E. T., Condeelis, J. S., and Patsialou, A. (2011). "Chemotaxis in cancer". In: *Nature Reviews Cancer* 11.8, pp. 573–587.

Shieh, A. C., Rozansky, H. A., Hinz, B., and Swartz, M. A. (2011). "Tumor cell invasion is promoted by interstitial flow-induced matrix priming by stromal fibroblasts". In: *Cancer research* 71.3, pp. 790–800.

Shields, J. D., Fleury, M. E., Yong, C., Tomei, A. A., Randolph, G. J., and Swartz, M. A. (2007). "Autologous chemotaxis as a mechanism of tumor cell homing to lymphatics via interstitial flow and autocrine CCR7 signaling". In: *Cancer cell* 11.6, pp. 526–538.

Standnes, D. C., Evje, S., and Andersen, P. Ø. (2017). "A novel relative permeability model based on mixture theory approach accounting for solid–fluid and fluid–fluid interactions". In: *Transport in Porous Media* 119.3, pp. 707–738.

Tomasek, J. J., Gabbiani, G., Hinz, B., Chaponnier, C., and Brown, R. A. (2002). "Myofibroblasts and mechano-regulation of connective tissue remodelling". In: *Nature reviews Molecular cell biology* 3.5, pp. 349–363.

Weis, J. A., Miga, M. I., Arlinghaus, L. R., Li, X., Chakravarthy, A. B., Abramson, V., Farley, J., and Yankeelov, T. E. (2013). "A mechanically coupled reaction–diffusion model for predicting the response of breast tumors to neoadjuvant chemotherapy". In: *Physics in Medicine & Biology* 58.17, p. 5851.

Papers

Paper I

A multiphase model for exploring tumor cell migration driven by autologous chemotaxis

By:
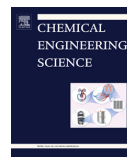Waldeland, Jahn Otto
Evje, Steinar

CHEMICAL
ENGINEERING
SCIENCE

A multiphase model for exploring tumor cell migration driven by autologous chemotaxis

Jahn O. Waldeland, Steinar Evje *

University of Stavanger, Faculty of Science and Technology, 4068 Stavanger, Norway

HIGHLIGHTS

- A multiphase model is developed that can describe autologous chemotaxis consistent with in vitro experiments.
- The role played by fluid-ECM, cell-ECM, and cell-fluid interaction forces are included.
- The model illustrates how autologous chemotaxis can be used as a means for metastasis.

ARTICLE INFO

ABSTRACT

It has been demonstrated that interstitial fluid (IF) flow can play a crucial role in tumor cell progression. In the seminal works by Swartz and collaborators (Fleury et al., 2006; Shields et al., 2007) it was discovered that due to this flow, chemokine ligands secreted by tumor cells selectively tend to bind to receptors (CCR7) on the downstream side of the cells that in turn stimulate cells to migrate in the direction of the flow. This migration process was denoted as autologous chemotaxis. Previous mathematical modeling of autologous chemotaxis apparently has been restricted to single-phase considerations. The purpose of this work is to explore how a multiphase approach can be used where the fluid and cancer cells are treated as two separate phases with their own momentum balance equations. A mathematical model is derived that sheds light on essential nonlinear coupling mechanisms and interactions that are involved. The role played by fluid-ECM (friction type of term) and cell-ECM interaction forces (adhesion forces) are demonstrated. In particular, a fluid generated stress term in the mathematical expression for the cell velocity is highlighted. This term reflects how the flowing fluid will try to push the cancer cells in the downstream direction whose effect must be counterbalanced by the cancer cells by creating a sufficiently strong cell-ECM resistance force. Moreover, in order to represent the autologous chemotaxis migration mechanism we include (i) a component to represent stagnant ECM concentration (collagen); (ii) a chemical component representing chemokine that can convect with the fluid; and (iii) a third chemical component to represent protease secreted by the cancer cells which is able to release ECM-bound chemokine through proteolytic activity. The resulting model allows us to demonstrate how the autologous chemotaxis transport mechanism is governed by formation of chemokine concentration gradients that are asymmetric and skewed in the flow direction. We test the model behavior for a flow system with an external imposed pressure gradient which is comparable with the laboratory experiments by Swartz and collaborators. Sensitivity to changes in circumstances like blocking of the CCR7 receptor needed for autologous chemotaxis and elimination of the pressure driven IF flow (i.e., no flow) are explored and discussed. We also illustrate the model behavior in an envisioned tumor setting where increased IF flow is produced from leaky blood vessels that sit on the inside of the tumor. An increased fluid flow towards the region on the outside of the tumor is then generated where it is adsorbed by lymphatic vessels and gives rise to a characteristic elevated IF pressure profile that decreases at the tumor periphery. In turn, this results in an autologous chemotactic driven migration of cancer cells at the rim of the tumor. The simulation illustrates how the autologous chemotactic cell migration mechanism discovered by Swartz and collaborators possibly can be used as a means for metastasis by generating aggressive cell migration towards lymphatic vessels.

© 2018 Elsevier Ltd. All rights reserved.

---

* Corresponding author.
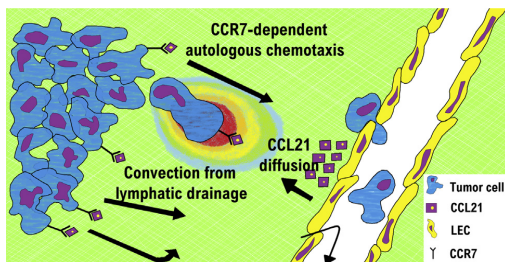 E-mail address: steinar.evje@uis.no (S. Evje).

1. Introduction

1.1. Interstitial fluid flow in the tumor microenvironment

Interstitial fluid flow, the movement of fluid around cells and through pores in the extracellular matrix (ECM), can have the ability to alter the tumor microenvironment which in turn can play a major role in tumor progression. One of the effects that interstitial fluid flow has on the tumor microenvironment, is creating a asymmetric pericellular gradient of chemotactic proteins which the cells migrate towards through chemotaxis. How such gradients arise are critical in order to understand these processes.

Some of the chemokines that tumor cell migration is sensitive to are CCL19 and CCL21, which are both ligands for the receptor CCR7. Autocrine signaling is a well-described phenomenon in cells, where the cell secrete chemokine, which may bind to the ECM to be subsequently released proteolytically and diffuse away from the cell. With the addition of interstitial fluid flow, this phenomenon takes on a new significance. The chemokine will still diffuse, but it will also advect in the direction of the flow, causing the cells to chemotactically migrate towards this asymmetric chemokine gradient created by the flow. See Fig. 1 for an illustration similar to the one used in Shields et al. (2007) which describes autologous chemotaxis as a means to metastasis. The flow direction is from the high pressure tumor toward the nearest low pressure draining lymphatic vessel, and this flow acts as a guidance mechanism for the cancer cells. This has been demonstrated in the seminal work by Shields et al. (2007) for breast cancer cells, which expresses a high density of CCR7 receptors such that the ligands can efficiently signal.

1.2. The mechanism suggested by Swartz and collaborators

The tumor cells often respond to extracellular cues based on gradients of morphogenetic and chemotactic proteins. One of these responses is a mechanism suggested in Shields et al. (2007) where tumor cells chemotact towards a draining lymphatic. The tumor cells create a pericellular gradient of proteins which in turn may be amplified under the influence of a subtle interstitial flow. The chemokine or morphogen has matrix binding properties (Patel et al., 2001) where the protein are secreted by the cells in precursor forms that contain specific motifs that bind to components of the ECM to be later released by cell-mediated proteolysis. A 2D mathematical model was presented in Fleury et al. (2006) based on single-phase considerations where the main objective was to demonstrate that the pericellular gradients formed by the cell-secreted morphogen can result in a significant asymmetry when

interstitial flow is introduced. This asymmetry is what is thought to drive the chemotactic migration of the cells in the direction of the flow. The model is a steady-state convection-diffusion equation for the concentration of the solute C_i of the form:

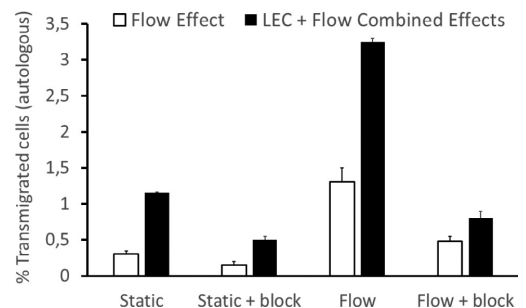$$v\nabla C_i = D_i \nabla^2 C_i + R_i \quad (i = p, m) \tag{1}$$

where v is the fluid velocity, solved using Brinkman's equation for a sphere, C_i refers to either protease C_p or morphogen C_m. In the case of cell-secreted protease the reaction term is assumed as a first-order protease degradation term, such that $R_p = -k_p C_p$ with a rate constant k_p. In the case of ECM-released morphogen the reaction term becomes $R_m = k_{ECM} C_p S$ where the morphogen bound to the ECM is only released by proteolysis (with rate constant k_{ECM} and S is the concentration of bound morphogen). The cancer cell is treated as a stationary semicircular disc which has either a constant surface concentration or a constant surface flux of protein. The interstitial fluid phase is considered as a constant velocity field which is used in the calculation of the gradients.

In the experimental results obtained in Shields et al. (2007), the tumor cells secreted the ligands CCL21 and CCL19 and expressed the receptor CCR7. When interstitial fluid flow was introduced, the tumor cells exhibited increased migration downstream. In the event of using antibodies to block the CCR7 receptor, the increased downstream migration ceased. Main observations from the experimental results in Shields et al. (2007) are schematically summed up in Fig. 2.

Further investigations are provided in the work by Shieh et al. (2011) where the role of fibroblasts and its interaction with cancer cells leading to increased cell migration, is elucidated. A main observation from these experiments, by examining the interplay between tumor cells, fibroblasts, and interstitial flow, is that flow guides fibroblast invasion, leading to concurrent and increased invasion of tumor cells through the ECM. Without interstitial flow, fibroblasts did not affect tumor cell invasion.

1.3. Interesting questions and challenges

However, to the best of our knowledge, its seems that previous modelling aimed at shedding light on basic mechanisms involved in autologous chemotaxis, have been restricted to single-flow descriptions. Such formulations typically are based on Darcy's equation or the more general Brinkman's equation, combined with appropriate transport-reaction equations that can account for the

Fig. 1. Figure motivated by (Shields et al., 2007) illustrating the tumor microenvironment where lymphatics drain interstitial fluid, creating a fluid flow toward the lymphatics. This fluid flow causes chemokine CCL21 to advect toward the lymphatic vessel and thereby creating a chemokine gradient in the direction of flow. Tumor cells armed with CCR7 receptor can sense this gradient and migrate toward it.

Fig. 2. This figure is a summary of the experimental results shown in Fig. 7A in Shields et al. (2007). We have focused on the results regarding the flow and its effect on cell migration as a function of ECM-released chemokine. The role of lymphatic endothelial cells (LEC) and secreted chemokine from them is not directly accounted for in the model we consider. In particular, we will assess the mathematical model in light of the results that show cell migration under flow, with and without CCR7 blocking, and static (no flow) conditions (white columns).

formation of chemokine gradients. Thus, some interesting questions from a modeling point of view that arise are:

(i) A single-phase model does not consider explicitly the complicated interplay taking place between the cancer cells and the IF flow. Such a model would require consistent formulation of mass balance and momentum balance equations for the cancer cells and IF with inclusion of various interaction forces (cell-ECM and fluid-ECM). In turn, these balance equations must be coupled to transport-reaction equations that can represent the autologous chemotaxis mechanism. What is a simplest possible multiphase system that can describe autologous chemotaxis as a result of cell-fluid flow coupled to a suitable transport-reaction system?

(ii) The IF flow is typically in the range 0.1–2.0 μm/s whereas the cell migration velocity is perhaps at least a 100-fold lower. The cell migration is strongly governed by cell-ECM interaction (e.g.m through integrin), which is imperative to a dynamic tumor environment. What is the natural mathematical formulation that can incorporate the cell-ECM interaction such that the flowing IF to a little extent is able to push the cancer cells in the downstream direction, consistent with the experimental observation in Shields et al. (2007), but largely is governed by a chemotactic migration mechanism?

(iii) Another secondary mechanism mentioned in Shields et al. (2007) for directed migration is that proteases are secreted by tumor cells that are also subject to the biasing effects of interstitial flow. This could in turn lead to increased migration in the direction of flow due to directed proteolysis. Proteolysis of ECM results in the creation of haptotactic gradients, which cells use to move in a directed fashion. How can this possible haptotactic cell migration mechanism naturally be taken into account in the mathematical model?

To set the stage we would like to cite the following interesting comment made in Shieh and Swartz (2011) which highlights some of the complexity:

"…interstitial flow can apply drag forces to the matrix, which can transmit stress to nearby cells through integrin attachments. Decoupling the mass transport aspects of interstitial flow from the direct application of fluid shear to the cell and indirect mechanical stimulation via the matrix and integrins remains difficult, if not impossible – after all, when fluid flows, it generates shear forces and transports solutes. Regardless, cells have a number of potential mechanisms by which they can sense the changes in interstitial flow associated with cancer."

Some essential interaction forces that the mathematical model should be able to account for are: (i) a drag force from the flowing interstitial fluid (IF) on the matrix (ECM); (ii) a direct shear stress on the cells from flowing IF; (iii) a direct interaction between cells and ECM, i.e., the cells must be sufficiently strongly attached to matrix/ECM to avoid being pushed directly in the direction of the flowing fluid; (iv) an indirect mechanical stimulation caused by the IF flow on the cancers cells via the matrix and integrins (integrin is essential protein involved in cell-ECM interaction).

1.4. Aim of this work

The main purpose of this work is to propose a minimal system that can account for downstream autologous chemotaxis transport effect. More precisely, we propose a simplest possible system of partial differential equations which accounts for both the interstitial fluid (IF) and cell phase dynamics and include correlations to

characterize cell-ECM and fluid-ECM interactions, in addition to the interaction between cell and fluid. In a realistic setting all these interactions most likely are coupled together in a complex and nonlinear manner. The approach is based on a general multiphase approach where the fluid and cancer cells are treated as two separate phases with their own momentum balance equations. A simplified model is derived that can shed light on essential nonlinear coupling mechanisms and interactions that are involved. In order to represent the autologous chemotaxis migration mechanism, we include (i) a component ρ to represent a stagnant ECM concentration (collagen); (ii) a chemical component C representing chemokine that can flow with the fluid through a convective term and also spread by diffusion; and (iii) a third chemical component G to represent protease secreted by the cancer cells which is able to release ECM-bound chemokine C through proteolysis of ECM. This may also result in the creation of haptotactic gradients in ρ, which cells can use to move in a directed fashion. The flow system we consider is not fully comparable with the one reported in Fig. 2 since we not explicitly represent the LEC component. This is a natural restriction since our main focus is on investigating the autologous chemotaxis mechanism. As reported in Shields et al. (2007), the main effect of including LEC is to amplify the downstream cancer cell migration governed by the chemokine gradient.

1.5. Main findings

In order to highlight some of the main findings, we briefly now introduce some essential variables that will be explained and described systematically in Section 2. Firstly, we assume that the cell phase and interstitial fluid are represented, respectively, by the volume fraction α_c and α_w such that $\alpha_c + \alpha_w = 1$. Moreover, we use $\hat{\zeta}_w, \hat{\zeta}_c$, and ζ to represent, respectively, the fluid-ECM interaction, cell-ECM interaction, and cell-fluid interaction forces. Finally, the IF velocity is denoted by $\mathbf{u}_w$ whereas interstitial cell velocity is represented by $\mathbf{u}_c$. It turns out that, subject to appropriate simplifying assumptions, an expression can be obtained for the cell velocity that takes the form

$$
\begin{aligned}
\mathbf{u}_c &= -\frac{[\alpha_c \hat{\zeta}_w] + \zeta}{\hat{\zeta}_c \hat{\zeta}_w + \zeta[\hat{\zeta}_c + \hat{\zeta}_w]} \nabla P_w - \frac{\alpha_c [\hat{\zeta}_w + \zeta]}{\hat{\zeta}_c \hat{\zeta}_w + \zeta[\hat{\zeta}_c + \hat{\zeta}_w]} \nabla (\Delta P) \\
&\quad - \frac{\alpha_c [\hat{\zeta}_w + \zeta]}{\hat{\zeta}_c \hat{\zeta}_w + \zeta[\hat{\zeta}_c + \hat{\zeta}_w]} \nabla \Lambda(C, \rho) \\
&= \mathbf{U}_T \frac{\alpha_c \hat{\zeta}_w + \zeta}{\alpha_c^2 \hat{\zeta}_w + \alpha_w^2 \hat{\zeta}_c + \zeta} - \frac{\alpha_c \alpha_w^2}{\alpha_c^2 \hat{\zeta}_w + \alpha_w^2 \hat{\zeta}_c + \zeta} \nabla (\Delta P) \\
&\quad \textbf{flow} - \textbf{generated} \quad \textbf{stress} \quad \textbf{dispersion} \\
&\quad - \frac{\alpha_c \alpha_w^2}{\alpha_c^2 \hat{\zeta}_w + \alpha_w^2 \hat{\zeta}_c + \zeta} \nabla \Lambda(C, \rho). \\
&\quad \textbf{chemotaxis/haptotaxis}
\end{aligned}
\tag{2}
$$

In the first equality of (2) we see that $\mathbf{u}_c$ involves three components: (i) A first component that depends on the IF pressure P_w signaling that the cancer cells feel a stress from the flowing fluid caused by the imposed external pressure gradient ∇P_w; (ii) A second component that involves the gradient of ΔP where ΔP denotes a stress due to cell-cell interaction. The effect of $\nabla(\Delta P)$ is to give rise to a (weak) diffusive like cell migration; (iii) A third component that involves the gradient of a function $\Lambda = \Lambda(C, \rho)$ which reflects cell migration in the direction of a positive gradient in the chemokine C (chemotaxis) and positive gradient in fiber ρ (haptotaxis) caused by cell-secreted protease which can degrade and remodel ECM through proteolysis. Main focus in this work is on chemotaxis, however, we also include dependence on ρ to illustrate the possibility to account for a hapotaxis effect. See for example the recent work (Oudin et al., 2016) for the possible role played

by haptotaxis. Note that all three terms involve coefficients that depend nonlinearly on the interaction forces expressed by $\hat{\zeta}_w, \hat{\zeta}_c$, and $\hat{\zeta}$. Hence, the resulting cell velocity $\mathbf{u}_c$ involves a tuned balance between these three different interactions forces.

The second equality of (2) represents an equivalent formulation of the three cell velocity components. In particular, it reflects how the first term is sensitive to the IF velocity $\mathbf{u}_w$. Herein, $\mathbf{U}_T = \alpha_c \mathbf{u}_c + \alpha_w \mathbf{u}_w$ is the total velocity which is dominated by the IF velocity $\mathbf{u}_w$ (which is much higher then the cell velocity $\mathbf{u}_c$). Fig. 2 reflects that flow + blocking of CCR7 gives rise to only a small degree of downstream cell migration when chemotaxis is nullified. Thus, it is clear that only a small cell migration effect is caused directly by the IF flow. Consequently, this term is useful as a means to extract information about how to set the strength of the cell-ECM interaction term $\hat{\zeta}_c$ relatively the strength of the fluid-ECM interaction term $\hat{\zeta}_w$. We test the model behavior for a flow system with an external imposed pressure gradient giving rise to a fluid velocity which is comparable with the one considered in the flow experiments in Shields et al. (2007). In particular, the model illustrates how a gradient in chemokine C is a result of protease G secreted by the cancer cells which interacts with ECM ρ and liberates chemokine whose concentration is skewed in the direction of IF flow. Sensitivity to changes in circumstances like blocking of the CCR7 receptor needed for autologous chemotaxis and elimination of the pressure driven IF flow are explored and discussed in Sections 4 and 5.

The model formulation is general enough to also use in a tumor setting where we can include source terms in the mass balance equation for IF that account for the fluid drainage caused by flow between blood vessels and lymphatic vessels. We illustrate the model behavior in an envisioned tumor setting where increased IF flow is produced from leaky blood vessels sitting on the inside of the tumor. This results in an increased fluid flow towards the region on the outside of the tumor where it is adsorbed by lymphatic vessels and gives rise to a characteristic elevated IF pressure profile P_w that decreases at the tumor periphery. In turn, this generates an autologous chemotactic driven migration of cancer cells at the rim of the tumor. The simulation illustrates how the autologous chemotactic cell migration mechanism discovered by Swartz and collaborators possibly can play a role in progression of a tumor and metastasis by generating aggressive cell migration in the direction of lymphatics. By this it is also illustrated how the model can be used as a tool to upscale laboratory experiments to a more realistic tumor setting.

2. A Fleury-Shield-Swartz multiphase model for autologous chemotaxis

The multiphase approach represents a general approach where more details of the involved physical forces and interactions between different phases (cell population, extracellular fluid, tissue, etc) can be taken into considerations. In this modeling framework, the tumor-host environment is considered as a mixture of two interacting dynamic continua: the cellular phase comprises tumor cells represented by a volume fraction α_c and density ρ_c moving with a velocity $\mathbf{u}_c$ and the extracellular fluid phase represented by the volume fraction α_w and density ρ_w moving with a velocity $\mathbf{u}_w$. The rigid extracellular matrix (ECM) also fills a part of the total volume, but this volume is in the following taken to be constant, i.e., there is no dynamic change in volume of ECM by degradation/deposition. Hence, we may write that

$$\alpha_c + \alpha_w = 1 \tag{3}$$

to account for the volume where cells and fluid can move. In the following Section 2.1, we first give a brief review of the cell-fluid

model studied in Evje (2017) developed in the context of a growing cell aggregate in gel where the cell migration mechanism essentially was dictated by cell-secreted protease G that degraded ECM ρ and created chemotactic and haptotactic cell migration. Then, in Section 2.2 we modify the model in order to better represent the cell-fluid-matrix system studied in Shields et al. (2007) and to make it suitable for taking into account an external interstitial fluid (IF) flow generated as a result of pressure difference at the boundary or due to drainage of IF caused by source terms. In particular, we also have to add a transport-reaction equation to represent the chemokine component and modify the equation for the protease such that it can spread by convection.

2.1. A previous cell-fluid model

The cell-fluid model studied in Evje (2017) takes the following form (we refer to the publication for more details, motivation, and interpretation, as well as (Standnes et al., 2017; Standnes and Andersen, 2017; Qiao et al., 2018; Evje and Wen, 2018) for related works in the context of water-oil flow in porous media):

$$(\alpha_c \rho_c)_t + \nabla \cdot (\alpha_c \rho_c \mathbf{u}_c) = \rho_c S_c, \quad S_c = \alpha_c \left(\lambda_{11} - \lambda_{12} \alpha_c - \lambda_{13} \frac{\rho}{\rho_M} \right)$$
$$(\alpha_w \rho_w)_t + \nabla \cdot (\alpha_w \rho_w \mathbf{u}_w) = -\rho_w S_c$$
$$\nabla(\alpha_c \Lambda(G, \rho)) + \alpha_c \nabla P_c = -\hat{\zeta}_c \mathbf{u}_c + \hat{\zeta}(\mathbf{u}_w - \mathbf{u}_c) + \varepsilon_c \nabla \cdot (\alpha_c \rho_c \nabla \mathbf{u}_c)$$
$$\alpha_w \nabla P_w = -\hat{\zeta}_w \mathbf{u}_w - \hat{\zeta}(\mathbf{u}_w - \mathbf{u}_c) + \varepsilon_w \nabla \cdot (\alpha_w \rho_w \nabla \mathbf{u}_w)$$
$$\rho_t = -\lambda_{21} G \rho + \rho \left(\lambda_{22} - \lambda_{23} \alpha_c - \lambda_{24} \frac{\rho}{\rho_M} \right)$$
$$G_t = \nabla \cdot (D_G \nabla G) - \lambda_{31} G + \lambda_{32} \alpha_c, \quad \mathbf{x} \in \Omega, \quad t > 0,$$
$$\tag{4}$$

where $\mathbf{u}_i = (u_i^x, u_i^y, u_i^z)$ for $i = c, w$. The parameters $\varepsilon_c, \varepsilon_w$ refer to the kinematic viscosity and we have assumed a linear relation between strain rate tensor and stress tensor (Newtonian fluids) (Kirby, 2010). The above model must be combined with appropriate pressure-density closure relations $\rho_i = \rho_i(P_i), i = c, w$ in addition to a functional form for the potential function Λ (expressing the force involved in chemotaxis and haptotaxis) and the capillary pressure $\Delta P = P_c - P_w$ (expressing cell-cell interaction). We have used

$$\Delta P = P_c - P_w = \gamma J(\alpha_w \rho_w). \tag{5}$$

Herein, $\gamma > 0$ is a coefficient (unit Pa) that depends linearly on the surface tension (unit Pa m) whereas $J(\alpha_w \rho_w)$ is a monotonic decreasing dimensionless function with respect to the fluid mass $\alpha_w \rho_w$. The ability of the cancer cells to generate an additional directional force is expressed through the potential function $\Lambda(G, \rho)$

$$\Lambda(G, \rho) = \Lambda_0 + \Lambda_1 \exp(-\xi_1 G - \xi_2 \rho), \tag{6}$$

where $\Lambda_0, \Lambda_1, \xi_1$, and ξ_2 are constant parameters with units, respectively, as $[\Lambda_0] = [\Lambda_1] = $ Pa and $[\xi_1] = [\xi_2] = $ m³/kg.

There is a drag force (that acts opposite of the direction of movement of the fluid) between the extracellular fluid represented by the fluid velocity $\mathbf{u}_w$ and the ECM structure (fibers). The drag represents the net force in the direction of the fluid flow and is caused by pressure and shear stress forces acting on the surface of the object. We use the following expression for this force (motivated by general multiphase flow modeling)

$$\hat{\zeta}_w = I_w \hat{k}_w \alpha_w^{r_w}, \quad \hat{k}_w > 0, \quad r_w < 2, \tag{7}$$

with $I_w = \frac{\mu_w}{K} > 0$. Similarly, there is a drag force between the cells and the ECM (fibers) that acts opposite of the direction of the movement of the cells represented by the cell fluid velocity $\mathbf{u}_c$,

$$\hat{\zeta}_c = I_c \hat{k}_c \alpha_c^{r_c}, \quad I_c, \hat{k}_c > 0, \quad r_c < 2, \tag{8}$$

where I_c (Pa s/m^2), $\hat{k}_c$ and r_c must be specified (the two last are dimensionless).

Finally, there is also an interaction force between the cell phase and the fluid which is caused by pressure (isotropic) and shear stress forces on the surface of the cell phase. This effect is accounted for through the term $\hat{\zeta}(\mathbf{u}_w - \mathbf{u}_c)$, see (4)$_{3,4}$ where

$$\hat{\zeta} = I\hat{k}\alpha_c\alpha_w, \qquad I, \hat{k} > 0, \tag{9}$$

where I (Pa s/m^2) remains to be determined as well as the dimensionless $\hat{k}$. Note that this force term will vanish when one of the phases vanishes.

In Evje (2017) it was investigated how the above model could be used to address issues like (i) the role of cell-cell and cell-substrate adhesion through capillary pressure; (ii) pattern formation which involves detachment of small cell clusters from the primary tumor; (iii) elevated pressure associated with the primary tumor and important for the interstitial fluid flow; (iv) sensitivity to the physical resistance forces from the surrounding ECM depending on whether fibers are aligned or arbitrary distributed. In particular, it was also explained how the above two-fluid model can be reduced to a model which is closely related to models studied by Chaplain and Lolas (2005, 2006) by imposing some simplifying assumptions. However, these assumptions (and the resulting model) are not appropriate when we want a model that allows us to study the interplay between cancer cells and interstitial fluid flow as investigated by Swartz and collaborators (Fleury et al., 2006; Shields et al., 2007; Shieh et al., 2011; Shieh and Swartz, 2011). Some essential differences are:

(i) In order to use the model in a tumor setting one should add source terms to the IF mass balance equation to account for increased fluid flow from leaky blood vessels and a related adsorption of IF through lymphatic vessels on the outside of the tumor rim;

(ii) For realistic modeling of the impact of the IF flow, both in a laboratory setting and tumor setting, it is crucial to include the fluid-ECM interaction term (7) to create the elevated IF pressure as a function of tumor conductivity and fluid rate. Similarly, it is also essential to account for the cell-ECM interaction term (8). This term is needed in order to ensure a realistic cell velocity relatively the IF velocity. While the later typically is taken to be in the range of 0.1–2.0 μm/s, the cell velocity is more in the range of 0.1 μm/min = 0.0017 μm/s (Polacheck et al., 2011; Haessler et al., 2012), i.e., a 100-fold lower.

(iii) Finally, the transport-reaction part of the model (4), i.e., the two last equations, must be modified and extended in order to describe the autologous chemotaxis mechanism elucidated in Shields et al. (2007).

2.2. A Fleury-Shields-Swartz cell-fluid model for autologous chemotaxis

First, we make the following assumptions in (4):

(i) incompressible phases: ρ_c, ρ_w are constant;

(ii) viscosity terms in the momentum balance are ignored, i.e., $\varepsilon_c = \varepsilon_w = 0$;

(iii) we add a source term $Q = Q_v - Q_l$ in the IF mass balance law (4)$_2$ to account for the drainage of interstitial fluid due to leaky blood vessels inside the tumor (intra-tumoral region) (described by Q_v) and adsorption through the lymphatic vessels on the outside of the tumor (described by Q_l).

The objective is to further modify this model to include the transport mechanism presented by Swartz et al. Hence, a new species is introduced to (4) which corresponds to the free CCL21 and described by the following transport-reaction equation:

$$C_t = \nabla \cdot (D_C \nabla C) - \nabla \cdot (\mathbf{u}_w C) + G\rho \left(\lambda_{41} - \lambda_{42} \left(\frac{C}{C_M}\right)^2 - \lambda_{43} \left(\frac{C}{C_M}\right)^{v_C} \right) - \lambda_{44}\alpha_c. \tag{10}$$

The CCL21 concentration C is governed by diffusion, advection and production by protease G that liberates ECM-bound CCL21. The production of chemokine is determined through a logistic growth term, which is activated only when both protease G and ECM ρ are present. The logistic term regulates the production of chemokine such that it will not exceed a maximum concentration C_M. The second λ_{42}-related term of the logistic function reduces the production as the chemokine increases. The third λ_{43}-related term stops the production when it reaches the maximum concentration C_M. In addition, the v_C coefficient defines when the production of chemokine is strongest. The last term in (10) with rate coefficient λ_{44} describes consumption of chemokine by the cancer cells. The chemokine may be consumed through cell binding and internalization. The kinetics of receptor-ligand interactions are highly specific and dynamic, we have therefore included a simplified consumption term in our model.

Further, the component G described by (4)$_6$ is assigned the role as cell-secreted protease species discussed in Shields et al. (2007). The transport-reaction equation associated with G takes the form

$$G_t = \nabla \cdot (D_G \nabla G) - \nabla \cdot (\mathbf{u}_w G) - \lambda_{31} G + \alpha_c \left(\lambda_{32} - \lambda_{33} \left(\frac{G}{G_M}\right)^{v_G} \right). \tag{11}$$

The new aspect here is that protease is transported by the fluid flow through a convective term $\nabla \cdot (\mathbf{u}_w G)$. A logistic growth term is used to regulate the production of protease in the same manner as for chemokine described above, except that there is no cell consumption term. From (4), combined with (10) and (11) and the assumptions (i)–(iii), we get

$$
\begin{aligned}
&(\alpha_c)_t + \nabla \cdot (\alpha_c \mathbf{u}_c) = S_c, \qquad S_c = \alpha_c \left(\lambda_{11} - \lambda_{12}\alpha_c - \lambda_{13} \frac{\rho}{\rho_M} \right) \\
&(\alpha_w)_t + \nabla \cdot (\alpha_w \mathbf{u}_w) = -S_c + Q, \quad Q = Q_v - Q_l \\
&\alpha_c \nabla P_c = -\hat{\zeta}_c \mathbf{u}_c + \hat{\zeta}(\mathbf{u}_w - \mathbf{u}_c) \\
&\alpha_w \nabla P_w = -\hat{\zeta}_w \mathbf{u}_w - \hat{\zeta}(\mathbf{u}_w - \mathbf{u}_c) \\
&\rho_t = -\lambda_{21} G\rho + \rho \left(\lambda_{22} - \lambda_{23}\alpha_c - \lambda_{24} \frac{\rho}{\rho_M} \right) \\
&G_t = \nabla \cdot (D_G \nabla G) - \nabla \cdot (\mathbf{u}_w G) - \lambda_{31} G \\
&\qquad + \alpha_c \left(\lambda_{32} - \lambda_{33}(\frac{G}{G_M})^{v_G} \right) \\
&C_t = \nabla \cdot (D_C \nabla C) - \nabla \cdot (\mathbf{u}_w C) \\
&\qquad + G\rho \left(\lambda_{41} - \lambda_{42} \frac{C}{C_M}^2 - \lambda_{43}(\frac{C}{C_M})^{v_C} \right) - \lambda_{44}\alpha_c.
\end{aligned}
\tag{12}
$$

Here we implicitly treat the cell phase as a fluid like phase but where we add cell-specific features to the momentum Eq. (12)$_3$ by letting the cell phase pressure P_c feel additional stress due to cell-cell interaction ΔP and migration due to chemotaxis/haptotaxis Λ through the relation

$$P_c = P_w + \Delta P(\alpha_w) + \Lambda(C, \rho). \tag{13}$$

This means that the stress P_c associated with the cancer cells differs from the IF pressure P_w because of the cell-cell stress term ΔP given by (5) and the chemotaxis/haptotaxis stress term

Λ. Since CCL21 has been identified as a source for chemotactic cell migration partly due to cell-secreted proteases that release CCL21 from ECM as reflected by Fig. 2, the potential function Λ is altered to depend on C and ρ such that it takes the following form

$$\Lambda(C, \rho) = \Lambda_0 - \frac{\Lambda_1}{1 + \exp(-\xi_1(C - C_M) - \xi_2(\rho - \rho_M))}. \tag{14}$$

This gives rise to the mechanism proposed by Fleury et al. (2006), Shields et al. (2007), where the cell migration due to chemotaxis is now dependent on the chemokine CCL21 concentration. We will see later, see for example Remark 3.1, from the general expression for the cell velocity $\mathbf{u}_c$, how cells will then generate directed motion towards the chemokine gradient. The inclusion of ρ means that the protease-dependent remodelling of ECM also can give rise to a haptotactic cell migration in the direction of positive gradient in ρ.

Remark 2.1. Using the transport mechanism suggested in Shields et al. (2007)) we consider that cells require CCR7 receptors for migration, which have the corresponding ligands CCL21 and CCL19. In our model as described by (10) we will only take CCL21 into account due to its matrix binding property, which may skew the chemokine gradient further downstream of the initial tumor through the advective term $\nabla \cdot (\mathbf{u}_w C)$ when liberated from the ECM by protease G. Including CCL19, which is secreted by the tumor cells, and assuming that we treat CCL19 and CCL21 as one component C, may not contribute in an essential new manner to the overall gradient due to the logistic growth function in (10). On the other hand, if we represent CCL19 and CCL21 by two different variables, say C and D, and add a new transport-reaction equation for D combined with inclusion of D in the Λ-function in (14), that could clearly increase the strength of the chemotactic migration. However, the two migration mechanisms would be of the same nature and may not add any essential new insight, to the best of our understanding.

Remark 2.2. The two momentum balance Eqs. $(12)_{3,4}$ are a consequence of the general momentum balance equations

$$0 = \nabla \cdot (\alpha_c \sigma_c) - \hat{\zeta}_c \mathbf{u}_c + \hat{\zeta}(\mathbf{u}_w - \mathbf{u}_c) + P_c \nabla \alpha_c$$
$$0 = \nabla \cdot (\alpha_w \sigma_w) - \hat{\zeta}_w \mathbf{u}_c - \hat{\zeta}(\mathbf{u}_w - \mathbf{u}_c) + P_w \nabla \alpha_w \tag{15}$$

combined with the simplified stress tensor $\sigma_i = -P_i I$ ($i = c, w$) that accounts for the isotropic pressure only and ignores the viscous stress tensor. This approach is similar to the one used in Breward et al. (2003) and slightly different from what was done in Evje (2017) as seen in $(4)_3$ where the stress-related term Λ appears as a separate term, which in turn was motivated by (Byrne and Owen, 2004). In (12) the stress term Λ is accounted for in (13).

In the next subsection, we give a brief summary related to vascular and lymphatic flow in the context of tumor dynamics represented by $Q = Q_v - Q_l$. We mostly follow along the lines of (Jain et al., 2014). This serves as a motivation for the numerical examples in Section 4 where we consider a one dimensional strip through a tumor microenvironment as sketched in Fig. 3 and include the IF drainage due to leaky blood vessels inside the tumor and adsorption via lymphatics in the surrounding microenvironment. We refer to (Wiig and Swartz, 2012) for a comprehensive review that integrates biophysical, biomechanical, and biological aspects of interstitial and lymph fluid flow. For more information about the possible role played by lymphatic drainage in the context of tumor cells we refer to the review paper (Swartz and Lund, 2012).

2.3. Vascular flow Q_v

Lymphatic flow is an important component of the circulation. In nearly all tissues, plasma leaks out of blood capillaries, flows
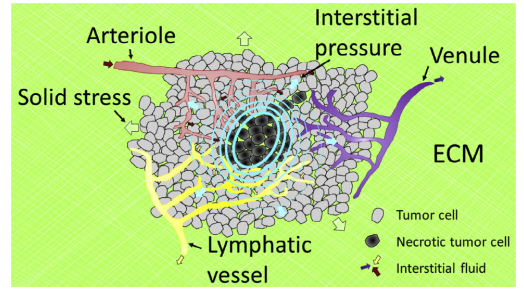
Fig. 3. Schematic figure of a tumor microenvironment motivated by an illustration in Koumoutsakos et al. (2013). Mechanical properties of the tumor microenvironment: radial solid stress exerted by the growing tumor (gray arrows), enhanced extracellular matrix (ECM) stiffness (green fibers), elevated levels of interstitial pressure (blue arrows), and increased interstitial flow (red, purple, and yellow arrows). (For interpretation of the references to colour in this figure legend, the reader is referred to the web version of this article.)

through the interstitium and drains into lymphatic vessels, where it passes through lymph nodes before being returned to the venous blood. The driving forces for interstitial flow are hydrostatic and osmotic pressure gradients between the vascular and interstitial space. The interstitial space of solid tumors is composed of a network of collagen fibers, along with other fibrillar and space-filling proteins and molecules, Interstitial fluid flow is governed in large part by the hydraulic conductivity of the interstitial space, a measure of the resistance to fluid flow in porous and fibrous media. The higher the conductivity, the more easily fluid will move through the extravascular space of the tissue. Starling's Law is used for the flow of fluid in the interstitium given by

$$Q_v = T_v(P_v^* - P_w - \sigma_T(\pi_v^* - \pi_w)) = T_v(\widetilde{P_{v^*}} - P_w),$$
$$T_v = L_v \frac{S_v}{V}, \tag{16}$$

with $\widetilde{P_{v^*}} = P_v^* - \sigma_T(\pi_v^* - \pi_w)$. Here L_v is the hydraulic conductivity (m² s/kg = m/Pa s) of the vessel wall, S_v/V (m⁻¹) the exchange area of blood vessels per unit volume of tissues V, P_v^* and P_w the vascular and interstitial fluid pressure, π_v^* and π_w the osmotic pressure in the vascular and interstitial space and σ_T the osmotic reflection coefficient for plasma proteins.

2.4. Lymphatic flow Q_l

The lymphatic network drains excessive fluid from the interstitial space and returns it back to the blood circulation. By doing so, it regulates the fluid balance in tissues and prevents formation of edema. Tumor lymphatics have two characteristics, common in many cancers. They are not functional in the intratumoral region, and they are hyperplastic and exhibit increased flow at the periphery. The loss of functionality is attributed to compressive solid stress that is developed in tumors. This stress has been shown to collapse intratumoral lymphatic vessels, and thus eliminates lymph flow. Similar to (16) we use an expression of the following form to express the fluid adsorption through lymphatics

$$Q_l = T_l(P_w - P_l^*), \qquad T_l = L_l \frac{S_l}{V}. \tag{17}$$

Here L_l is the hydraulic conductivity of the lymphatic vessel walls whereas S_l/V is the surface area of the lymphatic vessel per volume unit of tissues V and P_l^* is the effective lymphatic pressure. As we have mentioned earlier, intratumoral lymphatics are dysfunctional

and thus, it is common to consider lymphatic flow to be negligible inside the tumor.

2.5. Rewritten form of the Fleury-Shields-Swartz model

In this section we will rewrite the model (12) to make it more transparent. In particular, we will obtain explicit expressions for cell velocity $\mathbf{u}_c$ and IF velocity $\mathbf{u}_w$. From (12) we have, after we have made it dimensionless (see Appendix A) and also used (13)

$$
\begin{aligned}
&\alpha_{ct} + \nabla \cdot (\alpha_c \mathbf{u}_c) = S_c, \qquad S_c = \alpha_c\left(\lambda_{11} - \lambda_{12}\alpha_c - \lambda_{13}\frac{\rho}{\rho_M}\right)\\
&\alpha_{wt} + \nabla \cdot (\alpha_w \mathbf{u}_w) = -S_c + (Q_v - Q_l)\\
&\alpha_c \nabla(P_w + \Delta P(\alpha_w)) + \Lambda(C, \rho)) = -\hat{\zeta}_c \mathbf{u}_c + \hat{\zeta}(\mathbf{u}_w - \mathbf{u}_c)\\
&\alpha_w \nabla P_w = -\hat{\zeta}_w \mathbf{u}_w - \hat{\zeta}(\mathbf{u}_w - \mathbf{u}_c)\\
&\rho_t = -\lambda_{21} G\rho + \rho\left(\lambda_{22} - \lambda_{23}\alpha_c - \lambda_{24}(\frac{\rho}{\rho_M})\right)\\
&G_t = \nabla \cdot (D_G \nabla G) - \nabla \cdot (\mathbf{u}_w G) - \lambda_{31} G\\
&\quad + \alpha_c\left(\lambda_{32} - \lambda_{33}(\frac{G}{G_M})^{v_G}\right)\\
&C_t = \nabla \cdot (D_C \nabla C) - \nabla \cdot (\mathbf{u}_w C)\\
&\quad + G\rho\left(\lambda_{41} - \lambda_{42}(\frac{C}{C_M})^2 - \lambda_{43}(\frac{C}{C_M})^{v_C}\right) - \lambda_{44}\alpha_c
\end{aligned}
\tag{18}
$$

with $\mathbf{u}_i = (u_i^x, u_i^y, u_i^z)$ for $i = c, w$. The model is combined with the boundary condition

$$
P_w|_{\partial\Omega} = P^*, \qquad \frac{\partial}{\partial v}G\Big|_{\partial\Omega} = 0 \qquad \frac{\partial}{\partial v}C\Big|_{\partial\Omega} = 0, \qquad t > 0
$$

where P^* is a specified known pressure at the boundary of the domain Ω and v is the outward normal on $\partial\Omega$ and $i = c, w$. The corresponding initial data are

$$
\begin{aligned}
&\alpha_c(\mathbf{x}, t = 0) = \alpha_{c0}(\mathbf{x}), \quad \rho(\mathbf{x}, t = 0) = \rho_0(\mathbf{x}),\\
&G(\mathbf{x}, t = 0) = G_0(\mathbf{x}), \quad C(\mathbf{x}, t = 0) = C_0(\mathbf{x})
\end{aligned}
\tag{19}
$$

for $\mathbf{x} \in \Omega$. We now rewrite the model to reveal the essential components that govern the IF velocity $\mathbf{u}_w$ as well as the cell velocity $\mathbf{u}_c$.

We can write the momentum balance Eqs. (18)$_{3,4}$ as

$$
\begin{aligned}
&\alpha_w \nabla P_w = \hat{\zeta}\mathbf{u}_c - (\hat{\zeta}_w + \hat{\zeta})\mathbf{u}_w\\
&\alpha_c \nabla \Lambda(C, \rho) + \alpha_c \nabla(\Delta P) + \alpha_c \nabla P_w = -(\hat{\zeta}_c + \hat{\zeta})\mathbf{u}_c + \hat{\zeta}\mathbf{u}_w
\end{aligned}
\tag{20}
$$

2.5.1. Expressions for cell velocity and IF velocity

We can solve for $\mathbf{u}_w$ and $\mathbf{u}_c$ from the 2x2 linear system (20) and find that

$$
\begin{aligned}
\mathbf{u}_c = &-\frac{[\alpha_c \hat{\zeta}_w] + \hat{\zeta}}{\hat{\zeta}_c \hat{\zeta}_w + \hat{\zeta}[\hat{\zeta}_c + \hat{\zeta}_w]}\nabla P_w - \frac{\alpha_c[\hat{\zeta}_w + \hat{\zeta}]}{\hat{\zeta}_c \hat{\zeta}_w + \hat{\zeta}[\hat{\zeta}_c + \hat{\zeta}_w]}\nabla(\Delta P)\\
&-\frac{\alpha_c[\hat{\zeta}_w + \hat{\zeta}]}{\hat{\zeta}_c \hat{\zeta}_w + \hat{\zeta}[\hat{\zeta}_c + \hat{\zeta}_w]}\nabla \Lambda(C, \rho),\\
\mathbf{u}_w = &-\frac{[\alpha_w \hat{\zeta}_c] + \hat{\zeta}}{\hat{\zeta}_c \hat{\zeta}_w + \hat{\zeta}[\hat{\zeta}_c + \hat{\zeta}_w]}\nabla P_w - \frac{\alpha_c \hat{\zeta}}{\hat{\zeta}_c \hat{\zeta}_w + \hat{\zeta}[\hat{\zeta}_c + \hat{\zeta}_w]}\nabla(\Delta P)\\
&-\frac{\alpha_c \hat{\zeta}}{\hat{\zeta}_c \hat{\zeta}_w + \hat{\zeta}[\hat{\zeta}_c + \hat{\zeta}_w]}\nabla \Lambda(C, \rho).
\end{aligned}
\tag{21}
$$

Hence, the corresponding Darcy velocities $\mathbf{U}_c = \alpha_c \mathbf{u}_c$ and $\mathbf{U}_w = \alpha_w \mathbf{u}_w$ (also referred to as superficial velocity) are given by

$$
\begin{aligned}
\mathbf{U}_c := \ &\alpha_c \mathbf{u}_c = -\hat{\lambda}_c \nabla P_w - \hat{\lambda}_c \nabla(\Delta P) + \frac{\alpha_c \alpha_w \hat{\zeta}}{\hat{\zeta}_c \hat{\zeta}_w + \hat{\zeta}[\hat{\zeta}_c + \hat{\zeta}_w]}\nabla(\Delta P)\\
&- \hat{\lambda}_c \nabla \Lambda(C, \rho) + \frac{\alpha_c \alpha_w \hat{\zeta}}{\hat{\zeta}_c \hat{\zeta}_w + \hat{\zeta}[\hat{\zeta}_c + \hat{\zeta}_w]}\nabla \Lambda(C, \rho),
\end{aligned}
$$

$$
\begin{aligned}
\mathbf{U}_w := \ &\alpha_w \mathbf{u}_w = -\hat{\lambda}_w \nabla P_w - \frac{\alpha_c \alpha_w \hat{\zeta}}{\hat{\zeta}_c \hat{\zeta}_w + \hat{\zeta}[\hat{\zeta}_c + \hat{\zeta}_w]}\nabla(\Delta P)\\
&- \frac{\alpha_c \alpha_w \hat{\zeta}}{\hat{\zeta}_c \hat{\zeta}_w + \hat{\zeta}[\hat{\zeta}_c + \hat{\zeta}_w]}\nabla \Lambda(C, \rho),
\end{aligned}
\tag{22}
$$

with generalized mobility functions $\hat{\lambda}_c$ and $\hat{\lambda}_w$ of the form

$$
\begin{aligned}
\hat{\lambda}_c = \frac{[\alpha_c^2 \hat{\zeta}_w] + \alpha_c \hat{\zeta}}{\hat{\zeta}_c \hat{\zeta}_w + \hat{\zeta}[\hat{\zeta}_c + \hat{\zeta}_w]},\\
\hat{\lambda}_w = \frac{[\alpha_w^2 \hat{\zeta}_c] + \alpha_w \hat{\zeta}}{\hat{\zeta}_c \hat{\zeta}_w + \hat{\zeta}[\hat{\zeta}_c + \hat{\zeta}_w]},
\end{aligned}
\tag{23}
$$

and total mobility $\hat{\lambda}_T$ given by

$$
\hat{\lambda}_T = \hat{\lambda}_c + \hat{\lambda}_w = \frac{[\alpha_c^2 \hat{\zeta}_w] + [\alpha_w^2 \hat{\zeta}_c] + \hat{\zeta}}{\hat{\zeta}_c \hat{\zeta}_w + \hat{\zeta}[\hat{\zeta}_c + \hat{\zeta}_w]}.
\tag{24}
$$

Summing the two mass balance Eqs. (18)$_{1,2}$ and making use of (3), we find the following equation

$$
\nabla \cdot \mathbf{U}_T = \nabla \cdot (\mathbf{U}_c + \mathbf{U}_w) = Q_v - Q_l.
\tag{25}
$$

From (22), it follows after a summation that

$$
\mathbf{U}_T = \mathbf{U}_c + \mathbf{U}_w = -\hat{\lambda}_T \nabla P_w - \hat{\lambda}_c \nabla(\Delta P) - \hat{\lambda}_c \nabla \Lambda(C, \rho).
\tag{26}
$$

By using $\nabla\cdot$ on (26) and referring to (25), we then arrive at

$$
\begin{aligned}
&-(Q_v - Q_l) - \nabla \cdot (\hat{\lambda}_c \nabla(\Delta P)) - \nabla \cdot (\hat{\lambda}_c \nabla \Lambda(C, \rho))\\
&= \nabla \cdot (\hat{\lambda}_T \nabla P_w).
\end{aligned}
\tag{27}
$$

This gives an elliptic equation for P_w that can be solved subject to the boundary condition $P_w|_{\partial\Omega} = P^*$. This in turn allows us to compute $\mathbf{U}_T$ from (26). Next, we want to eliminate the explicit dependence on IF pressure P_w in (22). We refer to Appendix B for details. Here we only note that this gives us the following expressions, expressed in terms of interstitial velocity $\mathbf{u}_c$ and $\mathbf{u}_w$:

$$
\begin{aligned}
\mathbf{u}_c = &\ \mathbf{U}_T\left[\frac{\alpha_c \hat{\zeta}_w + \hat{\zeta}}{\alpha_c^2 \hat{\zeta}_w + \alpha_w^2 \hat{\zeta}_c + \hat{\zeta}}\right] - \left[\frac{\alpha_c \alpha_w^2}{\alpha_c^2 \hat{\zeta}_w + \alpha_w^2 \hat{\zeta}_c + \hat{\zeta}}\right]\nabla(\Delta P)\\
&- \left[\frac{\alpha_c \alpha_w^2}{\alpha_c^2 \hat{\zeta}_w + \alpha_w^2 \hat{\zeta}_c + \hat{\zeta}}\right]\nabla \Lambda(C, \rho),\\
\mathbf{u}_w = &\ \mathbf{U}_T\left[\frac{\alpha_w \hat{\zeta}_c + \hat{\zeta}}{\alpha_c^2 \hat{\zeta}_w + \alpha_w^2 \hat{\zeta}_c + \hat{\zeta}}\right] + \left[\frac{\alpha_c^2 \alpha_w}{\alpha_c^2 \hat{\zeta}_w + \alpha_w^2 \hat{\zeta}_c + \hat{\zeta}}\right]\nabla(\Delta P)\\
&+ \left[\frac{\alpha_c^2 \alpha_w}{\alpha_c^2 \hat{\zeta}_w + \alpha_w^2 \hat{\zeta}_c + \hat{\zeta}}\right]\nabla \Lambda(C, \rho).
\end{aligned}
\tag{28}
$$

2.5.2. Rewritten version of the model
The model (18) then takes the simpler form:

$$
\begin{aligned}
&\alpha_{ct} + \nabla \cdot (\alpha_c \mathbf{u}_c) = S_c\\
&\rho_t = -\lambda_{21} G\rho + \rho\left(\lambda_{22} - \lambda_{23}\alpha_c - \lambda_{24}(\frac{\rho}{\rho_M})\right)\\
&G_t = \nabla \cdot (D_G \nabla G) - \nabla \cdot (\mathbf{u}_w G) - \lambda_{31} G\\
&\quad + \alpha_c\left(\lambda_{32} - \lambda_{33}(\frac{G}{G_M})^{v_G}\right)\\
&C_t = \nabla \cdot (D_C \nabla C) - \nabla \cdot (\mathbf{u}_w C)\\
&\quad + G\rho\left(\lambda_{41} - \lambda_{42}(\frac{C}{C_M})^2 - \lambda_{43}(\frac{C}{C_M})^{v_C}\right) - \lambda_{44}\alpha_c,
\end{aligned}
\tag{29}
$$

where the interstitial cell celocity $\mathbf{u}_c$ is given by (28)$_1$. Similarly, $\mathbf{u}_w$ is given by (28)$_2$ and appears in the convective terms in the transport-reaction equations for G and C which reflect that the secreted protease G and released ECM-bound chemokine C flow

with the fluid flow velocity. Moreover, in order to compute $\mathbf{U}_T$ we first solve the elliptic problem for P_w

$$- (Q_v - Q_l) - \nabla \cdot (\hat{\lambda}_c \nabla (\Delta P + \Lambda(C, \rho))) = \nabla \cdot (\hat{\lambda}_T \nabla P_w),$$
$$P_w|_{\partial \Omega} = P^*. \tag{30}$$

Knowing P_w, we use (26) given by

$$\mathbf{U}_T = -\hat{\lambda}_T \nabla P_w - \hat{\lambda}_c \nabla (\Delta P) - \hat{\lambda}_c \nabla \Lambda(C, \rho) \tag{31}$$

which is required in the calculation of $\mathbf{u}_c$ and $\mathbf{u}_w$ in (28). Alternatively, we can write the model (29) in the form (see (61) in Appendix B for definition of $\hat{f}_c(\alpha_c)$ and $\hat{h}(\alpha_c)$)

$$\begin{aligned}
\alpha_{ct} + \nabla \cdot (\mathbf{U}_T \hat{f}_c(\alpha_c)) &= \nabla \cdot (\hat{h}(\alpha_c) \nabla (\Delta P(\alpha_c))) \\
&\quad + \nabla \cdot (\hat{h}(\alpha_c) \nabla (C, \rho)) + S_c \\
\rho_t &= -\lambda_{21} G\rho + \rho \left(\lambda_{22} - \lambda_{23} \alpha_c - \lambda_{24} \left(\frac{\rho}{\rho_M} \right) \right) \\
G_t &= \nabla \cdot (D_G \nabla G) - \nabla \cdot (\mathbf{u}_w G) - \lambda_{31} G \\
&\quad + \alpha_c \left(\lambda_{32} - \lambda_{33} \left(\frac{G}{G_M} \right)^{v_G} \right) \\
C_t &= \nabla \cdot (D_C \nabla C) - \nabla \cdot (\mathbf{u}_w C) \\
&\quad + G\rho \left(\lambda_{41} - \lambda_{42} \left(\frac{C}{C_M} \right)^2 - \lambda_{43} \left(\frac{C}{C_M} \right)^{v_C} \right) - \lambda_{44} \alpha_c.
\end{aligned} \tag{32}$$

The model (29)–(31), combined with (28), is subject to the boundary condition

$$\frac{\partial}{\partial v} G \bigg|_{\partial \Omega} = 0 \qquad \frac{\partial}{\partial v} C \bigg|_{\partial \Omega} = 0, \qquad t > 0 \tag{33}$$

where v is the outward normal on $\partial \Omega$ and $i = c, w$. The corresponding initial data are

$$\begin{aligned}
\alpha_c(\mathbf{x}, t = 0) &= \alpha_{c0}(\mathbf{x}), \quad \rho(\mathbf{x}, t = 0) = \rho_0(\mathbf{x}), \\
G(\mathbf{x}, t = 0) &= G_0(\mathbf{x}), \quad C(\mathbf{x}, t = 0) = C_0(\mathbf{x}).
\end{aligned} \tag{34}$$

Remark 2.3. Note that from the elliptic problem (30) we extract the IF pressure field P_w which largely determines the total velocity $\mathbf{U}_T$ through (31). This shows how an imposed pressure through the boundary pressure P^* (which is typically the case for laboratory experiments as in Shields et al. (2007)) strongly impact IF pressure P_w and in turn the resulting IF velocity $\mathbf{u}_w$ through its dependence on $\mathbf{U}_T$ via (28)$_2$. Similarly, we see from (30) the crucial role played by IF flow due to leaky blood vessels and adsorbing lymphatics through $Q = Q_v - Q_l$ which is relevant to include if we employ the model in a tumor setting.

Remark 2.4. Regarding the cell velocity $\mathbf{u}_c$, the expression (28)$_1$ identifies three different cell migration mechanisms:

$$\mathbf{u}_c = \mathbf{u}_{c,\text{fluidstress}} + \mathbf{u}_{c,\text{cell–cell}} + \mathbf{u}_{c,\text{chemotaxis/haptotaxis}}$$

with

$$\begin{aligned}
\mathbf{u}_{c,\text{fluidstress}} &= \mathbf{U}_T \left[\frac{\alpha_c \hat{\zeta}_w + \hat{\zeta}}{\alpha_c^2 \hat{\zeta}_w + \alpha_w^2 \hat{\zeta}_c + \hat{\zeta}} \right], \\
\mathbf{u}_{c,\text{cell–cell}} &= -\left[\frac{\alpha_c \alpha_w^2}{\alpha_c^2 \hat{\zeta}_w + \alpha_w^2 \hat{\zeta}_c + \hat{\zeta}} \right] \nabla (\Delta P), \\
\mathbf{u}_{c,\text{chemotaxis/haptotaxis}} &= -\left[\frac{\alpha_c \alpha_w^2}{\alpha_c^2 \hat{\zeta}_w + \alpha_w^2 \hat{\zeta}_c + \hat{\zeta}} \right] \nabla \Lambda(C, \rho).
\end{aligned} \tag{35}$$

The first term $\mathbf{u}_{c,\text{fluidstress}}$ represents a stress caused by the flowing IF on the cancer cells. Experiments as reported in Shields et al. (2007) and reflected in Fig. 2 indicate that cancer cells to a large extent will

resist the direct pushing force represented by this stress. The second term $\mathbf{u}_{c,\text{cell–cell}}$ accounts for a diffusive cell-cell repelling force that leads to a more or less weak non-directional migration. The third term $\mathbf{u}_{c,\text{chemotaxis/haptotaxis}}$ reflects a directional cell migration towards positive gradient in chemokine C and ECM component ρ.

A main objective of this work to provide a multiphase model that can illustrate and shed light on different aspects of the autologous chemotaxis cell migration mechanism. Note that all three terms in (35) involve coefficients that depend nonlinearly on the interaction forces expressed by $\hat{\zeta}_w, \hat{\zeta}_c$, and $\hat{\zeta}$. Hence, the resulting cell velocity $\mathbf{u}_c$ involves a more or less fine tuned balance between these three different forces. Next, we will consider correlations for these interaction forces, essentially motivated by multiphase creeping flow in porous media (Evje, 2017; Qiao et al., 2018), and then try to obtain more insight how parameters should be set to give a cell migration behavior which qualitatively is consistent with those reported and discussed in Shields et al. (2007). In addition, we need to set parameters associated with cell-cell stress term ΔP as expressed by (5) and the chemotaxis/haptotaxis stress term Λ given by (14) to achieve this consistency. For the sake of clearness and simplicity we will in the rest of this work restrict our investigations to a one-dimensional version of the model (29).

3. One-dimensional version of the Fleury-Shields-Swartz model

3.1. Specification of interaction force terms

We now focus on the 1D version of (29). We also assume that certain aspects of the fluid-cell interaction is ignored by setting $\hat{\zeta} = 0$. That is, we ignore a shear stress effect on the cancer cell aggregate caused by the flowing fluid. This simplification is completely consistent with traditional modeling of two-phase flow in porous media based on Darcy's extended law (Wu, 2016; Qiao et al., 2018). Consistent with (7) and (8), see also (Evje, 2017; Qiao et al., 2018) for more details and motivation, we consider the following choices for $\hat{\zeta}_w$ and $\hat{\zeta}_c$:

$$\hat{\zeta}_w = I_w \hat{k}_w \alpha_w^{r_w}, \qquad \hat{\zeta}_c = I_c \hat{k}_c \alpha_c^{r_c}, \qquad \hat{\zeta} = 0. \tag{36}$$

We may think of I_w, I_c as parameters reflecting "static" properties of the tissue like $I_w = \mu_w / K$, whereas $\hat{k}_w, \hat{k}_c$ can account for dynamic properties, i.e., various coupling mechanisms related to for example ECM fiber alignment and other changes in the microenvironment caused by the IF flow. It seems natural to interpret $\hat{\zeta}_w$ and $\hat{\zeta}_c$ as direct interaction forces (drag force effect), respectively, between fluid and ECM and cell and ECM whereas the ignored term $\hat{\zeta}$ may be linked to indirect mechanical stimulation caused by the IF flow on the cancers cells via the matrix and integrins, as mentioned in the introduction and discussed in Shieh and Swartz (2011). We now consider the dimensionless domain $\Omega = [0, 1]$. The cell and IF velocities u_c and u_w from (28) takes the form:

$$u_c = U_T \left[\frac{\alpha_c \hat{\zeta}_w}{\alpha_c^2 \hat{\zeta}_w + \alpha_w^2 \hat{\zeta}_c} \right] - \left[\frac{\alpha_c \alpha_w^2}{\alpha_c^2 \hat{\zeta}_w + \alpha_w^2 \hat{\zeta}_c} \right] (\Delta P)_x$$
$$\textbf{flow – generated stress} \quad \textbf{dispersion}$$
$$- \left[\frac{\alpha_c \alpha_w^2}{\alpha_c^2 \hat{\zeta}_w + \alpha_w^2 \hat{\zeta}_c} \right] (\Lambda(C, \rho))_x,$$
$$\textbf{chemotaxis/haptotaxis} \tag{37}$$

$$u_w = U_T \left[\frac{\alpha_w \hat{\zeta}_c}{\alpha_c^2 \hat{\zeta}_w + \alpha_w^2 \hat{\zeta}_c} \right] + \left[\frac{\alpha_c^2 \alpha_w}{\alpha_c^2 \hat{\zeta}_w + \alpha_w^2 \hat{\zeta}_c} \right] (\Delta P)_x$$
$$+ \left[\frac{\alpha_c^2 \alpha_w}{\alpha_c^2 \hat{\zeta}_w + \alpha_w^2 \hat{\zeta}_c} \right] (\Lambda(C, \rho))_x.$$

The corresponding Darcy velocities $U_c = \alpha_c u_c$ and $U_w = \alpha_w u_w$ are given by

$$
\begin{aligned}
U_c = \alpha_c u_c &= U_T\left[\frac{\alpha_c^2 \hat{\zeta}_w}{\alpha_c^2 \hat{\zeta}_w + \alpha_w^2 \hat{\zeta}_c}\right] - \left[\frac{\alpha_c^2 \alpha_w^2}{\alpha_c^2 \hat{\zeta}_w + \alpha_w^2 \hat{\zeta}_c}\right](\Delta P)_x \\
&\quad - \left[\frac{\alpha_c^2 \alpha_w^2}{\alpha_c^2 \hat{\zeta}_w + \alpha_w^2 \hat{\zeta}_c}\right](\Lambda(C,\rho))_x, \\
U_w = \alpha_w u_w &= U_T\left[\frac{\alpha_w^2 \hat{\zeta}_c}{\alpha_c^2 \hat{\zeta}_w + \alpha_w^2 \hat{\zeta}_c}\right] + \left[\frac{\alpha_c^2 \alpha_w^2}{\alpha_c^2 \hat{\zeta}_w + \alpha_w^2 \hat{\zeta}_c}\right](\Delta P)_x \\
&\quad + \left[\frac{\alpha_c^2 \alpha_w^2}{\alpha_c^2 \hat{\zeta}_w + \alpha_w^2 \hat{\zeta}_c}\right](\Lambda(C,\rho))_x.
\end{aligned}
\tag{38}
$$

Moreover, the model (29) takes the 1D form

$$
\begin{aligned}
&\alpha_{ct} + (\alpha_c u_c)_x = S_c \\
&\rho_t = -\lambda_{21} G\rho + \rho\left(\lambda_{22} - \lambda_{23}\alpha_c - \lambda_{24}\left(\frac{\rho}{\rho_M}\right)\right) \\
&G_t = D_G G_{xx} - (u_w G)_x - \lambda_{31} G \\
&\quad + \alpha_c\left(\lambda_{32} - \lambda_{33}\left(\frac{G}{G_M}\right)^{v_G}\right) \\
&C_t = D_C C_{xx} - (u_w C)_x \\
&\quad + G\rho\left(\lambda_{41} - \lambda_{42}\left(\frac{C}{C_M}\right)^2 - \lambda_{43}\left(\frac{C}{C_M}\right)^{v_C}\right) - \lambda_{44}\alpha_c,
\end{aligned}
\tag{39}
$$

where u_c and u_w are given by (37). In order to compute U_T we first solve the 1D version of the elliptic problem for P_w (30)

$$
\begin{aligned}
&-(Q_v - Q_l) - (\hat{\lambda}_c(\Delta P + \Lambda(C,\rho))_x)_x = (\hat{\lambda}_T P_{wx})_x, \\
&P_w|_{x=0} = P_L^*, \qquad P_w|_{x=1} = P_R^*.
\end{aligned}
\tag{40}
$$

Herein, by (23) and (24) and after we have made use of (36), we obtain the following expression for the mobility functions $\hat{\lambda}_c, \hat{\lambda}_w, \hat{\lambda}_T$:

$$
\begin{aligned}
\hat{\lambda}_c &= \frac{\alpha_c^2}{\zeta_c} = \frac{\alpha_c^{2-r_c}}{I_c \hat{k}_c}, \\
\hat{\lambda}_w &= \frac{\alpha_w^2}{\zeta_w} = \frac{\alpha_w^{2-r_w}}{I_w \hat{k}_w}, \\
\hat{\lambda}_T &= \frac{\alpha_c^2 \hat{\zeta}_w + \alpha_w^2 \hat{\zeta}_c}{\zeta_c \zeta_w} = \frac{I_w \hat{k}_w \alpha_c^{2-r_c} + I_c \hat{k}_c \alpha_w^{2-r_w}}{I_c I_w \hat{k}_c \hat{k}_w} = \frac{\alpha_c^{2-r_c}}{I_c \hat{k}_c} + \frac{\alpha_w^{2-r_w}}{I_w \hat{k}_w},
\end{aligned}
\tag{41}
$$

with $r_c, r_w \leqslant 2$. Knowing P_w, we use the 1D version of (31) given by

$$
U_T = -\hat{\lambda}_T(P_w)_x - \hat{\lambda}_c(\Delta P)_x - \hat{\lambda}_c(\Lambda)_x.
\tag{42}
$$

Thus, knowing U_T, we can evaluate the flux term $\alpha_c u_c = U_c$ completely which occurs in (39)$_1$ by referring to (37)$_1$ or (38)$_1$. Similarly, we can compute u_w from (37)$_2$ which is needed in (39)$_{3,4}$. The model (39) is combined with the boundary condition

$$
G_x|_{x=0,1} = 0, \qquad C_x|_{x=0,1} = 0, \qquad t > 0.
\tag{43}
$$

The corresponding initial data are

$$
\begin{aligned}
&\alpha_c(x, t=0) = \alpha_{c0}(x), \quad \rho(x, t=0) = \rho_0(x), \\
&G(x, t=0) = G_0(x), \quad C(x, t=0) = C_0(x)
\end{aligned}
\tag{44}
$$

for $x \in \Omega$.

3.2. What controls the strength of the flow-generated stress on cancer cells?

We have from (38) that

$$
\begin{aligned}
U_c &= U_T \hat{f}_c(\alpha_c) - \hat{h}(\alpha_c)(\Delta P(\alpha_w))_x - \hat{h}(\alpha_c)(\Lambda(C,\rho))_x, \\
U_w &= U_T \hat{f}_w(\alpha_c) + \hat{h}(\alpha_c)(\Delta P(\alpha_w))_x + \hat{h}(\alpha_c)(\Lambda(C,\rho))_x,
\end{aligned}
\tag{45}
$$

where the convective transport effect related to the cell phase and fluid phase, respectively, are represented by $\hat{f}_c$ and $\hat{f}_w$ given by

$$
\begin{aligned}
\hat{f}_c(\alpha_c) &= \frac{\alpha_c^2 \hat{\zeta}_w}{\alpha_c^2 \hat{\zeta}_w + \alpha_w^2 \hat{\zeta}_c} = \frac{M\alpha_c^{2-r_c}}{M\alpha_c^{2-r_c} + \alpha_w^{2-r_w}}, \quad M = \frac{I_w \hat{k}_w}{I_c \hat{k}_c} \\
\hat{f}_w(\alpha_c) &= \frac{\alpha_w^2 \hat{\zeta}_c}{\alpha_c^2 \hat{\zeta}_w + \alpha_w^2 \hat{\zeta}_c} = \frac{\alpha_w^{2-r_w}}{M\alpha_c^{2-r_c} + \alpha_w^{2-r_w}},
\end{aligned}
\tag{46}
$$

whereas cell-cell migration through ΔP and chemotaxis/haptotaxis migration through Λ are controlled by $\hat{h}(\alpha_c)$ given by

$$
\begin{aligned}
\hat{h}(\alpha_c) &= \frac{\alpha_c^2 \alpha_w^2}{\alpha_c^2 \hat{\zeta}_w + \alpha_w^2 \hat{\zeta}_c} = \frac{\alpha_c^{2-r_c} \alpha_w^{2-r_w}}{\alpha_c^{2-r_c} I_w \hat{k}_w + \alpha_w^{2-r_w} I_c \hat{k}_c} \\
&= \frac{1}{I_c \hat{k}_c} \frac{\alpha_c^{2-r_c} \alpha_w^{2-r_w}}{\alpha_c^{2-r_c} M + \alpha_w^{2-r_w}}.
\end{aligned}
\tag{47}
$$

There is a shear stress effect from IF flow on the cells which is manifested in the appearance of the first term in (45)$_1$ given by $U_T \hat{f}_c(\alpha_c)$. As discussed in Shieh and Swartz (2011), even with low IF flow velocity, shear stress can be high when there are small pores. Nonetheless, in tumors it is expected that the shear stress remains low because the matrix shields the cells from stress and local gradients in hydraulic conductivity divert flow from cells (Swartz and Fleury, 2007; Pedersen et al., 2010).

The strength of the term $U_T \hat{f}_c$ is controlled by the magnitude of U_T (for a fixed external pressure drop given by the difference between P_L^* and P_R^*) and the strength of $\hat{f}_c$. From (46)$_1$ it is clear that the latter is governed by M, the strength of fluid-ECM resistance force $I_w \hat{k}_w$ relatively the strength of cell-ECM resistance force $I_c \hat{k}_c$. The choice of $I_w \hat{k}_w$ is based on knowledge about the hydraulic conductivity of the porous media made up of fibers and cells. When we use the model to compare with the experimental results shown in Fig. 2, $I_c \hat{k}_c$ must then be set such that M becomes low enough to prevent a non-physical cell migration through the term $U_T \hat{f}_c(\alpha_c)$. This term then accounts for a direct resistance force generated by the cells and implicitly also for a stress shielding effect where aligned fibers perpendicular to flow direction lead to a reduced stress on cells embedded in matrix (Pedersen et al., 2010).

Remark 3.1. Chemotaxis is the result of a combination of signaling inputs to the cell, matrix compliance, and active cellular response such as the engagement of cell motility machinery (Shields et al., 2007). From the third term of (45)$_1$ we see that the strength of the chemotaxis migration is a result of the product $\hat{h}(\alpha_c)\frac{\partial \Lambda}{\partial C}(C,\rho) = \frac{-\Lambda_1 \xi_1 \hat{h}(\alpha_c)}{(1+\exp(-\xi_1[C-C_M]-\xi_2[\rho-\rho_M]))^2}$. Hence, the expression in (47) reflects that chemotaxis is also affected by M and the magnitude of the cell-ECM interaction $I_c \hat{k}_c$ through its dependence on $\hat{h}$ as well as the parameters Λ_1 and ξ_1 involved in (14). The two latter parameters may be interpreted as more detailed information about the degree of engagement of the cell motility machinery in response to chemokine gradient.

3.3. Choice of parameters

We now describe how we choose parameters that must be specified in order to solve the model presented in Section 3.1. We refer to Table 1 (with dimension) and Table 2 (dimensionless) for a compact description of parameters. In particular, all coefficients involved in the reaction equations for protease G, chemokine C, and ECM ρ as described by (39)$_{2,3,4}$ are specified here. In addition, we use maximal concentration $C_M = 0.3, G_M = 0.5, \rho_M = 1.0$ (dimensionless) and exponents $v_G = 1.0$ and $v_C = 0.2$ (dimensionless).

Table 1
Model parameters (dimensional) in the model (12) with relevant reference values.

Parameters	Description	Dimensional value
Reference variables		
T^*	Time	10^4 s
L^*	Length	10^{-2} m
u^*	velocity	10^{-6} m/s
D^*	diffusion	10^{-8} m²/s
ρ^*	ECM density	1 kg/m³
G^*	Protease	10^{-4} kg/m³
C^*	CCL21	10^{-4} kg/m³
P^*	Pressure	10^4 Pa
ρ_M	Maximal ECM density	ρ^*
G_M	Maximal Protease density	$0.5G^*$
C_M	Maximal Chemokine density	$0.3C^*$
Diffusion coefficients		
D_G	Protease	8×10^{-12} m²/s
D_C	CCL21	7×10^{-14} m²/s
Parameters of Λ		
ξ_1	Parameter characterizing Λ (dependence on C)	8×10^4 mm³/kg
ξ_2	Parameter characterizing Λ (dependence on ρ)	0 or 0.4 m³/kg
Λ_0	Parameter characterizing Λ	0 Pa
Λ_1	Parameter characterizing Λ	25,000 Pa
Production/decay rates		
λ_{11}	Proliferation of tumor cells	1.875×10^{-5} 1/s
λ_{12}	Decay of tumor cells	2.5×10^{-5} 1/s
λ_{13}	Decay of tumor cells	1.25×10^{-5} 1/s
λ_{21}	Degradation of ECM	10 m³/kg s
λ_{22}	Release/reconstruction of ECM	1.25×10^{-3} 1/ss
λ_{23}	Release/reconstruction of ECM	0 1/s
λ_{24}	Release/reconstruction of ECM	1.25×10^{-3} 1/s
λ_{31}	Natural decay of protease	2.5×10^{-3} 1/s
λ_{32}	Production by cells of protease	2.0×10^{-6} kg/m³ s
λ_{33}	Logistic term constant protease	2.0×10^{-6} kg/m³ s
ν_G	Related to logisitic function	1
λ_{41}	Proteolytically freed CCL21	3.2×10^{-3} m³/kg s
λ_{42}	Logistic term constant CCL21	1.44×10^{-4} m³/kg s
λ_{43}	Logistic term constant CCL21	3.2×10^{-3} m³/kg s
λ_{44}	Cell consumption CCL21	1×10^{-9} kg/m³ s
ν_C	Related to logistic function	0.2

Table 2
Dimensionless parameters that appear in the model (56).

Parameters (dimensionless)	Description	Dimensionless
Time and Space		
$\tilde{T}$	Time	50
$\tilde{L}$	Length	1
$\tilde{D}_G$	Protease	0.0008
$\tilde{D}_C$	CCL21	0.000007
Parameters of $\bar{\Lambda}$		
$\bar{\xi}_1$	Parameter characterizing Λ (dependence on C)	8
$\bar{\xi}_2$	Parameter characterizing Λ (dependence on ρ)	0, 0.4
$\bar{\Lambda}_0$	Parameter characterizing Λ	0
$\bar{\Lambda}_1$	Parameter characterizing Λ	2.5
Production/decay rates		
$\tilde{\lambda}_{11}$	Proliferation of tumor cells	0.1875
$\tilde{\lambda}_{12}$	Decay of tumor cells	0.25
$\tilde{\lambda}_{13}$	Decay of tumor cells	0.125
$\tilde{\lambda}_{21}$	Degradation of ECM	10
$\tilde{\lambda}_{22}$	Release/reconstruction of ECM	12.5
$\tilde{\lambda}_{23}$	Release/reconstruction of ECM	0
$\tilde{\lambda}_{24}$	Release/reconstruction of ECM	12.5
$\tilde{\lambda}_{31}$	Natural decay of protease	25
$\tilde{\lambda}_{32}$	Production by cells of protease	200
$\tilde{\lambda}_{33}$	Logistic term protease	200
ν_G	Related to logisitic function	1
$\tilde{\lambda}_{41}$	Proteolytically freed CCL21	32
$\tilde{\lambda}_{42}$	Logistic term constant CCL21	1.44
$\tilde{\lambda}_{43}$	Logistic term constant CCL21	32
$\tilde{\lambda}_{44}$	Cell consumption CCL21	0.1
ν_C	Related to logistic function	0.2

3.3.1. Parameters related to cell-ECM and fluid-ECM interaction

Regarding $\Delta P(\alpha_w)$ given by (5), we set $\gamma = 1000$ Pa as default and use $J(\alpha_w) = -\ln(\delta + \alpha_w)$ with $\delta = 0.01$ which determines the maximal cell-cell stress. This is similar to what was used in Evje (2017). As discussed above, we need to specify parameters involved in the interaction terms $\hat{\zeta}_w$ and $\hat{\zeta}_c$ in (36). We set $\hat{k}_w = \hat{k}_c = 1$, i.e., no dynamic change in the cell-ECM and fluid-ECM resistance force during the cell migration process. Next, we assume that the hydraulic conductivity associated with the cell aggregate microenvironment is of the order $\frac{K}{\mu_w} = 5 \cdot 10^{-13}$ m²/Pa s. More precisely, we set

$$I_w = \frac{\mu_w}{K} = 2 \cdot 10^{12} \text{Pa s/m}^2, \qquad I_c = 1000 I_w,$$
$$r_w = 0.0, \qquad r_c = 0.6. \tag{48}$$

The specified external pressure gradient $P_L^* - P_R^* = 10$ kPa combined with the above choice of I_w, $\hat{k}_w$, and r_w give rise to an IF velocity around 0.5 μm/s, which is in the range used in Shields et al.

(2007), Shieh et al. (2011), and Polacheck et al. (2011). We have set the cell-ECM resistance force I_c (how strongly the cells are attached to the ECM structure) to be a 1000-fold larger than the fluid-ECM resistance force. More motivation for this choice follows below when we discuss various simulation examples. The coefficient $r_w = 0.0$ correlates to a situation with Corey exponent 2 for two-phase flow in a porous media based on standard use of extended Darcy's law with inclusion of relative permeability functions, see (Wu, 2016; Evje, 2017; Qiao et al., 2018) for more details. The coefficient $r_c = 0.6$ corresponds to a fast decrease in cell-ECM resistance force ζ_c for lower fraction of cells, letting the cells become more motile. The resulting $\hat{f}_c$ and $\hat{h}$ functions are shown in Fig. 4 for the choice of parameters as given in (48). From (45)$_1$,
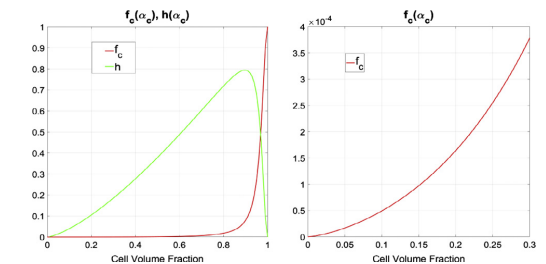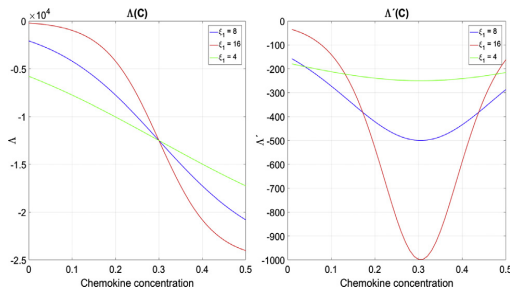

Fig. 4. Left: Plot showing $\hat{f}_c(\alpha_c)$ and $\hat{h}(\alpha_c)$ for the choice (36) with parameters as given in (48). **Right**: Zoomed in plot of $\hat{f}_c(\alpha_c)$ showing its increasing trend as a function of α_c.

Fig. 5. Plot of $\Lambda(C, \cdot)$ (left) and $\Lambda'(C, \cdot)$ (right) as a function of C with $C_M = 0.3$ where effect of ρ is ignored by setting $\xi_2 = 0$. These plots indicate the degree of engagement of the cell motility machinery in response to chemokine gradients and reflects that its response is highest for concentration C close to its maximal $C_M = 0.3$.

which characterizes $U_c = \alpha_c u_c$, it follows that $\hat{f}_c(\alpha_c)$ is related to the fluid-cell interaction, a stress effect on the cells due to the flowing fluid, where increasing cell volume fraction α_c enhances the ability of the fluid to push the cell in the flow direction. The function $\hat{h}_c(\alpha_c)$ is expressed in both the dispersive effect and in the directed motion by the cells driven by chemotaxis and/or haptotaxis.

3.3.2. The Λ potential function: chemotaxis and haptotaxis

From the third term of $(45)_1$ we see that the strength of the chemotaxis migration is a result of the product $\hat{h}(\alpha_c)\frac{\partial\Lambda}{\partial C}(C, \rho)$, see Remark 3.1. We refer to Fig. 5 for relevant illustrations related to Λ for different choices of ξ_1. We have used the choice $\xi_1 = 8$ in the numerical investigations, if nothing else is specified. The strength of the chemotaxis effect is also determined by Λ_1 which has been set to $\Lambda_1 = 25$ kPa for all simulations whereas $\Lambda_0 = 0$. Moreover, if nothing else is said, it is only chemotaxis that is taken into account whereas haptotaxis is ignored by setting $\xi_2 = 0$.

3.3.3. Initial and boundary data

Initially, we assume that chemokine produced by the cells have been bounded to ECM in a uniform manner. We do not explicitly track the concentration of chemokine bounded to ECM, but indirectly this is taken into account through the logistic reaction term in $(39)_4$ which describes the free chemokine C. As chemokine is released from ECM the IF will become saturated, and therby bringing the production of free chemokine to a halt. Initially, there is no protease G and no free chemokine C dissolved in IF whereas ECM initially is characterized by an evenly distributed fiber concentration ρ, i.e.,

$$\rho(x, t = 0) = 1, \quad G(x, t = 0) = 0, \quad C(x, t = 0) = 0. \quad (49)$$

We assume that the initial cell aggregate is placed in the center of the domain and is expressed by

$$\alpha_c(x, t = 0) = 0.2\exp(-[25(x - 0.5)]^2). \quad (50)$$

Thus, in order to be within the experimental setting of Shields et al., the initial cell fraction α_c is relatively small.

4. Results

By using a discretization method (see Appendix C for details) we solve the model (39) on a domain of length $L = 1$ cm subject to the initial conditions (49) and (50), together with the boundary condition (43). As a part of the solution method we also solve the model (40) for the IF pressure P_w, which is used to evaluate cell and

IF velocities (37) by means of (42). We use a grid of 100 cells and compute the solution after a time $T = 50$ (dimensionless) which amounts to approximately 5.8 days.

Firstly, we carry out simulation examples to mimic the experimental setting in Shields et al. (2007) where a high pressure P_L^* is imposed on the left hand side (LHS) of the domain, whereas a low pressure P_R^* is set at the right hand side (RHS). These examples are discussed in Sections 4.1,2,3,4.6. For these examples there is no fluid flow generated through the source term $Q = Q_v - Q_l$ which is set to zero. We focus on demonstrating (i) blocking of CCR7 and flow; (ii) autologous chemotaxis; (iii) cell motility as a function of cell-ECM interaction term; (iv) static condition (no IF flow).

Secondly, we consider a tumor setting in Sections 4.7 where $P_L^* = P_R^*$ whereas Q_v and Q_l are introduced to mimic, respectively, IF flow created by leaking blood vessels placed within the tumor and adsorbed through lymphatics placed in the environment outside the growing tumor. We use the model to gain some insight how autologous chemotaxis could possibly be exploited as a means for metastasis by generating aggressive cell migration towards lymphatics. If nothing else is said, we do not include proliferation/apoptosis by setting $S_c = 0$ in (39).

### 4.1. Blocking of CCR7 + Flow: The effect from the fluid-generated stress on the cell

In this example we ignore chemotaxis by setting $\xi_1 = 0$. Focus is on the effect from the term $U_T\hat{f}_c$ in $(45)_1$ in addition to the diffusive migration through the second term $\hat{h}(\Delta P)_x$. As boundary condition for the pressure P_w we set

$$P_L^* = P_{\text{ref}} + 10 \text{ kPa}, \qquad P_R^* = P_{\text{ref}}, \quad (51)$$

where P_{ref} corresponds to atmospheric pressure. By introducing this global pressure gradient, a steady fluid flow from left to right is generated corresponding to approximately 0.5 μm/s. The resulting cell migration is shown in Fig. 6 when we choose $I_c = 500I_w$, whereas the same case is shown in Fig. 7 for $I_c = 1000I_w$. The main observation from these two figures is that lowering the value of I_c implies that the cells to a less extent is able resist the stress from the flowing fluid and will cause the cells to migrate in the direction of flow. The effect is not of great significance, but as stated by Shields et al. (2007), when both chemotaxis and protease is blocked, the cells remain stationary when exposed to fluid flow. Thus, the value of I_c is chosen in the following to have a high value as given by (48) to ensure that the cancer cells largely resist the fluid flow.

4.2. Cell migration by means of autologous chemotaxis

We include the effect of chemotaxis by setting ξ_1 as prescribed in Section 3.3. The simulation results are shown in Fig. 8. Main observations are: The concentration profile of protease G does not travel far from the cell phase where it is produced but is clearly skewed in the flow direction. This is due to the decay rate of protease appearing on the RHS of $(39)_3$ (the term $-\lambda_{31}G$), causing it to decay outside the location of the cell aggregate. The chemokine component C described by $(39)_4$ is released at a regulatory rate through the logistic source term on the RHS which requires the presence of both the reacting protease G and ECM ρ. The released chemokine C convects in the direction of flow, creating a substantial asymmetry in the concentration profile, and as it does not have a decay term it will not degrade while it is advected. It is implicitly assumed that the concentration of matrix-bound CCL21 is uniformly distributed in the ECM and is considerably larger than the concentration of CCL21 dissolved in the fluid phase, considering it as a constant. The plots of cell velocity u_c, which is composed of three velocity components corresponding to flow-generated
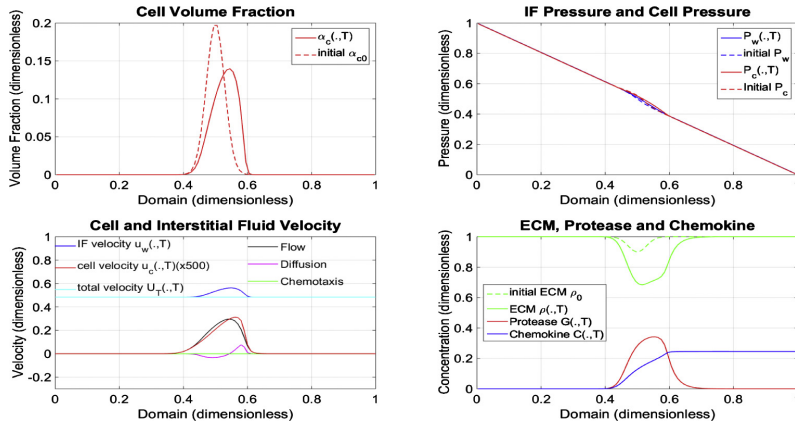
Fig. 6. An external imposed pressure gradient ($P_L^i > P_R^i$) with $Q = 0$. This gives rise to $U_T > 0$ and mobilizing of the stress-related term $U_T \hat{f}_c$ in $(45)_1$. When the value of I_c is relatively low ($I_c = 500 I_w$), the ability of the cancer cells to resist the fluid flow and remain stationary is reduced. This implies that the fluid flow is able to push the cells through the $U_T \hat{f}_c$ term, as reflected by the figure for the cell volume fraction, whose shape is skewed right. For this example there is no chemotaxis, i.e., $\xi_1 = 0$. This is clearly seen from the zero chemotactic cell velocity component (green line). The same case is studied in Fig. 7 with twice as strong I_c by setting $I_c = 1000 I_w$. This effectively reduces the cell migration in the fluid flow direction. Note that the cell phase velocity has been multiplied by 500 to include it the same figure as the IF velocity and total velocity u_T. (For interpretation of the references to colour in this figure legend, the reader is referred to the web version of this article.)
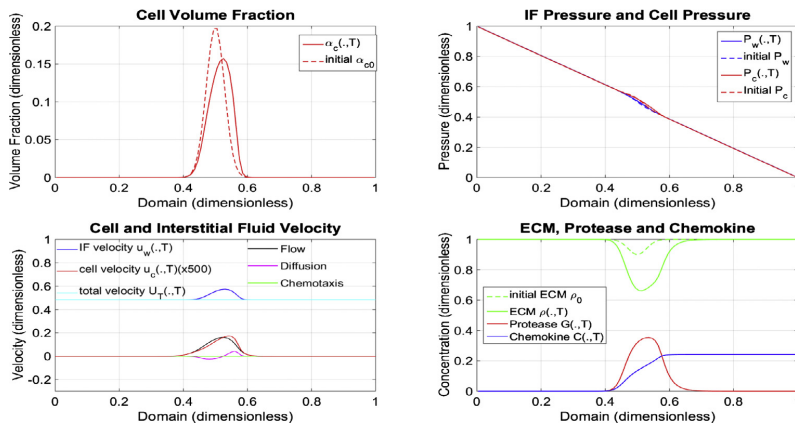
Fig. 7. The same situation as studied in Fig. 6 but with a stronger cell-ECM resistance force by setting $I_c = 1000 I_w$. This leads to a considerably weaker downstream migration through the term $U_T \hat{f}_c$. In particular, the tumor periphery does not migrate, it is cells within the tumor that migrate downstream. The example shown here and the previous example shown in Fig. 6, should be understood in the light of the experimental results by Shields et al. shown in Fig. 2 where CCR7 receptor is blocked but flow is included, giving rise to some migration in the flow direction.

stress, diffusion, and chemotaxis as reflected by $(37)_1$, clearly illustrate the different contributions to cell migration, according to the proposed cell-fluid model. The black line is the contribution of flow pushing the cells in the direction of the flow, the pink is cell migration due to diffusion/repulsive forces, whereas the green line is cell migration due to chemotaxis. The chemotaxis contribution is the dominant mechanism which directs the cells to migrate toward the positive chemokine gradient that has been formed in the downstream direction.

4.3. Cell motility expressed through the cell-ECM interaction term $\mathring{\zeta}_c$

In Shields et al. (2007), the authors used four different cell lines in the experiment. The cell lines have different ligand production and CCR7 expression. The results presented by Shields et al. shows

that the cell lines with the highest expression of functional CCR7 receptors and high ligand production are more invasive. In our model the value of r_c appearing in (36) can affect how invasive the cancer cells are. If $r_c = 0$, the cell-ECM resistance force $\mathring{\zeta}_c$ is constant and independent of the cell density. By setting $r_c < 0$ we "arrest" single cells (or low cell volume fraction) as the resistance force will go to infinity. What seems more natural is to set $r_c > 0$ where a higher value will make low cell concentration to experience less resistance force, making them more mobile. In Fig. 9 the value is increased from $r_c = 0.6$ to $r_c = 0.9$. Using this elevated value for r_c, the cells at the rim of the cell aggregate become more mobile and thereby also paves the way for more cells to migrate downstream. The cell phase velocity is doubled, compared to using $r_c = 0.6$ (see Fig. 8), indicating that increasing the value of r_c makes the cells more aggressive in the downstream direction. Perhaps
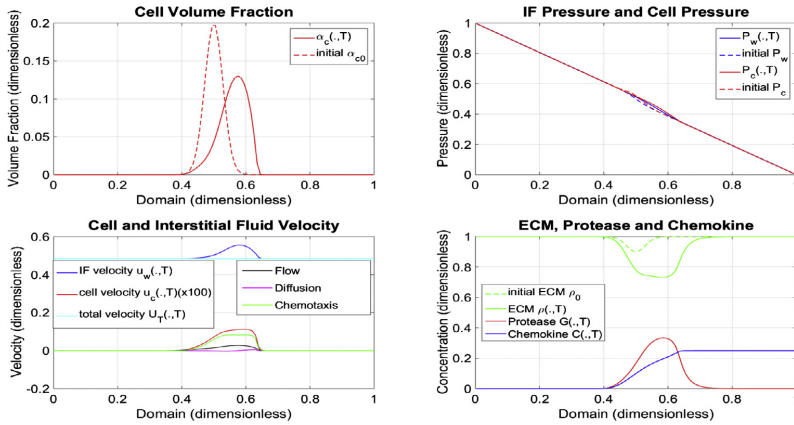
Fig. 8. The same case as studied in Fig. 7 but chemotaxis is now taken into account and I_c is set as prescribed in (48). There is now a dominating downstream cell migration driven by autologous chemotaxis in the sense that cells migrate towards the positive chemokine gradient, which in turn has been formed by chemokine C released from ECM by protease G secreted by the cells and brought downstream by the flowing fluid. The cell phase velocity is multiplied by 100 to include it the same figure as the IF velocity and total velocity u_T. The different cell velocity components (flow, diffusion, chemotaxis) show that chemotaxis is the far most dominating mechanism with a little help from the downstream flow-generated effect through $U_T\hat{f}_c$. Comparison with Fig. 7 (the cell volume fraction) also confirms this. The interstitial fluid phase velocity is of the order of 0.5 (dimensionless), which amounts to 0.5 µm/s.
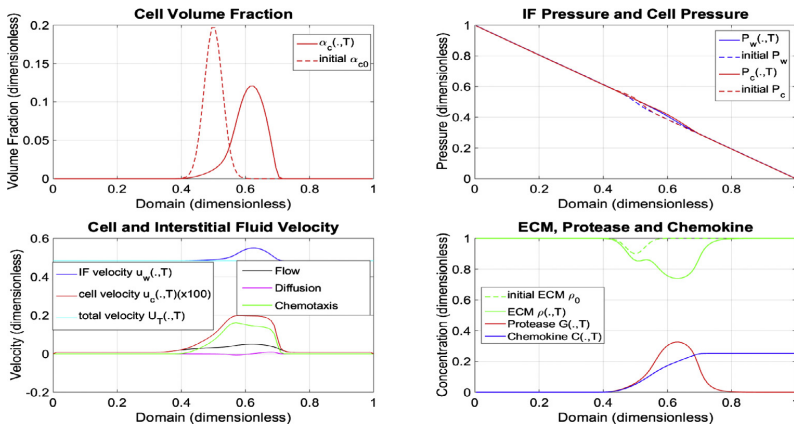
Fig. 9. Using the same parameters as in Fig. 8 with an increase of r_c from $r_c = 0.6$ to $r_c = 0.9$. Having an elevated r_c causes the cell phase to migrate further from the initial setup, and a higher fraction of the cells migrate. The dominating cell migration in the IF flow direction driven by autologous chemotaxis seen in this figure and in Fig. 8 is consistent with the experimental result by Shields et al. shown in Fig. 2 where flow + chemokine gives rise to a considerable increase in downstream migration.

information about the ligand production and CCR7 expression, which characterizes how aggressive the cells are, could be accounted for through the r_c exponent involved in the cell-ECM interaction term $\hat{\zeta}_c$.

4.4. The effect of proliferation and apoptosis

Next, we introduce cell proliferation/death by including S_c in (39)$_1$ to consider a more dynamic environment. The simulation results are shown in Fig. 10. By including cell proliferation, the concentration of protease G and chemokine C also increase. As the protease convects in the direction of the flow, ECM is degraded in the presence of the convected protease, which in turn will generate more cells as there is less ECM to compete for space. The cells will have a higher aptitude of generating new cells downstream of the starting position. In addition will new cells generated close to the

starting position, migrate towards the chemokine concentration gradient. With this increase of cell volume fraction due to proliferation, we move out of the scope of this paper. As the cell volume fraction increases, the impact of the $U_T\hat{f}_c$ in (45)$_1$ increases. As pointed out by Polacheck et al., there is an opposing mechanism to autologous chemotaxis which is observed for higher cell densities (Polacheck et al., 2011) giving rise to upstream cell migration. Clearly, this mechanism is not captured by the current model but pose an interesting challenge to be considered in future work.

4.5. Blocking of CCR7 + Flow: A possible role played by proteolysis

In Shields et al. (2007) the authors blocked the CCR7 receptors using antibodies, thus nullifying the chemotaxis mechanism. See the experimental results shown in Fig. 2 where flow + blocking of CCR7 is illustrated. Their result shows that the cells still migrated
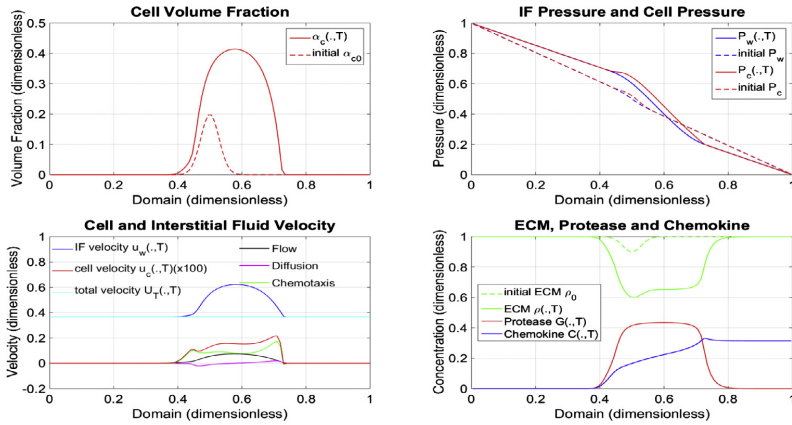
Fig. 10. The same case as studied in Fig. 8 but with the inclusion of cell proliferation/apoptosis through S_c. As protease G degrades ECM ρ and convects downstream of the cells, the cells experience less competition of space in the downstream direction. This causes the cell proliferation to occur mainly downstream. Allowing cell proliferation causes an increase in the liberation of chemokine and formation of a larger right-skewed gradient, which in turn increases the autologous chemotactic migration and total cell migration speed. The increase in cell volume fraction α_c also implies a stronger impact from the flow-generated cell migration term $U_T \hat{f}_c$ since $\hat{f}_c(\alpha_c)$ is an increasing function.

through a CCR7-independent mechanism which was, according to the authors a consequence of directed proteolysis. Inhibiting the proteases abolished all flow-enhanced migration.

The model suggests that there is a downstream cell migration through the $U_T \hat{f}_c$ term independent of chemotaxis. And, as illustrated in Figs. 6 and 7, this term gives rise to some downstream cell migration. However, this term is also independent of protease which contradicts the observation by Shields et al. that inhibiting the proteases abolished all flow-enhanced migration. One possibility is that the cell-ECM related term $\hat{\zeta}_c$ depends on protease. That is, the coefficient $\hat{k}_c$ in (36) (which is set to 1 for all simulations) could be made sensitive to the action of protease on ECM. In other words, the destruction/remodelling of ECM carried out by proteases could lead to a weakening of the cell-ECM resistance force, which sounds reasonable.

However, we will instead suggest another migration mechanism that depends on protease and ECM, namely haptotaxis. We turn off the chemotaxis mechanism by setting $\xi_1 = 0$. Haptotaxis is included in our model through $\Lambda(C, \rho)$, but so far has not been elaborated upon since we have set $\xi_2 = 0$. Haptotaxis is a process

in which cell migration is guided by gradients of surface-bound molecules, such as the non-moving ECM expressed by ρ in the model (Oudin et al., 2016). The interstitial flow convects protease, causing directed proteolysis, i.e., remodelling of ECM. This will in turn create some migration of cells expressed by the cell velocity component $\hat{h}(\alpha_c)\frac{\partial \Lambda}{\partial \rho}\rho_x$ where the shape of ρ (the positive gradient) is skewed in the flow direction. Fig. 11 illustrates this haptotactic cell migration effect when $\xi_2 = 0.4$ (dimensionless). As seen from the simulations, this effect is not of great significance, but it does contribute to the downstream migration. Thus, the model indicates that the haptotaxis mechanism could explain the effect Shields et al. observed when the CCR7 receptor was blocked but still experienced some migration in the direction of fluid flow.

4.6. Static condition (no flow)

Now we want to test the role played by the pressure driven interstitial fluid flow. As boundary condition for the pressure P_w we set

$$P_L^* = P_R^* = P_{\mathrm{ref}}. \tag{52}$$
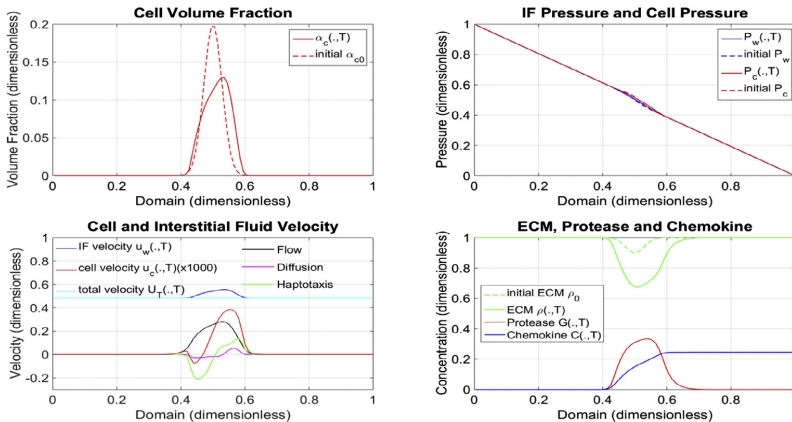
Fig. 11. Simulation run using the same parameters as in Fig. 8. However, in this case chemotaxis is turned off by setting $\xi_1 = 0$ and haptotaxis is turned on by setting $\xi_2 = 0.4$ (dimensionless). Note that cell velocity components and total cell velocity has been multiplied by 1000 for a more convenient illustration.
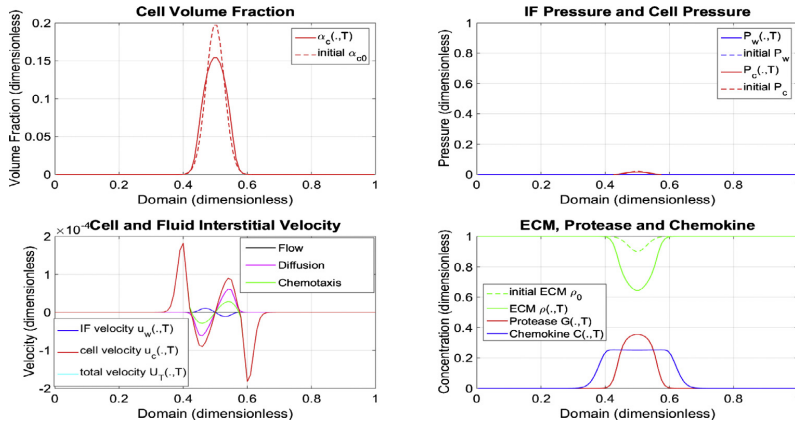
Fig. 12. The same case is applied in this scenario as in Fig. 8, however there is no global pressure differences as $P_l^* = P_R^* = P_{ref}$. As there is no flow, the ECM-released chemokine spread by diffusion only and produces a symmetric concentration profile. The cells in turn chemotact towards this concentration gradient. At the periphery of the tumor, the cells chemotact towards the center, as there is a negative chemokine concentration gradient. Since there is no flow to convect the components away from where the components are produced and released, the production will come to a halt. Thus, we may conclude that the minor cell migration seen for this case with no flow is consistent with the experimental result by Shields et al. shown in Fig. 2 (static).

Hence, there is no global pressure differences at the boundaries that will drive fluid across the domain. The results of the simulation are shown in Fig. 12. When there is no fluid flow to carry the chemokine or protease in a direction, the spreading will occur mainly due to diffusion and dispersion. In addition, the production of chemokine and protease is regulated, such that the production rate decreases as it approaches a maximum concentration, see the source term appearing on the RHS of $(39)_{3,4}$. The cell migration due to autologous chemotaxis is heavily dependent on interstitial fluid flow. In the case of no fluid flow, the chemokine concentration profile is symmetric and does not have the same effect for the cells to migrate towards as when there is fluid flow. In fact, the cells at the periphery of the tumor will migrate towards the center due to a negative chemokine concentration gradient. This prevents the cells from spreading from its initial position.

4.7. A tumor example: autologous chemotaxis as a means for metastasis

4.7.1. Background

Next, we consider an example motivated by a tumor setting where IF is generated from a vascular system located inside the tumor and adsorbed by the lymphatic system on the outside of the tumor. The source term S_c in (39) is included causing cell proliferation and apoptosis. Some parameters in the model have been changed to model the tumor setting. More precisely, the value of r_c is increased from $r_c = 0.6$ to $r_c = 0.9$ so that smaller fractions of cells become more motile. In addition, Λ_1 which characterizes the strength of the chemotactic migration, is increased by 50 % to take the value 3.75 (dimensionless) instead of 2.5, see Table 2. We have set the hydraulic conductivity to be lower in the region that surrounds the initial tumor then inside the tumor to mimic the observation that IF flow can induce ECM alignment perpendicular to the flow direction that leads to reduced permeability (conductivity) (Wiig and Swartz, 2012). This is naturally linked to the fact that the IF flow velocity is largest on the outside of the tumor periphery. The hydraulic conductivity reads

$$\frac{K}{\mu_w} = \begin{cases} 5 \times 10^{-12} \text{ m}^2/\text{Pa s}, & \text{for } x \in [0.4, 0.6]; \\[2mm] 5 \times 10^{-13} \text{ m}^2/\text{Pa s}, & \text{otherwise.} \end{cases} \tag{53}$$

Since the hydraulic conductivity K/μ_w dictates the value of fluid-ECM resistance force, $I_w = \frac{\mu_w}{K}$, the fluid-ECM resistance force within the tumor region becomes weaker. Hence, we may expect a relatively flat IF pressure profile within the tumor with a rapid decrease at the tumor margin. Further, we maintain the same value of the cell-ECM resistance force I_c as in the previous examples. In the following, we assume a pressure controlled source term $Q = Q_v - Q_l$ as described in Section 2.3 and 2.4 given by

$$Q_v = \frac{L_v S}{V}(P_v^* - P_w - \sigma_T(\pi_v - \pi_w)) = T_v(\widetilde{P}_v^* - P_w),$$

$$T_v = \frac{L_v S}{V}\chi_{(0.4<x<0.6)}(x)$$

$$Q_l = T_l(P_w - P_l^*),$$

$$T_l = \frac{L_l S_l}{V}\chi_{(0.2<x<0.3)\cup(0.7<x<0.8)}(x). \tag{54}$$

We have used the boundary condition for P_w as given by (52) in Section 4.6 (no flow). T_v and T_l have been set to be $T_v = 5 \cdot 10^{-7}$ (Pa s)$^{-1}$ and $T_l = 3.5 \cdot 10^{-7}$ (Pa s)$^{-1}$. The vascular pressure is prescribed such that $\widetilde{P}_v^* = P_{ref} + 1500$ Pa in $(54)_1$. The lymphatic pressure P_l^* in $(54)_2$ is set to be $P_l^* = P_{ref} - 500$Pa for the case shown in Figs. 13 and 15 whereas $P_l^* = P_{ref} - 1000$Pa for the case in Fig. 14. These choices are essentially based on the fact that it will ensure that a reasonable IF pressure profile is created (Wiig and Swartz, 2012; Jain et al., 2014) with a rapid decrease at the rim.

4.7.2. Autologous chemotaxis as a means for metastasis

We consider the following two cases (a) and (b), respectively, in Figs. 13 and 14:

4.7.2.1. Low accumulation of chemokine close to lymphatic vessel.
The drainage of chemokine C at the lymphatics is set to be 90 % of the fluid drainage, i.e., we include in the equation for chemokine $(39)_4$ a source term on the RHS of the form $-0.9CQ_l$, allowing some of the chemokine to accumulate at the lymphatics. The simulation result is shown in Fig. 13. Looking at the chemokine concentration we see that there are local variations that can give rise to varying degree of chemotactic migration. In particular, the cells at the tumor periphery is starting to sense the accumulated chemokines at the lymphatics, causing the outmost cells to migrate toward
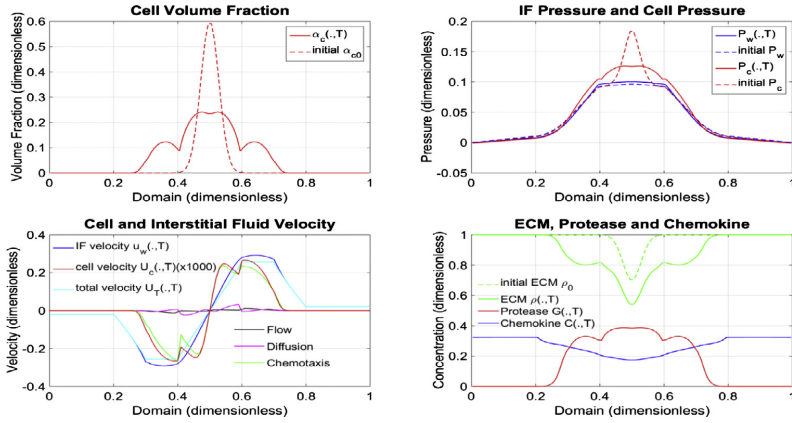
Fig. 13. IF is produced from leaky blood vessels placed in the central part of the tumor and is adsorbed by the lymphatics placed closer to the boundary $x = 0$ and $x = 1$, as prescribed by (53). Note the IF pressure P_w which is flat inside the tumor with a rapid decrease at the tumor margin. A relatively sharp increase in chemokine concentration C is formed at rim of the tumor where the lymphatics are placed and an accumulation of chemokine takes place. This seems to lead to a speeding up effect of the cancer cells. This is manifested by the cell volume fraction which reflects formation of a new "wave" of cells migrating more aggressively toward the lymphatics. Cell velocity is plotted in terms of $U_C = \alpha_c u_c$ (Darcy velocity).
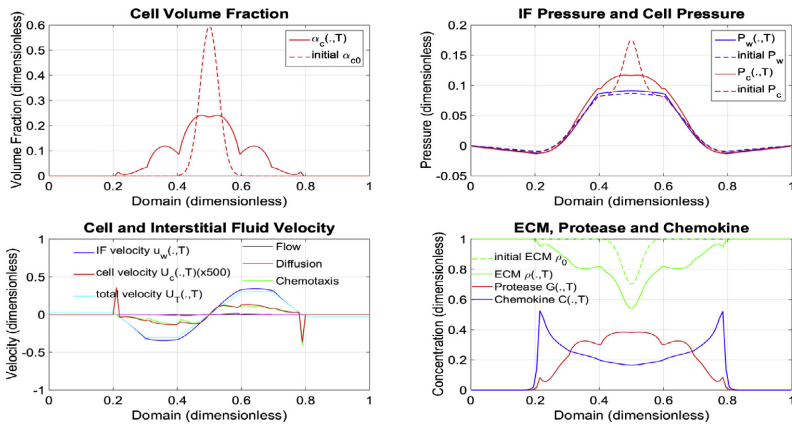
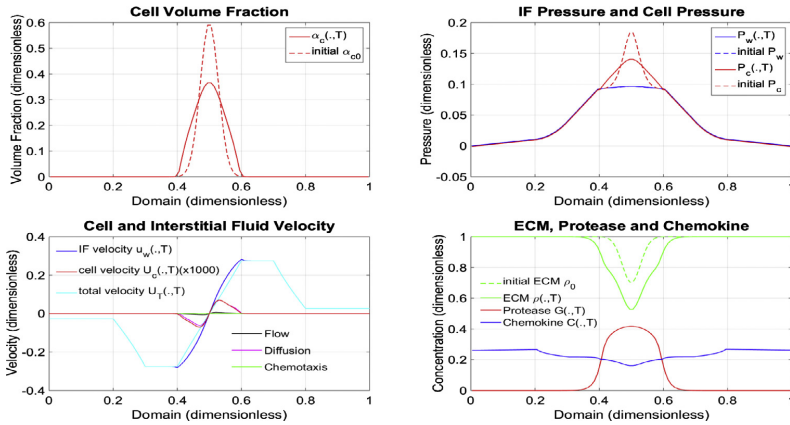**Fig. 14.** The same situation as in Fig. 13 but where the adsorption of chemokine at the lymphatics has been reduced whereas the adsorption of IF at lymphatics has been increased such that fluid enters from both sides of the lymphatics. In particular, this situation leads to a build-up of a high chemokine concentration at the lymphatics that triggers formation of a new wave of cells migrating with higher speed close to the lymphatics than further behind. Different "waves" correspond to different slopes in chemokine gradients. This illustration is relevant for the experimental observation by Shields et al. shown in Fig. 2 where flow + chemokine + LEC gives rise to a considerable increase in downstream migration compared to the case without LEC. LEC gives rise to additional chemokine gradient which increases the chemotactic cell migration.

the lymphatics with a higher velocity. As a consequence, there is a splitting of the cell aggregate and formation of a new "wave" of cells that move with a higher speed than cells closer to the center of the core.

4.7.2.2. High accumulation of chemokine close to lymphatic vessel. To further test the role of different chemokine gradients, we slightly change the setting such that a higher concentration can be formed close to the lymphatics. The source term Q_l describing adsorption of fluid is made stronger by setting the lymphatic pressure P_l^* to be $P_l^* = P_{ref} - 1000$Pa. In addition, the drainage of the chemokine is set to be 50 % of the fluid drainage, i.e., on the RHS of (39)$_4$ a source term is added of the form $-0.5CQ_l$. Thus, more chemokine can possibly accumulate at the lymphatic.

The simulation result is shown in Fig. 14. A striking difference between this case and the previous one is that there is now a stronger adsorption of fluid at lymphatics (due to the low pressure P_l^*) which force fluid to flow from the boundary toward the lymphatics. This will in turn prevent chemokine, which follows the fluid flow from the tumor toward the lymphatics, to pass by and instead lead to accumulation at the lymphatic vessels. The plot of C clearly illustrates this. As a consequence, two waves of high-speed cells are formed corresponding to two different chemokine gradients. Qualitatively, this may serve as an illustration of the situation sketched in Fig. 1 where lymphatic endothelial cells (LEC) secrete chemokine which lead to an additional chemokine concentration close to the lymphatics. In particular, it shows how the combination of effects may lead to a greatly enhanced chemotactic transcellular gradient to further drive tumor cells toward the lymphatic.

Fig. 15. The same situation as in Fig. 13 but now the CCR7 has been blocked by setting $\xi_1 = 0$. The aggressive cell migration toward lymphatics is completely abolished illustrating how the autologous chemotaxis possibly can play a key role in metastasis via lymphatics.

4.7.3. Blocking of CCR7

We consider the same situation as in Fig. 13. However, we now block the autologous chemotaxis effect by setting $\xi_1 = 0$ and thereby mimic the experimental blocking of CCR7 which showed that the chemotaxis migration effect was abolished. The simulation result is shown in Fig. 15 and clearly confirms that autologous chemotaxis is the essential driver for the cell migration toward lymphatics.

5. Discussion

In this paper we have used a multiphase modeling approach to develop a model that can shed light on autologous chemotaxis as a driver for downstream migration of tumor cells (Fleury et al., 2006; Shields et al., 2007). The multiphase model has mass and momentum equations that were formulated for the two phases: tumor cells and extracellular fluid. The system of equations in (12) is built on the general cell-fluid model discussed in Evje (2017) but where a chemokine component has been added to account for autologous chemotaxis. The model is simplified such that i) an elliptic equation for interstitial fluid pressure P_w is obtained that explains the elevated pressure associated with a tumor; (ii) the cell velocity can be divided into three distinguished parts as highlighted by $(45)_1$: $U_T\hat{f}_c$ is the fluid-generated stress that pushes the tumor cells with the flow, $\hat{h}(\Delta P)_x$ is the cell dispersive effect (arbitrary migration in all directions), and $\hat{h}\Lambda(C)_x$ accounts for the chemotactic migration.

We have through our model demonstrated transient cell migration by autologous chemotaxis. A central part of the model is the interaction between the chemical components, i.e., the cell-secreted protease G and ECM-released chemokine C. The protease component diffuses and convects with fluid flow, which in turn proteolytically releases ECM-bound chemokine that spreads by convection and diffusion leading to a skewed distribution in the flow direction. The tumor cells sense the chemokine gradient that is created by the afore-mentioned process and migrate toward positive gradients.

The interstitial fluid flow has a major impact on the behavior of our model. Introducing fluid flow to the system governs a positive chemokine gradient downstream which the cells will

migrate toward. The fluid flow bias the distribution of CCL21 released by protease. In the event of no fluid flow, the migration contribution of chemotaxis directed away from the tumor center is limited, as the chemokine gradient is minimal, see Fig. 12. Instead, at the tumor periphery, chemotaxis will keep the cells in check and not let the cells migrate away from the tumor. In addition, the fluid flow also exerts a shear stress on the cell phase which potentially can push the cells downstream, see for example Fig. 7.

Similarities between model behavior and experimental observations we would like to highlight are:

- Through our model we can visualize what is indicated through the reported experimental results in Shields et al. (2007): "*...the three tumor cell lines displayed marked increases in migration in the flow direction that could be inhibited by CCR7 blocking, indicating that the flow-enhanced migration was a CCR7-mediated chemotactic phenomenon, yet with no exogeneous CCR7 ligands or LECs to signal. ... These results clearly demonstrate that autologous chemotaxis toward gradients of CCR7 ligand occurred in these tumor cells under IF*".

- Four different cell lines were used in Shields et al. (2007) with varying degree of metastatic potential. Cell lines with the highest expression of functional CCR7 receptors and high chemokine production proved more invasive. As proposed in Section 4.3, the model can vary the metastatic potential in the cancer cells using the parameter r_c in (36) which may account for the CCR7 expression. Increasing the value of r_c results in more aggressive cancer cells causing more cells to migrate and they migrate further from their initial position, see Figs. 8 and 9.

- Blocking the CCR7 receptors in Shields et al. (2007) inhibited cell migration. Yet, there seems to be a CCR7-independent effect in response to interstitial fluid flow. The authors describe this as a consequence of directed proteolysis. In Fig. 11 we have used haptotaxis as a mechanism to explain the directed proteolysis, where the cells migrate towards gradients of ECM. In addition, the authors of (Shields et al., 2007) inhibited protease, ceasing all flow-enhanced migration. In the model there would still be flow-enhanced migration through the term $U_T\hat{f}_c$ in $(45)_1$ in the case of inhibiting protease, aside from arbitrary migration. In other words, when all other effects are inhibited, the fluid

flow still induce force on the cells, as shown in Fig. 7. However, the effect of this force can be made marginal by appropriate choice of parameters related to cell-ECM resistance force.

- One aspect of how cells may chemotact towards the lymphatics is investigated in Shields et al. (2007) but is not implemented in our model, namely, the possible role of lymphatic endothelial cells (LECs). LECs secrete CCR7 ligand CCL21 as a homing device for the cells to chemotact towards, see Fig. 1. As the cells migrate towards the lymphatics through autologous chemotaxis, the LECs act as an intensifier of the chemotactic signal, creating a steeper gradient towards the lymphatics. This role of LECs have not been accounted for directly in the model, however, the intensified downstream cell migration caused by accumulation of chemokine at lymphatics was demonstrated in Fig. 14.

Appendix A. Dimensionless version of the model (12)

The purpose of this section is to obtain dimensionless version of the model (12). We introduce characteristic length L^* and time T^* as well as characteristic concentrations and pressure: G^*, C^*, ρ^*, P^* with corresponding characteristic velocity u^* and diffusion D^*

$$u^* = \frac{L^*}{T^*}, \quad D^* = \frac{(L^*)^2}{T^*}.$$

Moreover, we define dimensionless variables as follows:

$$\tilde{\rho} = \frac{\rho}{\rho^*}, \quad \widetilde{G} = \frac{G}{G^*}, \quad \widetilde{C} = \frac{C}{C^*}, \quad \tilde{P}_i = \frac{P_i}{P^*}, \quad \tilde{u}_i = \frac{u_i}{u^*}, \quad i = c, w$$

and dimensionless space and time variables

$$\bar{x} = \frac{x}{L^*}, \quad \tilde{t} = \frac{t}{T^*}.$$

Similarly, we define dimensionless rates for the cell proliferation term and the ECM remodeling term related to S_c as well as dimensionless rates associated with protease and chemokine

$$\tilde{\lambda}_{11} = \lambda_{11}T^*, \quad \tilde{\lambda}_{12} = \lambda_{12}T^*, \quad \tilde{\lambda}_{13} = \lambda_{13}T^*,$$

$$\tilde{\lambda}_{21} = \lambda_{21}T^*G^*, \quad \tilde{\lambda}_{22} = \lambda_{22}T^*, \quad \tilde{\lambda}_{23} = \lambda_{23}T^*, \quad \tilde{\lambda}_{24} = \lambda_{24}T^*,$$

$$\tilde{\lambda}_{31} = \lambda_{31}T^*, \quad \tilde{\lambda}_{32} = \frac{\lambda_{32}T^*}{G^*}, \quad \tilde{\lambda}_{33} = \frac{\lambda_{33}T^*}{G^*},$$

$$\tilde{\lambda}_{41} = \frac{\lambda_{41}T^*G^*\rho^*}{C^*}, \quad \tilde{\lambda}_{42} = \frac{\lambda_{42}T^*G^*\rho^*}{C^*}, \quad \tilde{\lambda}_{43} = \frac{\lambda_{43}T^*G^*\rho^*}{C^*},$$

$$\tilde{\lambda}_{44} = \frac{\lambda_{44}T^*}{C^*},$$

and

$$\widetilde{D}_G = \frac{D_G}{D^*}, \quad \widetilde{D}_C = \frac{D_C}{D^*}, \quad \widetilde{Q} = QT^*.$$

Moreover, for the potential function $\Lambda(C, \rho)$ given by (14) we introduce dimensionless variables as follows:

$$\tilde{\xi}_1 = \xi_1 C^*, \quad \tilde{\xi}_2 = \xi_2 \rho^*, \quad \tilde{\Lambda}_0 = \frac{\Lambda_0}{P^*}, \quad \tilde{\Lambda}_1 = \frac{\Lambda_1}{P^*},$$

where $[\Lambda_0, \Lambda_1] = \text{Pa} = \frac{\text{kg}}{\text{m s}^2}$ and $[\xi_1] = [\xi_2] = \frac{\text{m}^3}{\text{kg}}$ such that

$$\Lambda(C, \rho) = \Lambda_0 - \frac{\Lambda_1}{1 + \exp(-\xi_1(C - C_M) - \xi_2(\rho - \rho_M))}$$

$$= \Lambda_0 - \frac{\Lambda_1}{1 + \exp(-\tilde{\xi}_1(\widetilde{C} - \widetilde{C}_M) - \tilde{\xi}_2(\tilde{\rho} - \tilde{\rho}_M))}$$

$$= \Lambda(\widetilde{C}, \tilde{\rho}).$$

Let us recall the model (12) which is given by

$$(\alpha_c)_t + \nabla \cdot (\alpha_c \mathbf{u}_c) = S_c, \quad S_c = \alpha_c\left(\lambda_{11} - \lambda_{12}\alpha_c - \lambda_{13}\frac{\rho}{\rho_M}\right)$$

$$(\alpha_w)_t + \nabla \cdot (\alpha_w \mathbf{u}_w) = -S_c + Q, \quad Q = Q_v - Q_l$$

$$\alpha_c \nabla P_c = -\hat{\zeta}_c \mathbf{u}_c + \hat{\zeta}(\mathbf{u}_w - \mathbf{u}_c)$$

$$\alpha_w \nabla P_w = -\hat{\zeta}_w \mathbf{u}_w - \hat{\zeta}(\mathbf{u}_w - \mathbf{u}_c)$$

$$\rho_t = -\lambda_{21}G\rho + \rho\left(\lambda_{22} - \lambda_{23}\alpha_c - \lambda_{24}\frac{\rho}{\rho_M}\right)$$

$$G_t = \nabla \cdot (D_G \nabla G) - \nabla \cdot (\mathbf{u}_w G) - \lambda_{31}G$$

$$\qquad + \alpha_c\left(\lambda_{32} - \lambda_{33}\left(\frac{G}{G_M}\right)^{v_G}\right)$$

$$C_t = \nabla \cdot (D_C \nabla C) - \nabla \cdot (\mathbf{u}_w C)$$

$$\qquad + G\rho\left(\lambda_{41} - \lambda_{42}\left(\frac{C}{C_M}\right)^2 - \lambda_{43}\left(\frac{C}{C_M}\right)^{v_C}\right) - \lambda_{44}\alpha_c,$$

$$\tag{55}$$

with $P_c = P_w + \Delta P + \Lambda$ and, according to (36), fluid-ECM, cell-ECM, and cell-fluid interaction terms are represented by

$$\hat{\zeta}_i = I_i \hat{k}_i \alpha_i^{r_i} \quad (i = c, w), \qquad \hat{\zeta} = I\hat{k}\alpha_w\alpha_c$$

where I and I_i have dimension Pa s/m² whereas $\hat{k}_i, \hat{k}$ and r_w, r_c are dimensionless. We use the transformation $(x, t) \to (\bar{x}, \tilde{t})$ combined with introducing the dimensionless variables defined above. This gives us the following dimensionless version of the model

$$(\alpha_c)_{\tilde{t}} + \nabla \cdot (\alpha_c \tilde{\mathbf{u}}_c) = \widetilde{S}_c, \qquad \widetilde{S}_c = \alpha_c\left(\tilde{\lambda}_{11} - \tilde{\lambda}_{12}\alpha_c - \tilde{\lambda}_{13}\left(\frac{\tilde{\rho}}{\tilde{\rho}_M}\right)\right)$$

$$(\alpha_w)_{\tilde{t}} + \nabla \cdot (\alpha_w \tilde{\mathbf{u}}_w) = -\widetilde{S}_c + \widetilde{Q}$$

$$\alpha_c \nabla \widetilde{P}_c = -\tilde{\hat{\zeta}}_c \tilde{\mathbf{u}}_c + \tilde{\hat{\zeta}}(\tilde{\mathbf{u}}_w - \tilde{\mathbf{u}}_c)$$

$$\alpha_w \nabla \widetilde{P}_w = -\tilde{\hat{\zeta}}_w \tilde{\mathbf{u}}_w - \tilde{\hat{\zeta}}(\tilde{\mathbf{u}}_w - \tilde{\mathbf{u}}_c)$$

$$\tilde{\rho}_{\tilde{t}} = -\tilde{\lambda}_{21}\widetilde{G}\tilde{\rho} + \tilde{\rho}\left(\tilde{\lambda}_{22} - \tilde{\lambda}_{23}\alpha_c - \tilde{\lambda}_{24}\left(\frac{\tilde{\rho}}{\tilde{\rho}_M}\right)\right),$$

$$\widetilde{G}_t = \nabla \cdot (\widetilde{D}_G \nabla \widetilde{G}) - \nabla \cdot (\tilde{\mathbf{u}}_w \widetilde{G}) - \tilde{\lambda}_{31}\widetilde{G}$$

$$\qquad + \alpha_c\left(\tilde{\lambda}_{32} - \tilde{\lambda}_{33}\left(\frac{\widetilde{G}}{\widetilde{G}_M}\right)^{v_G}\right)$$

$$\widetilde{C}_t = \nabla \cdot (\widetilde{D}_C \nabla \widetilde{C}) - \nabla \cdot (\tilde{\mathbf{u}}_w \widetilde{C})$$

$$\qquad + \widetilde{G}\tilde{\rho}\left(\tilde{\lambda}_{41} - \tilde{\lambda}_{42}\left(\frac{\widetilde{C}}{\widetilde{C}_M}\right)^2 - \tilde{\lambda}_{43}\left(\frac{\widetilde{C}}{\widetilde{C}_M}\right)^{v_C}\right) - \tilde{\lambda}_{44}\alpha_c$$

$$\tag{56}$$

with

$$\tilde{\hat{\zeta}}_c = \hat{\zeta}_c\frac{D^*}{P^*}, \quad \tilde{\hat{\zeta}}_w = \hat{\zeta}_w\frac{D^*}{P^*}, \quad \tilde{\hat{\zeta}} = \hat{\zeta}\frac{D^*}{P^*},$$

$$\widetilde{P}_c = \widetilde{P}_w + \tilde{\Delta}P + \tilde{\Lambda},$$

$$\tilde{\Lambda} = \tilde{\Lambda}_0 - \frac{\tilde{\Lambda}_1}{1 + \exp(-\tilde{\xi}_1(\widetilde{C} - \widetilde{C}_M) - \tilde{\xi}_2(\tilde{\rho} - \tilde{\rho}_M))}.$$

$$\tag{57}$$

Clearly, the model (56) takes exactly the same form as (55) but now in terms of non-dimensional variables as introduced above. In the following we will refer to this dimensionless version of the model and corresponding quantities dropping the "tilde" notation.

Appendix B. Elimination of explicit dependence on IF pressure P_w

We observe that we have the following expression for ∇P_w (in view of (26))

$$\nabla P_w = -\frac{\mathbf{U}_T}{\hat{\lambda}_T} - \frac{\hat{\lambda}_c}{\hat{\lambda}_T}\nabla(\Delta P) - \frac{\hat{\lambda}_c}{\hat{\lambda}_T}\nabla\Lambda(C, \rho). \tag{58}$$

Combining this with (22) we can derive expressions for the fluid velocities $\mathbf{U}_c$ and $\mathbf{U}_w$ as follows:

$$
\begin{aligned}
\mathbf{U}_c &= -\hat{\lambda}_c \nabla P_w - \hat{\lambda}_c \nabla(\Delta P) + \frac{\alpha_c \alpha_w \hat{\zeta}}{\hat{\zeta}_c \hat{\zeta}_w + \hat{\zeta}[\hat{\zeta}_c + \hat{\zeta}_w]} \nabla(\Delta P) \\
&\quad - \hat{\lambda}_c \nabla \Lambda(C, \rho) + \frac{\alpha_c \alpha_w \hat{\zeta}}{\hat{\zeta}_c \hat{\zeta}_w + \hat{\zeta}[\hat{\zeta}_c + \hat{\zeta}_w]} \nabla \Lambda(C, \rho) \\
&= \hat{\lambda}_c \left(\frac{\mathbf{U}_T}{\hat{\lambda}_T} + \frac{\hat{\lambda}_c}{\hat{\lambda}_T} \nabla(\Delta P) + \frac{\hat{\lambda}_c}{\hat{\lambda}_T} \Lambda(C, \rho) \right) - \hat{\lambda}_c \nabla(\Delta P) \\
&\quad + \frac{\alpha_c \alpha_w \hat{\zeta}}{\hat{\zeta}_c \hat{\zeta}_w + \hat{\zeta}[\hat{\zeta}_c + \hat{\zeta}_w]} \nabla(\Delta P) - \hat{\lambda}_c \nabla \Lambda(C, \rho) \\
&\quad + \frac{\alpha_c \alpha_w \hat{\zeta}}{\hat{\zeta}_c \hat{\zeta}_w + \hat{\zeta}[\hat{\zeta}_c + \hat{\zeta}_w]} \nabla \Lambda(C, \rho) \\
&= \mathbf{U}_T \frac{\hat{\lambda}_c}{\hat{\lambda}_T} - \left[\frac{\alpha_c^2 \alpha_w^2}{\alpha_c^2 \hat{\zeta}_w + \alpha_w^2 \hat{\zeta}_c + \hat{\zeta}} \right] \nabla(\Delta P) \\
&\quad - \left[\frac{\alpha_c^2 \alpha_w^2}{\alpha_c^2 \hat{\zeta}_w + \alpha_w^2 \hat{\zeta}_c + \hat{\zeta}} \right] \nabla \Lambda(C, \rho) \\
&= \mathbf{U}_T \hat{f}_c(\alpha_c) - \hat{h}(\alpha_c) \nabla(\Delta P) - \hat{h}(\alpha_c) \nabla \Lambda(C, \rho)
\end{aligned}
\tag{59}
$$

where we have used that

$$
\begin{aligned}
\frac{\hat{\lambda}_c^2 - \hat{\lambda}_c \hat{\lambda}_T}{\hat{\lambda}_T} &+ \frac{\alpha_c \alpha_w \hat{\zeta}}{\hat{\zeta}_c \hat{\zeta}_w + \hat{\zeta}[\hat{\zeta}_c + \hat{\zeta}_w]} \\
&= -\frac{\hat{\lambda}_c \hat{\lambda}_w}{\hat{\lambda}_T} + \frac{\alpha_c \alpha_w \hat{\zeta}}{\hat{\zeta}_c \hat{\zeta}_w + \hat{\zeta}[\hat{\zeta}_c + \hat{\zeta}_w]} \\
&= -\frac{\alpha_c^2 \alpha_w^2}{\alpha_c^2 \hat{\zeta}_w + \alpha_w^2 \hat{\zeta}_c + \hat{\zeta}},
\end{aligned}
\tag{60}
$$

in light of the expression (23) and (24) (after some algebraic manipulations) and where we have defined $\hat{f}_c, \hat{f}_w$ and $\hat{h}$ as follows:

$$
\begin{aligned}
\hat{f}_c(\alpha_c) &\overset{\text{def}}{:=} \frac{\hat{\lambda}_c}{\hat{\lambda}_T} = \frac{[\alpha_c^2 \hat{\zeta}_w] + \alpha_c \hat{\zeta}}{[\alpha_c^2 \hat{\zeta}_w] + [\alpha_w^2 \hat{\zeta}_c] + \hat{\zeta}}, \\
\hat{f}_w(\alpha_c) &\overset{\text{def}}{:=} \frac{\hat{\lambda}_w}{\hat{\lambda}_T} = \frac{[\alpha_w^2 \hat{\zeta}_c] + \alpha_w \hat{\zeta}}{[\alpha_c^2 \hat{\zeta}_w] + [\alpha_w^2 \hat{\zeta}_c] + \hat{\zeta}}, \\
\hat{h}(\alpha_c) &\overset{\text{def}}{:=} \frac{\alpha_c^2 \alpha_w^2}{\alpha_c^2 \hat{\zeta}_w + \alpha_w^2 \hat{\zeta}_c + \hat{\zeta}}.
\end{aligned}
\tag{61}
$$

Similarly, for $\mathbf{U}_w$ we get

$$
\begin{aligned}
\mathbf{U}_w &= -\hat{\lambda}_w \nabla P_w - \frac{\alpha_c \alpha_w \hat{\zeta}}{\hat{\zeta}_c \hat{\zeta}_w + \hat{\zeta}[\hat{\zeta}_c + \hat{\zeta}_w]} \nabla(\Delta P) \\
&\quad - \frac{\alpha_c \alpha_w \hat{\zeta}}{\hat{\zeta}_c \hat{\zeta}_w + \hat{\zeta}[\hat{\zeta}_c + \hat{\zeta}_w]} \nabla \Lambda(C, \rho) \\
&= \hat{\lambda}_w \left(\frac{\mathbf{U}_T}{\hat{\lambda}_T} + \frac{\hat{\lambda}_c}{\hat{\lambda}_T} \nabla(\Delta P) + \frac{\hat{\lambda}_c}{\hat{\lambda}_T} \nabla \Lambda(C, \rho) \right) \\
&\quad - \frac{\alpha_c \alpha_w \hat{\zeta}}{\hat{\zeta}_c \hat{\zeta}_w + \hat{\zeta}[\hat{\zeta}_c + \hat{\zeta}_w]} \nabla(\Delta P) \\
&\quad - \frac{\alpha_c \alpha_w \hat{\zeta}}{\hat{\zeta}_c \hat{\zeta}_w + \hat{\zeta}[\hat{\zeta}_c + \hat{\zeta}_w]} \nabla \Lambda(C, \rho) \\
&= \mathbf{U}_T \frac{\hat{\lambda}_w}{\hat{\lambda}_T} + \left[\frac{\alpha_c^2 \alpha_w^2}{\alpha_c^2 \hat{\zeta}_w + \alpha_w^2 \hat{\zeta}_c + \hat{\zeta}} \right] \nabla(\Delta P) \\
&\quad + \left[\frac{\alpha_c^2 \alpha_w^2}{\alpha_c^2 \hat{\zeta}_w + \alpha_w^2 \hat{\zeta}_c + \hat{\zeta}} \right] \nabla \Lambda(C, \rho) \\
&= \mathbf{U}_T \hat{f}_w(\alpha_c) + \hat{h}(\alpha_c) \nabla(\Delta P) + \hat{h}(\alpha_c) \nabla \Lambda(C, \rho),
\end{aligned}
\tag{62}
$$

after an application of (60) and the definitions in (61).

Appendix C. Discretization of the model

We solve the model (39) subject to the initial conditions (49) and (50) together with the boundary condition (43). The main steps in the solution approach are as follows, assuming that we have an approximate solution $(\alpha_c^n, \rho^n, G^n, C^n)$ at time level t^n and want to compute the approximate solution $(\alpha_c^{n+1}, \rho^{n+1}, G^{n+1}, C^{n+1})$ at the new time step t^{n+1}:

(i) First, we solve the elliptic, steady-state diffusion problem (40) for the IF pressure P_w^n;

(ii) Then we can compute the corresponding total velocity U_T^n from (42) as well as the corresponding cell and IF velocities u_c^n and u_w^n given by (37);

(iii) Armed with interstitial velocities u_c^n and u_w^n at time level t^n, we can compute updated cell volume fraction α_c^{n+1} and concentrations ρ^{n+1}, G^{n+1}, and C^{n+1} from (39) where we employ a standard upwind in space discretization (explicit in time) of convective terms whereas diffusion terms are treated implicitly in time.

References

Breward, C.J.W., Byrne, H.M., Lewis, C.E., 2003. A multiphase model describing vascular tumour growth. Bulletin Math. Biol. 65, 609–640.

Byrne, H.M., Owen, M.R., 2004. A new interpretation of the Keller-Segel model based on multiphase modelling. J. Math. Biol. 49, 604–626.

Chaplain, M.A.J., Lolas, G., 2005. Mathematical modelling of cancer cell invasion of tissue: the role of the urokinase plasminogen activation system. Math. Model. Met. Appl. Sci. 15 (11), 1685–1734.

Chaplain, M.A.J., Lolas, G., 2006. Mathematical modelling of cancer cell invasion of tissue: dynamic heterogeneity. Netw. Het. Media 1 (3), 399–439.

Evje, S., 2017. An integrative multiphase model for cancer cell migration under influence of physical cues from the microenvironment. Chem. Eng. Sci. 165, 240–259.

Evje, S., Wen, H.Y., 2018. A Stokes two-fluid model for cell migration that can account for physical cues in the microenvironment. SIAM J. Math. Anal. 50 (1), 86–118.

Fleury, M.E., Boardman, K.C., Swartz, M.A., 2006. Autologous morphogen gradients by subtle interstitial flow and matrix interactions. Biophys. J. 91, 113–121.

Haessler, U., Teo, J.C., Foretay, D., Renaud, P., Swartz, M.A., 2012. Migration dynamics of breast cancer cells in a tunable 3D interstitial flow chamber. Integr. Biol. 4, 401–409.

Jain, K.J., Martin, J.D., Stylianopoulos, T., 2014. The role of mechanical forces in tumor growth and therapy. Annu. Rev. Biomed. Eng. 16, 321–346.

Kirby, B.J., 2010. Micro- and Nanoscale Fluid Mechanics: Transport in Microfluidic Devices. Cambridge University Press.

Koumoutsakos, P., Pivkin, I., Milde, F., 2013. The fluid mechanics of cancer and its therapy. Annu. Rev. Fluid Mech. 45, 325–355.

Oudin, M.J., Jonas, O., Kosciuk, T., et al., 2016. Tumor cell-driven extracellular matrix remodeling drives haptotaxis during metastatic progression. Cancer Discov. 6, 516–531.

Patel, D.D., Koopman, W., Imai, T., Whichard, L.P., Yoshie, O., Krangel, M.S., 2001. Chemokines have diverse abilities to form solid phase gradients. Clin. Immunol. 99, 43–52.

Pedersen, J.A., Lichter, S., Swartz, M., 2010. Cells in 3D matrices under interstitial flow: effects of extracellular matrix alignment on cell shear stress and drag forces. J. Biomech. 43, 900–905.

Polacheck, W.J., Charest, J.L., Kamm, R.D., 2011. Interstitial flow influences direction of tumor cell migration through competing mechanisms. PNAS 108, 11115–11120.

Qiao, Y., Andersen, P.Ø., Evje, S., Standnes, D.C., 2018. A mixture theory approach to model co- and counter-current two-phase flow in porous media accounting for viscous coupling. Adv. Wat. Res. 112, 170–188.

Shieh, A.C., Swartz, M.A., 2011. Regulation of tumor invasion by interstitial fluid flow. Phys. Biol. 8.

Shieh, A.C., Rozansky, H.A., Hinz, B., Swartz, M.A., 2011. Tumor cell invasion is promoted by interstitial flow-induced matrix priming by stromal fibroblasts. Cancer Res. 71 (3).

Shields, J.D., Fleury, M.E., Yong, C., Tomei, A.A., Gwendalyn, J.R., Swartz, M.A., 2007. Autologous chemotaxis as a mechanism of tumor cell homing to lymphatics via interstitial flow and autocrine CCR7 signaling. Cancer Cell 11, 526–538.

Standnes, D.C., Andersen, P.Ø., 2017. Analysis of the impact of fluid viscosities on the rate of countercurrent spontaneous imbibition. Energy Fuels 31 (7), 6928–6940.

Standnes, D.C., Evje, S., Andersen, P.Ø., 2017. A novel relative permeability model based on mixture theory approach accounting for solid-fluid and fluid-fluid interactions. Tran. Por. Media 119, 707–738.

Swartz, M.A., Fleury, M.E., 2007. Interstitial flow and its effects in soft tissues. Annu. Rev. Biomed. Eng. 9, 229–256.

Swartz, M.A., Lund, A.W., 2012. Lymphatic and interstitial flow in the tumour microenvironment: linking mechanobiology with immunity. Nat. Rev. Cancer 12, 210–219.

Wiig, H., Swartz, M.A., 2012. Interstitial fluid and lymph formation and transport: physiological regulation and roles in inflammation and cancer. Physiol. Rev. 92, 1005–1060.

Wu, Y.S., 2016. Multiphase Fluid Flow in Porous and Fractured Reservoirs. Elsevier.

Paper II

Competing tumor cell migration mechanisms caused by interstitial fluid flow

By:

Waldeland, Jahn Otto

Evje, Steinar

Competing tumor cell migration mechanisms caused by interstitial fluid flow

Jahn O. Waldeland, Steinar Evje *

University of Stavanger, Faculty of Science and Technology, 4068 Stavanger, Norway

A B S T R A C T

In the seminal work by Swartz and collaborators (Shields et al., 2007) it was discovered that autologously secreted or activated (ECM-bound) chemokine forms local pericellular diffusion gradients skewed by fluid convection, and the cells subsequently chemotact up the flow-directed gradient. However, in (Polacheck et al., 2011) Kamm and collaborators found that there is a competing downstream and upstream migration transport mechanism. Their study showed that both mechanisms are present at the same time and the relative strength of these two stimuli governs the directional bias in migration for a cell population and is a function of cell density, interstitial flow rate, and CCR7 receptor availability. The main objective of this work is to give a possible explanation of these two different concurrent cell migration mechanisms by means of a theoretical model. Relying on multiphase modelling, separate momentum balance equations are formulated, respectively, for the cell phase and the interstitial fluid (IF) phase. In order to represent proteolytic activity and autologous chemotaxis a non-moving ECM component is included, as well as proteases secreted by the cancer cells and chemokine that can be released from ECM. The cell and IF momentum balance equations include cell-ECM and fluid-ECM resistance force terms (i.e., classical Darcy's equation terms), but also a cell-fluid interaction term that can account for a more indirect effect that fluid-generated stress may have on cancer cells. We illustrate how the cancer cells can work through this term and effectively avoid being pushed in the flow direction, and even create upstream migration by controlling its magnitude and sign. We think of this as the mathematical interpretation of the experimental observation by Kamm and collaborators that the fluid generated matrix adhesion tension on the upstream side of cells activates integrin adhesion complexes, resulting in activation of focal adhesion (FA) proteins. The model predicts that generally the strength of the upstream migration mechanism is sensitive to the cell volume fraction: a lower density of cells is subject to a weaker upstream migration effect; a higher density of cancer cells can more effectively generate upstream migration. This behavior is a result of the nonlinear coupling between cell-ECM, fluid-ECM, and cell-fluid interaction terms that naturally are involved in the mathematical expression for the net cell velocity.

© 2018 Elsevier Ltd. All rights reserved.

1. Introduction

1.1. Background

The phenomenon of lymph node metastasis has been recognized for a long time. However, the underlying mechanism by which malignant tumors leave the primary tumor site, invade the lymphatics and metastasize to lymph nodes are unclear. In Shields et al. (2007) it is suggested that interstitial flow caused by lymphatic drainage directs tumor cell migration by autocrine CCR7 signaling. The tumor cells utilize interstitial flow to create and amplify an autologous chemokine gradient of CCL21 and CCL19 ligands and thus chemotact toward the lymphatic in a process termed autologous chemotaxis. Further investigations are provided by Shieh et al. (2011) where the role of fibroblasts and its interaction with cancer cells leading to enhanced cell migration, is elucidated. Haessler et al. found in Haessler et al. (2012) that interstitial flow increases the percentage of cells that become migratory, and increases migrational speed for a subpopulation of cells. It also increases the migrational persistence of a subpopulation in the positive or negative flow direction. Polacheck et al. (2011) extended the study by Shields et al. (2007), demonstrating that the strength of flow as well as the cell seeding density affected the migration direction. Their work provides further evidence that CCR7-mediated autologous chemotaxis is the mechanism that

leads to cancer cell migration with the flow, but there is another mechanism that causes strain-induced migration against the flow. Experiments were conducted at two different seeding densities and at two different flow velocities by using a flow system as shown in Fig. 1 (left). The authors introduce two metrics, a stream-line migration metric and a directional migration metric, which quantify if the cells migrate parallel to the flow and if the cells migrate upstream/downstream, respectively. As interstitial flow is introduced, the cells at both densities migrate along streamlines, see Fig. 1A. In Fig. 1B it is shown that the low cell seeding density culture migrated with the flow in accordance with the behavior reported in Shields et al. (2007). However, for the high cell seeding density the migration is dominated by upstream migration. In addition, this migration against the flow direction is highly sensi-tive to the fluid velocity. In addition, when CCR7 is blocked and chemotaxis is negated, both high and low density cultures migrate upstream. Autologous chemotaxis is known to transport the cells downstream, but when canceling this effect the cells migrate upstream. Polacheck et al. (2014) further investigated the effects of interstitial fluid flow stresses imparted on cells. As the cell tries to maintain static equilibrium, all fluid stresses imparted on the cell must be balanced by tension in matrix adhesions. This force balance will give rise to a greater matrix adhesion tension on the upstream side of the cell, and this tension activates $\beta 1$-integrin adhesion complexes, resulting in localization and activation of focal adhesion (FA) proteins near the upstream membrane of the cell.

1.2. Interesting questions and challenges

In this work focus is on the observations made in Polacheck et al. (2011) which in turn is motivated by the investigations in Shields et al. (2007). The following hypothesis was proposed in Polacheck et al. (2011) based on the experimental observations summed up by the graphs shown in Fig. 1A and Fig. 1B:

"Motivated by the negative directional migration scores for both cell densities and flow rates when CCR7 is blocked, we hypothesize that a CCR7-independent stimulus competes with CCR7-dependent autolo-gous chemotaxis and when CCR7 is inhibited, stimulates cells to migrate upstream. The relative strength of these two stimuli governs the directional bias in migration for a cell population and is a function of cell density, interstitial flow rate, and CCR7 receptor availability". Some natural questions are:

- Previous modelling in the context of autologous chemotaxis has been restricted to single-flow descriptions based on Darcy's equations Shields et al. (2007) and Wiig and Swartz (2012). What is a simplest possible system where we take into account both the interstitial fluid (IF) and cell phase dynamics, A first version of such a cell-fluid model was presented in Waldeland and Evje (2018) and was used to shed light on basic mecha-nisms of autologous chemotaxis.
- Can this multiphase approach account for the upstream-generated motion that has been observed experimentally? Even more challenging, can it capture the delicate competition between the downstream autologous chemotactic driven trans-port mechanism and the integrin-mediated upstream migration mechanism, as reflected by the curves shown in Fig. 1B?
- In particular, why is it so that the upstream migration should increase with higher fluid velocity? And similarly, why will this migration mechanism become more dominating with higher cell density? In particular, why will the low density cell aggre-gate shift completely from a strongly dominated downstream transport to an upstream dominated migration when the CCR7 is blocked?
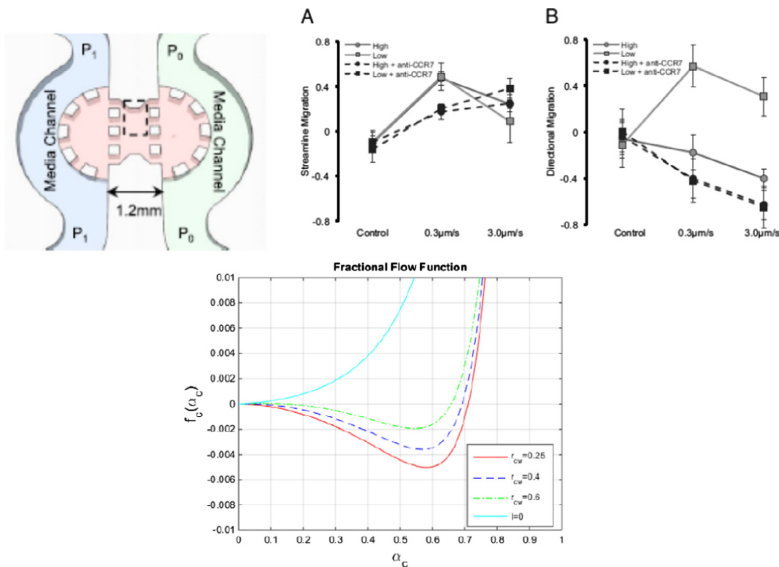
Fig. 1. **Top.** (left): The microfluidic flow system used in Polacheck et al. (2011). **Top** (right): Figure from Polacheck et al. (2011). Interstitial flow induces a bias in direction of tumor cell migration. "High" and "low" refer to seeding densities of $25 \cdot 10^4$ cells/mL and $5 \cdot 10^4$ cells/mL, respectively. (A) streamline migration. (B) directional migration. Reprinted with permission from PNAS. **Bottom**: Typical plot of the function $\bar{f}_c(\alpha_c)$ which characterizes the mechano-transductive driven cell migration in response to IF flow. The fact that the function can become negative, reflects upstream migration. The nonlinear behavior, i.e., the function is more flat for low values of α_c (cell volume fraction) whereas it decreases more dramatically for larger cell densities α_c, suggests that for low cell density the upstream migration is weak whereas it increases with higher cell densities and therefore outperforms the downstream autologous chemotaxis. Different curves refer to different choice of parameters that characterize the cell-ECM, fluid-ECM, and cell-fluid interaction terms. We refer to Sections 3–5 for details.

The main purpose of this paper is to illustrate how a cell-fluid model suggests an explanation of the possible competing upstream and downstream cell migration mechanisms. Our approach is based on so-called mixture theory (Drew and Passman, 1999; Rajagopal, 2007). In addition to mass balance equations, two separate momentum equations for the IF and cell phase are included that give room for accounting for the balance between pressure gradients (stress) and interaction terms; both fluid-ECM interaction, cell-ECM interaction, as well as cell-fluid interaction terms. Included in our flow system is also a component ρ to represent ECM (fiber), C to denote chemokine, and G to represent protease secreted by the cancer cells which is able to release chemokine bounded to ECM.

1.3. Main findings

For the sake of motivation we highlight the following main findings:

- The multiphase approach gives rise to a cell velocity $\mathbf{u}_c$ which takes the following form expressed in terms of the Darcy like $\mathbf{U}_c = \alpha_c \mathbf{u}_c$ where α_c, α_w are the volume fraction of cell and fluid such that $\alpha_c + \alpha_w = 1$:

$$\mathbf{U}_c = \mathbf{U}_T \hat{f}_c(\alpha_c) - \hat{h}(\alpha_c)\nabla(\Delta P(\alpha_c)) - \hat{h}(\alpha_c)\nabla\Lambda(C). \quad (1)$$

The cell velocity $\mathbf{U}_c$ involves three different velocity components: (i) $\mathbf{U}_T \hat{f}_c(\alpha_c)$ where $\mathbf{U}_T = \mathbf{U}_w + \mathbf{U}_c$ is the total velocity dictated essential by the interstitial fluid velocity $\mathbf{U}_w = \alpha_w \mathbf{u}_w$ and $\hat{f}_c(\alpha_c)$ is a function of cell-ECM interaction, fluid-ECM interaction, and cell-fluid interaction effect; (ii) $\nabla(\Delta P(\alpha_c))$ which represents the cell dispersive effect; (iii) $\nabla\Lambda(C)$ which represents the autologous chemotactic effect that amounts to motion in direction of a positive gradient in C (chemokine).
- Thanks to the fact that the cell-fluid momentum balance equations naturally allow for incorporating a fluid-cell drag force term, the term $\mathbf{U}_T \hat{f}_c(\alpha_c)$ has a built-in capacity to generate upstream migration, see Fig. 1 (bottom), corresponding to negative values of $\hat{f}_c(\alpha_c)$. This aspect was not accounted for in Waldeland and Evje (2018). Clearly, the appearance of the $\mathbf{U}_T$ term in front of $\hat{f}_c(\alpha_c)$ implies that this term is strongly correlated to the interstitial fluid velocity, in accordance with the observations reflected by the curves in Fig. 1.
- Hence, the cell velocity (1) can account for the experimentally observed competition between downstream autologous chemotactic driven migration and upstream stress-generated motion. The model can explain the sudden change from downstream to upstream motion when the CCR7 receptor is blocked and the effect from the last term in (1) is nullified. In addition, the model also suggests an explanation for the experimental observation that a low density cell aggregate has a dominating downstream migration generated by the last term in (1), whereas high seeding density of cells tend to be dominated by upstream migration (the first term in (1)), and this effect is amplified with higher IF velocity.

2. A Polacheck-Kamm cell-fluid model

2.1. A general cell-fluid model

In the multiphase modeling framework, the tumor-host environment is considered as a mixture of two interacting continua (Drew and Passman, 1999; Byrne and Owen, 2004; Rajagopal, 2007; Evje and Wen, 2018): the cellular phase comprises tumor cells represented by a volume fraction α_c moving with a velocity

$\mathbf{u}_c$ and the extracellular fluid phase represented by the volume fraction α_w moving with a velocity $\mathbf{u}_w$. In the recent work (Waldeland and Evje, 2018) a simplest possible cell-fluid model was formulated to describe autologous chemotaxis driven cell migration based on a proper modification of the general cell-fluid model presented and discussed in Evje (2017). The resulting model is summed up below, and we refer to Evje (2017) and Waldeland and Evje (2018) for more details:

$$
\begin{aligned}
&(\alpha_c \rho_c)_t + \nabla \cdot (\alpha_c \rho_c \mathbf{u}_c) = \rho_c S_c, \quad S_c = \alpha_c\left(\lambda_{11} - \lambda_{12}\alpha_c - \lambda_{13}\frac{\rho}{\rho_M}\right) \\
&(\alpha_w \rho_w)_t + \nabla \cdot (\alpha_w \rho_w \mathbf{u}_w) = -\rho_w S_c + \rho_w Q, \quad Q = Q_v - Q_l \\
&\alpha_c \nabla P_c = -\hat{\zeta}_c \mathbf{u}_c + \hat{\zeta}(\mathbf{u}_w - \mathbf{u}_c) + \varepsilon_c \nabla \cdot (\alpha_c \rho_c \nabla \mathbf{u}_c) \\
&\alpha_w \nabla P_w = -\hat{\zeta}_w \mathbf{u}_w - \hat{\zeta}(\mathbf{u}_w - \mathbf{u}_c) + \varepsilon_w \nabla \cdot (\alpha_w \rho_w \nabla \mathbf{u}_w) \\
&\rho_t = -\lambda_{21}G\rho + \rho\left(\lambda_{22} - \lambda_{23}\alpha_c - \lambda_{24}\left(\frac{\rho}{\rho_M}\right)\right) \\
&G_t = \nabla \cdot (D_G \nabla G) - \nabla \cdot (G\mathbf{u}_w) - \lambda_{31}G + \alpha_c\left(\lambda_{32} - \lambda_{33}\left(\frac{G}{G_M}\right)^{v_1}\right) \\
&C_t = \nabla \cdot (D_C \nabla C) - \nabla \cdot (C\mathbf{u}_w) \\
&\quad + G\rho\left(\lambda_{41} - \lambda_{42}\left(\frac{C}{C_M}\right)^2 - \lambda_{43}\left(\frac{C}{C_M}\right)^{v_2}\right) - \lambda_{44}\alpha_c, \quad \mathbf{x} \in \Omega.
\end{aligned}
$$
$$(2)$$

The cell phase is armed with cell-specific features in the momentum Eq. $(2)_3$ by letting the cell phase pressure P_c feel additional stress due to cell-cell interaction and migration-related stress due to chemotaxis through the relation

$$P_c = P_w + \Delta P(\alpha_c) + \Lambda(C). \quad (3)$$

This means that the stress P_c associated with the cancer cells differs from the IF pressure P_w because of the cell–cell stress term ΔP and the chemotaxis stress term Λ. Similar to Evje (2017) and Waldeland and Evje (2018) we use

$$\Delta P(\alpha_c) = \gamma J(1 - \alpha_c). \quad (4)$$

Herein, $\gamma > 0$ is a coefficient (unit Pa) that depends linearly on the surface tension (unit Pa m) whereas $J(\alpha_w)$ is a monotonic decreasing dimensionless function with respect to the fluid volume fraction α_w. The ability of the cancer cells to generate a force is expressed through the potential function $\Lambda(C)$ here set to be (Byrne and Owen, 2004; Evje, 2017; Waldeland and Evje, 2018)

$$\Lambda(C) = \Lambda_0 - \frac{\Lambda_1}{1 + \exp(-\xi_1(C - C_M))}, \quad (5)$$

where $\Lambda_0, \Lambda_1, \xi_1$ are constant parameters with units, respectively, as $[\Lambda_0, \Lambda_1] = $ Pa and $[\xi_1] = $ m³/kg. There is a drag force between the extracellular fluid represented by the fluid velocity $\mathbf{u}_w$ and the ECM structure (fibers) given by

$$\hat{\zeta}_w = I_w \hat{k}_w \alpha_w^{r_w}, \quad \hat{k}_w > 0, \quad r_w < 2, \quad (6)$$

with $I_w = \frac{\mu_w}{K} > 0$ and K is the permeability of the porous media and μ_w the fluid viscosity. Similarly, there is a drag force between the cells and the ECM (fibers) represented by the cell fluid velocity $\mathbf{u}_c$,

$$\hat{\zeta}_c = I_c \hat{k}_c \alpha_c^{r_c}, \quad I_c, \hat{k}_c > 0, \quad r_c < 2, \quad (7)$$

where I_c (Pa s/m²), $\hat{k}_c$ and r_c must be specified (the two last are dimensionless). Finally, there is also a drag force between the cell phase and the fluid. This effect is accounted for through the term $\pm \hat{\zeta}(\mathbf{u}_w - \mathbf{u}_c)$, see $(2)_{3,4}$ where

$$\hat{\zeta} = I\hat{k}\alpha_w\alpha_c^{1+r_{cw}}, \quad \hat{k} > 0, \quad r_{cw} > 0, \quad (8)$$

where I (Pa s/m²) remains to be determined as well as the dimensionless $\hat{k}$ and r_{cw}.

2.2. The mechanotransductive machinery mobilized by IF

Polacheck et al. (2014) observed that fluid which is flowing past a cell leads to the activation of a class of receptors called integrins, ultimately prompting upstream migration. As the cell tries to maintain static equilibrium, all fluid stresses imparted on the cell must be balanced by tension in matrix adhesions. This force balance will give rise to a greater matrix adhesion tension on the upstream side of the cell, and this tension activates L1-integrin adhesion complexes, resulting in localization and activation of focal adhesion (FA) proteins near the upstream membrane of the cell. How can this information be represented in the mathematical model? Which terms in the force balance as expressed by the two momentum Eqs. (2)$_{3,4}$, are effected? The term that feels the stress from the fluid flow is the cell-fluid drag force term $\hat{\zeta}$ given by (8). In a classical fluid mechanical setting this term represents a drag force effect where the fastest flowing fluid transfers momentum to the slower fluid phase. This effect is accounted for by setting the coefficient I to be positive (Qiao et al., 2018). However, in the cell-fluid context, as shown in Polacheck et al. (2011) and Polacheck et al. (2014), this may not be the case.

2.3. A Polacheck-Kamm model

Following (Waldeland and Evje, 2018) we assume (i) incompressible fluids; (ii) viscosity terms are ignored. This allows us to derive an explicit expression for the interstitial cell velocity $\mathbf{u}_c$ which reflects the competition between different migration mechanisms as well the role played by the different interaction terms $\hat{\zeta}_w, \hat{\zeta}_c$, and $\hat{\zeta}$. From (2) we obtain the following dimensionless simplified version (see Waldeland and Evje (2018) for details):

$$\alpha_{ct} + \nabla \cdot (\alpha_c \mathbf{u}_c) = S_c, \quad S_c = \alpha_c \left(\lambda_{11} - \lambda_{12}\alpha_c - \lambda_{13}\left(\frac{\rho}{\rho_M}\right) \right)$$

$$\alpha_{wt} + \nabla \cdot (\alpha_w \mathbf{u}_w) = -S_c + (Q_v - Q_l)$$

$$\alpha_c \nabla (P_w + \Delta P + \Lambda(C)) = -\hat{\zeta}_c \mathbf{u}_c + \hat{\zeta}(\mathbf{u}_w - \mathbf{u}_c)$$

$$\alpha_w \nabla P_w = -\hat{\zeta}_w \mathbf{u}_w - \hat{\zeta}(\mathbf{u}_w - \mathbf{u}_c)$$

$$\rho_t = -\lambda_{21} G\rho + \rho \left(\lambda_{22} - \lambda_{23}\alpha_c - \lambda_{24}\left(\frac{\rho}{\rho_M}\right) \right)$$

$$G_t = \nabla \cdot (D_G \nabla G) - \nabla \cdot (G\mathbf{u}_w) - \lambda_{31} G + \alpha_c \left(\lambda_{32} - \lambda_{33}\left(\frac{G}{G_M}\right)^{v_1} \right)$$

$$C_t = \nabla \cdot (D_C \nabla C) - \nabla \cdot (C\mathbf{u}_w)$$

$$+ G\rho \left(\lambda_{41} - \lambda_{42}\left(\frac{C}{C_M}\right)^2 - \lambda_{43}\left(\frac{C}{C_M}\right) v_2 \right) - \lambda_{44}\alpha_c. \tag{9}$$

The model is combined with the boundary conditions

$$P_w|_{\partial\Omega} = P^*, \quad \frac{\partial}{\partial v}G\bigg|_{\partial\Omega} = 0, \quad \frac{\partial}{\partial v}C\bigg|_{\partial\Omega} = 0, \quad t > 0 \tag{10}$$

where v is the outward normal on $\partial\Omega$ and P^* a known pressure at the boundary. Corresponding initial data are

$$\alpha_c(\mathbf{x}, t = 0) = \alpha_{c0}(\mathbf{x}), \quad \rho(\mathbf{x}, t = 0) = \rho_0(\mathbf{x}),$$
$$G(\mathbf{x}, t = 0) = G_0(\mathbf{x}), \quad C(\mathbf{x}, t = 0) = C_0(\mathbf{x}). \tag{11}$$

From the two momentum Eqs. (9)$_{3,4}$ we compute explicit expressions for the cell and fluid velocity, respectively, $\mathbf{u}_c$ and $\mathbf{u}_w$. The following expressions are found:

$$\mathbf{u}_c = \mathbf{U}_T \left[\frac{\hat{f}_c(\alpha_c)}{\alpha_c} \right] - \left[\frac{\hat{h}(\alpha_c)}{\alpha_c} \right] \nabla(\Delta P + \Lambda),$$
$$\mathbf{u}_w = \mathbf{U}_T \left[\frac{\hat{f}_w(\alpha_c)}{\alpha_w} \right] + \left[\frac{\hat{h}(\alpha_c)}{\alpha_w} \right] \nabla(\Delta P + \Lambda), \tag{12}$$

with fractional flow functions $\hat{f}_c(\alpha_c)$ and $\hat{f}_w(\alpha_c)$ given by

$$\hat{f}_c(\alpha_c) := \frac{\hat{\lambda}_c}{\hat{\lambda}_T} = \frac{[\alpha_c^2 \hat{\zeta}_w] + \alpha_c \hat{\zeta}}{[\alpha_c^2 \hat{\zeta}_w] + [\alpha_w^2 \hat{\zeta}_c] + \hat{\zeta}},$$

$$\hat{f}_w(\alpha_c) := \frac{\hat{\lambda}_w}{\hat{\lambda}_T} = \frac{[\alpha_w^2 \hat{\zeta}_c] + \alpha_w \hat{\zeta}}{[\alpha_c^2 \hat{\zeta}_w] + [\alpha_w^2 \hat{\zeta}_c] + \hat{\zeta}}, \tag{13}$$

$$\hat{h}(\alpha_c) = \frac{\alpha_c^2 \alpha_w^2}{\alpha_c^2 \hat{\zeta}_w + \alpha_w^2 \hat{\zeta}_c + \hat{\zeta}},$$

where the coefficients $\hat{\lambda}_c, \hat{\lambda}_w$, and $\hat{\lambda}_T$ (so-called mobility functions (Wu, 2016)) are given by

$$\hat{\lambda}_c = \frac{[\alpha_c^2 \hat{\zeta}_w] + \alpha_c \hat{\zeta}}{\hat{\zeta}_c \hat{\zeta}_w + \hat{\zeta}[\hat{\zeta}_c + \hat{\zeta}_w]},$$

$$\hat{\lambda}_w = \frac{[\alpha_w^2 \hat{\zeta}_c] + \alpha_w \hat{\zeta}}{\hat{\zeta}_c \hat{\zeta}_w + \hat{\zeta}[\hat{\zeta}_c + \hat{\zeta}_w]}, \tag{14}$$

and total mobility $\hat{\lambda}_T$ given by

$$\hat{\lambda}_T = \hat{\lambda}_c + \hat{\lambda}_w = \frac{[\alpha_c^2 \hat{\zeta}_w] + [\alpha_w^2 \hat{\zeta}_c] + \hat{\zeta}}{\hat{\zeta}_c \hat{\zeta}_w + \hat{\zeta}[\hat{\zeta}_c + \hat{\zeta}_w]}. \tag{15}$$

The model (9) then takes the more compact form:

$$\alpha_{ct} + \nabla \cdot (\alpha_c \mathbf{u}_c) = S_c$$
$$\rho_t = -\lambda_{21} G\rho + \rho \left(\lambda_{22} - \lambda_{23}\alpha_c - \lambda_{24}\frac{\rho}{\rho_M} \right)$$
$$G_t = \nabla \cdot (D_G \nabla G) - \nabla \cdot (G\mathbf{u}_w) - \lambda_{31} G$$
$$+ \alpha_c \left(\lambda_{32} - \lambda_{33}\left(\frac{G}{G_M}\right)^{v_1} \right)$$
$$C_t = \nabla \cdot (D_C \nabla C) - \nabla \cdot (C\mathbf{u}_w)$$
$$+ G\rho \left(\lambda_{41} - \lambda_{42}\left(\frac{C}{C_M}\right)^2 - \lambda_{43}\left(\frac{C}{C_M}\right)^{v_2} \right) - \lambda_{44}\alpha_c \tag{16}$$

where $\mathbf{u}_c$ is given by (12)$_1$. Moreover, in order to compute $\mathbf{U}_T$ we first solve the elliptic problem for P_w (see Waldeland and Evje (2018) for details)

$$-(Q_v - Q_l) - \nabla \cdot (\hat{\lambda}_c \nabla(\Delta P + \Lambda)) = \nabla \cdot (\hat{\lambda}_T \nabla P_w),$$
$$P_w|_{\partial\Omega} = P^*. \tag{17}$$

Knowing P_w, we can compute $\mathbf{U}_T$ needed in (12). We have the following expression for $\mathbf{U}_T$:

$$\mathbf{U}_T = -\hat{\lambda}_T \nabla P_w - \hat{\lambda}_c \nabla(\Delta P + \Lambda). \tag{18}$$

Note that we also need $\mathbf{u}_w$ given by (12)$_2$ to solve (16)$_{3,4}$. From the cell mass balance Eq. (16)$_1$ combined with (12)$_1$ we see that cell migration velocity $\mathbf{U}_c = \alpha_c \mathbf{u}_c$ is composed of three transport components:

(i) a convective term $\nabla \cdot (\mathbf{U}_T \hat{f}_c(\alpha_c))$ which is related to fluid-generated stress;
(ii) a diffusive term $-\nabla \cdot (\hat{h}(\alpha_c)\nabla(\Delta P(\alpha_c)))$ reflecting cell–cell adhesion;
(iii) a chemotaxis transport represented by $-\nabla \cdot (\hat{h}(\alpha_c)\nabla(\Lambda(C)))$.

All three transport mechanisms are concurrent and competing. Interestingly enough this appears to be a precise mathematical statement of the following comment made in Haessler et al. (2012): *"Therefore, in any given cell population, one may find a wide range of migrational behaviors; some may respond to flow by moving faster (but randomly), others may migrate in the flow direction through autologous chemotaxis, and still others may move in the opposite direction due to local stress gradient effects."*

The compelling question that catches our attention now is: Where is natural room for the upstream migrating mechanism?

This migration mechanism has been reported not to be governed by chemical gradients so the obvious and only candidate is the convective term that involves the nonlinear function $\hat{f}_c(\alpha_c)$.

2.3.1. Correlations for fluid-ECM, cell-ECM, and cell-fluid interaction

Consistent with the study in Waldeland and Evje (2018) of autologous chemotaxis we assume correlations of the following form:

$$\hat{\zeta}_w = I_w \hat{k}_w \alpha_w^{r_w}, \quad \hat{\zeta}_c = I_c \hat{k}_c \alpha_c^{r_c}, \quad \hat{\zeta} = I \hat{k} \alpha_w \alpha_c^{1+r_{cw}}. \tag{19}$$

A new aspect here compared to Waldeland and Evje (2018) is the correlation for $\hat{\zeta}$ representing cell-fluid interaction. In Waldeland and Evje (2018) it was set to zero. The form specified in (19), which is general, is largely motivated by recent studies of water–oil flow systems showing that this term can in fact account for highly relevant interaction forces to better match experimental behaviors (Qiao et al., 2018; Standnes et al., 2017) but subject to the condition that $I > 0$. However, as observed in experimental studies of cell-fluid dynamics, this drag can activate mechanotransductive machinery and lead to directed cellular migration

in the upstream direction (Polacheck et al., 2011, 2014). In order to generate a momentum translation opposite of fluid flow direction, intuitively one might suggest that the sign of I should be allowed to become negative, i.e., $I < 0$.

Remark 2.1. The cell momentum Eq. (9)₃ can be expressed as

$$\alpha_c \nabla P_c = -(\hat{\zeta}_c + \hat{\zeta})\mathbf{u}_c + \hat{\zeta}\mathbf{u}_w. \tag{20}$$

To a large extent P_c is dictated by IFP P_w (in particular, ignoring ΔP and Λ it follows that $P_c = P_w$). Consequently, the LHS of (20) gives a negative value (for the case with flow from left towards right) whose magnitude depends on the IF pressure gradient ∇P_w which must be balanced by corresponding terms on the RHS of (20). The presence of the term $\hat{\zeta}\mathbf{u}_w$ reflects that if the tumor cells can generate a force that has opposite direction of $\mathbf{u}_w$ (i.e., $\hat{\zeta}$ should have negative sign), this term can completely balance the pressure gradient $\alpha_c \nabla P_c$. Essentially, in view of (9)₄, $\hat{\zeta} \sim I$ must be of the same order as I_w then but with negative sign. Moreover, if $|\hat{\zeta}| \sim I$ is larger than I_w it will force the first term $-(\hat{\zeta}_c + \hat{\zeta})\mathbf{u}_c$ to generate a negative cell velocity $\mathbf{u}_c$ to
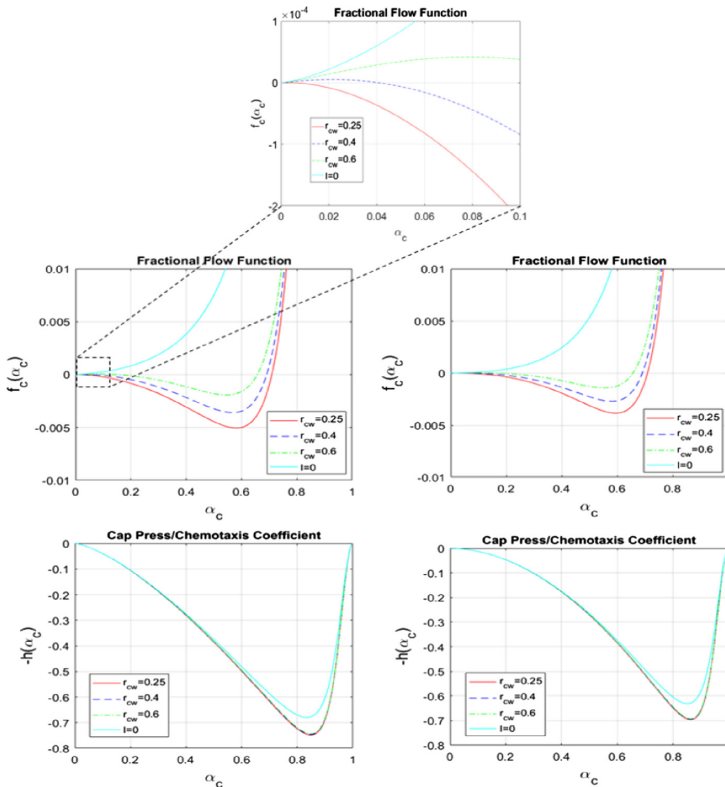
Fig. 2. Top. (left): Fractional flow function $\hat{f}_c(\alpha_c)$ corresponding to $I = -3.75I_w$ and different choices of $r_{cw} = 0.25, 0.4, 0.6$ with $r_c = 0.6$ which implies that small α_c are mobile since $\alpha_c^{r_c}$ quickly drops to zero. **Top** (right): $r_c = 0.1$ which means that the cell-ECM resistance force is stronger for low α_c through the $\alpha_c^{r_c}$-term, i.e., the cancer cells are less mobile. We also have included $\hat{f}_c(\alpha_c)$ for the case where $I = 0$, i.e., the cell-fluid interaction term is set to zero which shows that there is no longer room for upstream migration but instead gives rise to a non-chemical downstream migration not consistent with the experimental observations reflected by the graphs of Fig. 1B. **Bottom:** The function $-\hat{h}(\alpha_c)$ corresponding to $I = -3.75I_w$ and different choices of $r_{cw} = 0.25, 0.4, 0.6$ and $r_c = 0.6$ (left) and $r_c = 0.1$ (right). We also have included $-\hat{h}$ for the case where $I = 0$. The plots clearly show that the coefficient $\hat{h}(\alpha_c)$ to a minor extent is affected by the choice of interaction term $\hat{\zeta}$ through I and r_{cw}. Neither is it sensitive to the choice of r_c, the coefficient associated with cell-ECM resistance force $\hat{\zeta}_c$.

balance the LHS of (20) since the coefficient $(\hat{\zeta}_c + \hat{\zeta})$ is positive $(I_c \gg |I| \sim I_w)$. In other words, if negative drag $\hat{\zeta}$ (sufficiently large) then the first term on the RHS of (20) will supply a change in cell migration direction.

3. One-dimensional version of the Polacheck-Kamm model

3.1. 1D model

We consider a flow domain as in Fig. 1 (left) where fluid flows from left to right along a one-dimensional slab. It follows from (12) and (13) that u_c and u_w take the following form:

$$
\begin{aligned}
u_c &= U_T \left[\frac{\alpha_c \hat{\zeta}_w + \hat{\zeta}}{\alpha_c^2 \hat{\zeta}_w + \alpha_w^2 \hat{\zeta}_c + \hat{\zeta}} \right] \\
&\quad - \left[\frac{\alpha_c \alpha_w^2}{\alpha_c^2 \hat{\zeta}_w + \alpha_w^2 \hat{\zeta}_c + \hat{\zeta}} \right] (\Delta P(\alpha_c) + \Lambda(C))_x \\
&= U_T \left[\frac{\hat{f}_c}{\alpha_c} \right] - \left[\frac{\hat{h}}{\alpha_c} \right] (\Delta P)_x - \left[\frac{\hat{h}}{\alpha_c} \right] \Lambda_x := u_{c1} + u_{c2} + u_{c3},
\end{aligned}
\tag{21}
$$

$$
\begin{aligned}
u_w &= U_T \left[\frac{\alpha_w \hat{\zeta}_c + \hat{\zeta}}{\alpha_c^2 \hat{\zeta}_w + \alpha_w^2 \hat{\zeta}_c + \hat{\zeta}} \right] \\
&\quad + \left[\frac{\alpha_c^2 \alpha_w}{\alpha_c^2 \hat{\zeta}_w + \alpha_w^2 \hat{\zeta}_c + \hat{\zeta}} \right] (\Delta P(\alpha_c) + \Lambda(C))_x \\
&= U_T \left[\frac{\hat{f}_w}{\alpha_w} \right] + \left[\frac{\hat{h}}{\alpha_w} \right] (\Delta P)_x + \left[\frac{\hat{h}}{\alpha_w} \right] \Lambda_x := u_{w1} + u_{w2} + u_{w3}.
\end{aligned}
\tag{22}
$$

The corresponding averaged velocities (Darcy's like velocities) are given by

$$
U_c = U_T \hat{f}_c - \hat{h}(\Delta P)_x - \hat{h}\Lambda_x := U_{c1} + U_{c2} + U_{c3},
\tag{23}
$$

$$
U_w = U_T \hat{f}_w + \hat{h}(\Delta P)_x + \hat{h}\Lambda_x := U_{w1} + U_{w2} + U_{w3}.
\tag{24}
$$

Moreover, the 1D version of (16) is given by

$$
\begin{aligned}
\alpha_{ct} + (\alpha_c u_c)_x &= S_c \\
\rho_t &= -\lambda_{21} G \rho + \rho \left(\lambda_{22} - \lambda_{23}\alpha_c - \lambda_{24}\left(\frac{\rho}{\rho_M}\right) \right) \quad \text{(ECM)} \\
G_t &= D_G G_{xx} - (G u_w)_x - \lambda_{31} G \\
&\quad + \alpha_c \left(\lambda_{32} - \lambda_{33}\left(\frac{G}{G_M}\right)^{\nu_1} \right) \quad \text{(protease)} \\
C_t &= D_C C_{xx} - (C u_w)_x \quad \text{(chemokine)} \\
&\quad + G\rho \left(\lambda_{41} - \lambda_{42}\left(\frac{C}{C_M}\right)^2 - \lambda_{43}\left(\frac{C}{C_M}\right)^{\nu_2} \right) - \lambda_{44}\alpha_c,
\end{aligned}
\tag{25}
$$

where u_c is given by (21) and u_w by (22). Referring to (14) and (15), combined with the correlations (19), we introduce R_1 and R_2 to describe relative strength of interaction forces

$$
R_1 = \frac{I_w \hat{k}_w}{I_c \hat{k}_c}, \quad R_2 = \frac{I \hat{k}}{I_c \hat{k}_c}.
\tag{26}
$$

The following expressions for $\hat{\lambda}_c$, $\hat{\lambda}_w$, and $\hat{\lambda}_T$ involved in (17) are obtained:

$$
\hat{\lambda}_c = \frac{[\alpha_c^2 \hat{\zeta}_w] + \alpha_c \hat{\zeta}}{\hat{\zeta}_c \hat{\zeta}_w + \hat{\zeta}[\hat{\zeta}_c + \hat{\zeta}_w]} = \frac{1}{I_w \hat{k}_w} \cdot \frac{\alpha_c^{2-r_c}(R_1 + R_2 \alpha_c^{r_{cw}} \alpha_w^{1-r_w})}{1 + R_2 \alpha_c^{1+r_{cw}-r_c} \alpha_w^{1-r_w}(\alpha_w^{r_w} + \alpha_c^{r_c}/R_1)},
\tag{27}
$$

$$
\hat{\lambda}_w = \frac{[\alpha_w^2 \hat{\zeta}_c] + \alpha_w \hat{\zeta}}{\hat{\zeta}_c \hat{\zeta}_w + \hat{\zeta}[\hat{\zeta}_c + \hat{\zeta}_w]} = \frac{1}{I_w \hat{k}_w} \cdot \frac{\alpha_w^{2-r_w}(1 + R_2 \alpha_c^{1+r_{cw}-r_c})}{1 + R_2 \alpha_c^{1+r_{cw}-r_c} \alpha_w^{1-r_w}(\alpha_w^{r_w} + \alpha_c^{r_c}/R_1)},
\tag{28}
$$

and

$$
\begin{aligned}
\hat{\lambda}_T &= \hat{\lambda}_c + \hat{\lambda}_w = \frac{[\alpha_c^2 \hat{\zeta}_w] + [\alpha_w^2 \hat{\zeta}_c] + \hat{\zeta}}{\hat{\zeta}_c \hat{\zeta}_w + \hat{\zeta}[\hat{\zeta}_c + \hat{\zeta}_w]} \\
&= \frac{1}{I_w \hat{k}_w} \cdot \frac{\alpha_c^{2-r_w}(1 + R_2 \alpha_c^{1+r_{cw}-r_c}) + \alpha_c^{2-r_c}(R_1 + R_2 \alpha_c^{r_c w} \alpha_w^{1-r_w})}{1 + R_2 \alpha_c^{1+r_{cw}-r_c} \alpha_w^{1-r_w}(\alpha_w^{r_w} + \alpha_c^{r_c}/R_1)},
\end{aligned}
\tag{29}
$$

with $r_c, r_w \leqslant 2$. Having computed P_w from (17), we use the 1D version of (18) to compute U_T. Knowing U_T, we can evaluate the velocities u_c and u_w completely which occur in $(25)_{1,3,4}$, by referring to (21) and (22). It follows that the pressure driven part of average cell phase velocity U_c and fluid velocity U_w are governed, respectively, by $\hat{f}_c(\alpha_c)$ and $\hat{f}_w(\alpha_c)$ which according to (13) combined with (19) are given by

$$
\begin{aligned}
\hat{f}_c &:= \frac{\hat{\lambda}_c}{\hat{\lambda}_T} = \frac{\alpha_c^2 \hat{\zeta}_w + \alpha_c \hat{\zeta}}{\alpha_c^2 \hat{\zeta}_w + \alpha_w^2 \hat{\zeta}_c + \hat{\zeta}} \\
&= \frac{\alpha_c^{2-r_c}(R_1 + \alpha_c^{r_{cw}} \alpha_w^{1-r_w} R_2)}{R_1 \alpha_c^{2-r_c} + \alpha_w^{2-r_w} + R_2 \alpha_c^{1+r_{cw}-r_c} \alpha_w^{1-r_w}},
\end{aligned}
\tag{30}
$$

$$
\begin{aligned}
\hat{f}_w &:= \frac{\hat{\lambda}_w}{\hat{\lambda}_T} = \frac{\alpha_w^2 \hat{\zeta}_c + \alpha_w \hat{\zeta}}{\alpha_c^2 \hat{\zeta}_w + \alpha_w^2 \hat{\zeta}_c + \hat{\zeta}} \\
&= \frac{\alpha_w^{2-r_w}(1 + \alpha_c^{1+r_{cw}-r_c} R_2)}{R_1 \alpha_c^{2-r_c} + \alpha_w^{2-r_w} + R_2 \alpha_c^{1+r_{cw}-r_c} \alpha_w^{1-r_w}},
\end{aligned}
\tag{31}
$$

whereas counter-current motion is controlled by $\hat{h}(\alpha_c)$ given by

Table 1
Model parameters (dimensional) in the model (9) with relevant reference values. See Waldeland and Evje (2018) for more details and corresponding dimensionless variables.

Parameters	Description	Dimensional value
T^*	Reference time	10^4 s
L^*	Refence length	0.01 m
u^*	Reference velocity	10^{-6} m/s
D^*	Reference diffusion	10^{-8} m^2/s
P^*	Reference pressure	10^4 Pa
ρ^*	Reference ECM density	1 kg/m^3
G^*	Reference protease density	10^{-4} kg/m^3
C^*	Reference chemokine density	10^{-4} kg/m^3
ρ_M	Maximal ECM density	ρ^*
G_M	Maximal protease density	$0.5G^*$
C_M	Maximal chemokine density	$0.3C^*$
D_G	Protease	8×10^{-12} m^2/s
D_C	Chemokine	7×10^{-14} m^2/s
ξ_1	Parameter characterizing Λ (dependence on C)	$1.6/C^*$ or $8/C^*$
Λ_0	Parameter characterizing Λ	0 Pa
Λ_1	Parameter characterizing Λ	25,000 Pa
λ_{11}	Proliferation of tumor cells	0
λ_{12}	Decay of tumor cells	0
λ_{13}	Decay of tumor cells	0
λ_{21}	Degradation of ECM	10 m^3/kg s
λ_{22}	Release/reconstruction of ECM	1.25×10^{-3} 1/s
λ_{23}	Release/reconstruction of ECM	0 1/s
λ_{24}	Release/reconstruction of ECM	1.25×10^{-3} 1/s
λ_{31}	Natural decay of protease	5×10^{-3} 1/s
λ_{32}	Production by cells of protease	2×10^{-6} kg/m^3 s
λ_{33}	Logistic rate constant protease	2×10^{-6} kg/m^3 s
ν_G	Related to logistic function	1
λ_{41}	Proteolytically freed chemokine	3.2×10^{-3} m^3/kg s
λ_{42}	Logistic rate constant chemokine	1.4×10^{-4} m^3/kg s
λ_{43}	Logistic rate constant chemokine	3.2×10^{-3} m^3/kg s
λ_{44}	Cell consumption rate chemokine	2×10^{-9} kg/m^3 s
ν_C	Related to logistic function	0.2

$$\hat{h} := \frac{\alpha_c^2 \alpha_w^2}{\alpha_c^2 \hat{\zeta}_w + \alpha_w^2 \hat{\zeta}_c + \hat{\zeta}}$$

$$= \frac{1}{I_c \hat{k}_c} \cdot \frac{\alpha_c^{2-r_c} \alpha_w^{2-r_w}}{R_1 \alpha_c^{2-r_c} + \alpha_w^{2-r_w} + R_2 \alpha_c^{1+r_{cw}-r_c} \alpha_w^{1-r_w}}. \tag{32}$$

Recall that R_1 in (26) considers the relative strength of the fluid-ECM resistance force and the cell-ECM resistance force and appears as a dominating factor in the expression for $\hat{f}_c(\alpha_c)$ in $(30)_1$. This was explored in detail in Waldeland and Evje (2018). Now we also account for the R_2-related term. A careful study of the impact from R_1 and R_2 on the resulting fractional cell flow function $\hat{f}_c(\alpha_c)$ is provided in Appendix A. Main observations are:

- Reasonable choices of the parameters $I, \hat{k}$, and r_{cw} appearing in the cell-fluid interaction term $\hat{\zeta}$ in (19), give rise to cell fractional flow function $\hat{f}_c(\alpha_c)$ with a negative dip when $I < 0$. See Fig. 2 for illustrations.
- When $I < 0$, there are constraints on how parameters involved in the interaction terms, as represented by R_1 and R_2 given by (26), should be set in order to ensure well-defined mobility functions $\hat{\lambda}_c, \hat{\lambda}_w$ and fractional flow functions $\hat{f}_c, \hat{f}_w$.

To sum up, there is naturally room for generating upstream migration, in accordance with the experimental observations made in Polacheck et al. (2011, 2014). However, the analysis in Appendix A also indicates that the strength of the involved interaction forces must be "finely tuned" in order to avoid singular behavior manifested by coefficients that can blow up. Perhaps this mathematical observation can be understood as an expression of the experimental observation in Polacheck et al. (2014) that upstream cell migration requires the "*activation of a number of proteins like β1-integrin, vinculin, focal adhesion kinase (FAK), F action, and paxillin to create protrusion localizing to the upstream side of the cell*".

4. Results

For input data required to solve the model we refer to Table 1 and Waldeland and Evje (2018). We compute solutions after a time $T = 50$ (dimensionless) which amounts to approximately 5.8 days.

Choice of parameters

Regarding $\Delta P(\alpha_c)$, we set $\gamma = 1000$ Pa as default and use $J(\alpha_c) = -\ln(\delta + [1 - \alpha_c])$ with $\delta = 0.01$. This will generate a relatively weak diffusive cell migration effect due to cell–cell repulsive forces. We assume that the conductivity associated with the cell aggregate microenvironment is of the order $\frac{K}{\mu_w} = 5 \cdot 10^{-13}$ m²/Pa s (Swartz and Fleury, 2007; Pedersen et al., 2010). This implies that

$$I_w = \frac{\mu_w}{K} = 2 \cdot 10^{12} \text{ Pa s/m}^2, \quad \hat{k}_w = 1, \quad r_w = 0.0 \tag{33}$$

and corresponding values for the cell phase are set to

$$I_c = 200 I_w, \quad \hat{k}_c = 1, \quad r_c \in [0.1, 0.6]. \tag{34}$$

The coefficient $r_c = 0.6$ implies that the cell-ECM resistance force $\hat{\zeta}_c$ decreases rather quickly with decreasing α_c, i.e., small number of cells are more motile. A choice $r_c = 0.1$ reflects that the cell-ECM resistance force is stronger. We suggest the following set of parameters for the cell-fluid interaction term $\hat{\zeta}$:
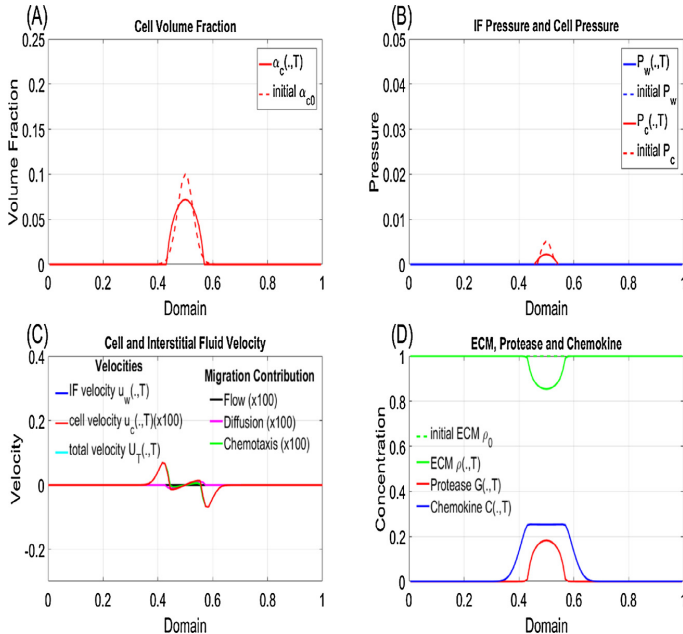
Fig. 3. The case with low cell volume fraction and no imposed fluid flow ($p_L^* = p_R^*$) and with $r_{cw} = 0.25$. (A) Although the autologous chemotaxis and mechanotransductive machinery is intact there is no directed cell migration, only a weak diffusive spreading. (B) No pressure gradient has been imposed. (C) Note that "Flow" = u_{c1}, "Diffusion" = u_{c2}, and "Chemotaxis" = u_{c3} with total cell velocity $u_c = u_{c1} + u_{c2} + u_{c3}$ (see (21)). Total velocity U_T is essentially zero giving rise to no contribution from $u_{c1} = U_T \frac{I_c}{\alpha_c}$ which controls upstream migration. Note that the green curve (chemotaxis) is masked by the red curve (total cell velocity). (D) Since u_w is essentially zero it follows that there is no skewed distribution of the chemokine C (similarly with protease G) but instead a dispersion driven spreading as described by $(25)_4$ with $u_w = 0$, which gives rise to a slight chemotactic driven cell migration that prevents cell spreading, see plot of cell velocity $u_{c3} = -\frac{h}{\alpha_c} \Lambda(C)_x$ in panel (C). This must be understood in view of the chemokine concentration C which has a symmetric distribution and decreases at the rim of the cell aggregate.

$$I = -3.75 I_w, \quad \hat{k} = 1, \quad r_{cw} \in [0.1, 0.6]. \tag{35}$$

In Fig. 2 (top) we have plotted the fractional flow function $\hat{f}_c(\alpha_c)$ for different choices of r_{cw} in the interval $[0.1, 0.6]$. Some observations:

- Thanks to the cell-fluid interaction term $\hat{\zeta}$ with negative coefficient I, the fractional flow function $\hat{f}_c(\alpha_c)$ contains a negative part that gives rise to an upstream advective transport through the term $u_{c1} = U_T \frac{\hat{f}_c(\alpha_c)}{\alpha_c}$, see (21). The nonlinear form of $\hat{f}_c(\alpha_c)$ in some interval from $[0, \alpha_c^*]$ reflects that the strength of the upstream migration vary with cell volume fraction.
- Without inclusion of the cell-fluid interaction term, i.e., $I = 0$, there is no room for upstream migration. Instead $\hat{f}_c(\alpha_c)$ becomes a non-negative and increasing function which gives rise to downstream migration where cancer cells are pushed by the IF flow, not consistent with experimental observations in Fig. 1B.
- Plots of the coefficient $\hat{h}(\alpha_c)$ is shown in Fig. 2 (bottom) for different parameters consistent with those used for plots of $\hat{f}_c(\alpha_c)$. The curves show little variation and reflect that cell migration due to the cell velocity u_{c2} (dispersion) and u_{c3} (autologous chemotaxis), see (21), is to a minor extent affected.

Low and high cell seeding volume fraction

In order to discuss the experimental results of Fig. 1B we consider a low cell volume fraction aggregate corresponding to

$$\alpha_c(x, t = 0) = 0.1 \exp(-[25(x - 0.5)]^2), \tag{36}$$

and a high cell volume fraction aggregate corresponding to

$$\alpha_c(x, t = 0) = 0.5 \exp(-[25(x - 0.5)]^2). \tag{37}$$

Low and high IF velocity

In light of the experimental results of Fig. 1B we shall consider two different fluid rates. A slow flow of fluid across the cell aggregate around $u_w \approx 0.25\,\mu m/s$ is ensured by setting

$$P_L^* = P_{ref} + 6.25\,kPa, \quad P_R^* = P_{ref}. \tag{38}$$

A high fluid flow velocity around $u_w \approx 2.5\,\mu m/s$ follows by setting

$$P_L^* = P_{ref} + 50\,kPa, \quad P_R^* = P_{ref}. \tag{39}$$

We strive to keep as many parameters as possible fixed when we consider the three different cases: (i) no fluid flow (i.e., $P_L^* = P_R^*$); (ii) low IF flow rate ($u_w \approx 0.3\,\mu m/s$); (iii) high IF flow rate ($u_w \approx 3\,\mu m/s$). However, some modifications seem natural.

- For the low cell volume fraction case (36) we set $r_c = 0.6$ to allow cells to be more mobile than for the case with high cell volume fraction (37) where we set $r_c = 0.1$. I.e., we use that $\alpha_c^{r_c}$ drops quicker to zero for $r_c = 0.6$ then $r_c = 0.1$.
- Parameters that determine the creation of chemokine gradients (i.e., all parameters λ_{ij} in (25)$_{2,3,4}$) are set to be the same for both low and high cell volume fraction case. We set the parameter ξ_1 in $\Lambda(C)$ given by (5), which characterizes the strength of the autologous chemotaxis, to be 5 times higher for the low cell volume fraction case, as compared to the high volume fraction case. This seems to be in line with the experimental observation
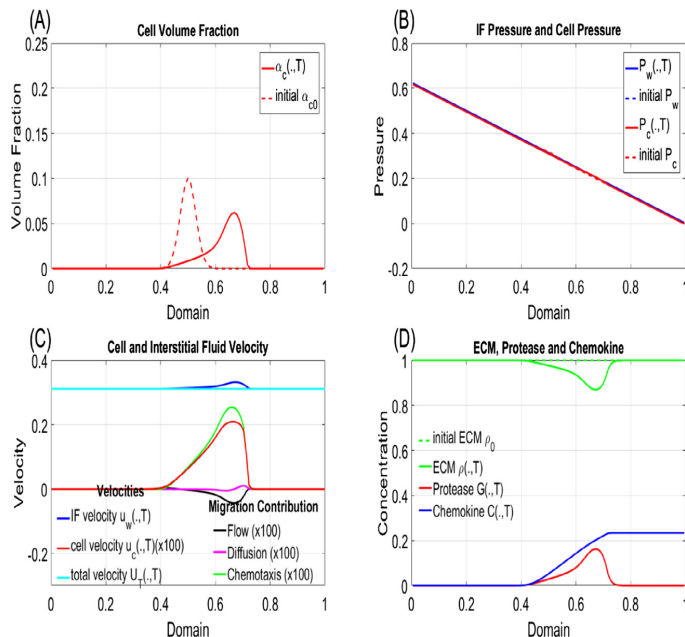
Fig. 4. The case with low cell volume fraction and slow fluid flow ($u_w \approx 0.3\,\mu m/s$) with $r_{cw} = 0.25$. The autologous chemotaxis and mechanotransductive machinery are now both mobilized. (A) Autologous chemotaxis dominates and gives rise to a pronounced downstream migration effect. (B) The IFP pressure gradient is a result of the boundary pressure which is set according to (38). (C) The dominating cell velocity component is represented by $u_{c3} = -\frac{\hat{h}}{\alpha_c} \Lambda(C)_x$ (chemotaxis) which is dictated by the positive downstream chemokine gradient C_x seen in panel (D). Note, however, the upstream cell velocity component $u_{c1} = U_T \frac{\hat{f}_c}{\alpha_c}$ (flow) that is present. In light of the plots in Fig. 2 (top, left), reducing r_{cw} would make the upstream migration more effective through the cell fractional flow function $\hat{f}_c$, increasing it would make it less efficient. (D) The chemokine gradient skewed by the fluid flow in the downstream direction is clearly seen.

that the low density case can produce a more efficient chemo-tactic driven migration then the high density case (Polacheck et al., 2011).

- The expression for the cell velocity component $u_{c1} = U_T\left[\frac{\hat{f}_c(\alpha_c)}{\alpha_c}\right]$ caused by fluid-generated stress, reflects a linear increase with total velocity U_T, which in turn is governed essentially by IF flow velocity u_w. This is consistent with the experimental observations in Polacheck et al. (2011, 2014) which state that at higher flow rates, the asymmetry on cell-matrix adhesions is higher, thus enhancing upstream migration. However, simulations reveal that the linear dependence on U_T gives rise to an upstream migration that is too dominating in some cases. This suggests that we should choose parameters involved in the cell-fluid interaction term $\hat{\zeta}$ such that we can make the impact from $\hat{f}_c(\alpha_c)$ slightly milder. The parameter r_{cw} characterizes how efficient the mechano-transduction machinery can transform the stimuli from the cell-fluid drag force term into an upstream migration effect through the fractional flow function $\hat{f}_c(\alpha_c)$, as illustrated in Fig. 2 (top). In the simulation cases we shall vary r_{cw} in the range $[0.1, 0.6]$.

4.1. Example A: Low cell volume fraction given by (36)

4.1.1. No IF flow
In Fig. 3 we show the cell migration (A) together with the corresponding cell pressure P_c and IF pressure P_w (B), cell velocity components u_{c1}, u_{c2}, u_{c3} and total cell velocity $u_c = u_{c1} + u_{c2} + u_{c3}$ and IF velocity u_w (C), as well as the distribution of protease G, chemokine C, and ECM ρ (D). Note that the cell velocity components have been multiplied by 100 in order to allow visualization in the same figure as IF velocity u_w. The balanced and modest downstream and upstream migration is confirmed by the plot of u_c-components showing a symmetric, unbiased behavior. Computed result is consistent with the "control" points of the graph of Fig. 1B.

4.1.2. Slow IF flow
Next, in Fig. 4 all parameters are set to be the same as in the previous case with the exception that we impose a pressure gradient as given by (38). As a result, the IF flow now generates a positive gradient in the chemokine concentration on the downstream side of the cells which results in a corresponding autologous chemotaxis driven migration in the direction of the fluid flow represented by $u_{c3} = -\frac{h}{\alpha_c}\Lambda(C)_x$. However, there is also a mobilization of the upstream migration mechanism seen by the cell velocity component $u_{c1} = U_T\frac{\hat{f}_c}{\alpha_c}$, although its impact is weak on the total cell migration. Computed result is consistent with the "square" points of the graph of Fig. 1B reflecting high dominance of downstream migration for the case with low IF velocity around 0.3 μm/s.

4.1.3. Fast IF flow
In Fig. 5 we increase the pressure gradient to obtain a high IF rate, as described by (39). The main effect is that the upstream migration component $u_{c1} = U_T\frac{\hat{f}_c}{\alpha_c}$ now becomes strong enough to clearly reduce the dominant downstream migration seen in Fig. 4. We have set $r_{cw} = 0.4$ in this example (instead of $r_{cw} = 0.25$), which will slightly modify $\hat{f}_c$ by reducing the decreasing trend, see plots in Fig. 2 (top, left), to avoid that the upstream migration becomes too strong. Note from the zoomed version of
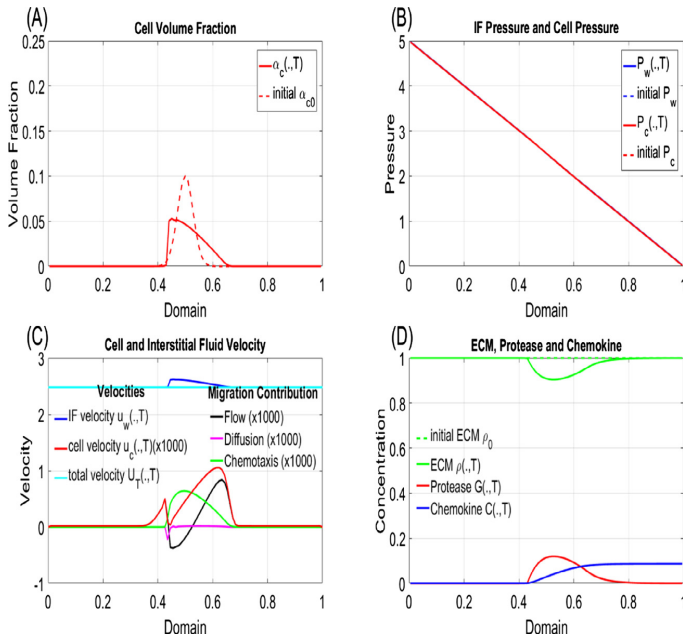
Fig. 5. Low cell volume fraction and fast fluid flow ($u_w \approx 2.5$ μm/s) with $r_{cw} = 0.4$. (A) The almost 10 times higher velocity U_T (compared to previous case) gives rise to formation of an upstream front and a reduced downstream migration effect. (B) The high IFP pressure gradient is a result of the boundary pressure condition (39). (C) The chemotaxis-driven component u_{c3} (green) is lower as compared to the previous case whereas the upstream migration mechanism through $u_{c1} = U_T\frac{\hat{f}_c}{\alpha_c}$ has been mobilized to a larger extent. Note that u_{c1} (Flow) becomes positive for small α_c at the left and right margin of the cell aggregate whereas it becomes negative for larger α_c in the central part. This is a consequence of the shape of $\hat{f}_c(\alpha_c)$ seen in Fig. 2 (top, left) for $r_{cw} = 0.4$. (D) The fast flowing fluid reduces the chemokine gradient (compare with Fig. 4) and thereby weakens the autologous chemotaxis effect through $u_{c3} = -\frac{h}{\alpha_c}\Lambda(C)_x$.

Fig. 2 (top, left) that $\hat{f}_c(\alpha_c)$ contains an increasing part for small α_c before it drops and become negative which explains the positive parts of u_{c3} shown in panel (C). Computed result is consistent with the "square" points of the graph of Fig. 1B reflecting dominating downstream migration with high IF velocity approximately equal to 3 µm/s, but clearly less dominating than for the previous case shown in Fig. 4 due to the almost 10-fold increase in U_T and thereby a strongly amplified upstream migration effect.

4.1.4. Blocking of CCR7: Slow IF flow

In Fig. 6 we are back to the same situation (and same parameter choice) as in Fig. 4, however, we block the autologous chemotaxis by setting $\xi_1 = 0$ to mimic the blocking of the CCR7 receptor in the experiments in Polacheck et al. (2011). Consequently, the autologous chemotaxis effect is abolished which results in a dominating upstream migration. Hence, computed result is consistent with the "square" points of the graph of Fig. 1B reflecting a sudden shift from a strong downstream dominance to a clear upstream dominance for the case with low IF velocity approximately equal to 0.3 µm/s.

4.1.5. Blocking of CCR7: Fast IF flow

In Fig. 7 we consider the same situation (and same parameter choice) as in Fig. 5, however, again we nullify the autologous chemotaxis effect by setting $\xi_1 = 0$. It is observed that this results in a strong migration against fluid flow, in particular on the upstream side of the aggregate. In fact, the cell migration is now largely dominated by the advective part of $(25)_1$ given by

$$\alpha_{ct} + (U_T \hat{f}_c(\alpha_c))_x = 0, \qquad (40)$$

where the relevant curve of $\hat{f}_c(\alpha_c)$ is shown in Fig. 2 (top, left), see the curve corresponding to $r_{cw} = 0.25$. It is known that the solution of this conservation law produces a "shock" wave (i.e. an accumulation of cells moving with the same speed) at the left hand side of the cell aggregate whereas a "rarefaction" wave solution is formed on the right hand side of the cell cluster where the speed of the cancer cells is decreasing with lower α_c (LeVeque, 2002). This is exactly what is shown in Fig. 7 (top, left). This computed result fits well with the "square" points of the graph of Fig. 1B for the case with high IF velocity approximately equal to 3 µm/s which reflects a much stronger upstream dominance compared to the case with low velocity 0.3 µm/s.

4.2. Example B: High cell volume fraction given by (37)

In the following we set $r_c = 0.1$ and also reduce ξ_1 by a factor 5.

4.2.1. No IF flow

This case shows behavior similar to what is shown in Fig. 3 (figures not included).

4.2.2. Slow IF flow

Next, in Fig. 8 we impose a pressure gradient as prescribed by (38). The upstream migration now has a more pronounced role and gives rise to a slightly dominating upstream migration. We may compare with the low cell volume fraction situation in Fig. 4. The essential difference between that example and the one shown in Fig. 8, is the initial cell volume fraction. Looking at the shape of the function $\hat{f}_c$ shown in Fig. 2 (top, right) we see that the upstream migration automatically becomes stronger for the
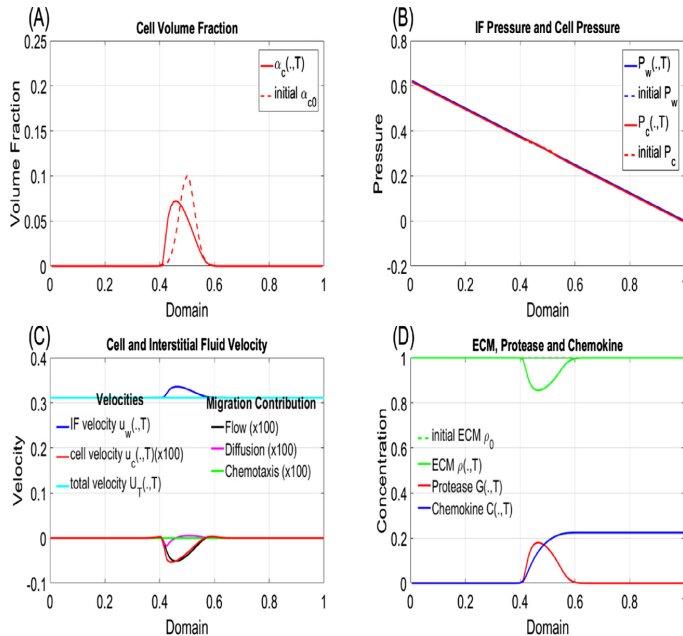
Fig. 6. The figures show what happens when we block CCR7 and thereby nullifies autologous chemotaxis by setting $\xi_1 = 0$ in (5) for the case with slow fluid velocity ($u_w \approx 0.3$ µm/s) shown in Fig. 4. Consistent with that example we use $r_{cw} = 0.25$. (A) The downstream migration comes to a halt and only an upstream migration takes place. (B) Pressure is as before for the case with slow fluid velocity. (C) The u_{c3} (chemotaxis) component is zero in the absence of the autologous chemotaxis mechanism via CCR7 receptors and the u_{c1} (flow) component takes over resulting in a dominating upstream effect. (D) Chemokine and protease distributions are essentially as before for the case with slow fluid velocity.
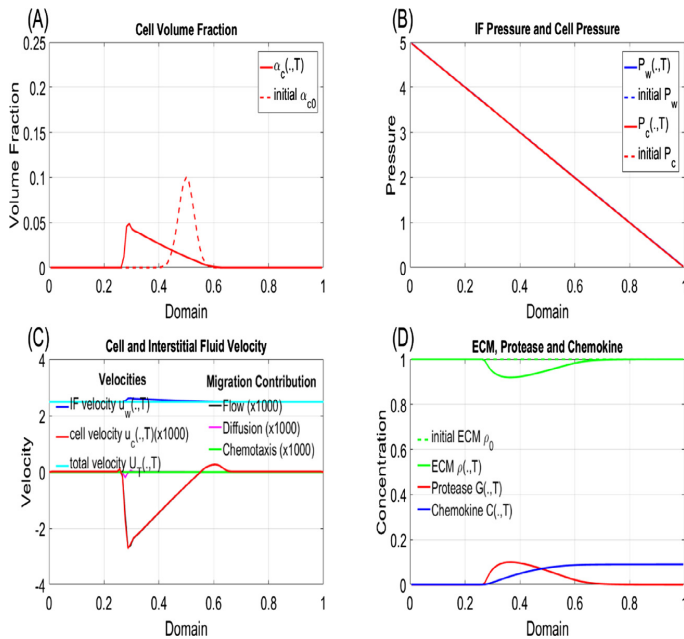
Fig. 7. Blocking of CCR7 with high fluid velocity ($u_w \approx 3\ \mu\text{m/s}$) and $r_{cw} = 0.25$. (A) The cell behavior is strongly dominated by the upstream migration effect. (B) The high IFP pressure gradient is a result of the boundary pressure condition (39). (C) The upstream migration mechanism is the same as for the previous example through the cell velocity component $u_{c1} = U_T \frac{f_c}{\alpha_c}$. However, a 10 times larger total velocity U_T, will strongly increase the effect of u_{c1}. Note that $u_{c3} = 0$ reflecting the blocking of CCR7. (D) The gradient in chemokine C is smaller due to the high fluid velocity.
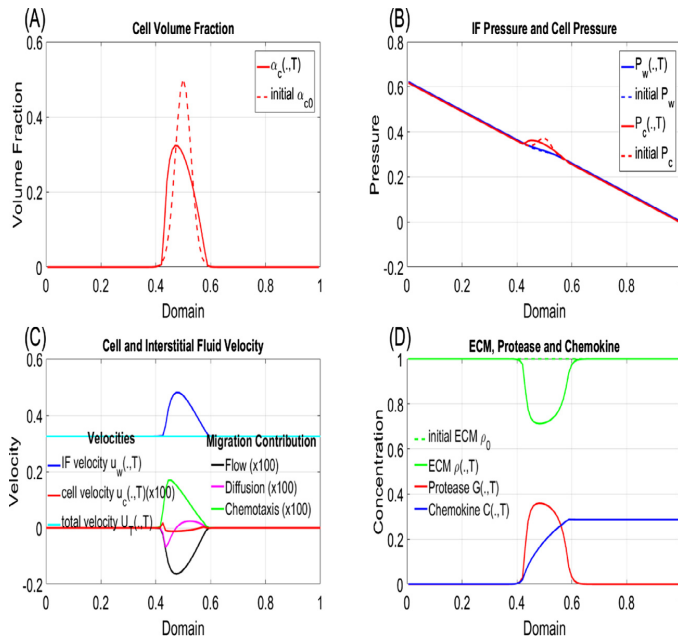
Fig. 8. The high cell volume fraction case with slow fluid flow ($u_w \approx 0.3\ \mu\text{m/s}$) and where we use $r_{cw} = 0.1$. (A) The cell volume fraction reflects a combination of downstream and upstream migration with a weak upstream dominance. (B) The difference between IFP P_w and cell pressure P_c represented by $\Delta P(\alpha_c)$ is now more pronounced due to the fact that α_c takes larger values in the central part of the cell aggregate. (C) Both the upstream migration represented by $u_{c1} = U_T \frac{f_c}{\alpha_c}$ and the downstream cell velocity component $u_{c3} = -\frac{h}{\alpha_c} \Lambda(C)_x$ give strong contributions and reflect the competition between the two different migration mechanisms. (D) The chemokine gradient is skewed in flow direction as before.
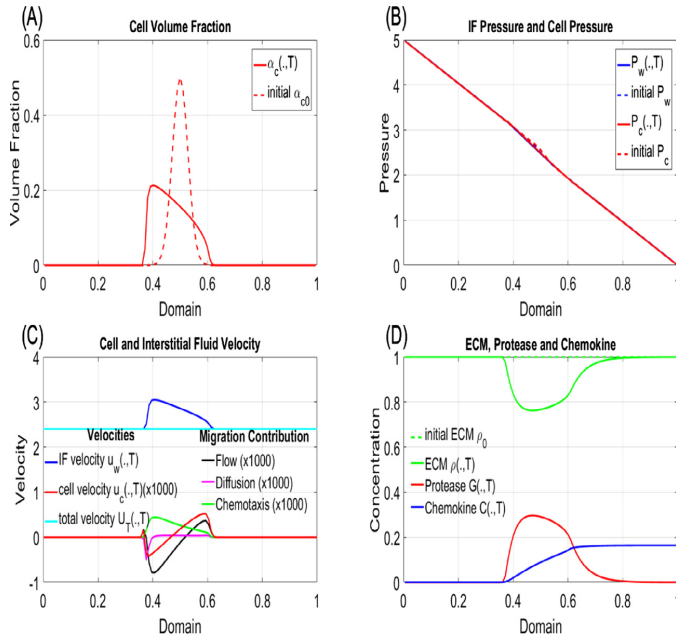
Fig. 9. This case is a continuation of the previous example. We only increase the pressure gradient to generate a higher IF velocity ($U_T \approx 2.5$ μm/s) with $r_{cw} = 0.6$. (A) The upstream cell migration is now much more dominating, in particular, on the upstream side of the cell aggregate. (B) Pressure distribution corresponding to the high fluid velocity case. (C) The upstream velocity $u_{c1} = U_T \frac{L_c}{\alpha_c}$ (flow) experiences a strong impact from the high total velocity term U_T. This explains the formation of the upstream moving front on the left side of the cell cluster. (D) The fast flowing fluid also reduces the chemokine gradient (compared to the previous example) and thereby reduces the autologous chemotaxis effect, as reflected by u_{c3} (chemotaxis) in panel (C).
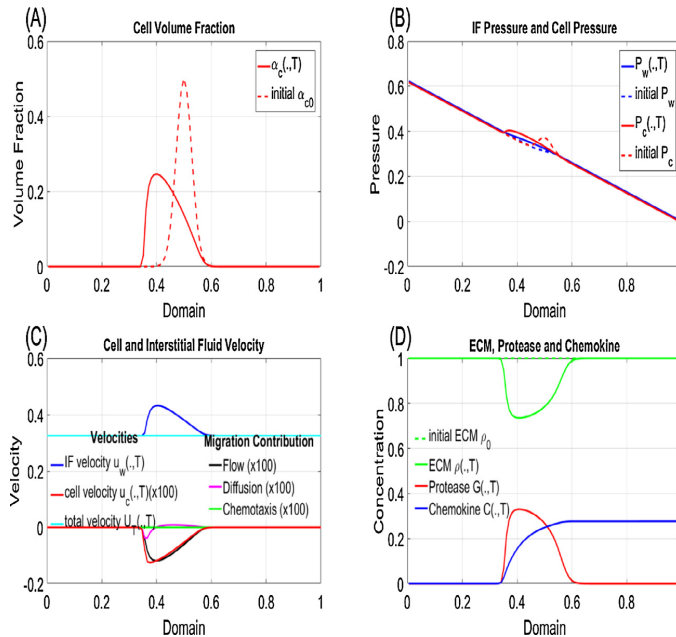
Fig. 10. We consider the same case as in Fig. 8, i.e., slow fluid velocity ($u_w \approx 0.3$ μm/s) and high cell volume fraction with $r_{cw} = 0.1$. However, we account for blocking of CCR7 by setting $\xi_1 = 0$. (A) The upstream migration completely dominates when CCR7 is blocked. (B) Pressure behavior as before. (C) The chemotaxis driven velocity component u_{c3} (chemotaxis) vanishes thereby allowing the upstream-driven component u_{c1} (flow) to dominate completely which in turn results in the upstream front seen in panel (A). (D) Chemokine and protease distribution are as before for similar flow regimes.

high cell volume fraction case due to the nonlinear decreasing form (concave). This explains why u_{c1} is stronger in Fig. 8 (panel C) as compared to the corresponding figure in Fig. 4. Computed result is consistent with the "circle" points of the graph of Fig. 1B for the high cell density showing a slight upstream dominated cell migration with fluid flow ≈ 0.3 μm/s.

4.2.3. Fast IF flow

In Fig. 9 we increase the pressure gradient to give a high IF velocity as prescribed by (39). This results in a largely dominated upstream migration due to the approximate 10 times increase in the total velocity U_T, which in turn affects the cell velocity component $u_{c1} = U_T \frac{\hat{f}_c}{\alpha_c}$. Computed result is consistent with the "circle" points of the graph of Fig. 1B which shows a clearly dominated upstream cell migration for the case with fluid flow ≈ 3 μm/s.

4.2.4. Blocking of CCR7: Slow IF flow

In Fig. 10 we have the same situation (same parameter choice) as in Fig. 8, however, we block the autologous chemotaxis by setting $\xi_1 = 0$. The main effect is a much more dominating upstream migration as compared to the results in Fig. 8, which involves a competition of the downstream and upstream migration mechanism. This is consistent with the "circle" points of the graph of Fig. 1B which shows a clearly dominated upstream cell migration for the case with fluid flow ≈ 0.3 μm/s and blocking of CCR7.

4.2.5. Blocking of CCR7: Fast IF flow

We consider the same situation as in Fig. 9, however, again we nullify the autologous chemotaxis effect. This results in a stronger upstream migration on the left hand side of the cell cluster compared with the previous case (results are not shown). This is also what the graph of Fig. 1B shows for the case with high fluid flow ≈ 3 μm/s and blocking of CCR7.

5. Discussion

We have demonstrated that the multiphase modeling approach is rich enough to include a representation of both the autologous chemotactic driven (CCR7-dependent pathway) downstream migration as well as a second CCR7-independent pathway that stimulates cells to migrate against the flow (Polacheck et al., 2011, 2014). In particular, we have demonstrated that this last non-chemical migration mechanism can be explained by a proper balance between cell-ECM, fluid-ECM, and cell-fluid interaction forces which is manifested in the cell velocity component $u_{c1} = U_T \frac{\hat{f}_c}{\alpha_c}$. More precisely, we have proposed correlations for these interactions, as expressed by (19), which are based on general fluid mechanical principles (largely borrowed from experience with multiphase water–oil–gas flow i porous media (Evje, 2017; Qiao et al., 2018)). However, a novel aspect here is that we must expand the range of the parameter I involved in the cell-fluid drag force term $\hat{\zeta}$ to take negative values in order to generate upstream migration. After all this may not be unexpected since the cancer cells is a "smart" fluid that can respond to indirect mechanical stimulation via the matrix and integrins (Shieh and Swartz, 2011). Some similarities and differences between the model predictions and the reported experimental behavior in Polacheck et al. (2011) and proposed interpretations are:

- In Polacheck et al. (2011) the cell velocity is estimated to be in the range of 0.1 μm/min $= 0.0017$ μm/s. The dimensionless velocity shown in the numerical examples generated by the model are typically in the range 0.001–0.005 (i.e., μm/s) which fits well with the above estimate.
- In Polacheck et al. (2011) it is suggested, based on the observation that blocking of CCR7 gave rise to dominating upstream migration of the same strength for both the low and high cell density, that this non-chemical migration mechanism is *independent* of cell density. Note that the mathematical model, armed with the correlations (19), suggests that the upstream migration through $\hat{f}_c(\alpha_c)$ *depends* on the cell volume fraction. Independence of cell density α_c amounts to a choice of parameters where the decreasing, negative part of the fractional flow function $\hat{f}_c(\alpha_c)$ shown in Fig. 2 (top) becomes linear.
- The mathematical model suggests that the upstream migration mechanism represented by $U_{c1} = U_T \hat{f}_c(\alpha_c)$ is somewhat sophisticated:
  (i) A higher cell volume fraction typically gives rise to a higher interstitial cell velocity. This is reflected by the $\hat{f}_c(\alpha_c)$ function which is inclined to be rather flat for low cell volume fractions and then decreases more rapidly for higher α_c.
  (ii) This upstream migration is not the same on the upstream side of the cell aggregate as the downstream. This is due to the fact that $\hat{f}_c(\alpha_c)$ is a *nonlinear* function. On the upstream side, migration against the flow tends to form a front (a shock solution in mathematical terms (LeVeque, 2002; Qiao et al., 2018)) of a high cell volume fraction that move with a rather uniform velocity. On the downstream side of the cell aggregate, there is a "thinning out" effect (formation of a rarefaction wave in mathematical terms (LeVeque, 2002; Qiao et al., 2018)) where the upstream cell velocity rapidly decreases with lower α_c. This was illustrated in Figs. 7 and 10. We may understand this difference as a natural consequence of the fact that on the downstream side cells are more or less shielded from fluid flow stress by neighbor cells positioned on upstream side. A parallel to this situation is described in Pedersen et al. (2010), Shieh and Swartz (2011), and Wiig and Swartz (2012), where the presence of extracellular matrix fibers surrounding the cancer cells, is suggested to shield a cell from stress from the flowing IF.

In summary, a multiphase mathematical model has been presented which describes directed cellular migration by both an CCR7-dependent downstream mechanism and an CCR7-independent mechanism that stimulates cells to migrate upstream. This allows the model to predict the directional bias in migration when these two competing mechanisms are active under different circumstances.

Conflict of interest

We hereby declare that the authors have no conflicts of interest related to this manuscript.

Appendix A. Supplementary material

Supplementary data associated with this article can be found, in the online version, at https://doi.org/10.1016/j.jbiomech.2018.09.011.

References

Byrne, H.M., Owen, M.R., 2004. A new interpretation of the Keller-Segel model based on multiphase modelling. J. Math. Biol. 49, 604–626.

Drew, D.A., Passman, S.L., 1999. Theory of Multicomponent Fluids. Springer.

Evje, S., 2017. An integrative multiphase model for cancer cell migration under influence of physical cues from the microenvironment. Chem. Eng. Sci. 165, 240–259.

Evje, S., Wen, H.Y., 2018. A Stokes two-fluid model for cell migration that can account for physical cues in the microenvironment. SIAM J. Math. Anal. 50 (1), 86–118.

Haessler, U., Teo, J.C.M., Foretay, D., Renaud, P., Swartz, M.A., 2012. Migration dynamics of breast cancer cells in a tunable 3D interstitial flow chamber. Integrative Biol. 4, 401–409.

LeVeque, R., 2002. Finite Volume Methods for Hyperbolic Problems. Cambridge Texts in Applied Mathematics. Cambridge University Press.

Pedersen, J.A., Lichter, S., Swartz, M.A., 2010. Cells in 3D matrices under interstitial flow: effects of extracellular matrix alignment on cell shear stress and drag forces. J. Biomech. 43, 900–905.

Polacheck, W.J., Charest, J.L., Kamm, R.D., 2011. Interstitial flow influences direction of tumor cell migration through competing mechanisms. PNAS 108, 11115–11120.

Polacheck, W.J., German, A.E., Mammoto, A.E., Ingber, D.E., Kamm, R.D., 2014. Mechanotransduction of fluid stresses governs 3D cell migration. PNAS 111, 2447–2452.

Qiao, Y.Y., Andersen, P.O., Evje, S., Standnes, D.S., 2018. A mixture theory approach to model co- and counter-current two-phase flow in porous media accounting for viscous coupling. Adv. Wat. Res. 112, 170–188.

Rajagopal, K.R., 2007. On a hierarchy of approximate models for flows of incompressible fluids through porous solids. Math. Mod. Met. Appl. Sci. 17, 215–252.

Shieh, A.C., Rozansky, H.A., Hinz, B., Swartz, M.A., 2011. Tumor cell invasion is promoted by interstitial flow-induced matrix priming by stromal fibroblasts. Cancer Res. 71 (3).

Shieh, A.C., Swartz, M.A., 2011. Regulation of tumor invasion by interstitial fluid flow. Phys. Biol., 8.

Shields, J.D., Fleury, M.E., Yong, C., Tomei, A.A., Gwendalyn, J.R., Swartz, M.A., 2007. Autologous chemotaxis as a mechanism of tumor cell homing to lymphatics via interstitial flow and autocrine CCR7 signaling. Cancer Cell 11, 526–538.

Swartz, M.A., Fleury, M.E., 2007. Interstitial flow and its effects in soft tissues. Annu. Rev. Biomed. Eng. 9, 229–256.

Standnes, D.C., Evje, S., Andersen, P.O., 2017. A novel relative permeability model based on mixture theory approach accounting for solid-fluid and fluid-fluid interactions. Tran. Por. Med. 119, 707–738.

Waldeland, J.O., Evje, S., 2018. A multiphase model for exploring cancer cell migration driven by autologous chemotaxis. Chem. Eng. Sci. 191, 268–287.

Wiig, H., Swartz, M.A., 2012. Interstitial fluid and lymph formation and transport: physiological regulation and roles in inflammation and cancer. Physiol. Rev. 92, 1005–1060.

Wu, Y.S., 2016. Multiphase Fluid Flow in Porous and Fractured Reservoirs. Elsevier.

III

Paper III

How tumor cells can make use of interstitial fluid flow in a strategy for metastasis

By:
Evje, Steinar
Waldeland, Jahn Otto

Paper IV

Enhanced cancer cell invasion caused by fibroblasts when fluid flow is present

By:
Urdal, Jone
Waldeland, Jahn Otto
Evje, Steinar

Paper V

Collective tumor cell migration in the presence of fibroblasts

By:
Waldeland, Jahn Otto
Polacheck, William
Evje, Steinar

Collective tumor cell migration in the presence of fibroblasts

Jahn O. Waldeland [a], William J. Polacheck [b], Steinar Evje [a],*

[a] University of Stavanger, Faculty of Science and Technology, 4068 Stavanger, Norway
[b] University of North Carolina at Chapel Hill and North Carolina State University, Joint Department of Biomedical Engineering, Chapel Hill, NC 27599, USA

ABSTRACT

In this work we investigate fibroblast-enhanced tumor cell migration in an idealized tumor setting through a computational model based on a multiphase approach consisting of three phases, namely tumor cells, fibroblasts and interstitial fluid. The interaction between fibroblasts and tumor cells has previously been investigated through this model (Urdal et al., 2019) to comply with reported *in vitro* experimental results (Shieh et al., 2011). Using the information gained from *in vitro* single-cell behavior, what will the effect of fibroblast-enhanced tumor cell migration be in a tumor setting? In particular, how will tumor cells migrate in a heterogeneous tumor environment compared to controlled *in vitro* microfluidic-based experiments? From what we know about the behavior of a tumor, is that collective invasion into adjacent tissue is frequently observed. Here, we want to elucidate how fibroblasts may guide tumor cells towards draining lymphatics to which tumor cells may subsequently intravasate and thus spread to other parts of the body. Fibroblasts can act as leader cells, where they create tracks within the extracellular matrix (ECM) by matrix remodeling and contraction. In addition, a heterotypic mechanical adhesion between fibroblasts and tumor cells also assist the fibroblasts to act as leader cells. Our simulation results show how the interaction between the two cell types yields collective migration of tumor cells outwards from the tumor where fibroblasts dictate the direction of migration. The model also describes how this well-orchestrated invasive behavior is the result of a proper combination of different interaction forces between cell-ECM, fibroblast-ECM, fluid-ECM and cell-fibroblast.

© 2019 The Author(s). Published by Elsevier Ltd. This is an open access article under the CC BY license (http://creativecommons.org/licenses/by/4.0/).

1. Introduction

1.1. Background

One of the distinct properties of cancer is the ability of the cancer cells to spread by invading the adjacent tissue, often followed by local or distant metastasis. Cell migration is often referred to as the movement of individual cells. However, most invasive solid tumors frequently exhibit collective invasion, where cohesive cohorts of cells invade the adjacent stroma while maintaining cell-cell contacts (Friedl et al., 2012). The morphologically organization of cohesive cohorts invading the stroma can vary considerably.

The invading cell groups may range from strands of just a few cells in diameter, to wide masses of cells. The size and shape of a collective invasion structure is probably determined by specific combinations of cell-cell adhesion, cell-matrix adhesion and proteolysis. Therefore, the organization of the front of the collective cells can vary, likely as a combined function of proteolysis, protrusion

and expansion, and the type of tissue encountered (Gray et al., 2010). Cells located at the front of the invading group are called leader cells. These cells play a special role during migration by sensing the microenvironment and dictating the speed and the direction of the entire cell cluster (Mayor and Etienne-Manneville, 2016). Cancer-associated fibroblasts (CAFs) can act similarly as the front of the collectively invading group, where cancer cells retain their epithelial traits. The CAFs would then lead the cells within tracks in the ECM generated by the fibroblasts (Gaggioli et al., 2007).

While epithelial-to-mesenchymal transition (EMT), a cell-biological program giving cancer cells multiple malignant traits such as loss of epithelial properties and acquisition of certain mesenchymal features in their stead, is widely accepted as an important mode of invasion, its precise roles in primary tumor behavior is not fully understood. As most primary tumor cells are involved in collective migration rather than the dispersal of individual carcinoma cells, this appears to conflict with the behavior of cells that has gone through EMT and lost cell-cell contacts. Therefore, an EMT program might not be necessary for carcinoma cell dissemination. However, EMT and collective tumor cell migration are perhaps not mutually exclusive (Lambert et al., 2018).

1.2. Purpose

This work is based on the computer models introduced and explored in Waldeland and Evje (2018) and Urdal et al. (2019) but used in a more realistic tumor setting. The model uses a multiphase approach describing three phases: tumor cells, interstitial fluid and fibroblasts. We will try to exemplify how tumor cells can invade to adjacent tissue without the need to undergo EMT by using fibroblasts as leader cells. Similar to Urdal et al. (2019), we allow direct mechanical interaction/coupling between fibroblasts and tumor cells motivated by the results of Labernadie et al. (2017). In addition, the moving fibroblasts may remodel the ECM, causing tumor cells to migrate in the tracks of ECM created by the fibroblasts as observed in Shieh et al. (2011), Gaggioli et al. (2007), Schwager et al. (2019).

In Urdal et al. (2019) the goal was to replicate the experimental results in Shieh et al. (2011) through a multiphase approach with regards to tumor cell and fibroblast migration. This was performed in a 1D setting where we, similar to the *in vitro* experimental setting, impose a global pressure gradient to achieve a constant interstitial fluid flow. This has yielded valuable information with regards to how the different parameters in our model need to be set in order to attain realistic fluid flow and cellular behavior. In this work we apply the same model in a 2D domain comprised of a tumor with a vascular system. Outside of the primary tumor we have placed fibroblast cells and draining lymphatics. This allows us to simulate the observed migration mechanisms *in vitro*, autologous chemotaxis and fibroblast enhanced tumor cell migration, simultaneously in a tumor environment. As opposed to the experimental setting, where both the fluid flow field and cell migration is essentially one-dimensional, a realistic tumor setting is highly heterogeneous. IF now originates from the vascular system and flows through the tissue to the draining lymphatics, creating a heterogeneous flow field which impacts the concentration distribution of chemical components. We want to investigate how fibroblast-enhanced tumor cell migration may occur in an envisioned tumor setting. In particular, what type of invasion does the inclusion and presence of fibroblasts impart on the tumor cells. In addition, will the fibroblasts act as leader cells to guide tumor cells towards lymphatics?

Variable	Description
$\alpha_c, \alpha_f, \alpha_w$	volume fraction cell, fibroblast, fluid
S_c, S_f	cell growth/death
$\mathbf{u}_c, \mathbf{u}_f, \mathbf{u}_w$	cell, fibroblast, fluid velocity
ρ, G, C, H	ECM, protease, chemokine, TGF
D_G, D_C, D_H	diffusion coefficients
ρ_M, G_M, C_M, H_M	maximal concentrations
P_w	IF pressure
ΔP_{cw}	cell-cell stress
Λ_C, Λ_H	chemokine, TGF chemotaxis stress
$\hat{\lambda}_c, \hat{\lambda}_f, \hat{\lambda}_T$	cell, fibroblast and total mobility
T_v, T_l	conductivity vascular/lymphatic wall
$\tilde{P}_v^*, \tilde{P}_l^*$	effective vascular/lymphatic pressure
$Q_v = T_v\left(\tilde{P}_v^* - P_w\right)$	produced fluid from vascular system
$Q_l = T_l\left(P_w - \tilde{P}_l^*\right)$	lymphatic drainage
M_C, M_H	percentage absorption at lymphatics
$\lambda_{21}, \lambda_{22}, \lambda_{23}, \lambda_{24}$	production/consumption ECM
$\lambda_{31}, \lambda_{32}, \lambda_{33}$	production/consumption protease
$\lambda_{41}, \lambda_{42}, \lambda_{43}, \lambda_{44}$	production/consumption chemokine
$\lambda_{51}, \lambda_{52}, \lambda_{53}, \lambda_{54}, \lambda_{55}$	production/consumption TGF
v_G, v_C, v_H	exponents of decay rate terms

2. Compact three-phase fibroblast-cell-fluid model

The model takes the following compact form (see Appendix A for details).

$$
\begin{aligned}
&\alpha_{ct} + \nabla \cdot (\alpha_c \mathbf{u}_c) = S_c \\
&\alpha_{ft} + \nabla \cdot (\alpha_f \mathbf{u}_f) = S_f, \qquad \alpha_c + \alpha_f + \alpha_w = 1 \\
&\rho_t = -\lambda_{21}G\rho + \rho\left(\lambda_{22} - \lambda_{23}\alpha_c - \lambda_{24}\left(\frac{\rho}{\rho_M}\right)\right) \\
&G_t = \nabla \cdot (D_G\nabla G) - \nabla \cdot (\mathbf{u}_w G) - \lambda_{31}G \\
&\quad + (\alpha_c + \alpha_f)\left(\lambda_{32} - \lambda_{33}\left(\frac{G}{G_M}\right)^{v_G}\right) \\
&C_t = \nabla \cdot (D_C\nabla C) - \nabla \cdot (\mathbf{u}_w C) - CM_C Q_l \\
&\quad + G\rho\left(\lambda_{41} - \lambda_{42}\left(\frac{C}{C_M}\right)^2 - \lambda_{43}\left(\frac{C}{C_M}\right)^{v_C}\right) - \lambda_{44}\alpha_c C \\
&H_t = \nabla \cdot (D_H\nabla H) - \nabla \cdot (\mathbf{u}_w H) - HM_H Q_l - \lambda_{51}H \\
&\quad + \alpha_f\left(\lambda_{52} - \lambda_{53}\left(\frac{H}{H_M}\right)^2 - \lambda_{54}\left(\frac{H}{H_M}\right)^{v_H}\right) - \lambda_{55}\alpha_f H.
\end{aligned}
\tag{1}
$$

The chemical components G, C and H are described by transport-reaction equations and are advected by the IF velocity $\mathbf{u}_w$. The explicit expressions for the interstitial velocities are as follows:

$$
\begin{aligned}
\mathbf{u}_c &= \frac{\hat{f}_c}{\alpha_c}\mathbf{U}_T - \frac{\hat{h}_1+\hat{h}_2}{\alpha_c}\nabla(\Delta P_{cw} + \Lambda_C) + \frac{\hat{h}_2}{\alpha_c}\nabla\Lambda_H \\
\mathbf{u}_f &= \frac{\hat{f}_f}{\alpha_f}\mathbf{U}_T + \frac{\hat{h}_2}{\alpha_f}\nabla(\Delta P_{cw} + \Lambda_C) - \frac{\hat{h}_2+\hat{h}_3}{\alpha_f}\nabla\Lambda_H \\
\mathbf{u}_w &= \frac{\hat{f}_w}{\alpha_w}\mathbf{U}_T + \frac{\hat{h}_1}{\alpha_w}\nabla(\Delta P_{cw} + \Lambda_C) + \frac{\hat{h}_3}{\alpha_w}\nabla\Lambda_H.
\end{aligned}
\tag{2}
$$

Note that each phase velocity in (2) is governed by four different terms, representing contributions to the overall phase velocity from separate mechanisms. Functional forms of $\hat{f}_c, \hat{f}_f, \hat{f}_w$ and $\hat{h}_1, \hat{h}_2, \hat{h}_3$ and $\Delta P_{cw}, \Lambda_C, \Lambda_H$ are described by (28), (29), (15), (16), respectively, in Appendix A. In order to find $\mathbf{U}_T$, we first solve an elliptic equation for P_w which takes the form

$$
\begin{aligned}
\nabla \cdot \left(\hat{\lambda}_T\nabla P_w\right) &= -T_v\left(\tilde{P}_v^* - P_w\right) + T_l\left(P_w - \tilde{P}_l^*\right) \\
&\quad - \nabla \cdot \left(\hat{\lambda}_c\nabla(\Delta P_{cw} + \Lambda_C(C))\right) - \nabla \cdot \left(\hat{\lambda}_f\nabla\Lambda_H\right) \\
P_w|_{\partial\Omega} &= P_B^*.
\end{aligned}
\tag{3}
$$

The explicit expressions for $\hat{\lambda}_c$ and $\hat{\lambda}_T$ are given by (30)$_{1,4}$ in Appendix A. We can use the calculated IF pressure P_w to find the total velocity $\mathbf{U}_T$

$$
\mathbf{U}_T = -\hat{\lambda}_T\nabla P_w - \hat{\lambda}_c\nabla(\Delta P_{cw} + \Lambda_C) - \hat{\lambda}_f\nabla\Lambda_H,
\tag{4}
$$

where $\hat{\lambda}_f$ is given by (30)$_2$. $\mathbf{U}_T$ is required in the calculation of the interstitial velocities $\mathbf{u}_c, \mathbf{u}_f$ and $\mathbf{u}_w$ in (2). The model 1- is subject to the boundary conditions

$$
\frac{\partial}{\partial v}G|_{\partial\Omega} = 0, \quad \frac{\partial}{\partial v}C|_{\partial\Omega} = 0, \quad \frac{\partial}{\partial v}H|_{\partial\Omega} = 0.
\tag{5}
$$

Remark 1. Looking at the cell velocity $\mathbf{u}_c$ given by (2)$_1$, we see that it consists of four different terms:

1. fluid generated stress, $\frac{\hat{f}_c}{\alpha_c}\mathbf{U}_T$;
2. diffusion, $-\frac{\hat{h}_1+\hat{h}_2}{\alpha_c}\nabla(\Delta P_{cw}(\alpha_c))$;
3. chemotaxis of **cells** towards increasing concentration gradient of **chemokines**, $-\frac{\hat{h}_1+\hat{h}_2}{\alpha_c}\nabla\Lambda_C(C)$;
4. counter-current effect of **fibroblasts** chemotaxis towards concentration gradient of **TGF**, $\frac{\hat{h}_2}{\alpha_c}\nabla\Lambda_H(H)$.

The first term represents a stress caused by the flowing IF on the cancer cells. This is a co-current transport effect. Cancer cells will to a large extent resist the direct pushing of fluid flow, as reported in Shields et al. (2007), Shieh et al. (2011). The next three terms represent counter-current transport effects. The second term represents migration due to diffusion, i.e., a more or less weak non-directional migration, causing fibroblasts and fluid to be squeezed in the opposite direction to give room for the tumor cells. This effect is also created in the third term as tumor cells chemotax towards positive chemokine gradients. The fourth term represents tumor cells that are pushed in the opposite direction of fibroblasts as fibroblasts chemotax towards positive TGF gradients. Note that $\Lambda_C(C), \Lambda_H(H)$ are decreasing functions.

Remark 2. Regarding the mechanical coupling between cells and fibroblasts, this is expressed through $\hat{\zeta}_{cf}$ in the general momentum balance Eqs. (14)$_{4,5}$. Still focusing on $\mathbf{u}_c$ described by (2)$_1$, this term will have an impact both on $\hat{f}_c$ and $\hat{h}_2$, as is seen from the expressions (28)$_1$ and (29)$_2$. Having that $\hat{\zeta}_{cf} > 0$ we may look at the transport effect through $\hat{h}_2$ which is given by

$$\hat{h}_2(\alpha_c, \alpha_f) = \frac{\hat{\lambda}_c \hat{\lambda}_f}{\hat{\lambda}_T} - \frac{\alpha_c \alpha_f \hat{\zeta}_{cf}}{\hat{\zeta}_c \hat{\zeta}_f + \hat{\zeta}_{cf}(\hat{\zeta}_c + \hat{\zeta}_f)}. \tag{6}$$

If we increase the cell-fibroblast interaction $\hat{\zeta}_{cf}$, $\hat{h}_2$ will eventually become negative (Urdal et al., 2019). This means that there is acceleration of tumor cells through $\frac{\hat{h}_2}{\alpha_c}\nabla\Lambda_H$ of $\mathbf{u}_c$, which essentially is fibroblast migration toward a positive gradient of TGF and felt by the nearby tumor cells that connect to fibroblasts mechanically. In addition, there is a corresponding deceleration of fibroblasts through $-\frac{\hat{h}_2+\hat{h}_3}{\alpha_f}\nabla\Lambda_H$ of $\mathbf{u}_f$ in (2)$_2$.

Remark 3. We include both TGF and tumor cells in our model, yet we have not implemented any direct effect TGF may have on tumor cells. In reality, TGF-β1 regulates a variety of tumor promoting and suppressive effect depending on which stage of development the tumor is in. During the early stages of development TGF acts as a tumor suppressor by inducing cell death and growth arrest. At later stages, TGF switches roles and enhances migration, invasion and survival of tumor cells (Massagué, 2008). However, the mathematical model is developed to comply with the experimental observations of Shieh et al. (2011) where TGF had no direct effect on the cancer cells.

3. Results

3.1. Choice of parameters

Most of the parameters used in this work are the same as in Urdal et al. (2019), Waldeland and Evje (2018). We refer to Table 1 for a precise description. We have performed thorough investigations in a 1D setting with regard to the choice of different parameters where these are set such that the model can capture the IF pressure and velocity behavior as well as the cellular behavior of in vitro 1D experimental results found in Shieh et al. (2011), Shields et al. (2007). In this work we perform 2D simulations in a more realistic tumor setting where the interstitial fluid flow field is created due to leaky blood vessels at the tumor margin and functional lymphatic vessels somewhere within the peritumoral region. This will potentially create a heterogenous IF velocity field. The main objective is to visualize to what extent the enhanced tumor cell behavior reported from in vitro experiments can give rise

Table 1
Model parameters (dimensional).

Parameter	Description	Value	Unit
Reference variables			
T^*	Time	10^4	s
L^*	Length	10^{-2}	m
u^*	Velocity	10^{-6}	m/s
D^*	Diffusion	10^{-8}	m²/s
ρ^*	ECM density	1	kg/m³
G^*	Protease	10^{-4}	kg/m³
C^*	Chemokine	10^{-4}	kg/m³
H^*	TGF	10^{-4}	kg/m³
P^*	Pressure	10^4	Pa
ρ_M	Maximum ECM density	ρ^*	kg/m³
G_M	Maximum protease density	$0.5G^*$	kg/m³
C_M	Maximum chemokine density	$0.3C^*$	kg/m³
H_M	Maximum TGF density	$0.5H^*$	kg/m³
Material constants			
D_G	Diffusion coefficient of protease	$8 \cdot 10^{-12}$	m²/s
D_C	Diffusion coefficient of chemokine	$7 \cdot 10^{-14}$	m²/s
D_H	Diffusion coefficient of TGF	$8 \cdot 10^{-12}$	m²/s
Production/decay rates			
λ_{21}	Degradation of ECM	10	m³/kgs
λ_{22}	Reconstruction of ECM	$1.25 \cdot 10^{-3}$	1/s
λ_{23}	Release of ECM	0	1/s
λ_{24}	Release of ECM	$1.25 \cdot 10^{-3}$	1/s
λ_{31}	Decay of protease	$2.5 \cdot 10^{-3}$	1/s
λ_{32}	Cell production of protease	$2 \cdot 10^{-6}$	kg/m³s
λ_{33}	Logistic term constant (protease)	$2 \cdot 10^{-6}$	kg/m³s
v_G	Exponent in logistic function of protease	1	–
λ_{41}	Proteolytically freed chemokine	$3.2 \cdot 10^{-3}$	m³/kgs
λ_{42}	Logistic term constant (chemokine)	$1.44 \cdot 10^{-4}$	m³/kgs
λ_{43}	Logistic term constant (chemokine)	$3.2 \cdot 10^{-3}$	m³/kgs
λ_{44}	Cell consumption of chemokine	$1 \cdot 10^{-9}$	1/s
v_C	Exponent in logistic function of chemokine	0.2	–
λ_{51}	Decay of TGF	$1 \cdot 10^{-5}$	1/s
λ_{52}	Production of TGF	$8.75 \cdot 10^{-7}$	kg/m³s
λ_{53}	Logistic term constant (TGF)	$5.5 \cdot 10^{-7}$	kg/m³s
λ_{54}	Logistic term constant (TGF)	0	kg/m³s
λ_{55}	Fibroblast consumption of TGF	$2 \cdot 10^{-6}$	1/s
v_H	Exponent in logistic function of TGF	0.2	–
Potential function, chemokine			
ξ_C	Parameter characterizing Λ_C	$8 \cdot 10^4$	m³/kg
Λ_{C0}	Parameter characterizing Λ_C	0	Pa
Λ_{C1}	Parameter characterizing Λ_C	$2.5 \cdot 10^4$	Pa
Potential function, TGF			
ξ_H	Parameter characterizing Λ_H	$1.6 \cdot 10^5$	m³/kg
Λ_{H0}	Parameter characterizing Λ_H	0	Pa
Λ_{H1}	Parameter characterizing Λ_H	$2.5 \cdot 10^4$	Pa
Capillary pressure function			
γ	Parameter characterizing ΔP	10^3	Pa
δ	Parameter characterizing ΔP	0.01	-

to more aggressive tumor cell behavior in this envisioned heterogenoues tumor setting. Hence, this summarizes our method:

1. Train our model using data from experimental results performed in a controlled in vitro setting, as reported in Shieh et al. (2011).
2. Expand the model, using the experience and parameters from step 1, to mimic a real-world tumor in a two-dimensional setting.

3.1.1. Interaction parameters

We have three distinct phases: cancer cells, fibroblasts and interstitial fluid. These three phases interact with ECM (the matrix

structure) and possibly also with one another. The interaction terms are expressed by $\zeta_c, \zeta_w, \zeta_f$ and ζ_{cf}, as reflected by the general momentum balance Eqs. (14)$_{4,5,6}$. The explicit correlations are specified in (17)–(20). The interaction terms between the cellular phases and the fluid phase have been neglected in this work, but is investigated in depth in Waldeland and Evje (2018), Evje and Waldeland (2019), which in turn is motivated by the experimental findings in Polacheck et al. (2011). As far as the correlations in 17–20 is concerned, the purpose of the coefficients $\hat{k}_w, \hat{k}_c$ and $\hat{k}_f$ is to represent dynamic properties of ECM, and is initially set as $\hat{k}_w = \hat{k}_c = \hat{k}_f = 1$. I_w, I_c and I_f are static parameters that reflect the conductivity of the tumor microenvironment.

The process of setting parameters starts with obtaining a reasonable pathological IF fluid flow velocity $\mathbf{u}_w$ and IFP P_w throughout the domain. The interstitial fluid flow is mainly constructed by the hydraulic conductivity of the interstitial space, i.e. the resistance to the fluid flow in porous and fibrous media. A high hydraulic conductivity yields a faster flowing fluid through the interstitial space (Wiig and Swartz, 2012). We have set the conductivity associated with the tumor microenvironment as $I_w^{-1} = \frac{K}{\mu_w} = 5 \cdot 10^{-13}$ m^2/Pa s to achieve interstitial fluid velocity of $\mathbf{u}_w = [0.1 - 0.7]$ μm/s. Then, we can apply the resistance forces ζ_c and ζ_f, seen in (18) and (19), between the cellular phases and ECM to achieve valid behavior of the cells based on expected behavior seen in experiments. The parameters involved in ζ_c and ζ_f in combination with the parameters used to express the chemotactic strength of the cells, see (16), can be considered unique for one type of cell line. Changes to these parameters will allow the tumor cells in the model to be more or less aggressive, more single cell invasion, or collective invasion and so on. Thus by tuning these parameters, we can simulate the effects of fibroblasts on metastatic progression for cancers of different origin, for example to determine whether fibroblasts play a more or less significant role in guiding single cell migration, as observed in fibrosarcoma or glioblastoma, or in guiding collective cell migration as seen in cancers of epithelial origin (Friedl and Wolf, 2003). Furthermore, we also have the ability to vary essential aspects of the tumor microenvironment through the parameter ζ_w given by (17) in combination with the placement and production/absorption rate of the vascular and lymphatic system, i.e., the parameters involved in the expression for Q_v and Q_l given by (21) and (22). These interaction forces are imperative for the behavior of the model, as they largely impact the functions $\hat{f}_c, \hat{f}_f, \hat{f}_w$ and $\hat{h}_1, \hat{h}_2, \hat{h}_3$ as given by (28) and (29), which determine the phase velocities $\mathbf{u}_c, \mathbf{u}_f, \mathbf{u}_w$ in (2). The following values are used as default:

$$
\begin{aligned}
&I_w = \frac{\mu_w}{K} = 2 \cdot 10^{12} \quad \text{Pa s/m}^2 \qquad \hat{k}_w = 1, \qquad r_w = 0.0, \\
&I_c = 2000 I_w \qquad\quad \text{Pa s/m}^2 \qquad \hat{k}_c = 1, \qquad r_c = 0.6, \\
&I_f = 100 I_w \qquad\quad\;\; \text{Pa s/m}^2 \qquad \hat{k}_f = 1, \qquad r_f = 0.6, \\
&I_{cf} = 1000 I_w, \qquad\;\; \text{Pa s/m}^2 \qquad\qquad\qquad r_{cf} = r_{fc} = 0.5.
\end{aligned}
\tag{7}
$$

We have set I_c, how strong cells are anchored to the ECM structure, to be a 2000-fold larger than the fluid-ECM resistance force ($I_c = 2000 I_w$). This is greater than we have operated with before. However, it serves better to illustrate how fibroblasts may enhance tumor cell migration despite the fact that the initial cell-ECM resistance force keeps cancer cells mostly stationary. As fibroblasts are much more mobile than cancer cells, the fibroblast-ECM resistance force is set 100 times larger than fluid-ECM resistance force, i.e. $I_f = 100 I_w$. We have assumed that not all fibroblast directly interact with cancer cells. Thus, the strength of this interaction is set to $I_{cf} = 1000 I_w$ to determine the strength of $\hat{\zeta}_{cf}$ in (20). If we were to set $I_{cf} \rightarrow \infty$, the tumor cells and fibroblasts would act as one phase in the regions where both phases are present.

3.1.2. Vascular and lymphatic flow parameters

The following values are used for parameters related to the vascular flow, Q_v, given by (21) and involved in the continuity equation for the IF (14)$_3$:

$$
T_v = 5 \cdot 10^{-7} \text{ 1/Pa s}, \qquad \widetilde{P}_v^* = 4000 \text{ Pa} \tag{8}
$$

and for lymphatic absorption Q_l in (22) we use

$$
T_l = 3.5 \cdot 10^{-7} \text{ 1/Pa s}, \qquad \widetilde{P}_l^* = 1000 \text{ Pa}. \tag{9}
$$

Equipped with the above values yield an IF velocity around 0.1–0.7 μm/s and IF pressure at the tumor margin around 3000–4000 Pa (i.e., 20–30 mmHg). We have assumed non-functional lymphatic vessels inside the tumor, and therefore no absorption of fluid within the tumor. Information about the placement of lymphatics is found in Fig. 2.

3.2. Initial and Boundary data

The initial primary tumor cell distribution is given by

$$
\alpha_c(x, y, t = 0) = 0.4 \exp\left(-100(x - 0.5)^2 - 100(y - 0.5)^2\right) \tag{10}
$$

where $(x, y) \in \Omega = [0, 1] \times [0, 1]$ (dimensionless). The initial fibroblast volume fraction α_f is restricted to surround one side of the primary tumor periphery. This will better illustrate the impact the fibroblasts have on the cancer cells. The initial condition can be seen in Fig. 1. The position of fibroblasts is motivated by von Ahrens et al. (2017), Lakiotaki et al. (2016), where CAFs are situated around the primary tumor close to its margin.

In particular, using the values assigned in (7)–(10), we get the IFP and the corresponding IF flow field seen in Fig. 2. Fig. 2 (A) shows where the vascular and lymphatic system are placed as well; vascular system in the center of the domain (inside the tumor), whereas four draining lymphatics are placed near the edge of the domain. In some of the simulation cases the lymphatics have changed positions and/or the conductivity of the tissue is decreased, causing a different flow pattern. This will be described within the respective cases. Fig. 3 shows IFP and IF flow field when the conductivity of the tissue is reduced by a factor 10 by increasing the parameter $\hat{k}_w$ in (17) from 1 to 10. In order to maintain the same level of the IF velocity we increase the transcapillary coefficient T_v by a factor of 10 and T_l by a factor of 2 as well as raise the intratumoral vascular pressure $\widetilde{P}_v^*$ and effective lymphatic pressure $\widetilde{P}_l^*$ by a factor of 1.5. Clearly, this leads to a higher level of the intratumoral IFP as well as a sharper drop of the IF pressure at the tumor margin (panel A and B), but also a slightly lower maximal IF velocity at the margin (panel C and D).
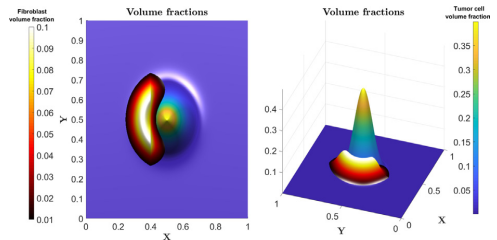

Fig. 1. Initial cell volume fractions: Fibroblasts are placed on one side of the tumor to make it easier to compare simulated cell migration with and without fibroblasts in the same figure.

3.3. Collective behavior due to the presence of fibroblasts

In Urdal et al. (2019) we developed a model that incorporates fibroblasts as a separate phase, in addition to tumor cells and interstitial fluid. We used the experimental results from Shieh et al. (2011) as a means to describe the behavior of fibroblasts. Furthermore, (Gaggioli et al., 2007) has shown that tumor cells may be led by fibroblast while migrating. We wanted to examine how this could play out in a more realistic tumor setting, using the mathematical model developed in Urdal et al. (2019). In this work, we include the following two fibroblast-enhanced cancer cell migration mechanisms.

1. Fibroblasts remodel the ECM, priming the matrix to enhance the tumor cell invasion.
2. Tumor cells migrate in the same direction of fibroblasts due to a direct mechanical interaction between them.

We represent ECM remodeling by fibroblast (i.e. point 1. above) through the dynamic cell-ECM interaction parameter $\hat{k}_c$. We use the same correlation as in Urdal et al. (2019), which is given by

$$\hat{k}_c(\alpha_f) = 1 - A(1 - \exp(-B\alpha_f)), \tag{11}$$

with prescribed constants A and B. We use values as found for the in vitro study (Urdal et al., 2019) with $A = 0.7$ and $B = 50$. Hence, $\hat{k}_c$ acts as a function of fibroblasts, α_f, where the presence of fibroblasts decreases the cell-ECM resistance force $\hat{\zeta}_c$ (see (18)). This accounts for the effect that fibroblasts prime the matrix in the direction they migrate and therefore pave the way for cells to follow their path.

Regarding point 2 above, we assign the direct fibroblast-cell mechanical interaction strength I_{cf} from (7) in such a way that it can be interpreted as not all fibroblasts link themselves to the tumor cells. This still allows, however, that fibroblasts create tracks within the ECM so that tumor cells may follow them without the necessity of direct interaction.

3.3.1. Partial mechanical coupling and ECM remodeling

As prescribed in (7), the strength of the mechanical coupling between cancer cells and fibroblasts is set to $I_{cf} = 1000I_w$. This implies that not all fibroblasts create a direct coupling with the cancer cells, yet some will maintain this ability. The simulated results are displayed in Fig. 4 and 5 after a time period of $T \approx 5.8$ days. Main observations are:

- Tumor cell migration is manifested as a strong finger like migration pattern outwards from the tumor, see Fig. 4, panel (A). Fibroblasts shown in panel (B) effectively migrate in the IF flow direction and pull cancer cells out of the primary tumor region so that the two cell types migrate in a coupled fashion where tumor cells follow fibroblasts through a primed matrix.
- The chemical components, chemokine and TGF-β, create pericellular concentration gradients in the direction of the lymphatics (Fig. 4, panel (C) and (D)). This causes both tumor cells and fibroblasts to migrate in that direction due to autologous chemotaxis, as reflected by panel (A) and (B).
- As fibroblasts migrate at a higher velocity through the ECM and are not fully anchored to the cancer cells, they also prime the matrix further from their initial position. This results in cells following the fibroblasts farther through the ECM, both by the now primed ECM and the direct mechanical coupling between cells and fibroblasts, as observed in Fig. 4 (A).
- Fig. 5 shows the total cell velocity $\mathbf{u}_c$ (A) and its different velocity components (B-E), as mentioned in Remark 1. Panel (A) illustrates that the migration is highest at the invasive strand-like front. Apparently, the more motile fibroblasts, enable the cancer cells that are coupled with the fibroblasts to migrate even farther from their initial position.
- Fig. 5 (F), which visualizes the different components of (2)$_1$, tells us that tumor cell migration due to chemotaxis towards chemokine (yellow region) is dominant close to the tumor periphery behind the more invasive front whereas migration owing to the mechanical coupling between fibroblasts and tumor cells is dominant outside of the periphery (orange region) of the primary tumor. The simulation suggests that the more aggressive tumor cell behavior is a result of the cell-fibroblast interaction.
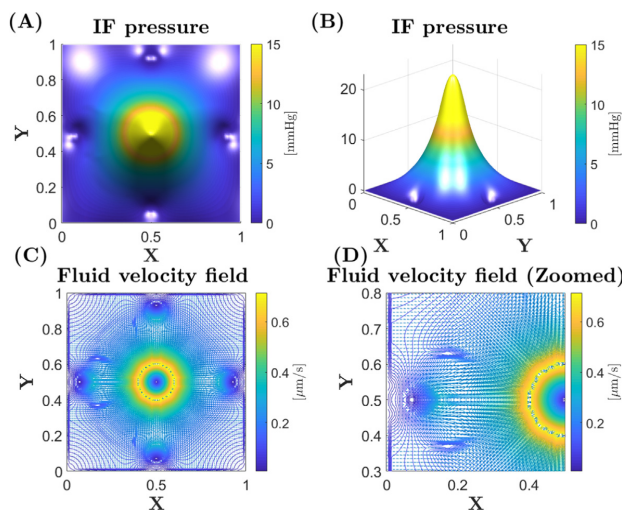
Fig. 2. Pressure and fluid flow velocity: (A) Interstitial fluid pressure P_w is elevated at the center of the tumor and decreases significantly towards its periphery. (B) Same interstitial fluid pressure as in (A) but seen from another angle. (C) Fluid velocity field corresponding to the interstitial pressure in (B), where we have the highest fluid velocity at the tumor periphery and leads to the draining lymphatics outside of the primary tumor. (D) Fluid velocity field zoomed in at $x \in [0.5, 1]$ and $y \in [0.3, 0.8]$.
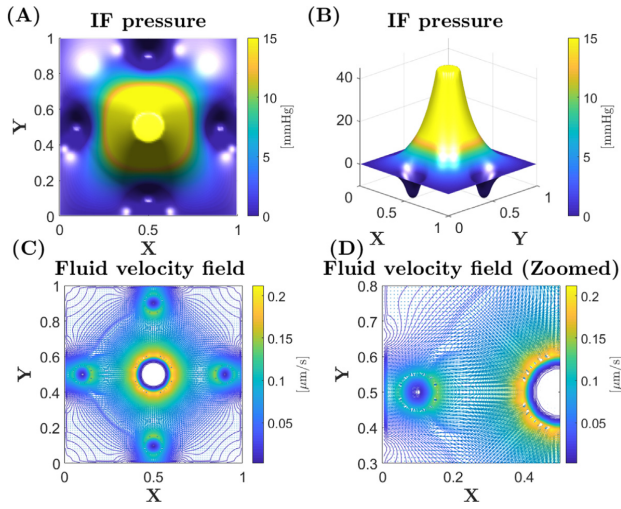
Fig. 3. Pressure and fluid flow velocity with decreased tissue conductivity: (A) Interstitial fluid pressure P_w is elevated at the center of the tumor and decreases significantly towards its periphery. The hydrostatic pressure in the vascular and lymphatic system is now $\tilde{P}_v^* = 6000$ Pa and $\tilde{P}_l^* = 1500$ Pa respectively. (B) Same interstitial fluid pressure as in (A) but seen from another angle. (C) Fluid velocity field is heavily dependent on the interstitial fluid pressure, thus we have outgoing fluid flow from the tumor periphery to the four lymphatics and nearly stagnant at the tumor core. (D) Fluid velocity field zoomed in at $x \in [0.5, 1]$ and $y \in [0.3, 0.8]$.
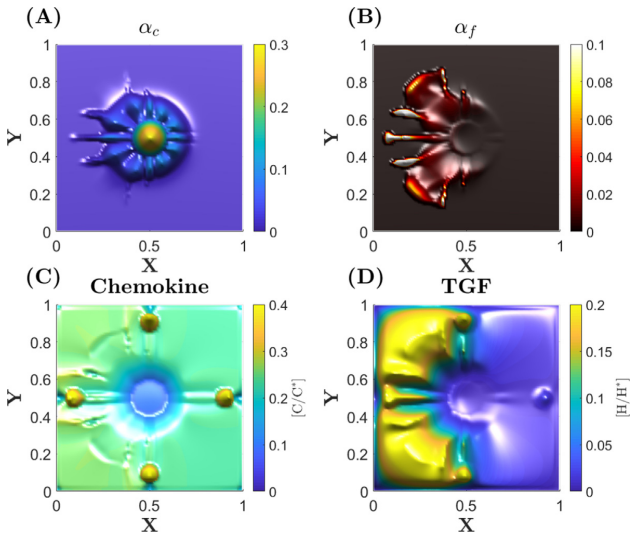
Fig. 4. Combined partial mechanical coupling and ECM remodeling: All variables are dimensionless. (A) Cancer cell volume fraction α_c shows migration towards the lymphatic vessel placed on the edge of the domain. The tumor cells follows the tracks made by the fibroblasts. On the right side of the tumor there clearly is a very small degree of invasion. (B) Fibroblast cell volume fraction α_f migrate at a higher velocity than tumor cells towards the edges of the domain. Fibroblasts chemotact towards the lymphatics as TGF-β accumulates and creates higher concentrations (positive gradients) in that direction. (C) Chemokine concentration C is proteolytically released from the ECM and creates a concentration gradient towards the lymphatics due to advection. (D) TGF-β concentration H is produced by fibroblasts and is advected towards the lymphatics by the interstitial fluid.

- Comparing the left and right side of Fig. 4 (A) shows that fibroblasts are necessary to activate the invasive behavior of tumor cells.

3.3.2. Partial mechanical coupling and ECM remodeling with reduced tissue conductivity

The mechanical properties of the tumor microenvironment affect the tumor cell invasiveness. We change the tissue conductiv-

ity, as mentioned above, by increasing $\hat{k}_w$ with a factor 10. The corresponding fluid flow field is similar to Fig. 2 but the magnitude is decreased, as seen in Fig. 3. With a decreased conductivity there is also a stronger connection between the vascular and the lymphatic system, causing the fluid flow to concentrate towards the lymphatics more directly than the previous case. The simulated results are shown in Fig. 6 and 7. Main observations are:
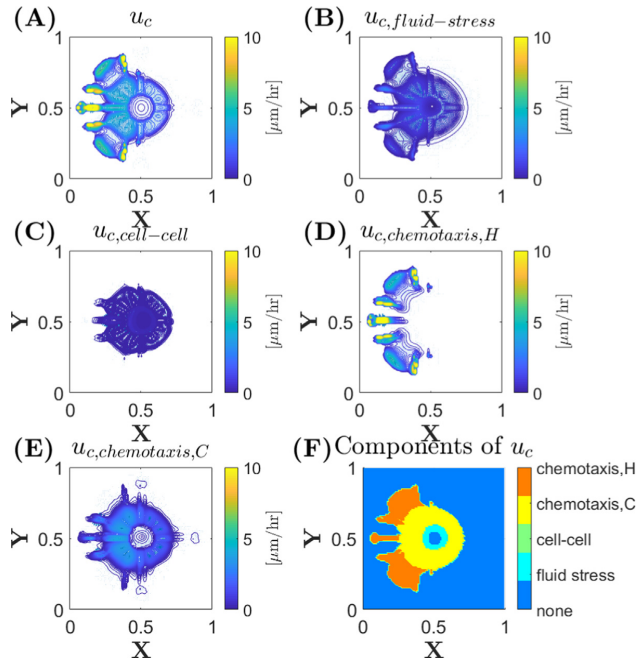
Fig. 5. Combined partial mechanical coupling and ECM remodeling: Tumor cell velocity. The highest tumor cell migration velocity is in the range 10–20 μm/hr. (A) Tumor cell velocity $\mathbf{u}_c$. The invading tumor cells furthest away from the primary tumor are migrating with the highest velocity. (B) Tumor cell velocity due to fluid generated stress, $\mathbf{u}_{c,fluid-stress} = \frac{\hat{f}_c}{z_c}\mathbf{U}_T$. Fluid generated stress imposed on the tumor cell does only slightly contribute to the total tumor cell velocity. (C) Tumor cell velocity by cell-cell interaction, $\mathbf{u}_{c,cell-cell} = -\frac{h_1+h_2}{z_c}\nabla(\Lambda P_{cw})$. Through our choice of parameters, random migration of tumor cells by diffusion is very low. (D) Tumor cell velocity due to chemotaxis of fibroblasts towards concentration gradient of TGF, $\mathbf{u}_{c,chemotaxis,H} = \frac{h_2}{z_c}\nabla\Lambda_H$. Through the mechanical interaction between the two cell types, we have momentum transfer between them. (E) Tumor cell velocity due to chemotaxis of tumor cells towards concentration gradient of chemokine, $\mathbf{u}_{c,chemotaxis,C} = -\frac{h_1+h_2}{z_c}\nabla\Lambda_C$. Chemotaxis towards chemokine contributes the most to the overall tumor cell migration behind the invasive front. (F) The components of $\mathbf{u}_c$, shown in subfigures (B)-(E), which is largest in magnitude in a given area. Each component is represented by a color, referenced on the right of the figure.

- Tumor cells do not seem to be more aggressive in terms of penetration distance or tumor cell velocity, as seen in Fig. 6 (A) and Fig. 7 (A). Rather than small fraction of tumor cells migrating from the primary tumor as in Fig. 4 (A), the cells now migrate in a more collective sheet-like manner away from the primary tumor, Fig. 6 (A).
- By decreasing tissue conductivity the tumor cells have increased directionality towards the lymphatics, as the direction of flow through the tissue plays a much larger part in this case. The fluid generated stress imposed on tumor cells, seen in Fig. 7 (B) and (F), is upregulated. In addition, the fluid flow creates both chemokine and fibroblast gradients towards lymphatics in a more direct manner, Fig. 6 (C and D).

3.3.3. Diagonally placed lymphatics

In the next example we have placed the lymphatics at the corners of the domain rather than in the center of the sides. We continue to use the same parameters as in the first case. In this instance we exemplify how fibroblasts guide cancer cells towards the lymphatics. Having the same initial conditions for tumor cells and fibroblasts, shown in Fig. 1, we expect that fibroblasts may change the direction of migration and thereby lead tumor cells to the lymphatics through ECM remodeling and direct mechanical adhesion.

The results can be seen in Fig. 8 and 9.

- The migration of fibroblasts are clearly diverted towards the lymphatics. This also causes tumor cells to follow the fibroblasts towards the lymphatics, as seen in Fig. 8 (A), (B) and Fig. 9 (F).

- The direction of the concentration gradients of both TGF and chemokine guides both cell phases towards the lymphatics, shown in Fig. 8 (C) and (D). The chemical components still accumulate near the lymphatics.

4. Discussion

4.1. Main conclusions

The multiphase model (1)–(5) has demonstrated how tumor cells can collectively invade the adjacent tissue by using fibroblasts as their leader cells to guide them towards the lymphatic system. There are two mechanisms accounted for in the computer model through which the fibroblasts enhance tumor cell migration: (i) Fibroblasts generate tracks in the tissue through remodeling and tumor cells are more inclined to invade in that direction. We express this by reducing cell-ECM drag force in $\hat{\zeta}_c$ given by (18) as expressed by the correlation (11), letting tumor cells invade more aggressively where fibroblasts are present. (ii) Tumor cells directly attach themselves to fibroblasts and since fibroblasts are more mobile, they increase the tumor cell velocity and thus they increase tumor cell aggressiveness and ability to invade. This effect is expressed in the $\hat{h}_2$-function in (29)₂ since this becomes negative when the cell-fibroblast interaction term $\hat{\zeta}_{cf}$ given by (20) becomes sufficiently large. This allows fibroblasts chemotaxis towards a positive TGF gradient to increase tumor cell velocity in the same direction, as expressed through the last term of $\mathbf{u}_c$ in (2)₁. It is
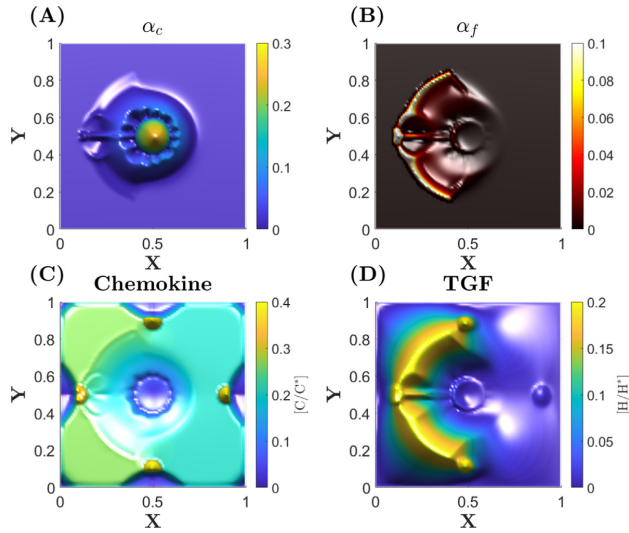
Fig. 6. Combined partial mechanical coupling and ECM remodeling with reduced tissue conductivity: All variables are dimensionless. (A) Cancer cell volume fraction α_c. Tumor cells migrate slowly towards the lymphatic, but in a more direct manner. (B) Fibroblast cell volume fraction α_f. Fibroblasts migrate outwards from their initial position. They also guide the tumor cells to migrate in their path, such that the tumor cells experience less resistance towards the lymphatic. (C) Chemokine concentration. Due to the decreased fluid flow velocity there is a greater concentration gradient of chemokine, as it will not be rapidly advected by the fluid. (D) TGF-β concentration. TGF-β concentration similarly to chemokine, but is instead produced by fibroblasts.
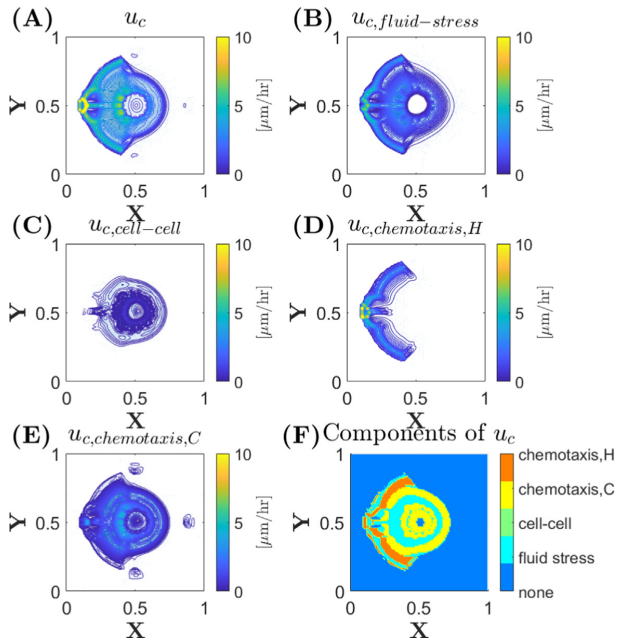

Fig. 7. Combined partial mechanical coupling and ECM remodeling with reduced tissue conductivity: Tumor cell velocity. The highest tumor cell migration velocity is in the range 10–20 µm/hr. (A) Tumor cell velocity $\mathbf{u}_c$. (B) Tumor cell velocity due to fluid generated stress, $\mathbf{u}_{c,fluid-stress} = \frac{\hat{t}_c}{\alpha_c}\mathbf{U}_f$. With decreased conductivity, fluid-generated stress has a larger impact on the total tumor cell velocity. (C) Tumor cell velocity by cell-cell interaction, $\mathbf{u}_{c,cell-cell} = -\frac{h_1+h_2}{\alpha_c}\nabla(\Lambda P_{cw})$. (D) Tumor cell velocity due to chemotaxis of fibroblasts towards concentration gradient of TGF, $\mathbf{u}_{c,chemotaxis,H} = \frac{h_2}{\alpha_c}\nabla\Lambda_H$. Tumor cells follow fibroblasts through a direct mechanical coupling. (E) Tumor cell velocity due to chemotaxis of tumor cells towards concentration gradient of chemokine, $\mathbf{u}_{c,chemotaxis,C} = -\frac{h_1+h_2}{\alpha_c}\nabla\Lambda_C$. Tumor cells chemotact towards the lymphatics. Tumor cell velocity due to chemotaxis is increased on the left side due to ECM remodeling by fibroblasts. (F) The components of $\mathbf{u}_c$, shown in subfigures (B)-(E), which contributes the most to the total tumor cell velocity in a given area. Each component is represented by a color, referenced on the right of the figure.
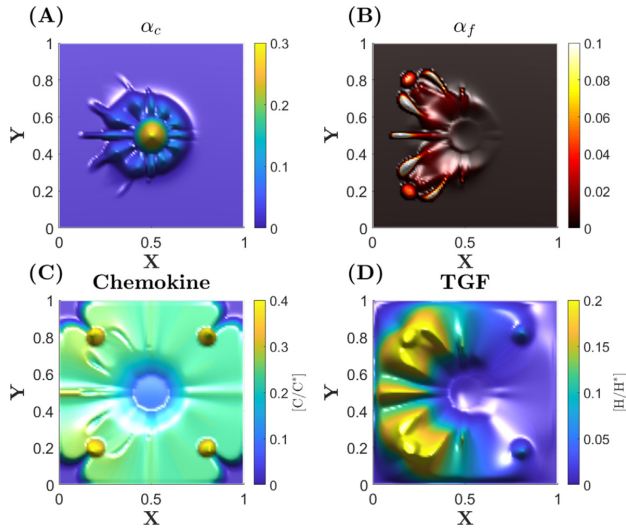
Fig. 8. Diagonally placed lymphatics: All variables are dimensionless. (A) Cancer cell volume fraction α_c. Tumor cells that are invading tend to veer towards the lymphatics which are now placed on the diagonals of the domain. (B) Fibroblast cell volume fraction α_f. Fibroblasts can clearly be seen to migrate in the direction of lymphatics. (C) Chemokine concentration. Chemokine continue to accumulate at the lymphatics. (D) TGF-β concentration. Similarly to chemokine, TGF-β accumulates at the lymphatics.
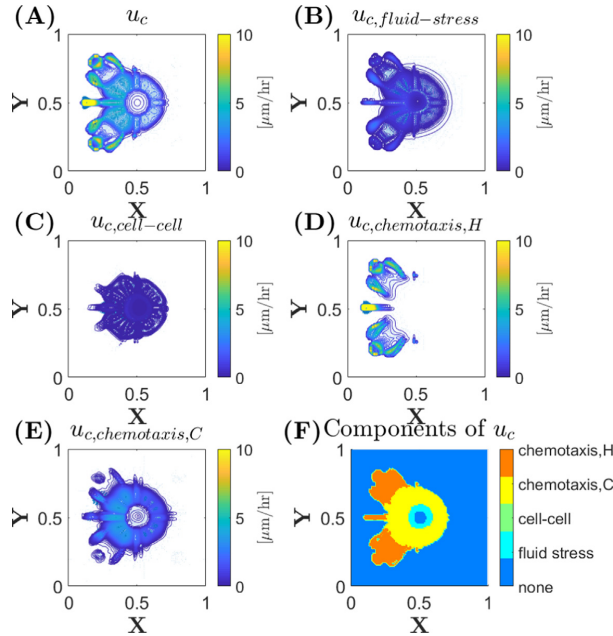
Fig. 9. Diagonally placed lymphatics: Tumor cell velocity. The highest tumor cell migration velocity is in the range 10–20 μm/hr. (A) Tumor cell velocity $\mathbf{u}_c$. Tumor cells migrate towards the lymphatics. (B) Tumor cell velocity due to fluid generated stress, $\mathbf{u}_{c,fluid-stress} = \frac{\hat{t}_c}{\alpha_c}\mathbf{U}_f$. Fluid generated stress imposed on the tumor cells does not have a strong contribution to the total velocity. (C) Tumor cell velocity by cell-cell interaction, $\mathbf{u}_{c,cell-cell} = -\frac{h_1+h_2}{\alpha_c}\nabla(\Lambda P_{cw})$. (D) Tumor cell velocity due to chemotaxis of fibroblasts towards concentration gradient of TGF, $\mathbf{u}_{c,chemotaxis,H} = \frac{h_2}{\alpha_c}\nabla\Lambda_H$. Through the direct mechanical coupling between fibroblasts and tumor cells, fibroblasts acts as leader cells and guide tumor cells toward the lymphatics. (E) Tumor cell velocity due to chemotaxis of tumor cells towards concentration gradient of chemokine, $\mathbf{u}_{c,chemotaxis,C} = -\frac{h_1+h_2}{\alpha_c}\nabla\Lambda_C$. The chemokine concentration gradient acts as a guide due to the accumulation of chemokine near the lymphatics. (F) The components of $\mathbf{u}_c$, shown in subfigures (B)–(E), which has the highest relative tumor cell migration velocity in a given area. Each component is represented by a color, referenced on the right of the figure.

evident that under these circumstances, fibroblasts are necessary to initiate aggressive tumor cell behavior.

One important aspect of the second effect, (ii), is that fibroblasts increase the aggressiveness of the tumor cells through mechanical coupling, but decreases the mobility of fibroblasts. Tumor cells, being less mobile than fibroblasts, slow the fibroblasts down through this coupling. However, fibroblasts also remodel the ECM, increasing tumor cell velocity. Therefore, this can be considered a positive feedback loop. Fibroblasts will migrate more aggressively if tumor cells do the same, and since fibroblasts increases tumor cell aggressiveness, fibroblasts themselves will in turn increase their aggressiveness.

In our simulation cases we study the effect of fibroblasts on tumor cell migration in a tumor setting, under different conditions with regards to placement of the lymphatic system and the tissue conductivity. The results indicate that.

- Placement of lymphatics greatly impacts the direction in which both fibroblasts and tumor cells migrate. This is mainly a result of the pericellular chemical concentration gradient of TGF and chemokine skewed in the direction of IF flow, which originates from the vascular system and is drained by the lymphatics. The fluid flow field is dependent on the location of the lymphatics.
- By decreasing the conductivity of the tissue, the fluid-ECM interaction term $\tilde{\zeta}_w$ in (17) increases, i.e., the fluid feels a stronger resistance force. This results in a higher contribution by the fluid generated stress imposed on the cells, letting the direction of fluid flow also guide tumor cells. Tumor cells thus displayed an enhanced collective migration towards the lymphatics when the conductivity was reduced. This is evident in Fig. 7 (F).
- Two different types of aggressive behavior have been observed. When hydraulic conductivity is relatively high, the cancer cells are inclined to develop elongated strands of connected tumor cells at the invasive front that move farther away from the primary tumor, as illustrated in Fig. 4. When hydraulic conductivity is reduced, the cancer cells tend to move collectively with a lower speed but more direction-specific towards a nearby draining lymphatic vessel, see Fig. 6. This is a result of the fact that changes in the tissue microenvironment will change the relative strength of the different tumor cell migration components, as expressed by $(2)_1$.

Studies have shown that tumors that had developed lymph node metastases expressed higher interstitial fluid pressure and elevated interstitial fluid velocity compared to tumors that had not metastasized (Hompland et al., 2012; Andersen et al., 2017). In our simulations we reproduce the measured IFP in metastasizing tumors, which lies in the range of 30–40 mmHg (4–5.5 kPa). The source of elevated IFP in tumors may be influenced by many features of the local and adjacent stroma. Through our model, we can see that by decreasing the conductivity of the tissue we need to set a higher effective vascular pressure, $\tilde{P}_v$, and conductivity of the vascular wall, T_v, to maintain realistic interstitial fluid velocity. It is known that tumors develop elevated IFP because they show high resistance to blood flow (i.e., P_v' in (21) is high), low resistance to transcapillary fluid flow (i.e., T_v in (21) is high), and impaired lymphatic drainage (i.e., Q_l in (22) is located to the peritumoral region) (Andersen et al., 2017).

As the conductivity is decreased, and thus the IFP is elevated, we observe in our results increased collective directionality towards the lymphatics. This may account for development of lymph node metastasis of *in vivo* tumors seen in tumors with elevated IFP (Hompland et al., 2012; Andersen et al., 2017). In addition, a study performed *in vitro* showed that cells cultured on stiffer substrates displayed sheet-like migration pattern,

which is a slow collective migration but is exhibiting increased directionality, whereas cells cultured on softer tissue displayed more mesenchymal behavior (Shukla et al., 2016). Collectively migrating tumor cells are most frequently observed in solid tumors (Friedl et al., 2012), which may explain the observations with regards to the increased number of lymph node metastasis found in Andersen et al. (2017) in tumors where IFP is increased.

Based on the work by Gaggioli et al. (2007), where fibroblasts create tracks within the tissue for the tumor cells to follow, we included fibroblasts with the ability to act as leader cells through ECM remodeling and direct mechanical interaction. Like tumor cells, fibroblasts also sense the decreased conductivity and have a reduced migration velocity, but increased directionality (Lautscham et al., 2014). This reduces the effect of the fibroblast-enhanced tumor cell migration as tumor cells are dependent on how the fibroblasts migrate. In summary, a multiphase approach has been used to illustrate the migration of tumor cells and fibroblasts in a realistic tumor setting, a model trained by experimental data observed *in vitro*. Fibroblast-enhanced tumor cell migration is present through two distinct mechanisms, i.e. through ECM remodeling and direct mechanical coupling between the phases. Moreover, we observe a collective migration of tumor cells outwards from the tumor and reducing the conductivity of the adjacent tissue increases the collective directionality. This yields results which can elucidate how fibroblasts guides tumor cells towards the lymphatics through collective migration. Furthermore, our model suggests that tumor cells are able to reach functioning lymphatic vessels through solely using fibroblasts as their guide as leader cells and without changes in the intrinsic migratory behavior of the cancer cells. These results support the strategy of targeting fibroblast-cancer cell interactions as a method to decrease metastasis in patients.

4.2. Future directions

Dense interstitial matrix and elevated interstitial fluid pressure have long been known to be barriers for drug delivery to solid tumors (Chauhan et al., 2011), and an emerging strategy for improving drug delivery has been to enzymatically degrade the matrix to increase hydraulic conductivity (Brown et al., 2003; Bookbinder et al., 2006; Perentes et al., 2009). However, there is some indication that degrading matrix leads to an increased rate of metastasis (Binder et al., 2014), and expression of matrix-targeting proteases by tumors has long been established as a marker for metastatic potential (Liotta et al., 1980). The results in the present study demonstrate a dominating collective directional migration toward the lymphatics with decreased hydraulic conductivity. However, with higher conductivity the tumor cell behavior becomes more aggressive with a deeper penetration (higher velocity) and formation of a strand-like invasive front. This suggests a possible mechanism for the increased metastasis. More broadly, it demonstrates that enzymatically targeting the interstitium and thereby increasing the hydraulic conductivity, could have detrimental side-effects that promote metastasis. Rather, since fibroblasts contribute greatly to the metastatic and aggressive behavior of cancer cells, as observed on the left versus right side of the computational domain in this study, the model suggests that targeting fibroblasts for therapeutic treatment would decrease the invasion of cancer cells. This is consistent with experimental work that has identified CAFs as among the predominant cell types present within the tumor microenvironment (Kalluri and Zeisberg, 2006). A high concentration of stromal CAFs are often associated with poor prognosis in humans, as fibroblasts have abilities that can support and promote tumors during growth and metastasis

(Togo et al., 2013; Dasari et al., 2018). Natural future work and development of the computer model could be to tune it towards preclinical model data and use it in a search for associations between metastatic propensity and conditions pertaining to the TMEs, as reported, for instance in the recent work (Andersen et al., 2017). Another natural application would be to add a therapeutic agent to the model with a prescribed impact on aspects of the TME or the migratory features of the cells, and then explore systematically for possibly barriers for efficient delivery and effect of this drug.

5. Conflict of interest

The authors declare that there is no conflict of interest related to this manuscript.

Appendix A. Three-phase fibroblast-cell-fluid model

In this work we use the multiphase model developed in Urdal et al. (2019) which in turn is motivated by the formulation in Evje (2017). The approach is closely related to modelling of creeping fluid flow in porous media by mixture theory (Drew and Passman, 1999; Rajagopal, 2007; Standnes et al., 2017; Qiao et al., 2018, 2019). However, in this Appendix we also include porosity in the derivation of the model, where choice of parameters and assuming a constant porosity in space and time will reduce the model to its original form found in Urdal et al. (2019).

The tumor microenvironment contains the extracellular matrix (ECM) that occupies a volume fraction ϕ_m where the rest of the volume is represented by pore space ϕ_p. Fibroblasts, tumor cells and interstitial fluid reside within the pore space. We have that

$$\phi_m + \phi_p = 1. \tag{12}$$

In the derivation we will use $\phi = \phi_p = \frac{V_p}{V_T}$ to represent the pore space and $\phi_m = \frac{V_m}{V_T} = 1 - \phi$ to represent the matrix, where V_T is total tissue volume ($V_T = V_p + V_m$). Thus, the tumor environment is considered a mixture of four interacting continua (Drew and Passman, 1999; Rajagopal, 2007): a stagnant matrix occupying a volume $1 - \phi$, a tumor cell phase represented by a volume fraction α_c moving within the pore space ϕ with a velocity $\mathbf{u}_c^p$, and similarly for the fibroblasts and interstitial fluid (volume fractions α_f and α_w with velocities $\mathbf{u}_f^p$ and $\mathbf{u}_w^p$). The pore space is filled by the three phases, giving the closure relation

$$\alpha_c + \alpha_f + \alpha_w = 1 \quad (\text{i.e.,} \quad \phi\alpha_c + \phi\alpha_f + \phi\alpha_w = \phi) \tag{13}$$

In addition to mass and momentum balance equations for the three phases we have included the following components:

- ECM component $\rho = \frac{m_\rho}{V_T}$ associated with matrix (mass per total tissue volume V_T).
- Protease $G = \frac{m_G}{\phi\alpha_w V_T}$ (mass per volume of solution) secreted by tumor cells.
- Chemokine $C = \frac{m_C}{\phi\alpha_w V_T}$ (mass per volume of solution) released by proteolytic activity.
- Transforming growth factor $H = \frac{m_H}{\phi\alpha_w V_T}$ (mass per volume of solution) released by fibroblasts.

Note that we can multiply the concentration of G, C and H by $\phi\alpha_w$ in order to express the concentration as mass per total volume tissue V_T. The resulting model, with inclusion of porosity and concentrations expressed in terms of mass per total volume tissue, becomes:

$$(\phi\alpha_c)_t + \nabla \cdot (\phi\alpha_c \mathbf{u}_c^p) = S_c, \quad S_c = \alpha_c\left(\lambda_{11} - \lambda_{12}\alpha_c - \lambda_{13}\frac{\rho}{\rho_M}\right)$$

$$(\phi\alpha_f)_t + \nabla \cdot \left(\phi\alpha_f \mathbf{u}_f^p\right) = S_f,$$

$$(\phi\alpha_w)_t + \nabla \cdot (\phi\alpha_w \mathbf{u}_w^p) = -S_c - S_f + Q, \quad Q = Q_v - Q_l$$

$$\alpha_c \nabla(P_w + \Delta P_{cw} + \Lambda_C) = -\hat{\zeta}_c \mathbf{u}_c^p + \hat{\zeta}_{cf}\left(\mathbf{u}_f^p - \mathbf{u}_c^p\right)$$

$$\alpha_f \nabla(P_w + \Lambda_H) = -\hat{\zeta}_f \mathbf{u}_f^p - \hat{\zeta}_{cf}\left(\mathbf{u}_f^p - \mathbf{u}_c^p\right)$$

$$\alpha_w \nabla P_w = -\hat{\zeta}_w \mathbf{u}_w^p$$

$$\rho_t = -\frac{\lambda_{21}}{\phi}G\rho + \frac{\rho}{\phi}\left(\lambda_{22} - \lambda_{23}\alpha_c - \lambda_{24}\left(\frac{\rho}{\rho_M}\right)\right) \tag{14}$$

$$(\phi\alpha_w G)_t = \nabla \cdot (D_G \nabla G) - \nabla \cdot (\phi\alpha_w \mathbf{u}_w^p G) - \lambda_{31}G$$
$$+ (\alpha_c + \alpha_f)\left(\lambda_{32} - \lambda_{33}\left(\frac{G}{G_M}\right)^{\nu_G}\right)$$

$$(\phi\alpha_w C)_t = \nabla \cdot (D_C \nabla C) - \nabla \cdot (\phi\alpha_w \mathbf{u}_w^p C) - CM_C Q_l$$
$$+ G\rho\left(\lambda_{41} - \lambda_{42}\left(\frac{C}{C_M}\right)^2 - \lambda_{43}\left(\frac{C}{C_M}\right)^{\nu_C}\right) - \lambda_{44}\alpha_c C,$$

$$(\phi\alpha_w H)_t = \nabla \cdot (D_H \nabla H) - \nabla \cdot (\phi\alpha_w \mathbf{u}_w^p H) - HM_H Q_l - \lambda_{51}H$$
$$+ \alpha_f\left(\lambda_{52} - \lambda_{54}\left(\frac{H}{H_M}\right)^2 - \lambda_{54}\left(\frac{H}{H_M}\right)^{\nu_H}\right) - \lambda_{55}\alpha_f H$$

where $\mathbf{u}_i^p = (u_i^x, u_i^y)$ for $i = c, w, f$ are interstitial velocities. The first six equations are mass and momentum balance equations for each of the phases, whereas the remaining equations account for ECM, protease, chemokine and TGF. The chemical components move by diffusion and advection. S_c and S_f are proliferation/apoptosis terms whereas the source term Q in $(14)_3$ describes the produced IF flow Q_v from the leaky vasculature and Q_l is the collected fluid by functional lymphatics in the peritumoral region. Similar to Evje (2017), Urdal et al. (2019) we use the following function for cell-cell interaction stress $\Delta P_{cw}(\alpha_c)$

$$\Delta P_{cw}(\alpha_c) = \gamma J(\alpha_c) = -\gamma \ln[\delta + (1 - \alpha_c)] \tag{15}$$

where $\gamma > 0$ is a coefficient (unit Pa) that depends linearly on the surface tension (unit Pa m) whereas $J(\alpha_c)$ is a monotonic increasing dimensionless function with respect to the cell volume fraction α_c. This accounts for the effect that tumor cells will try to reduce the cell-cell stress by moving towards a region with fewer tumor cells. The ability of the cancer cells and fibroblasts to generate a force and move is expressed through the potential function $\Lambda_A(A)$ with $A = C, H$ given by

$$\Lambda_A(A) = \Lambda_{A0} - \frac{\Lambda_{A1}}{1 + \exp[-\xi_A(A - A_M)]} \tag{16}$$

where $\Lambda_{A0}, \Lambda_{A1}$ and ξ_A are constant parameters with units, respectively, as $[\Lambda_{A0}, \Lambda_{A1}] = Pa$ and $[\xi_A] = m^3/kg$. Note that $\Lambda_A(A)$ for $A = C, H$ is a decreasing function reflecting that cells/fibroblasts will try to reduce the additional stress associated with it by moving towards a higher concentration of A.

There is a drag force between the extracellular fluid, represented by $\mathbf{u}_w$, and the ECM fibers. We use the following expression for this force

$$\hat{\zeta}_w = I_w \hat{k}_w \phi \alpha_w^{r_w}, \qquad \hat{k}_w > 0, \qquad r_w < 2, \tag{17}$$

with $I_w = \frac{\mu_w}{K}$ and K is the permeability of the porous media and μ_w the fluid viscosity. The coefficient r_w plays a similar role to the use of relative permeability functions in standard Darcy's equation approach extended to several phases. Similarly, there is a drag force between the cells and the ECM

$$\hat{\zeta}_c = I_c \hat{k}_c \phi \alpha_c^{r_c}, \qquad \hat{k}_c > 0, \qquad r_c < 2, \tag{18}$$

where I_c (Pa s/m^2), $\hat{k}_c$ and r_c must be specified (the last two are dimensionless). In addition, there is a similar drag force between the fibroblasts and the ECM

$$\hat{\zeta}_f = I_f \hat{k}_f \phi \alpha_f^{r_f}, \qquad \hat{k}_f > 0, \qquad r_f < 2, \tag{19}$$

where I_f (Pa s/m^2), $\hat{k}_f$ and r_f must be specified. Finally, there is a drag force between the cell phase and the fibroblast phase which accounts for the mechanical coupling between the two cell types. This drag force represent momentum transfer from the faster moving fluid (fibroblasts) to the slower moving fluid (cancer cells)

$$\hat{\zeta}_{cf} = I_{cf} \phi \alpha_c^{r_{cf}} \alpha_f^{r_{fc}}, \tag{20}$$

I_{cf} is a positive constant determining the order of magnitude of the cell-fibroblast interaction and r_{cf}, r_{fc} are related exponents determining further details of this interaction. The form of the different interaction terms $\zeta_w, \zeta_c, \zeta_f$ and ζ_{cf} is consistent with traditional modeling of multiphase flow in porous media based on Darcy's extended law (Standnes et al., 2017; Qiao et al., 2018; Qiao et al., 2019; Bear, 2018, 2016).

Interstitial flow is a relatively slow fluid movement through the interstitium driven by hydrostatic and osmotic pressure differences between the arterial and lymphatic vessels (Chary and Jain, 1989). The transcapillary exchange and formation of interstitial fluid is determined by a modified Starling's Law, where Q_v in (14)$_3$ is given by

$$Q_v = T_v(P_v^* - P_w - \sigma_T(\pi_v^* - \pi_w)) = T_v(\widetilde{P}_v^* - P_w),$$
$$T_v = L_v \frac{S_v}{V} \tag{21}$$

with $\widetilde{P}_v^* = P_v^* - \sigma_T(\pi_v^* - \pi_w)$. Here, L_v is the hydraulic conductivity of the capillaries (m^{2}s/kg = m/Pa s); S_v/V is the exchange area available for filtration per unit volume of tissues V; P_v^* and P_w are the hydrostatic pressures in the blood capillary and the interstitial compartments, respectively; π_v^* and π_w are the osmotic pressure in the capillary and interstitial compartments, respectively. σ_T is the capillary reflection coefficient.

The lymphatic vessels drain excessive fluid from the interstitial space, expressed by Q_l in (14)$_3$. The lymphatic system therefore regulates the fluid balance in tissues and prevents formation of edema. In a tumor microenvironment, the increased hydrostatic pressure causes the lymphatics within the tumor to be compressed and non-functional. Similar to (21), Q_l is expressed by

$$Q_l = T_l\left(P_w - \widetilde{P}_l^*\right), \qquad T_l = L_l \frac{S_l}{V} \tag{22}$$

Here L_l is the hydraulic conductivity of the lymphatics; S_l/V is the surface area of the lymphatics per volume unit of tissues V and $\widetilde{P}_l^*$ is the effective lymphatic pressure.

Remark 4. The model (14) is essentially the same as the one discussed in Urdal et al. (2019). One difference is the appearance of the porosity ϕ which is set to a constant and will not have a direct impact on the simulation results. In addition, since we now use the model in an envisioned tumor setting, which is different from the experimental setup explored in Urdal et al. (2019), some other changes can be found. First, we need the source term Q in (14)$_3$ to account for the characteristic fluid flow from the the intratumoral vascular system to the draining peritumoral lymphatics. We have also added some source terms to the equation of chemical components (G, C and H) in (14)$_{8,9,10}$. This is done primarily to be able to better control the production and decay of the chemical components, and add some more realistic features to the equations. In particular, we have added decay terms $-CM_CQ_l$ and $-HM_HQ_l$ to ensure that the accumulation of chemokine and TGF at the lymphactis do not reach unreasonable high values.

A.1. Rewritten version of the model

We have *implicit* expressions for the velocities, represented by the momentum balance Eqs. (14)$_{4,5,6}$. We can replace these equations with explicit expressions for the phase velocities (see (Urdal et al., 2019) for more details). First, we introduce velocities $\mathbf{u}_c, \mathbf{u}_f$ and $\mathbf{u}_w$ that are phase velocities relatively pore space, i.e.

$$\mathbf{u}_i = \phi \mathbf{u}_i^p \tag{23}$$

In addition, we assume that $\alpha_w G \approx G, \alpha_w C \approx C$ and $\alpha_w H \approx H$ in (14)$_{8,9,10}$, meaning that in the region outside the tumor α_w is close to 1 (i.e. the pore space outside the tumor is dominated by fluid) and we are mainly interested in the role played by the chemical components in generating migration of tumor cells and fibroblasts in this area. From (14), after we have made it dimensionless (see Appendix B), we then have

$$
\begin{aligned}
&(\alpha_c)_t + \nabla \cdot (\alpha_c \mathbf{u}_c) = S_c, \qquad S_c = \alpha_c\left(\lambda_{11} - \lambda_{12}\alpha_c - \lambda_{13}\frac{\rho}{\rho_M}\right)\\
&(\alpha_f)_t + \nabla \cdot (\alpha_f \mathbf{u}_f) = S_f,\\
&(\alpha_w)_t + \nabla \cdot (\alpha_w \mathbf{u}_w) = -S_c - S_f + Q, \qquad Q = Q_v - Q_l\\
&\alpha_c \nabla(P_w + \Delta P_{cw} + \Lambda_C) = -\frac{\hat{\zeta}_c}{\phi}\mathbf{u}_c + \frac{\hat{\zeta}_{cf}}{\phi}(\mathbf{u}_f - \mathbf{u}_c)\\
&\alpha_f \nabla(P_w + \Lambda_H) = -\frac{\hat{\zeta}_f}{\phi}\mathbf{u}_f - \frac{\hat{\zeta}_{cf}}{\phi}(\mathbf{u}_f - \mathbf{u}_c)\\
&\alpha_w \nabla P_w = -\frac{\hat{\zeta}_w}{\phi}\mathbf{u}_w\\
&\rho_t = -\lambda_{21}G\rho + \rho\left(\lambda_{22} - \lambda_{23}\alpha_c - \lambda_{24}\left(\frac{\rho}{\rho_M}\right)\right)\\
&G_t = \nabla \cdot (D_G\nabla G) - \nabla \cdot (\mathbf{u}_w G) - \lambda_{31}G\\
&\quad + (\alpha_c + \alpha_f)\left(\lambda_{32} - \lambda_{33}\left(\frac{G}{G_M}\right)^{\nu_G}\right)\\
&C_t = \nabla \cdot (D_C\nabla C) - \nabla \cdot (\mathbf{u}_w C) - CM_CQ_l\\
&\quad + G\rho\left(\lambda_{41} - \lambda_{42}\left(\frac{C}{C_M}\right)^2 - \lambda_{43}\left(\frac{C}{C_M}\right)^{\nu_C}\right) - \lambda_{44}\alpha_c C,\\
&H_t = \nabla \cdot (D_H\nabla H) - \nabla \cdot (\mathbf{u}_w H) - HM_HQ_l - \lambda_{51}H\\
&\quad + \alpha_f\left(\lambda_{52} - \lambda_{53}\left(\frac{H}{H_M}\right)^2 - \lambda_{54}\left(\frac{H}{H_M}\right)^{\nu_H}\right) - \lambda_{55}\alpha_f H
\end{aligned}
\tag{24}
$$

with $\mathbf{u}_i = (u_i^x, u_i^y, u_i^z)$ for $i = c, w, f$. The model is combined with the boundary condition

$$
\begin{aligned}
&P_w|_{\partial\Omega} = P_B^*, \quad \frac{\partial}{\partial\nu}G|_{\partial\Omega} = 0,\\
&\frac{\partial}{\partial\nu}C|_{\partial\Omega} = 0, \quad \frac{\partial}{\partial\nu}H|_{\partial\Omega} = 0, \quad t > 0
\end{aligned}
\tag{25}
$$

where ν is the outward normal on $\partial\Omega$. The corresponding initial data are

$$
\begin{aligned}
&\alpha_c(\mathbf{x}, t=0) = \alpha_{c0}(\mathbf{x}), \quad \alpha_f(\mathbf{x}, t=0) = \alpha_{f0}(\mathbf{x}), \quad \rho(\mathbf{x}, t=0) = \rho_0(\mathbf{x}),\\
&G(\mathbf{x}, t=0) = G_0(\mathbf{x}), \quad C(\mathbf{x}, t=0) = C_0(\mathbf{x}), \quad H(\mathbf{x}, t=0) = H_0(\mathbf{x})
\end{aligned}
\tag{26}
$$

We can find the explicit expressions for the cell velocity $\mathbf{u}_c$, fibroblast velocity $\mathbf{u}_f$ and the IF velocity $\mathbf{u}_w$ (refer (Urdal et al., 2019) for details).

$$
\begin{aligned}
\mathbf{u}_c &= \frac{\hat{f}_c}{\alpha_c}\mathbf{U}_T - \frac{\hat{h}_1 + \hat{h}_2}{\alpha_c}\nabla(\Delta P_{cw} + \Lambda_C) + \frac{\hat{h}_2}{\alpha_c}\nabla\Lambda_H\\
\mathbf{u}_f &= \frac{\hat{f}_f}{\alpha_f}\mathbf{U}_T + \frac{\hat{h}_2}{\alpha_f}\nabla(\Delta P_{cw} + \Lambda_C) - \frac{\hat{h}_2 + \hat{h}_3}{\alpha_f}\nabla\Lambda_H\\
\mathbf{u}_w &= \frac{\hat{f}_w}{\alpha_w}\mathbf{U}_T + \frac{\hat{h}_1}{\alpha_w}\nabla(\Delta P_{cw} + \Lambda_C) + \frac{\hat{h}_3}{\alpha_w}\nabla\Lambda_H
\end{aligned}
\tag{27}
$$

with fractional flow functions which describes co-current flow $\hat{f}_c, \hat{\zeta}_{fw}$ and $\hat{f}_f$, respectively, for the cell, fluid and fibroblast phase given by

$$\hat{f}_c(\alpha_c, \alpha_f) := \frac{\hat{\lambda}_c}{\hat{\lambda}_T}$$

$$= \frac{\alpha_c\left[\alpha_f \hat{\zeta}_{cf} + \alpha_c\left(\hat{\zeta}_{cf} + \hat{\zeta}_f\right)\right]}{\left(\alpha_c + \alpha_f\right)^2 \hat{\zeta}_{cf} + \alpha_c^2 \hat{\zeta}_f + \alpha_f^2 \hat{\zeta}_c + \frac{z_w^2}{\hat{\zeta}_w}\left(\hat{\zeta}_c \hat{\zeta}_{cf} + \hat{\zeta}_c \hat{\zeta}_f + \hat{\zeta}_{cf} \hat{\zeta}_f\right)}$$

$$\hat{f}_f(\alpha_c, \alpha_f) := \frac{\hat{\lambda}_f}{\hat{\lambda}_T}$$

$$= \frac{\alpha_f\left[\alpha_c \hat{\zeta}_{cf} + \alpha_f\left(\hat{\zeta}_{cf} + \hat{\zeta}_c\right)\right]}{\left(\alpha_c + \alpha_f\right)^2 \hat{\zeta}_{cf} + \alpha_c^2 \hat{\zeta}_f + \alpha_f^2 \hat{\zeta}_c + \frac{z_w^2}{\hat{\zeta}_w}\left(\hat{\zeta}_c \hat{\zeta}_{cf} + \hat{\zeta}_c \hat{\zeta}_f + \hat{\zeta}_{cf} \hat{\zeta}_f\right)} \quad (28)$$

$$\hat{f}_w(\alpha_c, \alpha_f) := \frac{\hat{\lambda}_w}{\hat{\lambda}_T}$$

$$= \frac{\frac{z_w^2}{\hat{\zeta}_w}\left(\hat{\zeta}_c \hat{\zeta}_{cf} + \hat{\zeta}_c \hat{\zeta}_f + \hat{\zeta}_{cf} \hat{\zeta}_f\right)}{\left(\alpha_c + \alpha_f\right)^2 \hat{\zeta}_{cf} + \alpha_c^2 \hat{\zeta}_f + \alpha_f^2 \hat{\zeta}_c + \frac{z_w^2}{\hat{\zeta}_w}\left(\hat{\zeta}_c \hat{\zeta}_{cf} + \hat{\zeta}_c \hat{\zeta}_f + \hat{\zeta}_{cf} \hat{\zeta}_f\right)},$$

and the $\hat{h}$ functions describing counter-current flow are given by

$$\hat{h}_1(\alpha_c, \alpha_f) := \frac{\hat{\lambda}_c \hat{\lambda}_w}{\hat{\lambda}_T}$$

$$= \frac{\alpha_c \frac{z_w^2}{\hat{\zeta}_w}\left[\alpha_c\left(\hat{\zeta}_f + \hat{\zeta}_{cf}\right) + \alpha_f \hat{\zeta}_{cf}\right]}{\left(\alpha_c + \alpha_f\right)^2 \hat{\zeta}_{cf} + \alpha_c^2 \hat{\zeta}_f + \alpha_f^2 \hat{\zeta}_c + \frac{z_w^2}{\hat{\zeta}_w}\left(\hat{\zeta}_c \hat{\zeta}_{cf} + \hat{\zeta}_c \hat{\zeta}_f + \hat{\zeta}_{cf} \hat{\zeta}_f\right)} \phi$$

$$\hat{h}_2(\alpha_c, \alpha_f) := \frac{\hat{\lambda}_c \hat{\lambda}_f}{\hat{\lambda}_T} - \frac{\alpha_c \alpha_f \hat{\zeta}_{cf}}{\hat{\zeta}_c \hat{\zeta}_f + \hat{\zeta}_{cf}\left(\hat{\zeta}_c + \hat{\zeta}_f\right)} \phi$$

$$= \frac{\alpha_c \alpha_f\left(\alpha_c \alpha_f - \frac{z_w^2}{\hat{\zeta}_w} \hat{\zeta}_{cf}\right)}{\left(\alpha_c + \alpha_f\right)^2 \hat{\zeta}_{cf} + \alpha_c^2 \hat{\zeta}_f + \alpha_f^2 \hat{\zeta}_c + \frac{z_w^2}{\hat{\zeta}_w}\left(\hat{\zeta}_c \hat{\zeta}_{cf} + \hat{\zeta}_c \hat{\zeta}_f + \hat{\zeta}_{cf} \hat{\zeta}_f\right)} \phi \quad (29)$$

$$\hat{h}_3(\alpha_c, \alpha_f) := \frac{\hat{\lambda}_f \hat{\lambda}_w}{\hat{\lambda}_T}$$

$$= \frac{\alpha_f \frac{z_w^2}{\hat{\zeta}_w}\left[\alpha_c \hat{\zeta}_{cf} + \alpha_f\left(\hat{\zeta}_c + \hat{\zeta}_{cf}\right)\right]}{\left(\alpha_c + \alpha_f\right)^2 \hat{\zeta}_{cf} + \alpha_c^2 \hat{\zeta}_f + \alpha_f^2 \hat{\zeta}_c + \frac{z_w^2}{\hat{\zeta}_w}\left(\hat{\zeta}_c \hat{\zeta}_{cf} + \hat{\zeta}_c \hat{\zeta}_f + \hat{\zeta}_{cf} \hat{\zeta}_f\right)} \phi.$$

where the coefficients $\hat{\lambda}_c, \hat{\lambda}_w, \hat{\lambda}_f$ and $\hat{\lambda}_T$ are generalized mobility functions given by

$$\hat{\lambda}_c = \frac{\alpha_c\left[\alpha_c\left(\hat{\zeta}_{cf} + \hat{\zeta}_f\right) + \alpha_f \hat{\zeta}_{cf}\right]}{\hat{\zeta}_c \hat{\zeta}_f + \hat{\zeta}_{cf}\left(\hat{\zeta}_c + \hat{\zeta}_f\right)} \phi$$

$$\hat{\lambda}_f = \frac{\alpha_f\left[\alpha_c \hat{\zeta}_{cf} + \alpha_f\left(\hat{\zeta}_c + \hat{\zeta}_{cf}\right)\right]}{\hat{\zeta}_c \hat{\zeta}_f + \hat{\zeta}_{cf}\left(\hat{\zeta}_c + \hat{\zeta}_f\right)} \phi$$

$$\hat{\lambda}_w = \frac{z_w^2}{\hat{\zeta}_w} \phi \quad (30)$$

$$\hat{\lambda}_T = \frac{\left(\alpha_c + \alpha_f\right)^2 \hat{\zeta}_{cf} + \alpha_c^2 \hat{\zeta}_f + \alpha_f^2 \hat{\zeta}_c + \frac{z_w^2}{\hat{\zeta}_w}\left(\hat{\zeta}_c \hat{\zeta}_{cf} + \hat{\zeta}_c \hat{\zeta}_f + \hat{\zeta}_{cf} \hat{\zeta}_f\right)}{\hat{\zeta}_c \hat{\zeta}_f + \hat{\zeta}_{cf}\left(\hat{\zeta}_c + \hat{\zeta}_f\right)} \phi,$$

Using the chosen correlations for the biomechanical interaction forces $\zeta_w, \zeta_c, \zeta_f$ and ζ_{cf} in (17)–(20) and by assuming constant porosity the model (24) then takes the simpler form

$$\alpha_{ct} + \nabla \cdot (\alpha_c \mathbf{u}_c) = S_c$$

$$\alpha_{ft} + \nabla \cdot (\alpha_f \mathbf{u}_f) = S_f$$

$$\rho_t = -\lambda_{21} G \rho + \rho\left(\lambda_{22} - \lambda_{23}\alpha_c - \lambda_{24}\left(\frac{\rho}{\rho_M}\right)\right)$$

$$G_t = \nabla \cdot (D_G \nabla G) - \nabla \cdot (\mathbf{u}_w G) - \lambda_{31} G$$

$$\quad + (\alpha_c + \alpha_f)\left(\lambda_{32} - \lambda_{33}\left(\frac{G}{G_M}\right)^{v_G}\right) \quad (31)$$

$$C_t = \nabla \cdot (D_C \nabla C) - \nabla \cdot (\mathbf{u}_w C) - Cr_C Q_l$$

$$\quad + G \rho\left(\lambda_{41} - \lambda_{42}\left(\frac{C}{C_M}\right)^2 - \lambda_{43}\left(\frac{C}{C_M}\right)^{v_C}\right) - \lambda_{44}\alpha_c C$$

$$H_t = \nabla \cdot (D_H \nabla H) - \nabla \cdot (\mathbf{u}_w H) - \lambda_{51} H$$

$$\quad + \alpha_f\left(\lambda_{52} - \lambda_{53}\left(\frac{H}{H_M}\right)^2 - \lambda_{54}\left(\frac{H}{H_M}\right)^{v_H}\right) - \lambda_{55}\alpha_f H,$$

The cell velocity $\mathbf{u}_c$ is given by $(27)_1$, fibroblast velocity $\mathbf{u}_f$ is given by $(27)_2$ and finally the interstital fluid velocity $\mathbf{u}_w$ is given by $(27)_3$. $\mathbf{u}_w$ appears in the advective terms in the transport-reaction equations for G, C and H which means that the chemical components flows with the interstitial fluid. In order to compute $\mathbf{U}_T$, which is used to calculate the interstitial velocities of the phases, we first solve the elliptic problem for P_w

$$\nabla \cdot \left(\hat{\lambda}_T \nabla P_w\right) = -T_v\left(\widetilde{P}_v^* - P_w\right) + T_l\left(P_w - \widetilde{P}_l^*\right)$$

$$\quad - \nabla \cdot \left(\hat{\lambda}_c \nabla (\Delta P_{cw} + \Lambda_C(C))\right) - \nabla \cdot \left(\hat{\lambda}_f \nabla \Lambda_H\right) \quad (32)$$

$$P_w|_{\partial\Omega} = P_B^*$$

Knowing IF pressure P_w we find the total velocity $\mathbf{U}_T$ by

$$\mathbf{U}_T = \mathbf{U}_c + \mathbf{U}_f + \mathbf{U}_w$$

$$\quad = -\hat{\lambda}_T \nabla P_w - \hat{\lambda}_c \nabla (\Delta P_{cw} + \Lambda_C) - \hat{\lambda}_f \nabla \Lambda_H, \quad (33)$$

where $\mathbf{U}_i, i = w, c, f$, is the superficial velocity and are given as the product of the interstitial phase velocity and its respective volume fraction $\mathbf{U}_i = \alpha_i \mathbf{u}_i$.

Appendix B. Non-Dimensionalization

In this section we want to obtain the dimensionless version of the model (14). We introduce characteristic length L^* and time T^* in addition to characteristic concentration and pressure: $G^*, C^*, H^*, \rho^*, P^*$ with corresponding characteristic velocity u^* and diffusion D^*

$$u^* = \frac{L^*}{T^*}, \quad D^* = \frac{(L^*)^2}{T^*}$$

with dimensionless space and time variables

$$\bar{x} = \frac{x}{L^*}, \quad \tilde{t} = \frac{t}{\phi T^*},$$

where the tilde emphasizes that it is a dimensionless variable. In addition, we choose dimensionless variables related to the concentrations of the chemical components, the phase pressures and velocities, in the following way

$$\tilde{\rho} = \frac{\rho}{\rho^*}, \quad \widetilde{G} = \frac{G}{G^*}, \quad \widetilde{C} = \frac{C}{C^*}, \quad \widetilde{H} = \frac{H}{H^*},$$

$$\widetilde{D}_G = \frac{D_G}{D^*}, \quad \widetilde{D}_C = \frac{D_C}{D^*}, \quad \widetilde{D}_H = \frac{D_H}{D^*},$$

$$\widetilde{P}_l = \frac{P_l}{P^*}, \quad \tilde{\mathbf{u}}_l = \frac{\mathbf{u}_l}{u^*}, \quad (l = c, f, w) \quad \widetilde{Q} = QT^*.$$

For production, decay and consumption of the chemical agents, we are going to use the following set of dimensionless expressions

$$\rho: \tilde{\lambda}_{21} = \lambda_{21} T^* G^*, \quad \tilde{\lambda}_{22} = \lambda_{22} T^*, \quad \tilde{\lambda}_{23} = \lambda_{23} T^*, \quad \tilde{\lambda}_{24} = \lambda_{24} T^*,$$

$$G: \tilde{\lambda}_{31} = \lambda_{31} T^*, \quad \tilde{\lambda}_{32} = \frac{\lambda_{32} T^*}{G^*}, \quad \tilde{\lambda}_{33} = \frac{\lambda_{33} T^*}{G^*},$$

$$C: \tilde{\lambda}_{41} = \frac{\lambda_{41} T^* G^* \rho^*}{C^*}, \quad \tilde{\lambda}_{42} = \frac{\lambda_{42} T^* G^* \rho^*}{C^*}, \quad \tilde{\lambda}_{43} = \frac{\lambda_{43} T^* G^* \rho^*}{C^*},$$

$$\quad \tilde{\lambda}_{44} = \lambda_{44} T^*,$$

$$H: \tilde{\lambda}_{51} = \lambda_{51} T^*, \quad \tilde{\lambda}_{52} = \frac{\lambda_{52} T^*}{H^*}, \quad \tilde{\lambda}_{53} = \frac{\lambda_{53} T^*}{H^*}, \quad \tilde{\lambda}_{54} = \frac{\lambda_{54} T^*}{H^*},$$

$$\quad \tilde{\lambda}_{55} = \lambda_{55} T^*.$$

The potential and capillary pressure functions are having units of pressure, and therefore they can be made dimensionless by dividing by the reference pressure, P^*:

$$\bar{\Lambda}_C = \frac{\Lambda_C}{P^*}, \quad \bar{\Lambda}_{C0} = \frac{\Lambda_{C0}}{P^*}, \quad \bar{\Lambda}_{C1} = \frac{\Lambda_{C1}}{P^*}, \quad \tilde{\xi}_C = \xi_C C^*,$$

$$\bar{\Lambda}_C = \frac{\Lambda_C}{P^*}, \quad \bar{\Lambda}_{H0} = \frac{\Lambda_{H0}}{P^*}, \quad \bar{\Lambda}_{H1} = \frac{\Lambda_{H1}}{P^*}, \quad \tilde{\xi}_H = \xi_H H^*,$$

$$\Delta\widetilde{P}_{cw} = \frac{\Delta P_{cw}}{P^*}, \quad \tilde{\gamma} = \frac{\gamma}{P^*}.$$

Note that using (16) the chemokine potential function can now be written (similar for TGF)

$$\bar{\Lambda}_C = \frac{\Lambda_C}{P^*} = \bar{\Lambda}_{C0} - \frac{\bar{\Lambda}_{C1}}{1 + \exp[-\xi_C(C - C_M)]}$$

$$= \bar{\Lambda}_{C0} - \frac{\bar{\Lambda}_{C1}}{1 + \exp\left[-\tilde{\xi}_C\left(\widetilde{C} - \widetilde{C}_M\right)\right]}.$$

Interaction coefficients

$$\tilde{\tilde{\zeta}}_c = \hat{\zeta}_c \frac{D^*}{P^*}, \qquad \tilde{\tilde{\zeta}}_f = \hat{\zeta}_f \frac{D^*}{P^*}, \qquad \tilde{\tilde{\zeta}}_w = \hat{\zeta}_w \frac{D^*}{P^*}, \qquad \tilde{\tilde{\zeta}}_{cf} = \hat{\zeta}_{cf} \frac{D^*}{P^*}.$$

Let's proceed with the details of rewriting the model (14) subject to the condition that phases are incompresible and using (23), which gives us

$$
\begin{aligned}
&(\phi \alpha_c)_t + \nabla \cdot (\alpha_c \mathbf{u}_c) = S_c \\
&(\phi \alpha_f)_t + \nabla \cdot (\alpha_f \mathbf{u}_f) = S_f, \\
&(\phi \alpha_w)_t + \nabla \cdot (\alpha_w \mathbf{u}_w) = -S_c - S_f + Q \\
&\alpha_c \nabla (P_w + \Delta P_{cw} + \Lambda_C) = -\frac{\hat{\zeta}_c}{\phi} \mathbf{u}_c + \frac{\hat{\zeta}_{cf}}{\phi} (\mathbf{u}_f - \mathbf{u}_c) \\
&\alpha_f \nabla (P_w + \Lambda_H) = -\frac{\hat{\zeta}_f}{\phi} \mathbf{u}_f - \frac{\hat{\zeta}_{cf}}{\phi} (\mathbf{u}_f - \mathbf{u}_c) \\
&\alpha_w \nabla P_w = -\frac{\hat{\zeta}_w}{\phi} \mathbf{u}_w \\
&(\rho \phi)_t = -\lambda_{21} G \rho + \rho \left(\lambda_{22} - \lambda_{23} \alpha_c - \lambda_{24} \left(\frac{\rho}{\rho_M} \right) \right) \\
&(\phi \alpha_w G)_t = \nabla \cdot (D_G \nabla G) - \nabla \cdot (\mathbf{u}_w G) - \lambda_{31} G \\
&\quad + (\alpha_c + \alpha_f) \left(\lambda_{32} - \lambda_{33} \left(\frac{G}{G_M} \right)^{\nu_G} \right) \\
&(\phi \alpha_w C)_t = \nabla \cdot (D_C \nabla C) - \nabla \cdot (\mathbf{u}_w C) - CM_c Q_l \\
&\quad + G \rho \left(\lambda_{41} - \lambda_{42} \left(\frac{C}{C_M} \right)^2 - \lambda_{43} \left(\frac{C}{C_M} \right)^{\nu_C} \right) - \lambda_{44} \alpha_c C, \\
&(\phi \alpha_w H)_t = \nabla \cdot (D_H \nabla H) - \nabla \cdot (\mathbf{u}_w H) - HM_H Q_l - \lambda_{51} H \\
&\quad + \alpha_f \left(\lambda_{52} - \lambda_{53} \left(\frac{H}{H_M} \right)^2 - \lambda_{54} \left(\frac{H}{H_M} \right)^{\nu_H} \right) - \lambda_{55} \alpha_f H
\end{aligned}
\tag{34}
$$

We use the transformation $(x, t) \rightarrow (\tilde{x}, \tilde{t})$ in combination with the dimensionless variables defined above. This yields the following dimensionless version of the model

$$
\begin{aligned}
&(\alpha_c)_{\tilde{t}} + \nabla \cdot (\alpha_c \tilde{\mathbf{u}}_c) = \widetilde{S}_c \\
&(\alpha_f)_{\tilde{t}} + \nabla \cdot (\alpha_f \tilde{\mathbf{u}}_f) = \widetilde{S}_f, \\
&(\alpha_w)_{\tilde{t}} + \nabla \cdot (\alpha_w \tilde{\mathbf{u}}_w) = -\widetilde{S}_c - \widetilde{S}_f + \widetilde{Q} \\
&\alpha_c \nabla \left(\widetilde{P}_w + \Delta \widetilde{P}_{cw} + \tilde{\Lambda}_C \right) = -\frac{\tilde{\tilde{\zeta}}_c}{\phi} \tilde{\mathbf{u}}_c + \frac{\tilde{\tilde{\zeta}}_{cf}}{\phi} (\tilde{\mathbf{u}}_f - \tilde{\mathbf{u}}_c) \\
&\alpha_f \nabla \left(\widetilde{P}_w + \tilde{\Lambda}_H \right) = -\frac{\tilde{\tilde{\zeta}}_f}{\phi} \tilde{\mathbf{u}}_f - \frac{\tilde{\tilde{\zeta}}_{cf}}{\phi} (\tilde{\mathbf{u}}_f - \tilde{\mathbf{u}}_c) \\
&\alpha_w \nabla \widetilde{P}_w = -\frac{\tilde{\tilde{\zeta}}_w}{\phi} \tilde{\mathbf{u}}_w \\
&\tilde{\rho}_t = -\tilde{\lambda}_{21} \widetilde{G} \tilde{\rho} + \tilde{\rho} \left(\tilde{\lambda}_{22} - \tilde{\lambda}_{23} \alpha_c - \tilde{\lambda}_{24} \left(\frac{\tilde{\rho}}{\rho_M} \right) \right) \\
&\left(\alpha_w \widetilde{G} \right)_t = \nabla \cdot \left(\widetilde{D}_G \nabla \widetilde{G} \right) - \nabla \cdot \left(\tilde{\mathbf{u}}_w \widetilde{G} \right) - \tilde{\lambda}_{31} \widetilde{G} \\
&\quad + (\alpha_c + \alpha_f) \left(\tilde{\lambda}_{32} - \tilde{\lambda}_{33} \left(\frac{\widetilde{G}}{G_M} \right)^{\nu_G} \right) \\
&\left(\alpha_w \widetilde{C} \right)_t = \nabla \cdot \left(\widetilde{D}_C \nabla \widetilde{C} \right) - \nabla \cdot \left(\tilde{\mathbf{u}}_w \widetilde{C} \right) - \widetilde{C} M_c \widetilde{Q}_l \\
&\quad + \widetilde{G} \tilde{\rho} \left(\tilde{\lambda}_{41} - \tilde{\lambda}_{42} \left(\frac{\widetilde{C}}{C_M} \right)^2 - \tilde{\lambda}_{43} \left(\frac{\widetilde{C}}{C_M} \right)^{\nu_C} \right) - \tilde{\lambda}_{44} \alpha_c \widetilde{C}, \\
&\left(\alpha_w \widetilde{H} \right)_t = \nabla \cdot \left(\widetilde{D}_H \nabla \widetilde{H} \right) - \nabla \cdot \left(\tilde{\mathbf{u}}_w \widetilde{H} \right) - \widetilde{H} M_H \widetilde{Q}_l - \tilde{\lambda}_{51} \widetilde{H} \\
&\quad + \alpha_f \left(\tilde{\lambda}_{52} - \tilde{\lambda}_{53} \left(\frac{\widetilde{H}}{H_M} \right)^2 - \tilde{\lambda}_{54} \left(\frac{\widetilde{H}}{H_M} \right)^{\nu_H} \right) - \tilde{\lambda}_{55} \alpha_f \widetilde{H}
\end{aligned}
\tag{35}
$$

References

Andersen, L.M.K., Wegner, C.S., Simonsen, T.G., Huang, R., Gaustad, J.V., Hauge, A., Galappathi, K., Rofstad, E.K., 2017. Lymph node metastasis and the physicochemical microenvironment of pancreatic ductal adenocarcinoma xenografts. Oncotarget 8, 48060–48074.

Bear, J., 2018. Modeling Phenomena of Flow and Transport in Porous Media. Theory and Application of Transport in Porous Media Interpore.

Binder, C., Chuang, E., Habla, C., Bleckmann, A., Schulz, M., Bathgate, R., Einspaner, A., 2014. Relaxins enhance growth of spontaneous murine breast cancers as well as metastatic colonization of the brain. Clin. Exp. Metastasis 31, 57–65.

Bookbinder, L.H., Hofer, A., Haller, M.F., Zepeda, M.L., Keller, G.A., Lim, J.E., Edgington, T.S., Shepard, H.M., Patton, J.S., Frost, G.I., 2006. A recombinant human enzyme for enhanced interstitial transport of therapeutics. J. Control Release 114, 230–241.

Brown, E., McKee, T., diTomaso, E., Pluen, A., Seed, B., Boucher, Y., Jain, R.K., 2003. Dynamic imaging of collagen and its modulation in tumors in vivo using second-harmonic generation. Nat. Med. 9, 796–800.

Chary, S.R., Jain, R.K., 1989. Direct measurement of interstitial convection and diffusion of albumin in normal and neoplastic tissues by fluorescence photobleaching. PNAS 86, 5385–5389.

Chauhan, V.P., Stylianopoulos, T., Boucher, Y., Jain, R.K., 2011. Delivery of molecular and nanoscale medicine to tumors: transport barriers and strategies. Annu. Rev. Chem. Biomol. Eng. 2, 281–298.

Dasari, S., Fang, Y., Mitra, A.K., 2018. Cancer associated fibroblasts: naughty neighbors that drive ovarian cancer progression. Cancers 10.

Drew, D.A., Passman, S.L., 1999. Theory of Multicomponent Fluids. Springer.

Evje, S., 2017. An integrative multiphase model for cancer cell migration under influence of physical cues from the microenvironment. Chem. Eng. Sci. 165, 240–259.

Evje, S., Waldeland, J.O., 2019. How tumor cells possibly can make use of interstitial fluid flow in a strategy for metastasis. Cel. Mol. Bioeng. 12 (3), 227–254.

Friedl, P., Wolf, K., 2003. Tumour-cell invasion and migration: diversity and escape mechanisms. Nat. Rev. Cancer 3 (5), 362–374.

Friedl, P., Locker, J., Sahai, E., Segall, J.E., 2012. Classifying collective cancer cell invasion. Nat. Cell Biol. 14 (8), 777–783.

Gaggioli, C. et al., 2007. Fibroblast-led collective invasion of carcinoma cells with differing roles for RhoGTPases in leading and following cells. Nat. Cell. Biol. 9, 1392–1400.

Gray, R.S., Cheung, K.J., Ewald, A.J., 2010. Cellular mechanisms regulating epithelial morphogenesis and cancer invasion. Curr. Opin. Cell Biol. 22 (5), 640–650.

Hompland, T., Ellingsen, C., Øvrebø, K.M., Rofstad, E.K., 2012. Interstitial fluid pressure and associated lymph node metastasis revealed in tumors by dynamic contrast-enhanced MRI. Cancer Res. 72, 4899–4908.

Kalluri, R., Zeisberg, M., 2006. Fibroblasts in cancer. Nat. Rev. Cancer 6, 392–401.

Labernadie, A. et al., 2017. A mechanically active heterotypic E-cadherin/N-cadherin adhesion enables fibroblasts to drive cancer cell invasion. Nat. Cell. Biol. 19, 224–236.

Lakiotaki, E., Sakellariou, S., Evangelou, K., Liapis, G., Patsouris, E., Delladetsima, I., 2016. Vascular and ductal elastotic changes in pancreatic cancer. APMIS 124, 181–187.

Lambert, A.W., Pattabiraman, D.R., Weinberg, R.A., 2018. Emerging biological principles of metastasis. Cell 168 (4), 670–691.

Lautscham, L.A. et al., 2014. Biomembrane-mimicking lipid bilayer system as a mechanically tunable cell substrate. Biomaterials 35, 3198–3207.

Liotta, L.A., Tryggvason, K., Garbisa, S., Foltz, C.M., Shafie, S., 1980. Metastatic potential correlates with enzymatic degradation of basement membrane collagen. Nature 284 (67–68), 1980.

Massagué, J., 2008. TGFbeta in cancer. Cell 134, 215–230.

Mayor, R., Etienne-Manneville, S., 2016. The front and rear of collective cell migration. Nat. Rev. Mol. Cell Biol. 17 (2), 97–109.

Perentes, J.Y. et al., 2009. In vivo imaging of extracellular matrix remodeling by tumor-associated fibroblasts. Nat. Meth. 6, 143–145.

Polacheck, W.J., Charest, J.L., Kamm, R.D., 2011. Interstitial flow influences direction of tumor cell migration through competing mechanisms. PNAS 108, 11115–11120.

Qiao, Y., Andersen, P.Ø., Evje, S., Standnes, D.C., 2018. A mixture theory approach to model co- and counter-current two-phase flow in porous media accounting for viscous coupling. Adv. Water. Resour. 112, 170–188.

Qiao, Y., Wen, H., Evje, S., 2019. Compressible and viscous two-phase flow in porous media based on mixture theory formulation. Netw. Het. Media 14 (3), 489–536.

Rajagopal, K.R., 2007. On a hierarchy of approximate models for flows of incompressible fluids through porous solids. Math. Mod. Met. Appl. Sci. 17, 215–252.

Schwager, S.C., Taufalele, P.V., Reinhart-King, C.A., 2019. Cell-cell mechanical communication in cancer. Cel. Mol. Bioeng. 12 (1), 1–12.

Shieh, A.C., Rozansky, H.A., Hinz, B., Swartz, M.A., 2011. Tumor cell invasion is promoted by interstitial flow-induced matrix priming by stromal fibroblasts. Cancer Res. 71, 790–800.

Shields, J.D. et al., 2007. Autologous chemotaxis as a mechanism of tumor cell homing to lymphatics via interstitial flow and autocrine CCR7 signaling. Cancer Cell 11, 526–538.

Shukla, V.C., Higuita-Castro, N., Nana-Sinkam, P., Ghadiali, S.N., 2016. Substrate stiffness modulates lung cancer cell migration but not epithelial to mesenchymal transition. J. Biomed. Mater. Res. A. 104, 1182–1193.

Standnes, D.C., Evje, S., Andersen, P.O., 2017. A novel relative permeability model based on mixture theory approach accounting for solid-fluid and fluid-fluid interactions. Tran. Por. Media 119, 707–738.

Togo, S., Polanska, U.M., Horimoto, Y., Orimo, A., 2013. Carcinoma-Associated Fibroblasts are a promising therapeutic target. Cancers 5, 149–169.

Urdal, J., Waldeland, J.O., Evje, S., 2019. Enhanced cancer cell invasion caused by fibroblasts when fluid flow is present. Biomech. Model. Mechanobiol. 18 (4), 1047–1078.

von Ahrens, D., Bhagat, T.D., Nagrath, D., Maitra, A., Verma, A., 2017. The role of stromal cancer-associated fibroblasts in pancreatic cancer. J. Hematol. Oncol. 10.

Waldeland, J.O., Evje, S., 2018. A multiphase model for exploring cancer cell migration driven by autologous chemotaxis. Chem. Eng. Sci. 119, 268–287.

Waldeland, J.O., Evje, S., 2018. Competing tumor cell migration mechanisms caused by interstitial fluid flow. J. Biomech. 81, 22–35.

Wiig, H., Swartz, M.A., 2012. Interstitial fluid and lymph formation and transport: physiological regulation and roles in inflammation and cancer. Physiol. Rev. 92, 1005–1060.

Wu, Y.S., 2016. Multiphase Fluid Flow in Porous and Fractured Reservoirs. Elsevier.

VI

Paper VI

In silico investigations of intratumoral heterogeneous interstitial fluid pressure

By:

Waldeland, Jahn Otto
Gaustad, Jon-Vidar
Rofstad, Einar K.
Evje, Steinar

Submitted

In silico investigations of intratumoral heterogenous interstitial fluid pressure

Jahn Otto Waldeland[1] · Jon-Vidar Gaustad[2] · Einar K. Rofstad[2] · Steinar Evje[1,*]

Abstract Recent preclinical studies have shown that interstitial fluid pressure (IFP) within tumors can be heterogenous [Andersen, et al. (2019), Translational Oncology, 12:1079-1085]. In that study tumors of two xenograft models, respectively, HL-16 cervical carcinoma and Panc-1 pancreatic carcinoma, were investigated. Significant heterogeneity in IFP was reported and it was proposed that this was associated with division of tissue into compartments separated by thick connective tissue bands for the HL-16 tumors and with dense collagen-rich extracellular matrix for the Panc-1 tumors. We consider a previously developed computational model which accounts for tumor cells, fibroblasts and interstitial fluid. The model has been trained to comply with experimental *in vitro* results reported in [Shieh, et al.(2011) Cancer Res. 71:790-800] which has identified autologous chemotaxis, ECM remodeling, and cell-fibroblast interaction as drivers for invasive tumor cell behavior. The in silico model is informed with parameters that characterize the leaky intratumoral vascular network, the peritumoral lymphatics which collect the fluid, and the density of ECM as represented through the hydraulic conductivity of the interstitial space. To adhere to the situation that not much detailed information is available for these parameters we generate them randomly but constrained by information from the preclinical study to ensure that the resulting IFP lies within a pathological reasonable range. The in silico cervical carcinoma model illustrates that sparse ECM was associated with uniform intratumoral IFP in spite of heterogenous microvascular network, whereas compartment structures resulted in more heterogenous IFP. Similarly, the in silico pancreatic model shows that heterogeneity in the microvascular network combined with dense ECM structure prevents IFP to even out and gives rise to heterogenous IFP. The computer model illustrates how a heterogenous invasive front might form where groups of tumor cells detach from the primary tumor and form isolated islands, a behavior which is natural to associate with metastatic propensity. However, unlike experimental studies, the current version of the in silico model does not show an association between metastatic propensity and elevated IFP.

Keywords cervical carcinoma, pancreatic carcinoma, mathematical modeling, fibroblast, ECM, interstitial fluid pressure, hydraulic conductivity, vascular network, lymphatics

1 Introduction

1.1 PDAC characteristics

Pancreatic ductal adenocarcinoma (PDAC) patients develop lymph node metastases early and have a particularly poor prognosis. Most PDACs are resistant to chemotherapy and radiation treatment [1] and surgery is the only treatment modality that may result in cure [2]. Metastatic spread into and through lymphatics and lymph nodes occurs frequently in PDAC patients. The microenvironment of PDACs is characterized by an abundant desmoplastic stroma that may occupy up to 80% of the tumor volume [3–5]. The PDAC stroma consists of a dynamic assortment of extracellular matrix components including fibronectin, collagen, proteoglycans, and hyaluronic acid, nonmalignant cells including fibroblasts, endothelial cells, and immune cells, and

[1]University of Stavanger, NO-4068 Stavanger, Norway
[2]Department of Radiation Biology, Institute for Cancer Research, Oslo University Hospital, Oslo, Norway
*Corresponding author. E-mail: steinar.evje@uis.no

soluble proteins such as growth factors and cytokines [5]. Recent investigations have revealed that the PDAC stroma represents a physical barrier to the delivery of chemotherapeutic agents and simultaneously supports tumor growth and promotes metastatic dissemination [3–5]. The development of an abundant stroma during tumor growth distorts the architecture of the normal pancreas, resulting in an abnormal configuration of blood vessels and lymphatics in PDACs [6–8]. Geometric resistance to blood flow is high in microvascular networks showing high fractions of low-diameter vessels, resulting in elevated microvascular pressure. Preclinical and clinical investigations have revealed that PDACs may show highly elevated interstitial fluid pressure (IFP) [9–11] as well as high fractions of hypoxic tissue [12–14]. The dense desmoplastic stroma has been suggested to be a determinant of the aggressive metastatic growth of PDACs [3–5]. There is some evidence that PDAC metastasis is promoted by direct interactions between the parenchymal tumor cells and the cellular and/or matrix components of the stroma [15,16]. It has been searched for associations between lymph node metastasis and features of the physicochemical microenvironment in an attempt to identify mechanisms leading to metastatic dissemination and growth. Two different xenografts were used as preclinical models of human PDAC in [17]. In both models, lymph node metastasis was associated with high IFP rather than high fraction of hypoxic tissue or high microvascular density.

1.2 Cervical carcinoma characteristics

Locally advanced squamous cell carcinoma of the uterine cervix is treated with radiation therapy alone or radiation therapy in combination with chemotherapy and/or surgery. The recommended treatment in the western world is aggressive concurrent cisplatin-based chemoradiotherapy [18,19], a treatment that results in a 5-year overall survival rate of 60-70% and a high incidence of severe treatment-induced complications, including hematological and gastrointestinal toxicities [20]. The most important tumor-related prognostic factors are tumor volume, stage of disease, and lymph node status [21]. During growth, cervical carcinomas develop a highly hostile physicochemical tumor microenvironment characterized by severe hypoxia, interstitial hypertension, low microvascular density, low extracellular pH, high lactate concentration, low glucose concentration, and energy deprivation [22,23]. This microenvironment causes treatment resistance and promotes malignant progression of the disease, and during the last decade, it has become increasingly clear that the prognostic and predictive values of these microenvironmen-

tal abnormalities are significant. Thus, extensive hypoxia in the primary tumor has been shown to be associated with locoregional treatment failure and poor disease-free and overall survival rates in patients with advanced disease [24–27], and studies of cervical carcinoma patients treated with radiation therapy alone have shown that high interstitial fluid pressure (IFP) in the primary tumor is linked to high probability of pelvic recurrence and distant metastases [28–30]. Moreover, the disease-free and overall survival rates have been shown to be particularly poor for cervical cancer patients with high lactate concentration in the primary tumor [31,32]. Interestingly, Fyles et al. [29] have measured both IFP and oxygen tension in the primary tumor of more than 100 patients with advanced cervical carcinoma, and their study showed no correlation between either IFP or hypoxic fraction and established tumor-related prognostic factors. Furthermore, they observed that the independent prognostic effect of IFP for recurrence and survival was strong, whereas the independent prognostic effect of tumor hypoxia was of borderline significance and was limited to patients without nodal metastatic growth[29].

1.3 CAFS

Fibroblasts in normal tissue are usually single cells residing in the interstitial space. Fibroblasts are non-epithelial and non-immune cells which likely originate from a mesenchymal lineage [33]. Fibroblasts that are recruited into tumor masses, called tumor-associated fibroblasts (TAFs) or cancer-associated fibroblasts (CAFs), are the main cellular components of the surrounding stroma of many solid cancers. Evidently, these CAFs provide a range of different cytokines, growth factors, tissue remodeling enzymes and ECM components, all of which regulate the tumor stroma [34,35]. Gaggioli et al. [36] discovered that fibroblasts may act as leader cells of a collective group of following carcinoma cells. This would allow cancer cells to retain their epithelial features, which is observed in solid tumors *in vivo* and also *in vitro* [37,38], while having a mesenchymal-like cell to lead them to invade the adjacent stroma. Furthermore, Gaggioli proposed that cancer cells move within paths in behind fibroblasts. These paths are created by the fibroblasts both through proteolytic activity and force-mediated matrix remodeling [39]. Fibroblast-enhanced tumor cell migration was investigated by Shieh et al. in the presence of interstitial flow where, similar to Gaggioli et al., the fibroblasts created tracks within the ECM for cancer cells to follow [40]. Later, Labernadie et al. identified another possible mechanism to which fibroblasts lead cancer cells, a heterotypic cell-cell adhesion

between the two types of cell. More specifically, there is a direct mechanical coupling between the fibroblast N-cadherin and the tumor cell E-cadherin [41]. These two mechanisms have been accounted for and are the subject of investigations through a computer model in [42, 43] based on a cell-fibroblast-fluid multiphase formulation. In [42] the proposed cell-fibroblast-fluid model was trained with data from the *in vitro* experiments reported in [40]. A first version of an *in silico* version of the model was explored in the recent work [43] where focus was on demonstrating how tumor cells can invade adjacent tissue by using fibroblasts as leader cells. Motivated by the results of Labernadie et al [41] direct mechanical interaction between fibroblasts and tumor cells are included in the computer model. In addition, the in silico model accounts for the mechanism that moving fibroblasts may remodel ECM, causing tumor cells to migrate in the tracks of ECM created by the fibroblasts, as observed in [36, 40, 44].

1.4 Motivation and objective

The purpose of the study reported in [45] was to determine whether tumors may show significant heterogeneity in IFP in the central region, and moreover, to reveal whether any heterogeneity may have consequences for the assessment of microenvironment-induced tumor aggressiveness. The study was based on the hypothesis that heterogeneous IFP in the central tumor region, if present, is caused by structures that prevent efficient fluid flow in the interstitial space (i.e., related to conductivity). Detailed comparative studies of IFP and tumor histology were carried out using preclinical tumor models, respectively, HL-16 cervical carcinoma xenografts and Panc-1 pancreatic carcinoma xenografts, known to show significant intertumor heterogeneity of the extracellular matrix. At the same time, the occurence of lymph node metastasis was assessed as a measure of the tumor aggressiveness. It was found that when IFP of HL-16 and Panc-1 was measured at two different positions in the tumor center, the values could differ by a factor of up to 1.5 in both tumor models. Moreover, the propensity of the tumors to develop lymph node metastases was associated with the higher but not with the lower of the two IFP values. We are interested in an *in silico* tumor model that can shed light on the observations from studying these preclinical models [45]. Central questions are: (i) Can the in silico model explain the homogeneous IFP observed for HL-16 cervical carcinoma when ECM is without compartments and Panc-1 pancreatic carcinoma when ECM is sparse? (ii) Can the in silico model explain the IFP heterogeneity observed for cervical carcinoma when com-

partments are present? And why should the dense ECM structure for pancreatic carcinoma give rise to IFP heterogeneity? (iii) How does the tumor cell invasion respond to heterogeneities associated with the ECM structure and the corresponding IFP?

2 Method

A brief description of the main components and main mechanisms in the formulation of the in silico tumor model is given in the following. We refer to [42, 43, 46] for more details.

2.1 Cell-fibroblast-fluid model

The mathematical model takes the following form (see Table 1 for description of variables):

$$
\begin{aligned}
&(\alpha_c)_t + \nabla \cdot (\alpha_c \mathbf{u}_c) = S_c \\
&(\alpha_f)_t + \nabla \cdot (\alpha_f \mathbf{u}_f) = S_f, \qquad \alpha_c + \alpha_f + \alpha_w = 1 \\
&(\alpha_w)_t + \nabla \cdot (\alpha_w \mathbf{u}_w) = -S_c - S_f + Q, \quad Q = Q_v - Q_l \\
&\alpha_c \nabla (P_w + \Delta P_{cw} + \Lambda_C) = -\hat{\zeta}_c \mathbf{u}_c + \hat{\zeta}_{cf}(\mathbf{u}_f - \mathbf{u}_c) \\
&\alpha_f \nabla (P_w + \Delta P_{fw} + \Lambda_H) = -\hat{\zeta}_f \mathbf{u}_f - \hat{\zeta}_{cf}(\mathbf{u}_f - \mathbf{u}_c) \\
&\alpha_w \nabla P_w = -\hat{\zeta}_w \mathbf{u}_w \\
&\rho_t = -\lambda_{21} G\rho + \rho\Big(\lambda_{22} - \lambda_{23}\alpha_c - \lambda_{24}(\frac{\rho}{\rho_M})\Big) \qquad (1)\\
&G_t = \nabla \cdot (D_G \nabla G) - \nabla \cdot (\mathbf{u}_w G) - \lambda_{31} G \\
&\qquad + (\alpha_c + \alpha_f)\Big(\lambda_{32} - \lambda_{33}(\frac{G}{G_M})^{\nu_G}\Big) \\
&C_t = \nabla \cdot (D_C \nabla C) - \nabla \cdot (\mathbf{u}_w C) - C M_C Q_l \\
&\qquad + G\rho\Big(\lambda_{41} - \lambda_{42}(\frac{C}{C_M})^2 - \lambda_{43}(\frac{C}{C_M})^{\nu_C}\Big) - \lambda_{44}\alpha_c C \\
&H_t = \nabla \cdot (D_H \nabla H) - \nabla \cdot (\mathbf{u}_w H) - H M_H Q_l - \lambda_{51} H \\
&\qquad + \alpha_f\Big(\lambda_{52} - \lambda_{53}(\frac{H}{H_M})^2 - \lambda_{54}(\frac{H}{H_M})^{\nu_H}\Big) - \lambda_{55}\alpha_f H
\end{aligned}
$$

where $\mathbf{u}_i = (u_i^x, u_i^y)$ for $i = c, f, w$. Eq. $(1)_{1\text{-}3}$ represents the mass balance equations for cancer cells, fibroblasts and interstitial fluid, respectively. The next three equations, $(1)_{4\text{-}6}$, are the corresponding momentum balance equations. The RHS of $(1)_4$ is separated into two terms: $-\hat{\zeta}_c \mathbf{u}_c$ representing the resistance against migration felt by cancer cells from the ECM whereas $\hat{\zeta}_c f(\mathbf{u}_f - \mathbf{u}_c)$ represents the drag force exerted by fibroblasts on cancer cells. $\Delta P_{cw}(\alpha_c)$ and $\Delta P_{fw}(\alpha_f)$ are functions quantifying the elevated pressure seen in the cell phase compared to interstitial fluid. The potential function $\Lambda_C(C)$ represents additional phase pressure that accounts for chemotaxis toward chemokine C. Similarly, The RHS of $(1)_5$ accounts for fibroblast-ECM interaction and

Table 1 Variables for the model (1)

Variable	Description
$\alpha_c, \alpha_f, \alpha_w$	volume fraction of cell, fibroblast and fluid
S_c, S_f	cell growth/death
$\mathbf{u}_c, \mathbf{u}_f, \mathbf{u}_w$	interstitial cell, fibroblast and fluid velocity
ρ, G, C, H	ECM component, protease, chemokine and TGF
P_w	IF pressure
$\Delta P_{fw}, \Delta P_{cw}, \Lambda_C, \Lambda_H$	caf-caf, cell-cell, chemokine, and TGF chemotaxis stress
$\hat{\zeta}_c, \hat{\zeta}_f, \hat{\zeta}_w, \hat{\zeta}_{cf}$	cell-ECM, fibroblast-ECM, fluid-ECM and cell-fibroblast interaction coefficients
λ_{ij}	production/decay rates
D_G, D_C, D_H	diffusion coefficients associated with G, C, H
ν_G, ν_C, ν_H	exponents in logistic function associated with chemical component G, C, H
M_C, M_H	absorption percentage of chemical component C, H into lymphatics
T_v, T_l	conductivity of vascular vessel wall, lymphatic vessel wall
$\widetilde{P}_v^*, \widetilde{P}_l^*$	effective vascular pressure, lymphatic pressure
$\Omega, \Omega_v, \Omega_l$	tumor region, region of intratumoral vascular, peritumoral lymphatic network

cell-fibroblast interaction, respectively, whereas the potential function $\Lambda_H(H)$ accounts for chemotaxis of fibroblasts towards positive gradient in growth factor H. The four remaining equations, $(1)_{7\text{-}10}$, are transport-reaction equations for the ECM and three chemical components, protease, chemokine and TGF.

2.2 Interaction coefficients

The interaction coefficients $\hat{\zeta}_w$, $\hat{\zeta}_c$, $\hat{\zeta}_f$, and $\hat{\zeta}_{cf}$ which are used in the model are as follows [42,43]:

$$\hat{\zeta}_w = I_w \hat{k}_w \alpha_w^{r_w}, \qquad \hat{\zeta}_c = I_c \hat{k}_c \alpha_c^{r_c},$$
$$\hat{\zeta}_f = I_f \hat{k}_f \alpha_f^{r_f}, \qquad \zeta_{cf} = I_{cf} \alpha_c^{r_{cf}} \alpha_f^{r_{fc}}. \qquad (2)$$

The parameters I_w, I_c and I_f (Pa s/m^2) represent static properties of the tissue, whereas $\hat{k}_w$, $\hat{k}_c$ and $\hat{k}_f$ (dimensionless) can account for dynamic properties related to for instance ECM remodeling and fiber alignment or various ECM heterogeneities. The coefficients r_w, r_c, r_f, r_{cf} and r_{fc} (dimensionless) play a similar role to the use of relative permeability functions in standard Darcy's equation approach extended to several phases [47]. I_{cf} is a constant determining the order of magnitude of the cell-fibroblast interaction. We use $I_{cf} = 1000 I_w$ which assumes that not all fibroblasts directly interact with cancer cells. We assume that fibroblasts remodel and degrade the ECM, making it easier for the cancer cells to migrate in their path. This is represented through the following equation:

$$\hat{k}_c = 1 - A\big(1 - \exp(-B\alpha_f)\big) \qquad (3)$$

where A, B are dimensionless constants.

2.3 Starling law

In nearly all tissue, plasma leaks out of blood capillaries, flows through the interstitium and drains into lymphatic vessels, where it passes through lymph nodes before being returned to the venous blood [48]. This circulation is expressed on the RHS of $(1)_3$ through the term $Q = Q_v - Q_l$. The main contributors to interstitial flow Q_v are hydrostatic and osmotic pressure gradients between the vascular and interstitial space. Starling Law is used for the flow of fluid into the interstitium given by

$$Q_v = T_v\big(P_v^* - P_w - \sigma_T(\pi_v^* - \pi_w)\big) = T_v\big(\widetilde{P}_v^* - P_w\big)$$
$$T_v = L_v \frac{S_v}{V} \qquad (4)$$

where $\widetilde{P}_v^* = P_v - \sigma_T(\pi_v^* - \pi_w)$. Here L_v is the hydraulic conductivity (m^{2}s/kg=m/Pa s) of the vessel wall, S_v/V (m^{-1}) the exchange area of blood vessel per unit volume of tissues V. P_v^* and P_w the vascular and interstitial fluid pressure, π_v^* and π_w the osmotic pressure in the vascular and interstitial space and σ_T the osmotic reflection coefficient for plasma proteins.

The lymphatic system drains excessive fluid from the interstitial space and returns it back to the blood circulation, as expressed by Q_l. Tumor lymphatics in cancers are typically not functional in the intratumoral region [48]. The loss of functionality is caused by compressive solid stress that is developed in tumors. Through this stress the intratumoral lymphatic vessels collapse, and therefore lymphatic flow is eliminated. Similar to the expression of Q_v in (4), we use an expression of the following form to express the absorption of fluid through the lymphatics

$$Q_l = T_l(P_w - \widetilde{P}_l^*), \qquad T_l = L_l \frac{S_l}{V}. \qquad (5)$$

Here L_l is the hydraulic conductivity of the lymphatic vessel walls whereas S_l/V is the surface area of the lymphatic vessel per volume unit of tissues V and $\widetilde{P}_l^*$ is the effective lymphatic pressure.

2.4 Cancer cell velocity

From (1) an expression for the interstitial cell velocity $\mathbf{u}_c$ can be derived [42,43]:

$$\mathbf{u}_c = \frac{\hat{f}_c}{\alpha_c}\mathbf{U}_T - \frac{\hat{h}_1 + \hat{h}_2}{\alpha_c}\nabla(\Delta P_{cw}(\alpha_c)) \qquad (6)$$

$$- \frac{\hat{h}_1 + \hat{h}_2}{\alpha_c}\nabla(\Lambda_C(C)) + \frac{\hat{h}_2}{\alpha_c}\nabla\Lambda_H(H) + \frac{\hat{h}_2}{\alpha_c}\nabla(\Delta P_{fw}(\alpha_f))$$

$$\mathbf{u}_f = \frac{\hat{f}_f}{\alpha_f}\mathbf{U}_T + \frac{\hat{h}_2}{\alpha_f}\nabla(\Delta P_{cw}(\alpha_c)) + \frac{\hat{h}_2}{\alpha_f}\nabla(\Lambda_C(C)) \qquad (7)$$

$$- \frac{\hat{h}_2 + \hat{h}_3}{\alpha_f}\nabla\Lambda_H(H) - \frac{\hat{h}_2 + \hat{h}_3}{\alpha_f}\nabla(\Delta P_{fw}(\alpha_f)).$$

We refer to Table 4 for more information related to the functions $\hat{f}_c$, $\hat{f}_f$, and $\hat{h}_1, \hat{h}_2, \hat{h}_3$. The terms on the RHS of (6) represent five different migration mechanisms, resulting in the overall velocity $\mathbf{u}_c$:

(i) Fluid-generated stress
(ii) Diffusion
(iii) Chemotaxis of cells toward concentration gradients in chemokine
(iv) Migration due to fibroblast chemotaxis toward concentration gradients in TGF
(v) Migration due to fibroblast diffusion.

Fluid generated stress (i) represents a co-current transport effect, where the two phases of cancer cell and fluid move in the same direction. The next term (ii) represents diffusive migration of tumor cells whereas (iii) accounts for directional migration of tumor cells towards higher concentration of chemokine C. The two last terms (iv) and (v) represent the mechanical interaction between cancer cells and fibroblasts, as fibroblasts move in the direction of higher concentration of TGF H and spread by diffusion, respectively.

2.5 Summary of the essential aspects of the in silico tumor model

Below is a short summary of the mechanisms of the model which indicates how the model can represent different aspects mentioned in the introduction. (i) First, the computer model has been trained to comply with experimental *in vitro* results reported in [40] which has identied autologous chemotaxis, ECM remodeling, and cell-fibroblast interaction as drivers for invasive tumor

cell behavior. The parameters are given in Table 5 and 7 (Appendix) and characterize the aggressivity of the cell line that is studied. (ii) Second, the computer model is informed with data pertaining to the leaky intratumoral microvascular network, the peritumoral collecting lymphatic network, and the density of ECM as represented through the hydraulic conductivity of the interstitial space motivated by observations from the xenograft models reported in [45]. To comply for the situation that not much detailed information are available for these parameters we generate them randomly through a 2D gaussian variogram but constrained by information from the preclinical study [45] to ensure that the resulting intratumoral IFP lies within a pathological reasonable range. (i.e., 10-45 mmHg). A special feature of the cell-fibroblast-fluid model (1) is that it incorporates essential information pertaining to the possibly role played by elevated IFP and interstitial fluid flow. Main mechanisms are:

1. Fluid is produced from the leaky vascular system residing near the periphery of the initial tumor and is absorbed by lymphatics found in the region outside of the primary tumor, characterized by the source terms in $(1)_3$ given by $Q = Q_v - Q_l$. Consequently, the resulting fluid flow field is directed from the vascular to the lymphatic system [49,50].

2. Tumors develop elevated IFP because they show high resistance to blood flow (i.e., $\widetilde{P}_v^*$ in (4) is high), low resistance to transcapillary fluid flow (i.e., T_v in (4) is high), and impaired lymphatic drainage (i.e., Q_l in (5) is located to the peritumoral region). The resistance to blood flow is determined primarily by the density of the microvascular network and the diameter and tortuosity of the vessels. The transcapillary fluid flow is influenced strongly by the permeability of the vessel walls. The lymphatic drainage is determined by the density of the peritumoral lymphatic network and the tumor-induced dilation of the peritumoral lymphatics.

3. The chemical component G (proteases) and H (TGF) are secreted and produced by the two cell types, cancer cells α_c and fibroblasts α_f, whereas chemokine C is released from ECM, as described by $(1)_{7,8,9,10}$. These chemical components diffuse and advect with the fluid flow through $\mathbf{u}_w$, creating chemical gradients downstream of the flow [40].

4. Cancer cells and fibroblasts migrate towards positive gradients of their respective chemotactic chemical, chemokine C and transforming growth factor (TGF) H. Chemotaxis is represented through the potential functions Λ_C and Λ_H appearing in $(1)_{4,5}$. Considering that higher concentrations tend to accumulate in the direction of the lymphatic network,

cancer cells may use these gradients as a means of lymph node metastasis [40]. Our motivation has been to account for autologous chemotaxis which has been observed from in vitro experiments [40,51, 52] and proposed as a possible mechanism for guiding tumor cells toward lymphatics [8,17,49]. Expression of the chemokine CCL21 in lymphatic vessels correlated with increased lymph node metastasis in pancreatic patients [53,54], as did overexpression of CCR7 in pancreatic tumor cells in vivo [54] and supports the choice of autologous chemotaxis as a driver for tumor cell dissemination in the computer model.

5. A large resistance force is imposed on the cancer cells making it difficult for them to migrate on their own, i.e., the cell-ECM interaction coefficient $\hat{\zeta}_c$ in (2) takes a large value. Fibroblasts, on the other hand, are considered much more mobile. In addition, fibroblasts reduce the resistance to migration experienced by cancer cells through the functional form of $\hat{k}_c$ given by (3). Cancer cells may attach themselves onto fibroblasts and/or follow tracks where fibroblasts have migrated due to the diminished resistance in their wake. This yields a largely fibroblast-dependent cancer cell migration, consistent with experimental observations [36,40,41].

3 Results

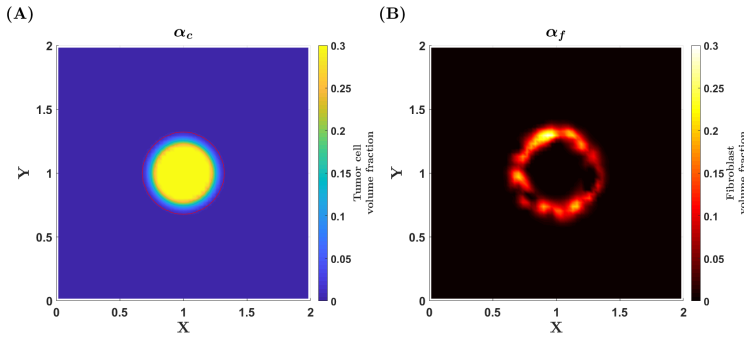## 3.1 Initial volume fraction of fibroblasts and tumor cells

The initial volume fraction of tumor cells and fibroblasts, i.e., the primary tumor and the corresponding fibroblast distribution at time $t = 0$ before the simulation of the growth of the in silico tumor starts, are shown in Figure 1 and is used for all the following cases. (A) shows the primary tumor at time $t = 0$ having a cancer cell volume fraction equal to approximately 0.3 in the center and quickly decreasing towards the periphery. This can be considered an ideal tumor whose margin is smooth and has no heterogeneity or indication of metastatic propensity. The fibroblast volume fraction in (B) is somewhat heterogeneous. Fibroblasts are assumed to surround the tumor in a bandlike region [55, 56]. The fibroblast volume fraction is generated randomly as a Gaussian variogram in 2-D since this represents information related to the ECM status that is not accessible. Simulations are done subject to the condition that the net effect of cell proliferation/apoptosis is zero, i.e., $S_c = S_f = 0$ in $(1)_{1,2,3}$.

3.2 Model input parameters

The workflow when we apply the in silico tumor model is as follows: (i) We assume that the tumor cells are equipped with migration mechanisms as found from in vitro studies [40] as discussed in [42] and reflected by (6) and (7). The chosen set of parameters may be considered as characteristic for the aggressivity of the cell line under investigation. We refer to Table 7 for the specific values used that determine autologous chemotaxis pertaing to chemokine and TGF. The mobility of the fibroblasts and tumor cells is determined by the parameters involved in (6) and (7). We refer to Table 4 and 5 for values used. (ii) The variation in IFP and ECM structure as reflected by the in vivo experimental observations in Figure 2 (A,B,E,F) is accounted for by letting parameters associated with the tissue conductivity through $\hat{k}_w$ in (2), the vascular network through Q_v and the collecting lymphatic network through Q_l vary, possibly, in a heterogenous manner. Further details are given below.

3.3 Intratumoral vascular network, peritumoral lymphatic network, and tissue conductivity

The in silico model (1)-(5) is informed with parameters that characterize the leaky intratumoral vascular network, as expressed through T_v and $\tilde{P}_v^*$ in (4), the peritumoral lymphatics which collect the fluid as expressed through T_l and P_l^* in (5), and the density of ECM as represented by the hydraulic conductivity of the interstitial space through $\hat{k}_w$ involved in the fluid-ECM interaction term $\hat{\zeta}_w$ in (2). In order to take into account that the information about filtration coefficients T_v and T_l is not made available to us, we generate these values randomly through a 2D gaussian variogram. With some constraints on the values generated, we acquire IFP values that are within a pathological reasonable range, i.e., around 10-45 mmHg, as seen in Figure 2 (C). We set maximal intravascular pressure $P_v^* = 6000$ Pa (45 mmHg) and inner lymphatic pressure $P_l^* = 600$ Pa (4.5 mmHg) which typically gives a minimum IFP around -2 mmHg in the peritumoral region which is within the range of -3 to +3 mmHg assumed for normal tissues [57,45], while we vary the other variables $\hat{k}_w$, T_v and T_l for the case with cervical carcinoma as indicated in Table 2.

Fig. 1 Tumor cell and fibroblast status when the simulation of the in silico tumor model starts. **(A)** Initial cancer cell volume fraction. It is assumed the tumor is an ideal tumor, having a constant volume fraction of 0.3. The red contour line shows a volume fraction of 0.01. **(B)** Initial fibroblast volume fraction. The distribution of fibroblasts are generated through a Gaussian variogram, yielding random volume fractions around the tumor.

Table 2 Parameters characterizing the TME of cervical carcinoma

| Case	Variable	Description	Values
Sparse	$\hat{k}_w$	fluid-ECM resistance force	$2.5 - 5$
	$T_v T^*$	Density of leaky blood vessels	$1 \cdot 10^{-4} - 6 \cdot 10^{-3}$ (1/Pa)
	$T_l T^*$	Density of collecting lymphatics	$1 \cdot 10^{-4} - 2 \cdot 10^{-3}$ (1/Pa)
Compartments	$\hat{k}_w$	fluid-ECM resistance force	$\{1, 150\}$
	$T_v T^*$	Density of leaky blood vessels	$1 \cdot 10^{-4} - 6 \cdot 10^{-3}$ (1/Pa)
	$T_l T^*$	Density of collecting lymphatics	$1 \cdot 10^{-4} - 2 \cdot 10^{-3}$ (1/Pa)

3.4 In silico tumor representing cervical carcinoma with homogenous/compartmentalized ECM

We consider an ensemble composed of 50 realizations of $\hat{k}_w$, T_v, and T_l within the range as specified in Table 2 (sparse) to mimic the situation shown in Figure 2 (panel A and E) with homogenous ECM and Table 2 (compartments) to mimic the situation shown in Figure 2 (panel B and F) with compartments. The intervals we allow $\hat{k}_w$, T_v, and T_l to vary within are guided by the information that we want the in silico cervical model to span out IFP in the interval 10 - 45 mmHg consistent with the experimental observations. We represent the tumor histology in Figure 2 E and F through our parameter that accounts for the resistance to fluid flow, $\hat{k}_w$. The experimental case with homogeneous ECM is translated into a uniform $\hat{k}_w$ (panel G), whereas the compartment case is represented by high value $\hat{k}_w$ bands (panel H).

The spatial distribution related to T_v has a Gaussian variogram with practical range of 30 voxels in x and y direction. $T_v T^*$ (where T^* is the reference time, see Table 6) has a standard deviation of 10^{-3} and a mean value of $1.5 \cdot 10^{-3}$. Meanwhile, the spatial distribution of $T_l T^*$ has a Gaussian variogram with practical range of 2 voxels in x and y direction. Each tumor has a different standard deviation and mean value, ranging

from $10^{-4} - 10^{-3}$ and $5 \cdot 10^{-5} - 5 \cdot 10^{-4}$ for the standard deviation and mean value, respectively. The value of $T_l T^*$ cannot exceed four times the mean value of the Gaussian variogram or be negative. See Figure 3 for a typical example.

The distribution of the corresponding different IFPs, as generated by the in silico model and evaluated at two different, fixed positions in the intratumoral region, is shown in Figure 2 (panel C). The ventral IFP and dorsal IFP that describe the axes are merely a description to where the pressure measurements where conducted on the tumor in [45], and we only continue to use the same terminology for our two fixed points within the tumor to be consistent. Comparison with Figure 2 (panel A) reveals that the in silico cervial model largely behaves similarly to the in vivo result reported in [45] showing a homogeneous intratumoral IFP. Moreover, for the compartment case shown in Figure 2 (panel D) the resulting IFP distribution is much more heterogenous, similar to the experimental results in Figure 2 (panel B). As seen from Table 2, the only difference between the two cases is that $\hat{k}_w$ for homogenous ECM can vary within a small interval whereas for the case with arbitrary, high-resistant bands $\hat{k}_w$ will take a very high value where the bands are located. Next, we want to illustrate more details by exploring one of the in silico models shown in Figure 2, first for the case with homogenous ECM
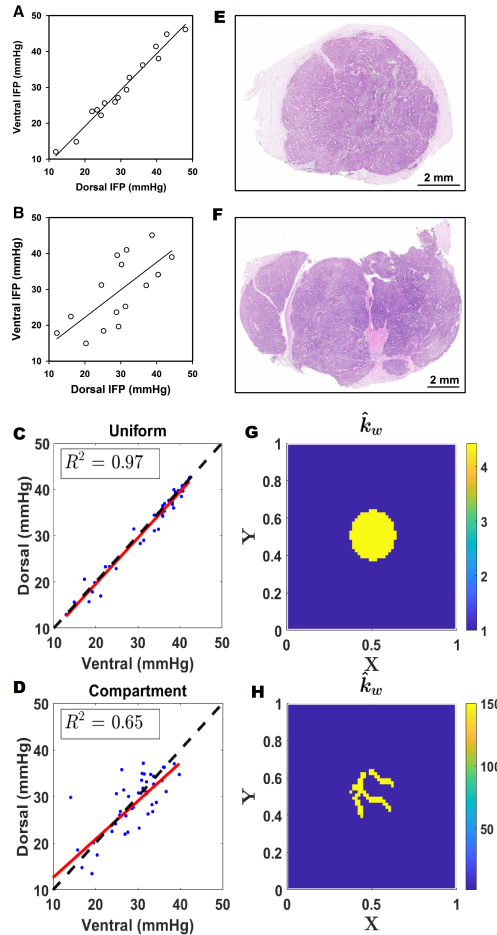
Fig. 2 HL-16 cervical carcinom. Experimental results for (i) homogeneous ECM (A,E); (ii) ECM with compartments (B,F). **A,B** IFP measured at two different locations within a tumor for a total of 15 tumors in both **A** and **B**, for homogeneous ECM seen in **E** and ECM with compartments seen in **F**, respectively. The coefficient of determination for the two plots in **A** and **B** is $R^2 = 0.97$ and $R^2 = 0.49$ respectively. IFP measurements at two locations using 50 simulated tumors are shown in **C** and **D**, with corresponding example tumors seen in **G** and **H**, which are considered representative for **E** and **F**. Panels **(A)**, **(B)**, **(E)** and **(F)** were reproduced from [45][DOI: 10.1016/j.tranon.2019.05.012]

(panel C), then for the case with compartments (panel D). We use one of the high pressure tumors found in Figure 2 (C) as our homogeneous case, without any other preferences than the high pressure. The corresponding tumor with compartments, which has all the same parameters except for the inverse tissue resistance $\hat{k}_w$, is also used for convenience.

3.4.1 Homogenous ECM, high maximal IFP

For this instance we find that the maximal IFP is around 35 mmHg whereas the "measured" dorsal pressure is 29 mmHg and ventral pressure is 32 mmHg. The simulated growth of this in silico model is then computed up to a time $T = 50$ (around 5.8 days). In Figure 3 is an illustration of T_v (panel A), and T_l (panel B). Strong heterogenity is seen both for T_v and T_l. Moreover, in Figure 4 the resulting interstitial fluid pressure (IFP) P_w is shown in panel A whereas the fluid velocity field $\mathbf{u}_w$ is
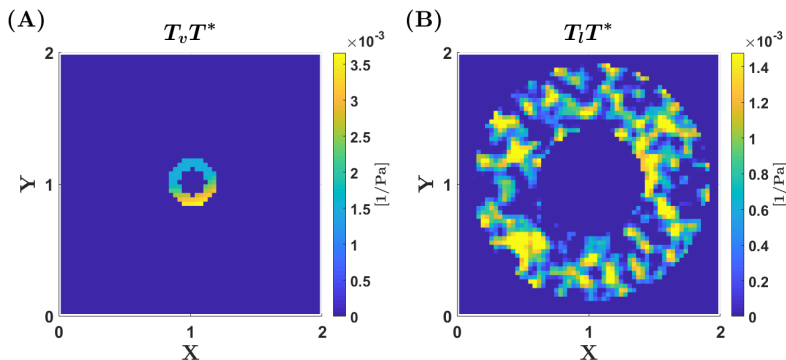
Fig. 3 Parameters characterizing the vascular and lymphatic system, homogenous ECM: **(A)** Vascular filtration constant T_v. The vascular system is placed at the periphery of the primary tumor. **(B)** Lymphatic filtration constant T_l where the lymphatic network is placed in the peritumoral region. The vascular and lymphatic field are both generated through a Gaussian variogram, creating random fields. The filtration constants are multiplied by T^* to yield the unit [1/Pa].

illustrated in panel B. In particular, we observe that the heterogeneity associated with the leaky vascular system through T_v does not lead to heterogenous IFP. In panel C and D the corresponding invasive tumor cell and fibroblast behavior are illustrated. Cancer cells (panel C) are themselves fairly immobile due to the high cell-ECM resistance force through the parameter I_c, see Table 5. Yet, when following fibroblasts (panel D) through direct attachment and/or created tracks they become much more mobile. A strong core of cancer cells remains, as shown in panel C. There are, however, cancer cells following fibroblasts and therefore migrate in sheets away from the primary tumor. Considering the chemical concentration profiles, panel E (chemokine) and panel F (TGF), positive chemical gradients are formed in the vicinity of the lymphatic network. Clearly, the migration of cancer cells rely heavily on fibroblasts. The migration pattern seen in Figure 4 does not explain the possible metastatic behavior where groups of tumor cells are able to detach from the primary tumor and form isolated islands. As an illustration of the potential aggressive behavior involved in the cell-fibroblast interaction we modify the parameters $\{\lambda_{5i}\}_{i=1}^5$ involved in $(1)_{10}$ to give a more heterogenous distribution of the growth factor H, which in turn will make the migration of fibroblasts more heterogenous. We now use $\lambda_5 = (2 \cdot 10^{-5}, 4 \cdot 10^{-7}, 2 \cdot 10^{-7}, 4 \cdot 10^{-7}, 4 \cdot 10^{-10})$ (see Table 7 for comparison). Essentially, both the level of production and consumption of the growth factor are reduced and the distribution is less influenced by the fibroblasts through the low value of λ_{55}. The result is shown in Figure 5. The change in migration pattern is striking: isolated groups of fibroblasts have formed with corresponding isolated islands of tumor cells. If we

were to consider a tumor with homogeneous histology having low maximal IFP, we generally see less heterogeneous invasion into the tissue compared to Figure 4C (data not shown). How far into the tissue the tumor cells invade does not change when the IFP is reduced, yet the results show different tumor cell distribution at the invasive front.

3.4.2 Compartmentalized ECM, high maximal IFP

We use T_l as for the homogenous case discussed above but now ECM contains compartments which affect T_v. In Figure 6 is an illustration of T_v (panel A) and T_l (panel B). Strong heterogenity is seen both for T_v and T_l and $\hat{k}_w$ is as shown in Figure 2 (H) and reflects the compartmentalized ECM structure which bears similarity to what is seen experimentally in Figure 2 (panel E). The simulated growth of this in silico model is then computed up to a time $T = 50$ (around 5.8 days). The resulting two "measured" IFPs are, respectively, 25 and 23 mmHg, while the maximal IFP is closer to 35 mmHg. In Figure 7 the resulting interstitial fluid pressure (IFP) P_w is shown in panel A whereas the fluid velocity field $\mathbf{u}_w$ is illustrated in panel B. In particular, we observe that the heterogeneity associated with the leaky vascular system through T_v now generates a much more heterogenous IFP within the tumor. Other observations are:

(i) We have assumed the same distribution of the peritumoral lymphatics through T_l as before, see Figure 6B. However, the vascular distribution through T_v, (A), is now dependent on the location of thick ECM bands, causing no fluid production from the vessels within the bands.
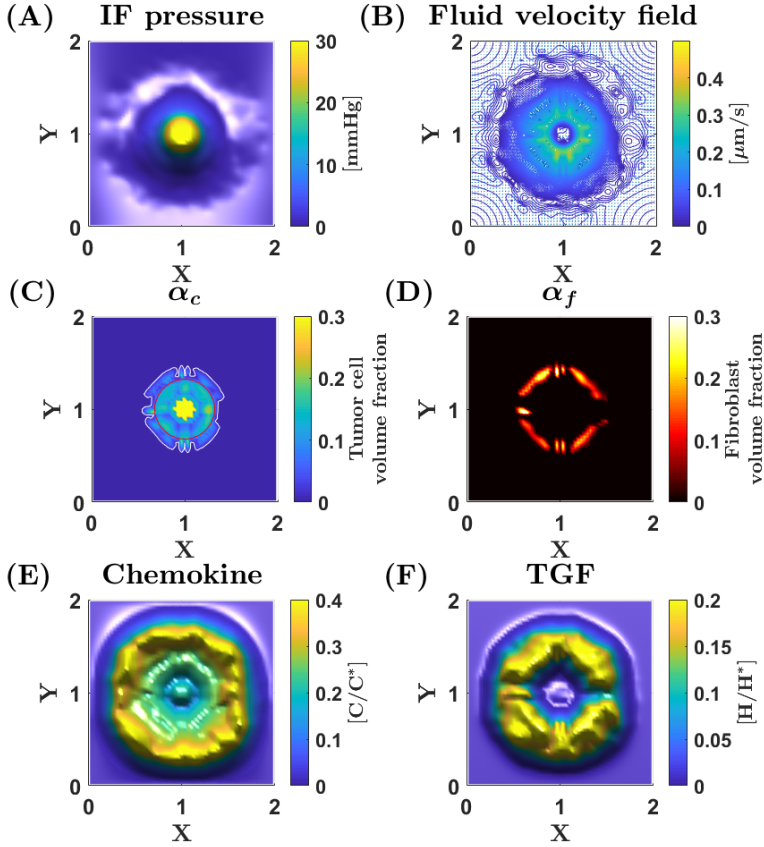
Fig. 4 Simulation results, homogenous ECM: **(A)** Interstitial fluid pressure in mmHg. The pressure is largest within the tumor due to the leaky vascular system, and decreases quickly at its margin. **(B)** Fluid velocity field. The fluid originates from the primary tumor and is flowing towards the lymphatics. The effectiveness of the collecting peritumoral lymphatics determines how far the fluid will flow out from the tumor margin. **(C)** Tumor cell volume fraction at the end of the simulation. The invasive front is fairly homogeneous. The red circle shows the initial tumor cell volume $\alpha_c = 0.01$. The white line is also tumor cell volume fraction $\alpha_c = 0.01$, illustrating the invasive front after simulated period. **(D)** Fibroblast volume fraction at the end of simulation. The fibroblasts have not migrated far from their initial position seen in Figure 1 (B). **(E)** Distribution of chemokine which is released from the ECM through proteolytic decay, transported through the ECM and is causing tumor cell chemotaxis towards the lymphatics. **(F)** TGF is produced by fibroblasts and is transported through the ECM. Fibroblasts chemotact towards positive gradients in TGF.

ii) The tumor cell migration behavior seen in Figure 7C largely is a result of the CAFs migration behavior as reflected in Figure 7D. The invasion front is quite heterogeneous. In particular, in the north-east direction an isolated island of tumor cells is about to form. The distribution of chemokine and TGF (which play a role in the chemotaxis of tumor cells and CAFs, respectively) is shown in panel E and F. The distribution is largely a result of the IF velocity field shown in Figure 7B. The simulation suggests that the more heterogenous distribution of the TGF

growth factor H due to the presence of the different compartments has triggered this metastatic behavior.

(iii) We increase the heterogeneity in growth factor distribution by changing $\{\lambda_{5i}\}$ as for the previous case. The resulting behavior of the in silico model is shown in Figure 8. Again, we see that the more collective groups of CAFs (panel B) trigger a more aggressive tumor cell migration (panel A).

The tumor cell invasion into the tissue seen in Figure 7C is quite heterogeneous, much due to the heterogeneous
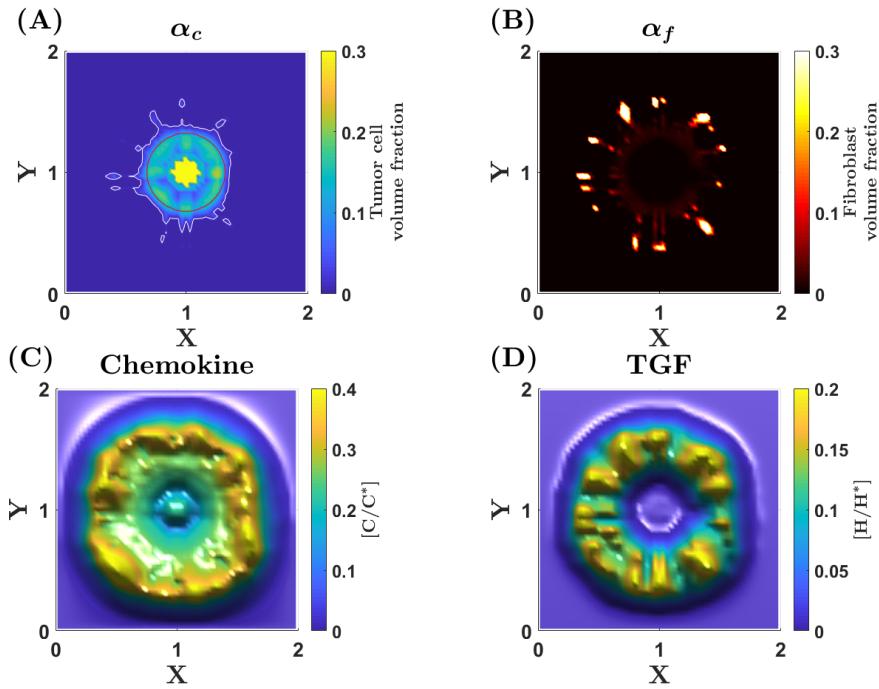
Fig. 5 Increased aggressiveness, homogenous ECM: The production of TGF is now altered to yield a more heterogeneous distribution in the tissue. **(A)** Cancer cell volume fraction. Compared to the case in Figure 4 (C), the tumor cells invade further into the normal tissue while also acting more heterogeneous. **(B)** Fibroblast volume fraction at the end of the simulation. The fibroblasts play an important role in causing tumor cell migration to be more aggressive. **(C)** Chemokine concentration C remains similar as in Figure 4 (E). **(D)** Transforming growth factor concentration, H, is now much more heterogeneous, which causes the fibroblasts to chemotact in different directions and in terms of isolated groups.
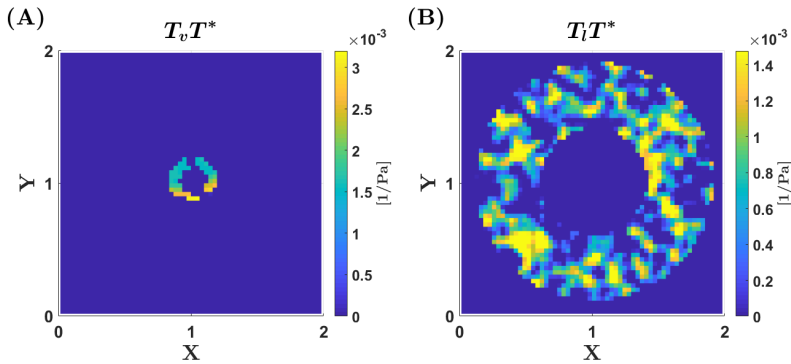
Fig. 6 Parameters characterizing the vessel system, compartmentalized ECM: **(A)** Vascular filtration constant T_v has the same values as Figure 3 (A), yet now also the ECM bands affect the filtration constant T_v, decreasing it to very low values within the bands.. **(B)** Lymphatic filtration constant T_l is exactly the same as for the homogenenous case, seen in Figure 3 (B).
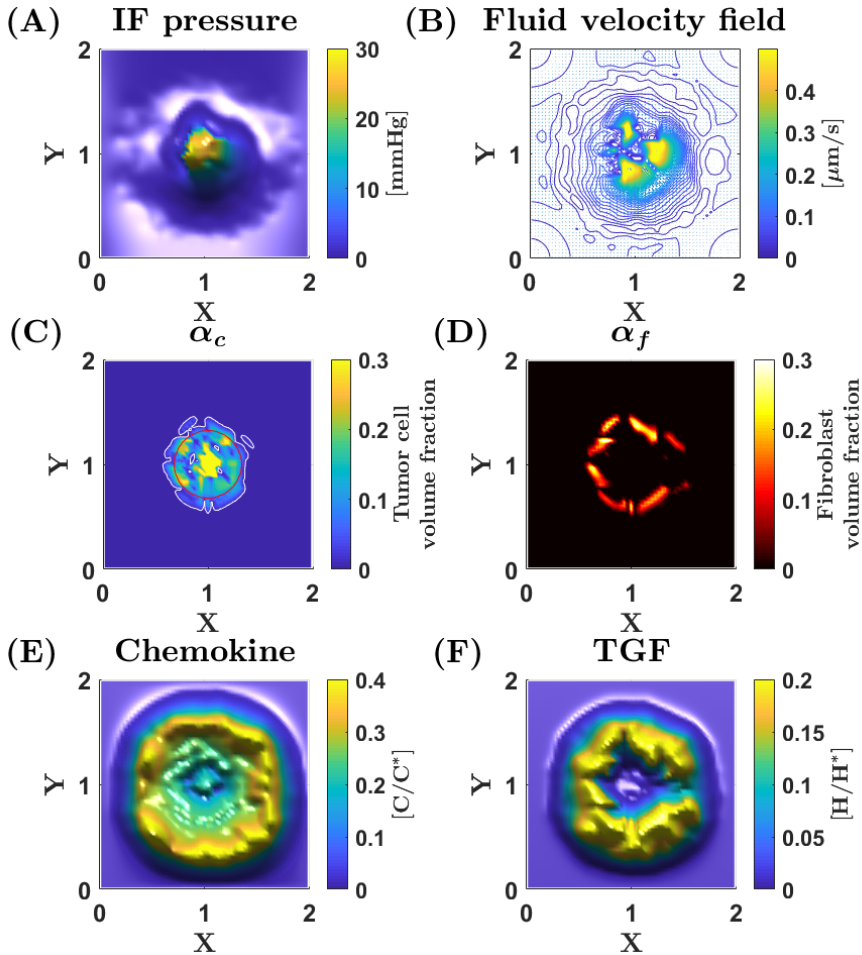
Fig. 7 Simulation results, compartmentalized ECM: **(A)** Interstitial fluid pressure in mmHg. The IFP is highly heterogeneous throughout the tumor due to the compartments. The compartments have the effect of preventing the IFP to even itself out within the tumor. **(B)** Interstitial fluid velocity as a result of the IFP. Since the pressure is very heterogeneous with locally elevated pressures caused by ECM bands with very high resistance to fluid flow, the fluid velocity field also becomes heterogeneous. There are peaks in fluid velocity where fluid may exit the tumor and is not blocked by the ECM bands seen in Figure 2 (H). **(C)** Tumor cell volume fraction at the end of the simulation. At the upper part of the tumor it is evident that some tumor cells are about to detach from the primary tumor. **(D)** Fibroblast volume fraction distribution is fairly heterogeneous in its invasion into the tissue. **(E)** The chemokine distribution is somewhat similar as in the previous cases, leading the cancer cells towards the lymphatics through chemotaxis. **F** TGF produced by the fibroblasts and transported towards the lymphatics, which causes the fibroblasts to migrate towards lymph vessels.

IFP. If we were to use a case with low maximum IFP, we typically see less heterogeneous invasion into the tissue. The low IFP causes less room for heterogeneous pressure between the different compartments and therefore the tumor migration is also less heterogeneous. In addition, if we were to halve the IFP of the case seen in Figure 7, we would no longer see the isolated islands.

3.5 In silico tumor representing pancreatic carcinoma with sparse/dense ECM

Now we focus on the experimental findings for pancreatic cancer reported in [45]. The situation shown in Figure 9 (panel A and E) for Panc-1 pancreatic carcinoma xenograft model with sparse ECM bears similarities to
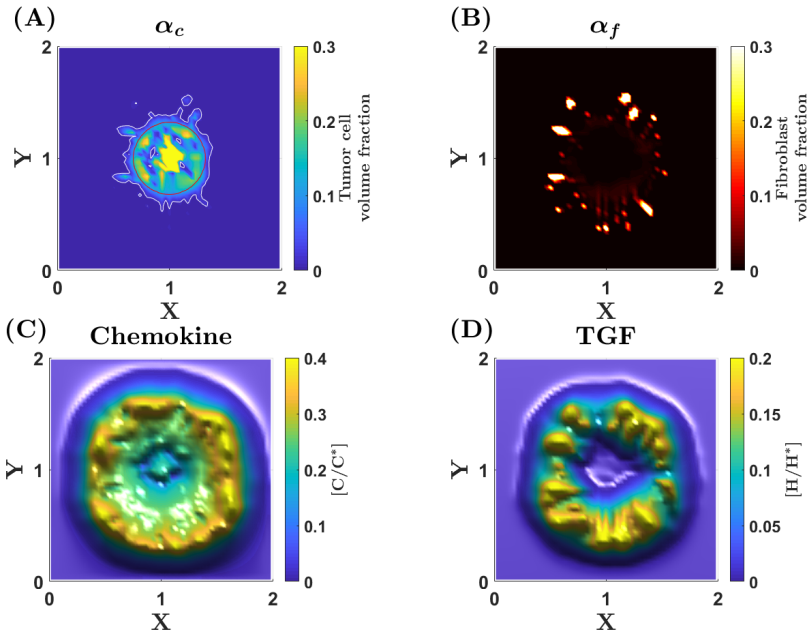
Fig. 8 Increased aggressiveness, compartmentalized ECM. **(A)** Tumor cell volume fraction distribution now has fingers migrating out from the tumor, compared to the previous case seen in Figure 7 (C). **(B)** Fibroblast is migrating in groups towards the lymphatics, causing the fingering effect seen in (A). **(C)** Chemokine concentration C is somewhat similar to the previous cases. **(D)** Transforming growth factor concentration H is reflected by the fibroblast concentration seen in (B). The chemical distribution is heterogeneous and has positive gradients in the direction of the lymphatics.

Table 3 Parameters characterizing the TME of pancreatic carcinoma

Case	Variable	Description	Values
Sparse	$\hat{k}_w$	fluid-ECM resistance force	$2.5 - 5$
	$T_v T^*$	Density of leaky blood vessels	$1 \cdot 10^{-4} - 6 \cdot 10^{-3}$ (1/Pa)
	$T_l T^*$	Density of collecting lymphatics	$1 \cdot 10^{-4} - 2 \cdot 10^{-3}$ (1/Pa)
Dense	$\hat{k}_w$	fluid-ECM resistance force	$12 - 35$
	$T_v T^*$	Density of leaky blood vessels	$0.5 \cdot 10^{-4} - 1 \cdot 10^{-3}$ (1/Pa)
	$T_l T^*$	Density of collecting lymphatics	$1 \cdot 10^{-4} - 2 \cdot 10^{-3}$ (1/Pa)

the case with HL-16 cervical carcinoma with homogenous ECM, which was explored above. In particular, the simulations carried out for that case seem representative for the case with pancreatic cancer with sparse ECM with input parameters for $\hat{k}_w$, T_v, and T_l as indicated in Table 3. Hence, we focus on the case with dense ECM. The dense ECM is accounted for by letting the resistance force through $\hat{k}_w$ vary within a larger interval and with higher values but such that it takes a constant value for each in silico tumor. At the same time we assume that this denser, desmoplastic ECM increases the collapse of leaky vascular vessels giving rise to a lower value of T_v, as reflected by the interval given in Table 3 (dense). This is necessary in order to ensure that

the resulting IFP values remain within a pathological reasonable range. We assume that the lymphatic network is characterized as before. Again, an ensemble of 50 in silico pancreatic tumors are generated. The corresponding IFP at two different positions (ventral and dorsal) are recorded and plotted in Figure 9 (panel D). Analogous to Figure 2 the ventral IFP and dorsal IFP seen on the axes only describe that the measurements are performed at two different positions. Similar to the experimental results shown in Figure 9 (panel B), the resulting IFP shows a heterogenous distribution. In the following, we take a closer look at the mechanisms behind this possible heterogenous intratumoral IFP.
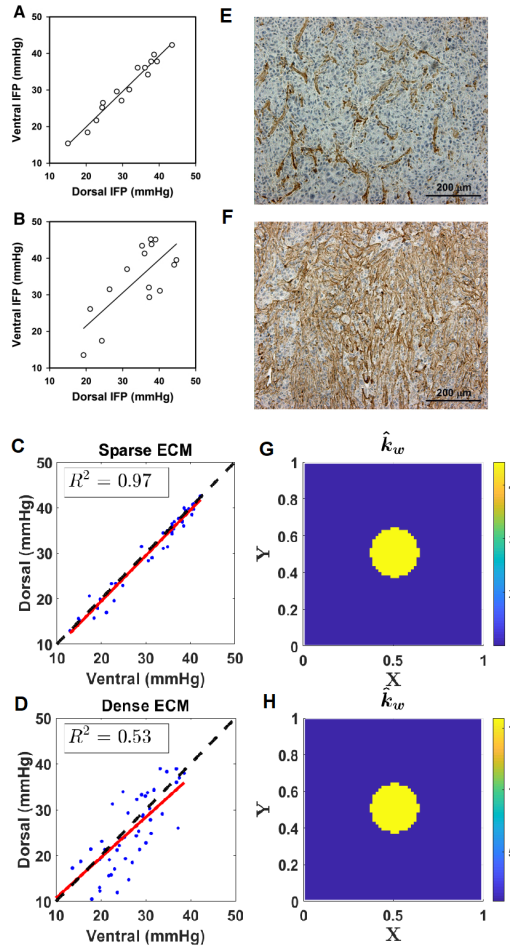
Fig. 9 Panc-1 pancreatic carcinoma. Experimental results for (i) sparse ECM (A,E); (ii) dense ECM (B,F). **A,B** IFP measurements taken at two different places within a tumor for a total of 15 of each type of histology, corresponding to **E** and **F**. The respective coefficient of determination for **A** and **B** are $R^2 = 0.96$ and $R^2 = 0.54$. The computational model uses 50 tumors of each type of histology to plot the two IFP measurements in **C** and **D**. Within each plot the R^2 value is shown. The corresponding histology is represented by $\hat{k}_w$ in **G** and **H**.P anels **(A)**, **(B)**, **(E)** and **(F)** were reproduced from [45][DOI: 10.1016/j.tranon.2019.05.012]

3.5.1 Dense ECM, high maximal IFP

We choose the same member from the stochastic generated ensemble as the homogeneous HL-16 cervical with respect to T_l distribution as well as the initial fibroblast distribution and simulate tumor growth for a time period of $T = 50$ (5.8 days). The results are shown in Figure 10-12. Some essential points are:

(i) The heterogeneity in the microvascular network through T_v is seen in Figure 10 (panel A) as well as for T_l (panel B). The dense ECM is reflected by a high

value of $\hat{k}_w$ around 15. Corresponding to this characterization of TME, the resulting IFP shown in Fig. 11 (panel A) is high (maximum around 45 mmHg) and heterogeneous within the tumor. The dorsal and ventral IFP take the values 35 and 28, respectively. The heterogenous IF velocity is shown in panel B.

(ii) The tumor cell migration behavior is seen in Figure 11 (panel C) and is largely a result of the CAFs migration behavior seen in panel D. The invasive front is fairly regular with no indication of metastatic propensity. This is naturally linked to the homoge-
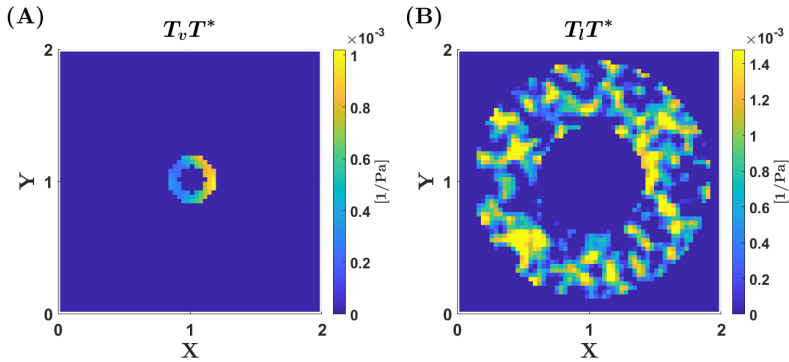
Fig. 10 Parameters characterizing the vascular and lymphatic system, dense ECM: **(A)** The vascular filtration constant T_v that determines the fluid production from the blood vessels within the tumor. **(B)** T_l characterizing the lymphatic network, which is placed in the area surrounding the primary tumor. The value of both T_v and T_l is generated through a Gaussian variogram, while the placement of the vessels is constant.

nous distribution of chemokine (panel E) and TGF growth factor (panel F). However, we may allow the distribution of the TGF factor H becoming more heterogenous (as a result of the heterogenous T_l) by modifying the values of the rate coefficients represented by $\{\lambda_{5i}\}$ involved in the transport-reaction equation for H in $(1)_{10}$. We modify λ_{5i} as we did for the in silico cervical model. Figure 12 (panel A) shows how the cell-fibroblast interaction now results in formation of many isolated islands which is natural to link to high metastatic propensity. This is a consequence of the heterogenous distribution of TGF (panel D) and the resulting heterogenous distribution of CAFs (panel B).

Similar to what we have explained for the two previous cases, a low IFP inside the tumor does not decrease the distance tumor cells migrate from the primary tumor. In this particular case the invasive front is homogeneous for both high and low IFP.

4 Discussion

4.1 Conclusions

The in silico cervical cancer model has demonstrated that homogenous and sparse ECM was associated with a relatively constant (uniform) intratumoral IFP despite the fact that a heterogenous microvascular network was assumed by generating T_v as a 2D gaussian variogram and constrained such that the resulting IFP vary in the pathological relevant range 10-45 mmHg. Inclusion of compartments separated with high-resistant bands was associated with heterogenous intratumoral IFP when the heterogenous T_v was generated as for

the case with homogenous ECM structure. This confirms the underlying hypothesis suggested in [45] that structures within the ECM that prevent fluid flow are responsible for heterogenous IFP observed for HL-16 cervical carcinoma.

For pancreatic cancer the in silico model demonstrated that dense ECM structure (but homogenous) combined with heterogenous microvascular density through the randomly generated T_v gave rise to a heterogenous intratumoral IFP. The dense ECM structure, as reflected by a high resistance force to fluid flow through a uniform but high $\hat{k}_w$, implies that the heterogeneity in T_v is translated into a heterogenous IFP. In conclusion, the in silico model confirms that tissue stromal elements represented a barrier against interstitial convection, thus preventing local differences in IFP from being leveled out by intratumoral fluid flow for the case with Panc-1 pancreatic carcinoma [45].

By changing the parameters λ_{5i} that regulate the production/consumption of TGF a more heterogeneous distribution were achieved which gave rise to more aggressive behavior in both tumor cells and fibroblasts (Figures 5,8,12). These figures are included in order to illustrate that the in silico model is able to yield a large variety of results depending on the set parameters. It is also important to note, that this attribute of the model could be used in the manner of tuning parameters to better comply with an individual tumor where more specific information is available. For instance, in our simulations we have assumed the characteristics with regards to the cell-substrate resistance force, cell-cell adhesion, chemotaxis coefficients and so on, are the same for both tumor types. While this is a clean way of performing simulations, it is not necessarily true and
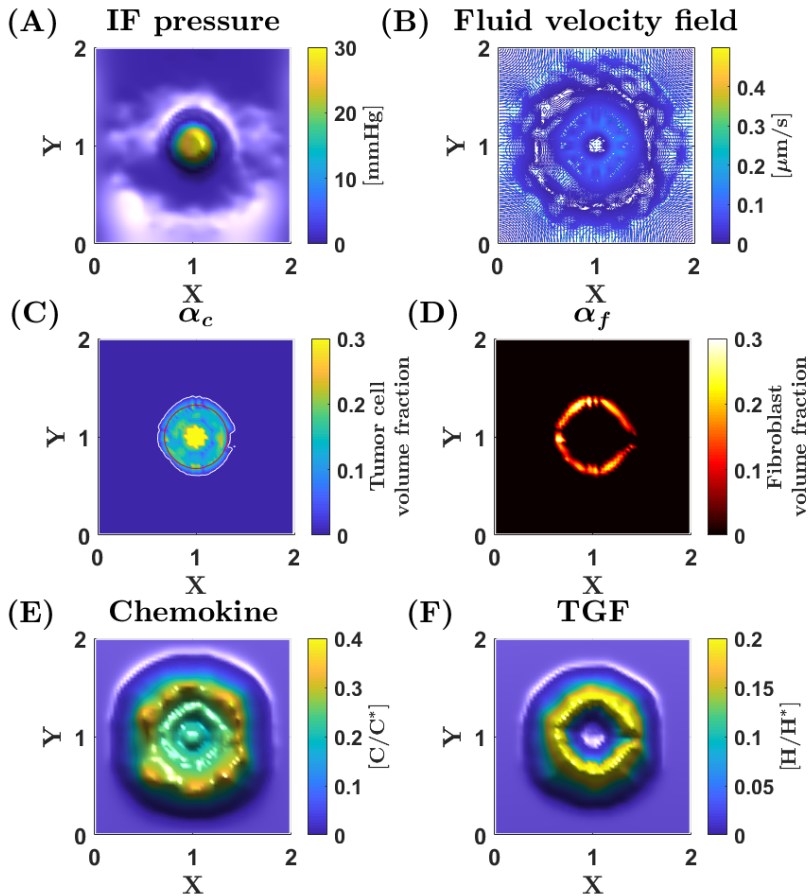
Fig. 11 Simulation results, dense ECM: **(A)** The resulting IFP is clearly correlated to the vascular filtration constant T_v shown in Figure 10A. The resistance to fluid flow within the tumor is high (high $\hat{k}_w$ value), which causes the pressure not to be evened out, leading to heterogeneous IFP. **(B)** Interstitial fluid velocity is low for this type of histology, even though it has a similar magnitude in IFP as for previous cases. This is caused by the high resistsance to fluid flow within the tumor, leading to a lower exit velocity of the fluid. **(C)** The tumor cell volume fraction is homogeneous and the invasion is quite limited. **(D)** Fibroblasts show little aggressive behavior and have not migrated far from their initial position. **(E)** Due to the low fluid velocity, the chemokine is not transported far from where it is being produced. The same applies to the TGF distribution in **(F)**.

one could envision to use different sets of parameters for the two tumors.

The proposed in silico model, previously explored and tested in [42,43], accounts for fluid-sensitive migration mechanisms found from in vitro studies [40,51] which involve autologous chemotaxis related to cancer cells and fibroblasts, combined with ECM remodelling and cell-fibroblast interaction. The combination of the leaky intratumoral vascular network and the peritumoral lymphatic network which collects this fluid gives rise to elevated IFP. This situation might be associated

with high metastatic propensity because hem- and lymphangiogenic factors, proteolytic enzymes, cytokines, and other metastasis-promoting molecules are transported from the primary tumor into peritumoral lymphatics [58,45]. The in silico model has demonstrated that when tumor cells are armed with these mechanisms, the progression of the tumor can result in aggressive behavior where groups of tumor cells detach from the primary tumor and form isolated islands. It is natural to link this behavior to increased metastatic propensity. In fact, the study in [59], though in the con-
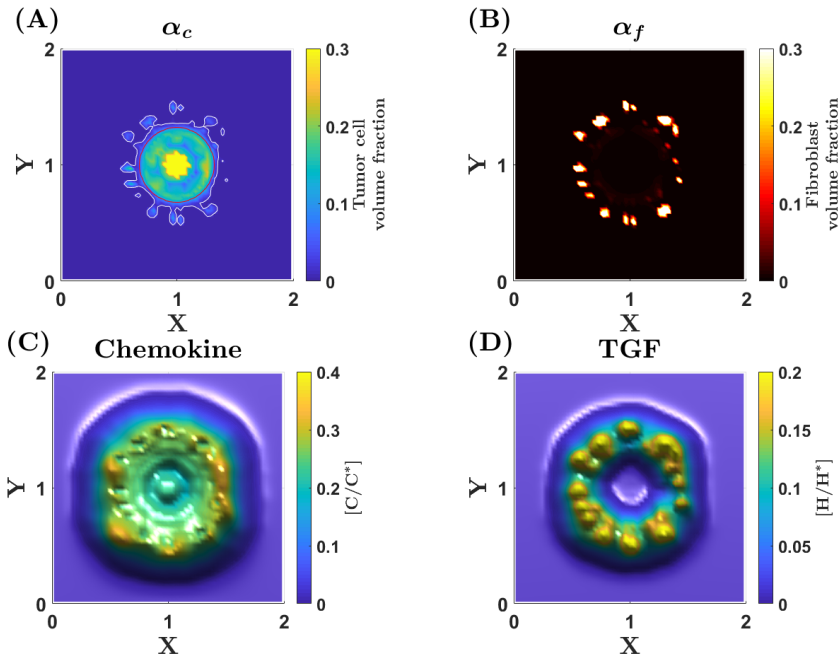
Fig. 12 Increased aggressiveness, dense ECM. **(A)** The cancer cells now invade much further into the surrounding tissue, leading to both isolated islands and fingering. **(B)** Fibroblasts migrate in small clusters outwards from the primary tumor, thereby guiding groups of cancer cells effectively away from the primary tumor. **(C)** The chemokine concentration remains close to the primary tumor while at the same time is heterogeneous in its concentration profile. **(D)** Transforming growth factor concentration H distribution is heterogeneous, causing fibroblasts to move in clusters.

text of lung cancer, found a direct association between formation of isolated islands composed of groups of tumor cells and metastatic propensity. The prognosis of lung adenocarcinomas with tumor islands was significantly worse than those without. The in silico model suggests that the combination of heterogenous fibroblast migration and cell-fibroblast interaction can be a driver for this aggressive behavior.

The findings in [45] have suggested that the common assumption that resistance to interstitial fluid flow is low in tumor tissue is not necessarily valid for tumors developing a complex, dense, and heterogeneous stroma. The suggested in silico model has more precisely illustrated the mechanisms that most likely are at play. In particular, it has demonstrated how barriers against interstitial convection may have significant implications for the distribution of all kinds soluble molecules produced and secreted by cancer and stromal cells. This also will carry over to the distribution of chemical therapeutic agents. The computer model therefore can be interesting to use to explore barriers for efficient delivery of therapeutic drugs.

4.2 Limitations of the model

A limitation of the current version of the in silico model is that it does not explain the reported correlation that seems to exist between high IFP and high metastatic propensity, as found in [45,17] and related work [49]. Presuming that isolated islands is a means to metastasis, the model does not indicate that higher IFP tumors tend to have more isolated islands. Both high IFP tumors and low IFP tumors show a similar tendency to generate isolated islands. More precisely, this behavior seems to depend more strongly on a heterogenous distribution of the TGF concentration H than on the level of IFP. In fact, we found that the parameter family λ_{5i} in $(1)_{10}$ which controls the production, consumption and decay of TGF, largely affected the level of heterogenity in TGF distribution in the peritumoral region. Apparently, the computer model is lacking some sort of aggressivity when it comes to fluid-sensitive migration mechanisms. On the other hand, as found in [60, 61], computer models that include the combination of downstream migration driven by autologous chemotaxis

and strain-induced upstream mechanisms as explored in [51,52] suggest that aggressive tumor cell behavior is correlated to higher IFP. An interesting extension of the computer model discussed in this work would be to account for both these mechanisms.

The computer model explored in this work has been designed to capture bulk-level aspects of tumor growth and metastatic propensity and constrained by data from the study of preclinical models in [45]. In that sense the model we consider bears similarities to the computer models explored in [62,63] which focus on capturing first-order effects pertaing to tumor growth and avoid representing many different parameters which are impractical or impossible to measure clinically (e.g., immune response, extracellular matrix status, genetic mutations, detailed representation of the angionesis, etc.). Extended computer models may also involve a multiscale approach where one can explore tumor growth by considering major biological events at both tissue, cellular, and subcellular scale [64]. This has been outside the scope of the current investigations.

References

1. E. Castellanos, J. Berlin, D.B. Cardin, Current Oncology Reports **13**(3), 195 (2011)
2. J.M. Winter, M.F. Brennan, L.H. Tang, M.I. DAngelica, R.P. DeMatteo, Y. Fong, D.S. Klimstra, W.R. Jarnagin, P.J. Allen, Annals of Surgical Oncology **19**(1), 169 (2012)
3. C.J. Whatcott, C.H. Diep, P. Jiang, A. Watanabe, J. LoBello, C. Sima, G. Hostetter, H.M. Shepard, D.D. Von Hoff, H. Han, Clinical Cancer Research **21**(15), 3561 (2015)
4. M.F. Bijlsma, H.W. van Laarhoven, Cancer and Metastasis Reviews **34**(1), 97 (2015)
5. C. Feig, A. Gopinathan, A. Neesse, D.S. Chan, N. Cook, D.A. Tuveson, Clinical Cancer Research **18**(16) (2012)
6. D. Mahadevan, D.D. Von Hoff, Molecular Cancer Therapeutics **6**(4), 1186 (2007)
7. A. Neesse, P. Michl, K.K. Frese, C. Feig, N. Cook, M.A. Jacobetz, M.P. Lolkema, M. Buchholz, K.P. Olive, T.M. Gress, et al., Gut **60**(6), 861 (2011)
8. D.M. Fink, M.M. Steele, M.A. Hollingsworth, Cancer Letters **381**(1), 217 (2016)
9. P.P. Provenzano, C. Cuevas, A.E. Chang, V.K. Goel, D.D. Von Hoff, S.R. Hingorani, Cancer Cell **21**(3), 418 (2012)
10. V.P. Chauhan, Y. Boucher, C.R. Ferrone, S. Roberge, J.D. Martin, T. Stylianopoulos, N. Bardeesy, R.A. DePinho, T.P. Padera, L.L. Munn, et al., Cancer Cell **26**(1), 14 (2014)
11. C.C. DuFort, K.E. DelGiorno, M.A. Carlson, R.J. Osgood, C. Zhao, Z. Huang, C.B. Thompson, R.J. Connor, C.D. Thanos, J.S. Brockenbrough, et al., Biophysical Journal **110**(9), 2106 (2016)
12. N. Dhani, S. Serra, M. Pintilie, J. Schwock, J. Xu, S. Gallinger, R. Hill, D. Hedley, British Journal of Cancer **113**(6), 864 (2015)
13. N. Dhani, A. Fyles, D. Hedley, M. Milosevic, in *Seminars in Nuclear Medicine*, vol. 45 (Elsevier, 2015), vol. 45, pp. 110–121
14. I. Lohse, C. Lourenco, E. Ibrahimov, M. Pintilie, M.S. Tsao, D.W. Hedley, Cancers **6**(1), 459 (2014)
15. D. Singh, G. Upadhyay, R.K. Srivastava, S. Shankar, Biochimica et Biophysica Acta (BBA)-Reviews on Cancer **1856**(1), 13 (2015)
16. E. Fokas, E. O'Neill, A. Gordon-Weeks, S. Mukherjee, W.G. McKenna, R.J. Muschel, Biochimica et Biophysica Acta (BBA)-Reviews on Cancer **1855**(1), 61 (2015)
17. L.M.K. Andersen, C.S. Wegner, T.G. Simonsen, R. Huang, J.V. Gaustad, A. Hauge, K. Galappathi, E.K. Rofstad, Oncotarget **8**(29), 48060 (2017)
18. L. Barbera, G. Thomas, in *Seminars in Oncology*, vol. 36 (Elsevier, 2009), vol. 36, pp. 155–169
19. Z. Al-Mansour, C. Verschraegen, Current Opinion in Oncology **22**(5), 503 (2010)
20. J.A. Green, J.J. Kirwan, J. Tierney, C.L. Vale, P.R. Symonds, L.L. Fresco, C. Williams, M. Collingwood, Cochrane Database of Systematic Reviews (3) (2005)
21. A.H. Klopp, P.J. Eifel, in *Seminars in Radiation Oncology*, vol. 22 (Elsevier, 2012), vol. 22, pp. 143–150
22. M. Höckel, P. Vaupel, in *Seminars in Oncology*, vol. 28 (Elsevier, 2001), vol. 28, pp. 36–41
23. P.W. Vaupel, D.K. Kelleher, International Journal of Hyperthermia **28**(6), 518 (2012)
24. M. Höckel, C. Knoop, K. Schlenger, B. Vorndran, E. Bauβnann, M. Mitze, P.G. Knapstein, P. Vaupel, Radiotherapy and Oncology **26**(1), 45 (1993)
25. M. Höckel, K. Schlenger, B. Aral, M. Mitze, U. Schäffer, P. Vaupel, Cancer Research **56**(19), 4509 (1996)
26. A.W. Fyles, M. Milosevic, R. Wong, M.C. Kavanagh, M. Pintilie, A. Sun, W. Chapman, W. Levin, L. Manchul, T.J. Keane, et al., Radiotherapy and Oncology **48**(2), 149 (1998)
27. K. Sundfør, H. Lyng, C.G. Tropé, E.K. Rofstad, Radiotherapy and Oncology **54**(2), 101 (2000)
28. M. Milosevic, A. Fyles, D. Hedley, M. Pintilie, W. Levin, L. Manchul, R. Hill, Cancer Research **61**(17), 6400 (2001)
29. A. Fyles, M. Milosevic, M. Pintilie, A. Syed, W. Levin, L. Manchul, R.P. Hill, Radiotherapy and Oncology **80**(2), 132 (2006)
30. S.G. Yeo, J.S. Kim, M.J. Cho, K.H. Kim, J.S. Kim, Clinical Cancer Research **15**(19), 6201 (2009)
31. G. Schwickert, S. Walenta, K. Sundfør, E.K. Rofstad, W. Mueller-Klieser, Cancer Research **55**(21), 4757 (1995)
32. S. Walenta, M. Wetterling, M. Lehrke, G. Schwickert, K. Sundfør, E.K. Rofstad, W. Mueller-Klieser, Cancer Research **60**(4), 916 (2000)
33. C. Croft, J Anat **105**, 189 (1969)
34. A. Desmouliere, C. Guyot, G. Gabbiani, International Journal of Developmental Biology **48**(5-6), 509 (2004)
35. R. Kalluri, M. Zeisberg, Nature Reviews Cancer **6**(5), 392 (2006)
36. C. Gaggioli, S. Hooper, C. Hidalgo-Carcedo, R. Grosse, J.F. Marshall, K. Harrington, E. Sahai, Nature Cell Biology **9**(12), 1392 (2007)
37. X. Zheng, J.L. Carstens, J. Kim, M. Scheible, J. Kaye, H. Sugimoto, C.C. Wu, V.S. LeBleu, R. Kalluri, Nature **527**(7579), 525 (2015)
38. K.R. Fischer, A. Durrans, S. Lee, J. Sheng, F. Li, S.T. Wong, H. Choi, T. El Rayes, S. Ryu, J. Troeger, et al., Nature **527**(7579), 472 (2015)

39. J. Barbazán, D.M. Vignjevic, Current Opinion in Cell Biology **56**, 71 (2019)
40. A.C. Shieh, H.A. Rozansky, B. Hinz, M.A. Swartz, Cancer Research **71**(3), 790 (2011)
41. A. Labernadie, T. Kato, A. Brugués, X. Serra-Picamal, S. Derzsi, E. Arwert, A. Weston, V. González-Tarragó, A. Elosegui-Artola, L. Albertazzi, et al., Nature Cell Biology **19**(3), 224 (2017)
42. J. Urdal, J.O. Waldeland, S. Evje, Biomechanics and Modeling in Mechanobiology **18**(4), 1047 (2019)
43. J.O. Waldeland, W.J. Polacheck, S. Evje, Journal of Biomechanics p. DOI: 10.1016/j.jbiomech.2019.109568 (2019)
44. S.C. Schwager, P.V. Taufalele, C.A. Reinhart-King, Cellular and Molecular Bioengineering **12**(1), 1 (2019)
45. L.M.K. Hansem, R. Huang, C.S. Wegner, T.G. Simonsen, J.V. Gaustad, A. Hauge, E.K. Rofstad, Translational Oncology **12**(8), 1079 (2019)
46. J.O. Waldeland, S. Evje, Chemical Engineering Science **191**, 268 (2018)
47. S. Evje, Chemical Engineering Science **165**, 240 (2017)
48. R.K. Jain, J.D. Martin, T. Stylianopoulos, Annual Review of Biomedical Engineering **16**, 321 (2014)
49. T. Hompland, C. Ellingsen, K.M. Øvrebø, E.K. Rofstad, Cancer Research **72**(19), 4899 (2012)
50. A. dEsposito, P.W. Sweeney, M. Ali, M. Saleh, R. Ramasawmy, T.A. Roberts, G. Agliardi, A. Desjardins, M.F. Lythgoe, R.B. Pedley, et al., Nature Biomedical Engineering **2**(10), 773 (2018)
51. W.J. Polacheck, J.L. Charest, R.D. Kamm, Proceedings of the National Academy of Sciences **108**(27), 11115 (2011)
52. W.J. Polacheck, A.E. German, A. Mammoto, D.E. Ingber, R.D. Kamm, Proceedings of the National Academy of Sciences **111**(7), 2447 (2014)
53. J. Guo, W. Lou, Y. Ji, S. Zhang, Oncology Letters **5**(5), 1572 (2013)
54. J. Sperveslage, S. Frank, C. Heneweer, J. Egberts, B. Schniewind, M. Buchholz, F. Bergmann, N. Giese, J. Munding, S.A. Hahn, et al., International Journal of Cancer **131**(4), E371 (2012)
55. D. Von Ahrens, T.D. Bhagat, D. Nagrath, A. Maitra, A. Verma, Journal of Hematology & Oncology **10**(1), 76 (2017)
56. E. Lakiotaki, S. Sakellariou, K. Evangelou, G. Liapis, E. Patsouris, I. Delladetsima, Apmis **124**(3), 181 (2016)
57. S.J. Lunt, A. Fyles, R.P. Hill, M. Milosevic, Future Oncol. (2008)
58. H. Wiig, M.A. Swartz, Physiological Reviews **92**(3), 1005 (2012)
59. M.L. Onozato, A.E. Kovach, B.Y. Yeap, V. Morales-Oyarvide, V.E. Klepeis, S. Tammireddy, R.S. Heist, E.J. Mark, D. Dias-Santagata, A.J. Iafrate, et al., The American Journal of Surgical Pathology **37**(2), 287 (2013)
60. J.O. Waldeland, S. Evje, Journal of Biomechanics **81**, 22 (2018)
61. S. Evje, J.O. Waldeland, Cellular and Molecular Bioengineering **12**(3), 227 (2019)
62. J.A. Weis, M.I. Miga, L.R. Arlinghaus, X. Li, V. Abramson, A.B. Chakravarthy, P. Pendyala, T.E. Yankeelov, Cancer Research **75**(22), 4697 (2015)
63. J.A. Weis, M.I. Miga, T.E. Yankeelov, Computer Methods in Applied Mechanics and Engineering **314**, 494 (2017)
64. M.M. Rahman, Y. Feng, T.E. Yankeelov, J.T. Oden, Computer Methods in Applied Mechanics and Engineering **320**, 261 (2017)

Appendix A: Input parameters

Table 4 Functions involved in cell migration given by Eq. (6) and (7)

Function		Description	Values
$\Delta P_{cw}(\alpha_c)$	=	$-\gamma_c \ln(\delta_c + [1-\alpha_c])$	(δ_c=0.01; γ_c=1 kPa)
$\Delta P_{fw}(\alpha_f)$	=	$\gamma_f \alpha_f^{\delta_f}$	(δ_f=10; γ_f=7.5 kPa)
$\Lambda_C(C)$	=	$\Lambda_{C0} - \frac{\Lambda_{C1}}{1+\exp(-\xi_C(C-C_M))}$	($\{\Lambda_{C0}, \Lambda_{C1}\}$={0,25} kPa; $\xi_C = 8/C^*$ m^3/kg)
$\Lambda_H(H)$	=	$\Lambda_{H0} - \frac{\Lambda_{H1}}{1+\exp(-\xi_H(H-H_M))}$	($\{\Lambda_{H0}, \Lambda_{H1}\}$={0,50} kPa; $\xi_H = 16/H^*$ m^3/kg)
$\hat{f}_c(\alpha_c, \alpha_f)$	=	$\frac{\alpha_c[\alpha_f\hat{\zeta}_{cf}+\alpha_c(\hat{\zeta}_{cf}+\hat{\zeta}_f)]}{(\alpha_c+\alpha_f)^2\hat{\zeta}_{cf}+\alpha_c^2\hat{\zeta}_f+\alpha_f^2\hat{\zeta}_c+\frac{\alpha_w^2}{\zeta_w}(\hat{\zeta}_c\hat{\zeta}_f+\hat{\zeta}_c\hat{\zeta}_f+\hat{\zeta}_{cf}\hat{\zeta}_f)}$	(see Eqs. (2) and (3))
$\hat{f}_f(\alpha_c, \alpha_f)$	=	$\frac{\alpha_f[\alpha_c\hat{\zeta}_{cf}+\alpha_f(\hat{\zeta}_{cf}+\hat{\zeta}_c)]}{(\alpha_c+\alpha_f)^2\hat{\zeta}_{cf}+\alpha_c^2\hat{\zeta}_f+\alpha_f^2\hat{\zeta}_c+\frac{\alpha_w^2}{\zeta_w}(\hat{\zeta}_c\hat{\zeta}_f+\hat{\zeta}_c\hat{\zeta}_f+\hat{\zeta}_{cf}\hat{\zeta}_f)}$	(see Eqs. (2) and (3))
$\hat{h}_1(\alpha_c, \alpha_f)$	=	$\frac{\alpha_c\frac{\alpha_w^2}{\zeta_w}[\alpha_c(\hat{\zeta}_f+\hat{\zeta}_{cf})+\alpha_f\hat{\zeta}_{cf}]}{(\alpha_c+\alpha_f)^2\hat{\zeta}_{cf}+\alpha_c^2\hat{\zeta}_f+\alpha_f^2\hat{\zeta}_c+\frac{\alpha_w^2}{\zeta_w}(\hat{\zeta}_c\hat{\zeta}_f+\hat{\zeta}_c\hat{\zeta}_f+\hat{\zeta}_{cf}\hat{\zeta}_f)}$	(see Eqs. (2) and (3))
$\hat{h}_2(\alpha_c, \alpha_f)$	=	$\frac{\alpha_c\alpha_f(\alpha_c\alpha_f-\frac{\alpha_w^2}{\zeta_w}\hat{\zeta}_{cf})}{(\alpha_c+\alpha_f)^2\hat{\zeta}_{cf}+\alpha_c^2\hat{\zeta}_f+\alpha_f^2\hat{\zeta}_c+\frac{\alpha_w^2}{\zeta_w}(\hat{\zeta}_c\hat{\zeta}_f+\hat{\zeta}_c\hat{\zeta}_f+\hat{\zeta}_{cf}\hat{\zeta}_f)}$	(see Eqs. (2) and (3))
$\hat{h}_3(\alpha_c, \alpha_f)$	=	$\frac{\alpha_f\frac{\alpha_w^2}{\zeta_w}[\alpha_c\hat{\zeta}_c+\alpha_f(\hat{\zeta}_c+\hat{\zeta}_{cf})]}{(\alpha_c+\alpha_f)^2\hat{\zeta}_{cf}+\alpha_c^2\hat{\zeta}_f+\alpha_f^2\hat{\zeta}_c+\frac{\alpha_w^2}{\zeta_w}(\hat{\zeta}_c\hat{\zeta}_f+\hat{\zeta}_c\hat{\zeta}_f+\hat{\zeta}_{cf}\hat{\zeta}_f)}$	(see Eqs. (2) and (3))

Table 5 Parameters characterizing the mobility of tumor cells and fibroblasts by Eq. (2)

Variable	Description	Values
$I_w, \hat{k}_w, r_w$	fluid-ECM interaction	$2\cdot10^{12}$ (Pa s/m^2), 1, 0
$I_c, \hat{k}_c, r_c$	cell-ECM interaction	$2000 I_w$ (Pa s/m^2), 0.6
$I_f, \hat{k}_f, r_f$	fibroblast-ECM interaction	$100 I_w$ (Pa s/m^2), 1, 0.6
I_{cf}, r_{cf}, r_{fc}	cell-fibroblast interaction	$1000 I_w$ (Pa s/m^2), 0.5, 0.5
A, B	Reduced cell-ECM resistance (see Eq. (3))	0.7, 50

Table 6 Reference variables

Variable	Description	Values
T^*	Reference time	10^4 s
L^*	Reference length	0.01 m
u^*	Reference velocity	10^{-6} m/s
D^*	Reference diffusion	10^{-8} m^2/s
P^*	Reference pressure	10^4 Pa
ρ^*	Reference ECM density	1 kg/m^3
G^*	Reference protease density	10^{-4} kg/m^3
C^*	Reference chemokine density	10^{-4} kg/m^3
H^*	Reference TGF density	10^{-4} kg/m^3
ρ_M, G_M, C_M, H_M	Max ECM, protease, chemokine, TGF density	ρ^*, $0.5G^*$, $0.3C^*$, $0.2H^*$

Table 7 Parameters for autologous chemotaxis described by Eqs. $(1)_{7,8,9,10}$

Variable	Description	Values
D_G	Diffusion coefficient protease	8×10^{-12} m^2/s
D_C	Diffusion coefficient chemokine	14×10^{-12} m^2/s
D_H	Diffusion coefficient TGF	8×10^{-12} m^2/s
$\lambda_{11}, \lambda_{12}, \lambda_{13}$	Proliferation/Decay tumor cells	$0, 0, 0$
λ_{21}	Degradation ECM	10 m^3/kg s
λ_{22}	Release/Reconstruction ECM	1.25×10^{-3} 1/s
λ_{23}	Release/Reconstruction ECM	0 1/s
λ_{24}	Release/Reconstruction ECM	1.25×10^{-3} 1/s
λ_{31}	Natural decay protease	2.5×10^{-3} 1/s
λ_{32}	Production protease from cells	2×10^{-6} kg/m^3 s
λ_{33}	Logistic rate constant protease	2×10^{-6} kg/m^3 s
ν_G	Logistic rate exponent	1.0
λ_{41}	Proteolytically freed chemokine	3.2×10^{-3} m^3/kg s
λ_{42}	Logistic rate constant chemokine	1.4×10^{-4} m^3/kg s
λ_{43}	Logistic rate constant chemokine	3.2×10^{-3} m^3/kg s
λ_{44}	Cell consumption rate chemokine	2.0×10^{-8} 1/s
ν_C, M_C	Logistic rate exponent, absorption percentage	0.2, 50%
λ_{51}	Natural decay of TGF	2×10^{-5} m^3/kg s
λ_{52}	Proteolytically freed TGF	1.4×10^{-6} m^3/kg s
λ_{53}	Logistic rate constant TGF	4×10^{-6} m^3/kg s
λ_{54}	Logistic rate constant TGF	5.5×10^{-7} 1/s
λ_{55}	Cell consumption rate TGF	4×10^{-3} 1/s
ν_H, M_H	Logistic rate exponent, absorption percentage	0.2, 50%